SiC AND B_4C AS ELECTROCATALYST SUPPORT MATERIALS FOR LOW TEMPERATURE FUEL CELLS

Thesis Presented for the Degree of
DOCTOR OF PHILISOPHY

Department of Chemical Engineering
University of Cape Town

Prepared by:
Colleen Jackson
MSc Chemical Engineering, University of Cape Town, South Africa

Supervised by:
Dr. Pieter B.J. Levecque (University of Cape Town, RSA)
Dr. Denis Kramer (University of Southampton, UK)
Prof. Andrea E. Russell (University of Southampton, UK)

October 2017

Abstract

SiC and B_4C as Alternative Catalyst Support Materials for Low Temperature Fuel Cells

By Colleen Jackson

Department of Chemical Engineering

University of Cape Town

Supported nano-catalyst technologies are key for increasing the catalyst utilisation and achieving economically feasible platinum metal loadings in hydrogen polymer electrolyte fuel cells (PEFCs). High surface area carbons are commonly utilised as support materials for platinum due to low cost, large surface areas and high conductivity. However, PEFCs using this technology undergo oxidation of carbon supports, significantly reducing the lifetime of the fuel cell.

In this work, silicon carbide and boron carbide are investigated as alternative catalyst support materials to carbon, for the oxygen reduction reaction for low temperature fuel cells. Electrochemical testing, accelerated degradation studies as well as advanced characterisation techniques were used to clarify the structure-property relationships between catalyst morphology, metal-support interaction, ORR activity and surface adsorption onto the Pt nanoparticles. Extended X-ray Absorption Fine Structure (EXAFS) analysis gave insights into the shape of the clustered nanoparticles while X-ray Photoelectron Spectroscopy (XPS) and *in-situ* X-ray Absorption Near-Edge Spectroscopy (XANES) analysis provided information into how the metal-support interaction influences surface adsorption of intermediate species.

Electronic metal-support interactions between platinum and the carbide supports were observed which influenced the electrochemical characteristics of the catalyst, in some cases increasing the oxygen reduction reaction activity, hydrogen oxidation reaction activity and Pt stability on the surface of the support.

Contents

Plagiarism Declaration

"This thesis/dissertation has been submitted to the Turnitin module (or equivalent similarity and originality checking software) and I confirm that my supervisor has seen my report and any concerns revealed by such have been resolved with my supervisor."

Name: Colleen Jackson

Student Number: JCKCOL002

Signed

Signature:

Date: 31/10/2017

Inclusion of Publications in this Doctoral Thesis

I confirm that I have been granted permission by the University of Cape Town's Doctoral Degrees Board to include the following publications in my PhD thesis, and where co-authorships are involved, my co-authors have agreed that I may include the publications:

a) Jackson, C., Smith, G.T., Inwood, D.W., Leach, A.S., Whalley, P.S., Callisti, M., Polcar, T., Russell, A.E., Levecque, P., Kramer, D. 2017. *Nature Communications*. 8:15802.

b) (Submitted) Jackson, C., Smith, G.T., Markiewicz, M, Inwood, D.W., Leach, A.S., Whalley, P.S., Kucernak, A., Russell, A.E., Kramer, D., Levecque, P. 2017. *Journal of Electroanalytical Chemistry*.

Name: Colleen Jackson

Student Number: JCKCOL002

Signature: Signed

Date: 31/10/2017

Acknowledgements

I have been overwhelmed by all the support I've received during my Ph.D., and the project wouldn't have run so smoothly or been as successful without the help of the people listed below.

Thank you to *Pieter Levecque*, for seeing potential in me after my MSc, for guiding me through my Ph.D. and for being a reliable, consistently available and helpful supervisor. I'm so grateful for the support you've given to me over the years.

Denis Kramer, the vast amount of knowledge you have imparted on me is only the beginning of all I've learnt from you. Your ambition and drive for success is what stands out the most to me, so thank you for including me, at least in part, on your journey.

To *Andrea E. Russell*, thank you for welcoming me into your group and of course, for all the snacks at the beamline. To the *Russell Group,* for the tea and ice cream breaks, and for including me in your group without hesitation.

Graham Smith, you've played such a significant role during my Ph.D., both as academic support and emotional support. Thank you for all the work you've put into my project and for the late night TEM imaging. More importantly, for all the times I thought, 'I can't do this', or 'I'm not good enough', you've been there to reassure and encourage me to persevere, thank you.

Thank you, *Anthony Kucernak*, for giving me the opportunely to work in your laboratory and for your guidance and patience with me during our work together. To the *Kucernak Group*, for being so welcoming, I've thoroughly enjoyed our brief time together.

To *Dave Inwood*, for all you taught me about X-ray absorption modelling and for your willingness to help with the analysis.

Matthew Markiewicz, for teaching me how to do the floating electrode measurements and for your patience and helpfulness whilst teaching me.

To the people who took the time out of their projects and lives to help run my beamtimes, *Andrew Leach*, *Penny Whalley*, *Veronica Celorrio*, *Haoliang (Howard) Huang*, *Dave Inwood*, *Graham Smith* and *Andrea E. Russell*.

HySA Catalysis and the *Catalysis Institute* for being my home for so long and for providing a great work environment for its students. Also to *Shiro Tanaka*, for your enthusiasm about research and our interesting conversations about electrocatalysis and fuel cells.

Thank you to all the institutions which provided instrument access. To the *Electron Microscope at UCT* for efficient work ethic and always friendly faces, to the beamline scientists, *Giannantonio Cibin* and *Diego Gianolio*, at *Diamond Light Source* for your support and to the *Analytical Laboratory* in the Chemical Engineering Department at UCT for your hard work.

To my *friends and family* for their support throughout my studies, in particular my parents for believing in my ability, to Urania, Kevin, Jaimie, Tyler and Graham for our Friday night gettogethers and to Michelle for your consistent friendship and support.

Lastly, thank you to my funding sources, the Royal Society in the form of a Royal Society-Newton Advanced Fellowship and University of Cape Town for financial support through a UCT PhD Mobility Grant.

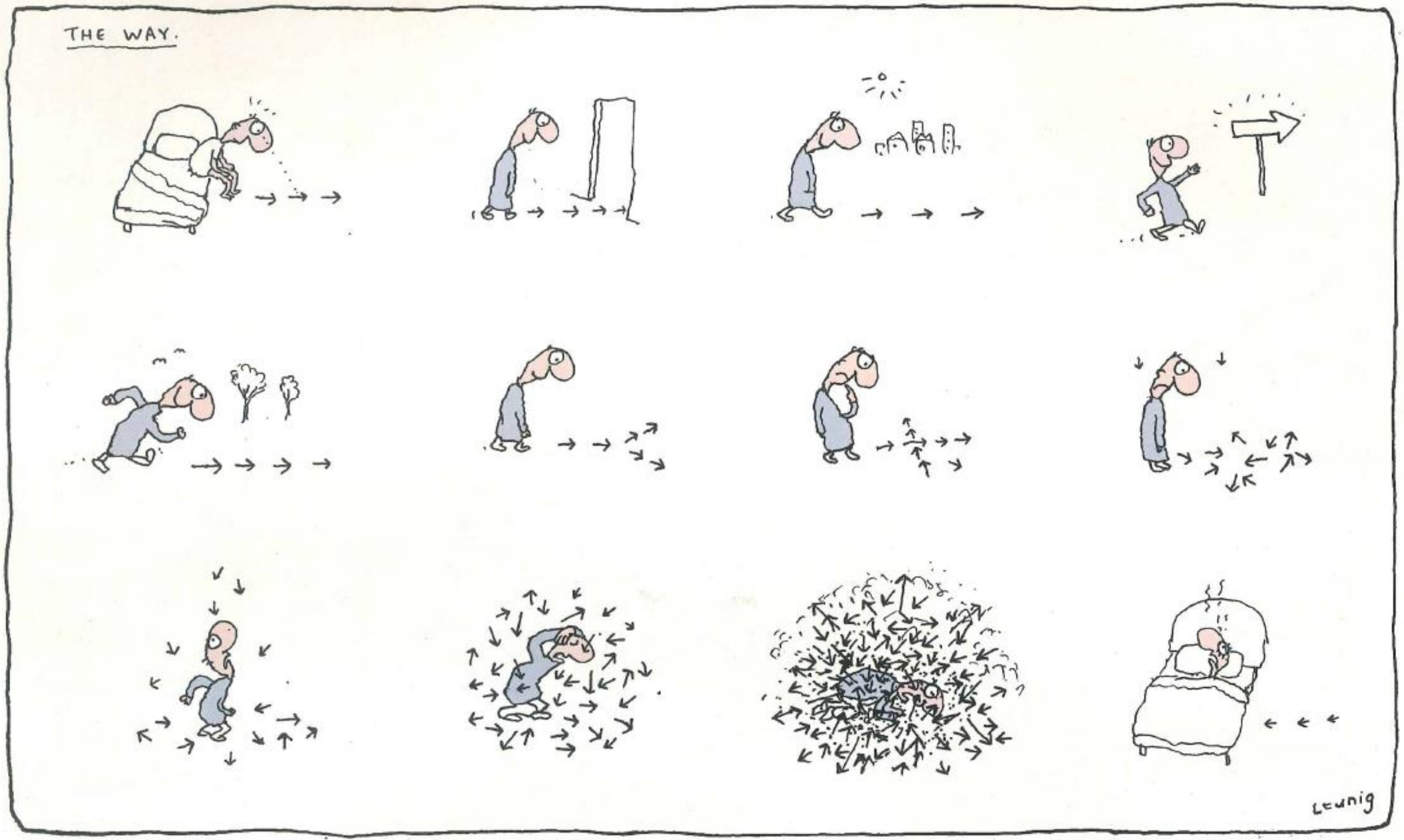
THE WAY.
Leunig

Chapter 1

Introduction

The multi-electron reaction of the oxygen reduction reaction is widely studied in fundamental research into fuel cells and energy [1]. Research is focused on the kinetic activity, stability and cost of the cathode catalysts of the hydrogen PEFC since these are identified as the current challenges to improving the viability of fuel cells for future electricity applications [2]. More specifically, the cathode catalyst improvement is of priority since the oxygen reduction reaction (ORR) is the efficiency limiting reaction [2]. In order for fuel cells to be considered in demanding applications such as automobiles and on the electrical grid, the oxygen reduction efficiency and long-term catalyst durability are important research and development areas. Platinum group metals and platinum based alloys deposited on high surface area carbon are the typical catalysts used for ORR. However, the stability of these catalysts is reduced due to carbon corrosion and the subsequent platinum agglomeration at high cathodic potentials [3]. One approach to this challenge is to investigate alternative catalyst support materials which would provide a high stability and stronger metal-support interactions in acidic environments and at high cathodic potentials [3,4].

Strong metal-support interactions (SMSI) have been shown to increase ORR activity as well as catalyst stability, since a change in the support electronic structure is suggested to influence the d-band electronic structure of a catalyst due to electronic equilibrium between the catalyst and the support [5]. Research into alternative catalyst support materials has predominantly focused on thermodynamically stable metal oxides, such as titanium dioxide [6,7] which demonstrated higher ORR activities when compared to Pt/C catalysts [8]. Despite the higher activity and stability of these catalysts, low surface areas and low electrochemical conductivity of alternative supports are common downfalls of these materials [9]. Transition metal carbides, such as tungsten carbides, were also investigated as a platinum support material with promising electrical conductivity, however, they were found to be unstable at potentials above 0.8 V, as non-conductive oxides are formed on the catalyst surface which decreased the electrical conductivity of the catalyst [10].

Silicon carbide (SiC) and boron carbide (B_4C) exhibit high chemical inertness [9] and a high stability when exposed to acids [11, 12]. SiC is considered chemically inert since the corrosion rate in acids is ≤ 0.002 in/year [13] and B_4C is electrochemically inert when exposed to potentials of up to 2 V in acid [14]. In addition to chemical durability, SiC and B_4C were previously synthesised with high volumetric surface areas of 361 $m^2.m^{-3}$ [15] and 194 $m^2.m^{-3}$ [16] respectively, far exceeding carbon (6.60 $m^2.m^{-3}$) [17].

1.1 Fuel Cell Overview

A hydrogen PEFC consists of two electrodes, the anode and the cathode, which lie on either side of a proton conducting electrolyte membrane, as shown in Figure 1.1. A common electrolyte is a polymer electrolyte ion-exchange membrane (PEM). The electrodes consist of the catalyst layer, the diffusion layer, and the backing layer. A standard catalyst used at the PEFC anode and cathode is platinum supported on carbon [18]. The Pt/C catalyst decreases the activation energy of the half reaction at each electrode, while functioning as proton and electron conductors, being gas permeable, water regulating and corrosion resistant.

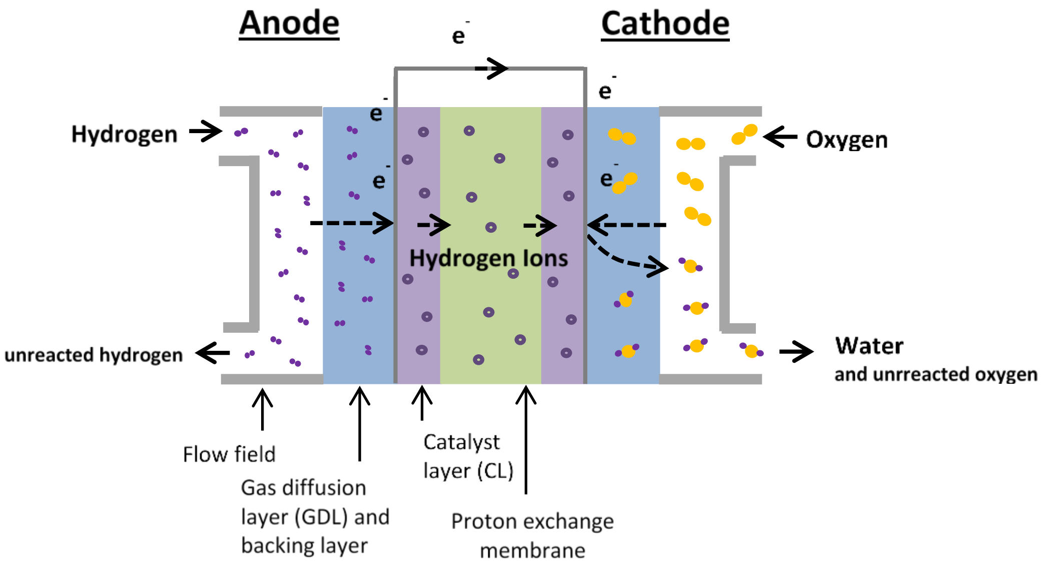

Figure 1.1: Schematic of a hydrogen PEFC.

The half reactions at the electrodes are as follows:

$$Hydrogen\ Oxidation: \quad H_2 \rightarrow 2H^+ + 2e^- \quad \text{Equation 1.1}$$

$$Oxygen\ Reduction: \quad \frac{1}{2}O_2 + 2H^+ + 2e^- \rightarrow H_2O \quad \text{Equation 1.2}$$

$$Overall\ Reaction: \quad H_2 + \frac{1}{2}O_2 \rightarrow H_2O \qquad \text{Equation 1.3}$$

Platinum is the most active element for the oxygen reduction reaction (ORR), as shown by the volcano-shaped plot in Figure 1.2. The relationship between the rate of the cathode reaction and the oxygen adsorption energy shows a volcano-shaped trend, with platinum closest to the peak. Improvement to ORR activity can be made by producing platinum alloyed with metals which have smaller oxygen binding energies than pure platinum [19].

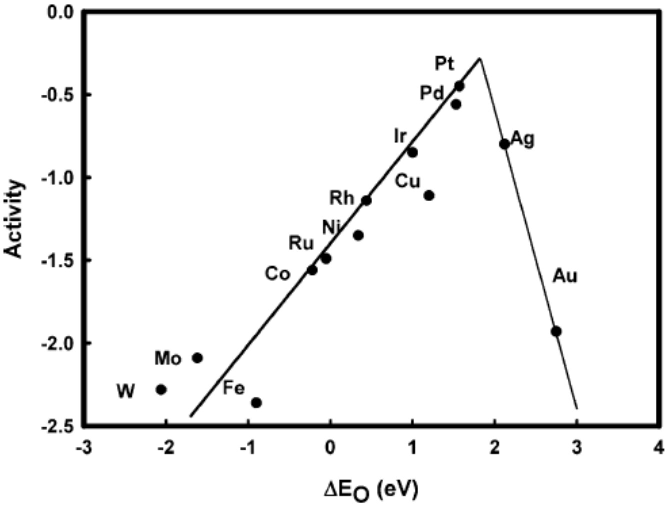

Figure 1.2: Trends in oxygen reduction activity plotted as a function of the oxygen binding energy [19].

The mechanism used to describe the multi-electron oxygen reduction reaction is the modified Wroblowa *et al.* [20] mechanism, as demonstrated in Figure 1.3. This mechanism shows that adsorbed oxygen can be directly reduced to water (via k_1 path) and via an adsorbed peroxide intermediate (via k_2 path). The adsorbed peroxide can be electrochemically reduced to water (via k_3 path), electrochemically decomposed back to adsorbed oxygen (via k_4 path) and/or desorbed as peroxide into the bulk solution (via k_6 path) [21]. The cathode potential (E_C^O) is 1.229 V vs. SHE under standard conditions [22], however, the slow kinetics of the oxygen reduction reaction results in a high overpotential at the cathode [19].

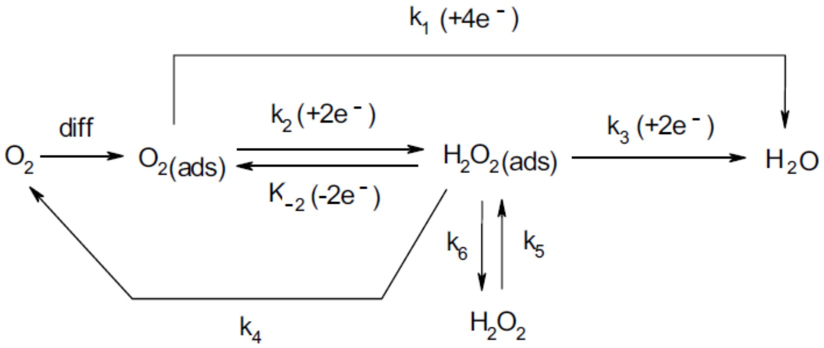

Figure 1.3: Proposed oxygen reduction mechanism on noble metals [22].

Carbon is typically used as an electrochemical support material for platinum nanoparticles since it has a high conductivity, desirable transport properties, high surface area which allows for good catalyst particle distribution and is a low-cost material. Although the thermodynamic oxidation of carbon is favoured at potentials above 0.207 V vs. RHE [23], it is kinetically stable under fuel cell operating conditions [24].

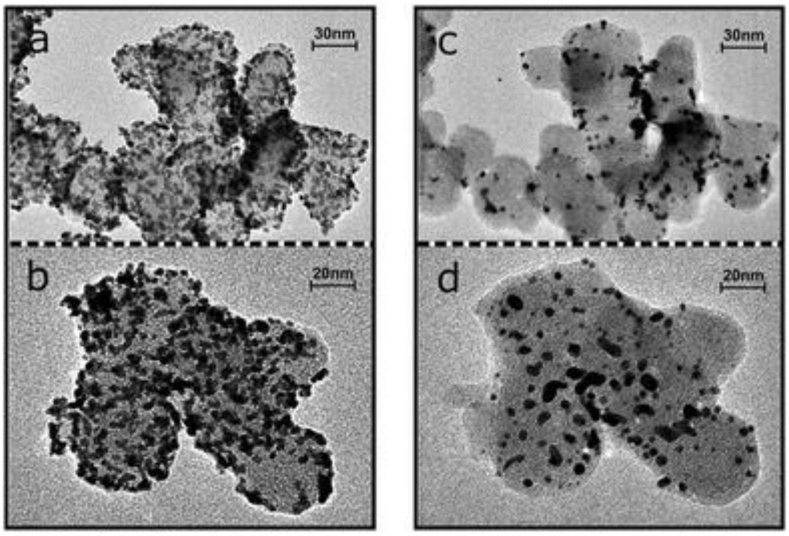

Figure 1.4: IL-TEM of two representative areas of catalyst I before (a and b) and after (c and d) 2 h accelerated degradation treatment consisting of potential cycling between 0.4 and 1.4 V vs. RHE at 1 V.s^{-1} [25].

Despite carbon being kinetically stable under normal cathode potentials, the cathode experiences potentials of up to 1.44 V vs. RHE under start up and shut down fuel cell operations. The high potentials of 1.44 V vs. RHE at the cathode result from hydrogen starvation at the anode, which causes the electrolyte potential to drop from 0 to -0.59 V vs.

RHE when the anode is exposed to an oxidant. This reaction at the anode increases the cathodic interfacial potential difference to 1.44 V vs. RHE, at this potential the cathode catalyst layer is rapidly corroded [4]. In addition, the process of carbon corrosion is partially catalysed platinum [22]. As studied by Dubau *et al.* [26], the formation of holes in the membrane results in hydrogen crossover which form radical species that partake in irreversible corrosion of the high surface area carbon at the cathode, further degrading the catalyst support material. Moreover, amorphous and defected graphitic carbon is more prone to corrosion at lower potentials and higher potentials than highly ordered graphitic carbon [27].

Upon carbon corrosion, the attachment of platinum on the carbon surface is weakened, leading to platinum detachment from the surface. This detachment of Pt leads to platinum agglomeration and platinum dissolution, both resulting in a loss of electrochemically active surface area and therefore loss of ORR mass activity. The TEM images in Figure 1.4 demonstrate the platinum agglomeration and dissolution as a result of carbon corrosion, due to the catalysts' exposure to potentials of 1.4 V. One of the main causes of PEFC performance degradation is the loss of electrochemically active surface area during fuel cell operations [28]. Moreover, carbon corrosion causes an increase in overpotential, and subsequent decrease in fuel cell efficiency, due to increased electrode resistance from a decrease in electrical contact with the current collector [22].

1.2 Corrosion Resistant Supports

A number of approaches have been employed to reduce support corrosion at high potentials, namely, nanostructured thin film catalysts (NSTF), highly graphitised carbon blacks and alternative supports e.g. metal oxides, borides or carbides [2].

The NSTF whiskers have shown resistivity that reduces electrochemical corrosion of the films [17]. However, the disadvantage of NSTFs is the poor water management properties at low temperatures resulting in flooding at the cathode [17]. Graphitised carbon blacks have been used to improve carbon corrosion. Graphitisation of carbon results in a more electrochemically stable support [29]. Additionally, the increased sp^2-hybridized carbons in graphitized carbon, forming the anchoring centres for Pt [30], results in a stronger metal-support interaction. This stronger metal-support interaction is proposed to decrease the sintering of Pt nanoparticles on the graphitised carbon surface [29]. However, there are thermodynamic limitations to the corrosion resistance of carbon and therefore alternative supports to carbon, such as metal oxides and carbides, are investigated.

Titanium oxides have received interest as electrochemically stable catalyst supports with high electrical conductivity of ~10^3 $S.cm^{-1}$ [31]. Krstajic *et al.* [32] stated that due to strong metal-support interactions, TiO_2 is an effective support material which increased the ORR activity of Pt by allowing less strongly adsorbed intermediates to be reduced easily. Contradictory to this, Dieckmann & Langer [33] compared the oxygen reduction activity of Pt/ Ti_nO_{2n-1} ($4 \leq n \leq 10$) to Pt/graphite and the titanium oxide support was shown to decrease the capacity of platinum to catalyse reactions when compared to graphite. Furthermore, the very low surface areas of titanium oxides (~3 $m^2.g^{-1}$), were not comparable to that of carbon (250 $m^2.g^{-1}$) [34]. This low surface area leads to low Pt nanoparticle distribution on the support, resulting in large platinum particle sizes [35]. Antimony doped tin dioxide (SnO_2:Sb) has shown promising electrical conductivity between 10^2-10^3 $S.cm^{-1}$ [36], while carbon electrical conductivity is ~4 $S.cm^{-1}$ [9]. However, the antimony and tin from the Pt/ SnO_2:Sb has been shown to leach from the support at low potentials and poison the Pt catalyst [37]. Additionally, like most inorganic metal oxides [38-43] the support surface area is low and commonly results in large platinum catalyst particles (10 – 20 nm). This low surface area has also shown to impact the Pt utilisation on the support, due to the link between electrical conductivity, support morphology and surface area [44].

Transition metal carbides have demonstrated promising electrochemical activities and durability [45]. High surface area W_2C microspheres prepared by Ganesan & Lee [39] obtained a surface area of 176 $m^2.g^{-1}$, with a 7.5 wt% platinum loading and 6 nm Pt particles. The electrochemically active surface area was recorded as four times that of 20 wt% Pt–Ru/C with a mass activity of more than double for the methanol oxidation reaction, however, tungsten carbides are unstable at potentials above 0.8 V vs. RHE [46]. Pt on nanosized cubic vanadium carbide on carbon particles exhibited a 2.4 times higher ORR mass activity when compared to a commercial Pt/C catalyst, however, stability tests were not mentioned [47]. Metal carbides have shown potential as support materials for the cathode catalyst as they have demonstrated high surface areas and activities, however, more electrochemically stable carbides need to be developed. Therefore, the properties of silicon carbide (SiC) and boron carbide (B_4C) are outlined in Section 1.3.

1.3 Silicon Carbide (SiC) and Boron Carbide (B_4C)

Important factors to consider when working on alternative catalyst support materials are low cost, high corrosion resistance, high electrical conductivity, high surface area and particle structure [2].

1.3.1 Electrical Conductivity

SiC and B_4C are both extrinsic semiconductor materials. SiC has over 200 polytypes, the most common polytypes are 3C-, 4H and 6H-SiC. It is well known that 3C-SiC is the more electrically conductive polytype, with a band gap of 2.3 eV while 4H- and 6H-SiC exhibit band gaps of 3.2 and 3.0 eV [48]. The band gap is the energy difference between the electron valence band and the electron conduction band, therefore it is the energy needed for the material to start conducting electrons. The electrical conductivity of undoped SiC is 0.001 $S.cm^{-1}$ [49]. Boron carbide (B_4C) has diamond-like mechanical properties and is also known for its electrical conductivity since it is used in thermoelectric devices [50]. B_4C has an electrical conductivity of 0.3 $S.cm^{-1}$ at room temperature [51]. Moreover, Cai *et al.* [50] showed silicon doping of B_4C to increases the electrical conductivity by two orders of magnitude, however, the electrical conductivity of undoped B_4C reported by Cai *et al.* (0.05 $S.cm^{-1}$) was far lower than that measured by Wood & Emin [51] (0.3 $S.cm^{-1}$).

1.3.2 Chemical Stability, Electrochemical Stability and Electrochemical Activity

SiC is considered to be chemically inert since the corrosion rate in over 100 different acids, including sulphuric acid, perchloric and aqua regia, is < 0.002 in/year [13], SiC is also electrically stable at high temperatures [52]. Honji *et al.* [53] first proposed SiC as a catalyst support for phosphoric acid fuel cells, the SiC surface area was 10 $m^2.g^{-1}$ with Pt nanoparticles in the range of 3 - 8 nm. The Pt/SiC catalyst showed similar activity to Pt/C at 0.7 V vs. RHE. Later work on SiC nanowires reportedly showed promising results for ORR activity, with a current density of 290 $\mu A.cm^{-2}$ at 0.57 V vs. RHE and high stability [54]. Lv *et al.* [55] also investigated the electrochemical stability of SiC and found the electrochemical stability to be high as minimal change was seen to the cyclic voltammogram over a 48 hour period at 1.2 V vs RHE.

B_4C is also known for its chemical resistance [14]. Grubb & McKee [56] investigated Pt/B_4C catalysts for the anode of the phosphoric acid fuel cell, these catalysts showed better stability and mass activity to Pt/C and Pt/graphite catalysts, this increase in activity was attributed to stability and a support promotional effect. Lv *et al.* [57] prepared platinum deposited on nano-B_4C catalysts and stated the ECSA to be higher at 88 $m^2.g^{-1}$ compared to Pt/C's 62 $m^2.g^{-1}$ with an intrinsic activity which was similar to that of Pt/C.

1.3.3 Support Surface Area and Structure

The support surface area is an important consideration since this surface area should be sufficient to allow for a good dispersion of Pt nanoparticles, to enhance the Pt utilisation and to reduce the risk of Pt agglomeration on the surface. It is necessary for the catalyst support material to form pore structures with pore sizes larger than 25 nm to avoid diffusion limitations [2]. The pore sizes of a typical carbon support, Vulcan XC-72R, is 20 – 100 nm with micro particle sizes of around 50 nm clustered together to form macro particles (50 – 100 µm).

The surface area of SiC is typically in the range of 25 – 80 $m^2.g^{-1}$ [58,59] and B_4C materials are approximately 3 – 20 $m^2.g^{-1}$ [60-62]. However, Parmentier *et al.* [63] prepared high surface area SiC via carbothermal reduction of prepared SiO_2/C at 1250 – 1450 °C and in inert atmosphere, this method obtained a surface area of 120 $m^2.g^{-1}$ and an average pore size of 15 nm. Borchardt *et al.* [16] produced ordered mesoporous boron carbide via precursor nanocasting at temperatures of up to 1300 °C, the mesoporous structures obtained surface areas of 300 – 770 $m^2.g^{-1}$, with pore sizes ranging from 2.4 – 10 nm. Low temperature chemical vapour deposition is the preferred preparation method for B_4C [64], however, most research papers are not geared towards boron carbide as a catalyst support and therefore surface area and pore size are not reported. Other methods described to produce high surface area SiC and B_4C materials are reported in Table 1.1, the mass specific surface areas are corrected for the material density in order to compare these materials to Vulcan XC-72R. As shown in the table, SiC and B_4C vol/vol surface area may exceed that of carbon depending on the preparation method.

Table 1.1: Comparison of SiC and B_4C surface areas to Vulcan XC-72R.

Material	Preparation Method	Surface Area / $m^2.g^{-1}$	Surface Area per Volume / $m^2.m^{-3}$	Reference
Vulcan XC-72R	-	250	6.60	[17]
SiC	Chemical vapour deposition	30	9.63	[58]

SiC	Gas-solid reaction	25	8.03	[59]
SiC	Carbothermal reduction	120	38.5	[63]
SiC	Modified sol-gel method	112	36.0	[64]
Ordered mesoporous SiC	Ordered mesoporous carbons with silicon powder	147	47.2	[65]
Ordered mesoporous SiC	Direct Pyrolysis	1325	361	[15]
B_4C	Pressureless sintering	3	0.76	[60]
B_4C	Commercial	27	6.8	[62]
Ordered mesoporous B_4C	Precursor nanocasting	770	194	[16]

1.4 Aims and Objectives

This investigation focuses on evaluating the viability of SiC and B_4C as catalyst supports for the ORR at the cathode of the hydrogen PEFC. In addition, these support materials will be used to further the understanding of metal-support interactions and their influence on adsorbates during electrochemical reactions.

Chapter 1: This chapter highlights the current challenges and research studies on cathode catalysts. Additionally, a background on the properties of SiC and B_4C, such as electrical conductivity, stability, surface area and electrochemical performance, is outlined.

Chapter 2: Outlines the theoretical and practical descriptions of the experimental methods used in this work. These experimental methods include the catalyst synthesis, electrochemical characterisations, physical characterisations and X-ray absorption spectroscopy.

Chapter 3: Pt/SiC was investigated as an alternative catalyst support material for the ORR in acidic media. Electrochemical, as well as advanced characterisation techniques, were used to clarify the structure-property relationships between catalyst morphology, metal-support interaction, and ORR activity. Extended X-ray Absorption Fine Structure (EXAFS) analysis gave insights into the shape of the clustered nanoparticles, while X-ray Photoelectron Spectroscopy (XPS) and *in-situ* X-ray Absorption Near-Edge Spectroscopy (XANES) analysis provided information into electronic effects and how these relate to metal-support interactions.

Chapter 4: (Part 1) Platinum was deposited onto commercial boron carbide, using an in-house organo-metallic chemical deposition method. These catalysts were physically and electrochemically characterised to determine the feasibility of boron carbide as an alternative catalyst support material to carbon. **(Part 2) A verbatim reproduction of a published article** [66]. Pt supported graphite-rich B_4C composites (BC) are compared to commercial Pt/C catalysts to investigate the electronic metal-support interactions. Electrochemical, as well as advanced *ex-situ* characterisation techniques, were used to explain the relationships between the electronic structures of the materials and ORR activity.

Chapter 5: (Part 1) Further investigation into the role of strong metal-support interactions on species adsorption onto the platinum surface in an acidic media. Hydrogen and CO adsorption were investigated using cyclic voltammograms, CO stripping voltammetry and CO displacement techniques. **(Part 2) A verbatim reproduction of a submitted publication** [67]. An investigation into the kinetic HOR activity of Pt/BC and Pt/C catalysts under high mass transport and low catalyst loading conditions. A link between HOR activity and *in-situ* X-ray absorption spectroscopy (XAS) is made, which was used to investigate the platinum particle shape, interatomic distances and d-band vacancy changes due to ion adsorption at a range of potentials (0.2 – 1.1 V vs. RHE).

Chapter 6: The overall conclusions of this thesis and future outlook on alternative catalyst support materials.

Some of the results are repeated between Chapters 3, 4 and 5 since parts of the thesis (i.e. Chapters 4.2 and 5.2) have been published/submitted for publication and data needed to be included as a benchmark or for completeness.

1.5 References

1. Whitesides, G.M. & Crabtree, G.W. 2007. *Science.* 315(5813):796-798.
2. Schmidt, T.J. 2012. *ECS Transactions.* 45(2):3-14.
3. Huang, S., Ganesan, P. & Popov, B.N. 2011. *Applied Catalysis B: Environmental.* 102(1–2):71-77.
4. Reiser, C.A., Bregoli, L., Patterson, T.W., Yi, J.S., Yang, J.D., Perry, M.L. & Jarvi, T.D. 2005. *Electrochemical and Solid-State Letters.* 8(6):A273-A276.
5. Cheon, J.Y., Kim, J.H., Kim, J.H., Goddeti, K.C., Park, J.Y. & Joo, S.H. 2014. *Journal of the American Chemical Society.* 136(25):8875-8878.
6. Lewera, A., Timperman, L., Roguska, A. & Alonso-Vante, N. 2011. *The Journal of Physical Chemistry C.* 115(41):20153-20159.
7. Dulub, O., Hebenstreit, W. & Diebold, U. 2000. *Physical Review Letters.* 84(16):3646-3649.
8. Xiong, L. & Manthiram, A. 2004. *Electrochimica Acta.* 49(24):4163-4170.
9. Antolini, E. & Gonzalez, E.R. 2009. *Solid State Ionics.* 180(9–10):746-763.
10. Weigert, E.C., Stottlemyer, A.L., Zellner, M.B. & Chen, J.G. 2007. *The Journal of Physical Chemistry C.* 111(40):14617-14620.
11. Krasotkina, N.I., Yakovleva, V.S., Voronin, N.I. & Shmitt-Fogelevich, S. 1968. *Refractories.* 9(11-12):723-726.
12. Samsonov, G.V. 1962. *Boron, its compounds and alloys.* US Atomic Energy Commission, Division of Technical Information.
13. Liquiflo Chemical Processing Pumps 2015. *Chemical Resistance Chart.* Available: http://www.liquiflo.com/v2/files/pdf/lit/Chemical_Resistance_Chart.pdf [29/04/2015].
14. Ding, H. & Hihara, L. 2006. *ECS Transactions.* 1(4):103-114.
15. Nghiem, Q.D. & Kim, D. 2008. *Chemistry of Materials.* 20(11):3735-3739.
16. Borchardt, L., Kockrick, E., Wollmann, P., Kaskel, S., Guron, M.M., Sneddon, L.G. & Geiger, D. 2010. *Chemistry of Materials.* 22(16):4660-4668.

17. Debe, M.K. 2012. *ECS Transactions*. 45(2): 47-68.
18. Lim, B., Jiang, M., Camargo, P.H.C., Cho, E.C., Tao, J., Lu, X., Zhu, Y. & Xia, Y. 2009. *Science.* 324(5932):1302-1305.
19. Nørskov, J.K., Rossmeisl, J., Logadottir, A., Lindqvist, L., Kitchin, J.R., Bligaard, T. & Jónsson, H. 2004. *The Journal of Physical Chemistry B*. 108(46): 17886-17892.
20. Wroblowa, H.S., Yen-Chi-Pan & Razumney, G. 1976. *Journal of Electroanalytical Chemistry and Interfacial Electrochemistry.* 69(2):195-201.
21. Markovic, N.M., Schmidt, T.J., Stamenkovic, V. & Ross, P.N. 2001. *Fuel Cells.* 1(2):105-116.
22. Zhang, H., Wang, X., Zhang, J.L. & Zhang, J.W. 2008. *Electrocatalysts and Catalyst Layers Fundamentals and Applications.* London: Springer.
23. Pourbaix, M. 1974. *Atlas of electrochemical equilibria in aqueous solutions.* National Association of Corrosion Engineers.
24. Hoogers, G. 2002. *Fuel Cell Technology Handbook.* Taylor & Francis.
25. Hartl, K., Hanzlik, M. & Arenz, M. 2011. *Energy and Environmental Science*. 4:234-238.
26. Dubau, L., Castanheira, L., Chatenet, M., Maillard, F., Dillet, J., Maranzana, G., Abbou, S., Lottin, O., De Moor, G., Kaddouri, A.E., Bas, C., Flandin, L. & Caqué, N. 2014. *International Journal of Hydrogen Energy.* 39(36):21902.
27. Castanheira, L., Dubau, L., Mermoux, M., Berthomé, G., Caqué, N., Rossinot, E., Chatenet, M. & Maillard, F. 2014. *ACS Catalysis.* 4(7):2258-2267.
28. Knights, S.D., Colbow, K.M., St-Pierre, J. & Wilkinson, D.P. 2004. *Journal of Power Sources.* 127(1–2):127-134.
29. Wang, J., Yin, G., Shao, Y., Wang, Z. & Gao, Y. 2008. *The Journal of Physical Chemistry C.* 112(15):5784-5789.
30. Coloma, F., Sepulveda-Escribano, A., Fierro, J.L.G. & Rodriguez-Reinoso, F. 1994. *Langmuir.* 10(3):750-755.
31. Bartholomew, R.F. & Frankl, D.R. 1969. *Physical Review.* 187(3):828-833.
32. Krstajic, N.V., Vracar, L.M., Radmilovic, V.R., Neophytides, S.G., Labou, M., Jaksic, J.M., Tunold, R., Falaras, P. Falaras, P. 2007. *Surface Science.* 601(9):1949-1966.
33. Dieckmann, G.R. & Langer, S.H. 1998. *Electrochimica Acta.* 44(2–3):437-444.
34. Slavcheva, E., Nikolova, V., Petkova, T., Lefterova, E., Dragieva, I., Vitanov, T. & Budevski, E. 2005. *Electrochimica Acta.* 50(27):5444-5448.

35. Ioroi, T., Siroma, Z., Fujiwara, N., Yamazaki, S. & Yasuda, K. 2005. *Electrochemistry Communications.* 7(2):183-188.
36. Saadeddin, I., Pecquenard, B., Manaud, J.P., Decourt, R., Labrugère, C., Buffeteau, T. & Campet, G. 2007. *Applied Surface Science.* 253(12):5240-5249.
37. Cognard, G., Ozouf, G., Beauger, C., Dubau, L., López-Haro, M., Chatenet, M. & Maillard, F. 2017. *Electrochimica Acta.* 245:993-1004.
38. Pang, H.L., Zhang, X.H., Zhong, X.X., Liu, B., Wei, X.G., Kuang, Y.F. & Chen, J.H. 2008. *Journal of Colloid and Interface Science.* 319(1):193-198.
39. Ganesan, R. & Lee, J.S. 2006. *Journal of Power Sources.* 157(1):217-221.
40. Lasch, K., Hayn, G., Jörissen, L., Garche, J. & Besenhardt, O. 2002. *Journal of Power Sources.* 105(2):305-310.
41. Chen, Z., Qiu, X., Lu, B., Zhang, S., Zhu, W. & Chen, L. 2005. *Electrochemistry Communications.* 7(6):593-596.
42. Suzuki, Y., Ishihara, A., Mitsushima, S., Kamiya, N. & Ota, K. 2007. *Electrochemical and Solid-State Letters.* 10(7):B105-B107.
43. Chhina, H., Campbell, S. & Kesler, O. 2006. *Journal of Power Sources.* 161(2):893-900.
44. Cognard, G., Ozouf, G., Beauger, C., Jiménez-Morales, I., Cavaliere, S., Jones, D., Roziére, J., Chatenet, M. et al. 2017. Electrocatalysis. 8(1):51-58.
45. Liu, Y., Kelly, T.G., Chen, J.G. & Mustain, W.E. 2013. *ACS Catalysis.* 3(6):1184-1194.
46. Zellner, M.B. & Chen, J.G. 2005. *Catalysis Today.* 99(3–4):299-307.
47. Hu, Z., Chen, C., Meng, H., Wang, R., Shen, P.K. & Fu, H. 2011. *Electrochemistry Communications.* 13(8):763-765.
48. Wijesundara, M.J. & Azevedo, R. 2011. SiC Materials and Processing Technology. In Springer New York. 33-95.
49. Zhang, J., Carraro, C., Howe, R.T. & Maboudian, R. 2007. *Surface and Coatings Technology.* 201(22–23):8893-8898.
50. Cai, K., Nan, C. & Min, X. 1999. *Materials Science and Engineering: B.* 67(3):102-107.
51. Wood, C. & Emin, D. 1984. *Physical Review B.* 29(8):4582-4587.
52. Young, D.J., Du, J. Zorman, C.A. & Ko, W.H. 2004. *Sensors Journal, IEEE.* 4(4):464-470.
53. Honji, A., Mori, T., Hishinuma, Y. & Kurita, K. 1988. *Journal of the Electrochemical Society.* 135(4):917-918.
54. Niu, J.J. & Wang, J.N. 2009. *Acta Materialia.* 57(10):3084-3090.

55. Lv, H., Mu, S., Cheng, N. & Pan, M. 2010. *Applied Catalysis B: Environmental.* 100(1–2):190-196.
56. Grubb, W.T. & McKee, D.W. 1966. *Nature*. 210(5032): 192-194.
57. Lv, H., Peng, T., Wu, P., Pan, M. & Mu, S. 2012. *Journal of Materials Chemistry.* 22(18):9155-9160.
58. Moene, R., Makkee, M. & Moulijn, J.A. 1998. *Applied Catalysis A: General.* 167(2):321-330.
59. Keller, N., Pham-Huu, C., Roy, S., Ledoux, M.J., Estournes, C. & Guille, J. 1999. *Journal of Materials Science.* 34(13):3189-3202.
60. Kuzenkova, M.A., Kislyi, P.S., Grabchuk, B.L. & Bodnaruk, N.I. 1979. *Journal of the Less Common Metals.* 67(1):217-223.
61. Schwetz, K.A. & Vogt, G. 1980. *US Patent number 4195066 A*. United States Patent and Trademark Office.
62. H. C. Starck 2015. Advanced Ceramic Powders. Available: http://www.hcstarck.com/hcs-admin/file/8a8181e225548334012554ce05db17e4.de.0/Advanced_Ceramic_Powders_0614_HC_Starck.pdf;jsessionid=888619103A3C85B4D756D48C2E9CBBF3.s1 [17/02/2015].
63. Parmentier, J., Patarin, J., Dentzer, J. & Vix-Guterl, C. 2002. *Ceramics International.* 28(1):1-7.
64. Jin, G. & Guo, X. 2003. *Microporous and Mesoporous Materials.* 60(1–3):207-212.
65. Liu, Z., Shen, W., Bu, W., Chen, H., Hua, Z., Zhang, L., Li, L., Shi, J. Tan, S. 2005. *Microporous and Mesoporous Materials.* 82(1–2):137-145.
66. Jackson, C., Smith, G.T., Inwood, D.W., Leach, A.S., Whalley, P.S., Callisti, M., Polcar, T., Russell, A.E., Levecque, P., Kramer, D. 2017. *Nature Communications*. 8:15802.
67. (Submitted) Jackson, C., Smith, G.T., Markiewicz, M, Inwood, D.W., Leach, A.S., Whalley, P.S., Kucernak, A., Russell, A.E., Kramer, D., Levecque, P. 2017. *Journal of Electroanalytical Chemistry.*

Chapter 2

Experimental Methods and Techniques

This chapter outlines the background theoretical descriptions of the experimental methods used in this work. These experimental methods include the catalyst synthesis method, electrochemical characterisations, physical characterisations and advanced characterisations. The detailed, step by step procedures are described in the relevant chapters.

2.1 Platinum Deposition Method

An in-house platinum deposition technique, modified from the Organo-Metallic Chemical Vapour Deposition (OMCVD) method, was used to deposit Pt onto the support materials. OMCVD involves the formation of a thin solid film on a substrate material by a chemical reaction of vapour-phase metal-organic precursors, in a vacuum [1]. This deposition method is a one-stage process and avoids synthesis steps such as impregnation, washing, drying, calcination and activation. However, the implications of trace organic fragments on electrochemical cleanliness of the metal have not been discussed.

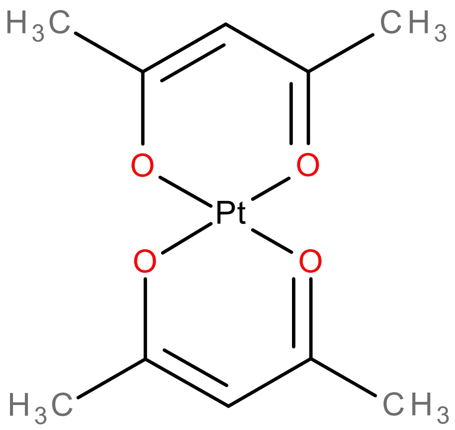

Figure 2.1: Molecular structure of platinum (II) acetylacetonate.

Platinum (II) acetylacetonate ($P(acac)_2$) is the precursor used in this synthesis process due to its low decomposition temperature of 210-240 °C [2]. $Pt(acac)_2$ forms part of the β-diketonate family complexes, this is a compound of the form $M(CH_3COCHCOCH_3)_2$, where M is the metal. The molecular structure of $Pt(acac)_2$ is given in Figure 2.1.

The Pt-O_{acac} bond is suggested to decompose, leaving Pt metal on the surface of the substrate. The Pt-O_{acac} bond strength is 180 $kJ.mol^{-1}$ and metal de-coordination is assumed to not take place [3].

The modified in-house procedure deposited Pt under an argon atmosphere, therefore precursor deposition occurred from the liquid phase rather than the vapour phase. Precursor deposition from the liquid phase is an assumption which was made based on the phase diagram of the precursor used in this study, assuming Clausius–Clapeyron relation from Equation 2.1.

$$Ln(P) = B - \frac{A}{T} \qquad \text{Equation 2.1}$$

Where P is pressure in atmospheres, T is temperature in Kelvin, A and B are the Clausius-Clapeyron constants for $Pt(acac)_2$, which are 12737 (A) and 20.19 (B) [4].

The vapourisation temperature under 2 bar pressure is therefore calculated to be 380 °C for $Pt(acac)_2$. However, the $Pt(acac)_2$ melting point is 250 °C, with a decomposition temperature of ~265 °C [5]. As described previously [6], the precursors are likely to melt and decompose before reaching the vapourisation temperature, therefore decomposition occurs from the liquid phase rather than the vapour phase. The platinum deposition under argon provided less oxidation of the metal during deposition, when compared to vacuum prepared catalysts, and the average Pt particle size was reported to be in a slightly larger and more favourable range [6].

The catalysts were prepared in a standard in-house reactor, shown in Figure 2.2. This provided a gas tight sealed environment while the precursors were heated in a tubular furnace.

Figure 2.2: Reactor used for preparation of chemical deposition catalysts [6].

2.2 Electrochemical Characterisation

2.2.1 Cyclic Voltammetry and CO Stripping Voltammetry

Cyclic Voltammetry (CV) is a potentiodynamic electrochemical measurement where the potential of the working electrode is swept between two potential limits, while the current response is measured. Oxidation produces a positive (anodic) current response, while reduction produces a negative (cathodic) current response. Reactions occur at varying peak potentials depending on the activation energy required for the reaction to occur. Thus, half-cell reactions with low activation energies occur at lower potentials, whereas high reaction energies occur at higher potentials. This information allows for cyclic voltammograms to be useful in identifying the potentials at which electrochemical reactions occur. The typical cyclic voltammogram of a polycrystalline Pt electrode in an acidic environment is shown in Figure 2.3.

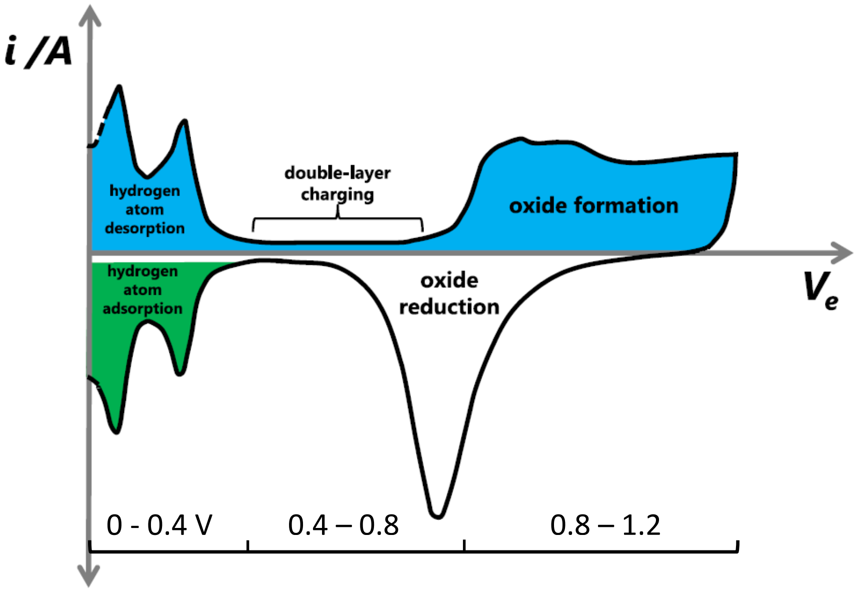

Figure 2.3: Cyclic voltammogram of a platinum electrode at a scan rate of 100 mV.s^{-1} in a low-oxygen 0.5 M H_2SO_4 electrolyte. Modified from Kumsa *et al.* [7] which was redrawn from Angerstein-Kozlowska *et al.* [8].

The reversible hydrogen adsorption and desorption regions occur between 0.05 V and 0.4 V vs. RHE, this region is attributed to the underpotential deposition (H_{UPD}) of a hydrogen monolayer in the negative-going sweep and the desorption of protons (H^+) in the positive-going sweep [9]. The hydrogen electro-adsorption (Equation 2.2) and the hydrogen electro-desorption (Equation 2.3) reaction is as follows [10]:

$$Pt + H^+ + e^- \rightarrow Pt - H_{ads} \qquad \text{Equation 2.2}$$

$$Pt - H_{ads} \rightarrow Pt + H^+ + e^- \qquad \text{Equation 2.3}$$

The multiple peaks in the H_{UPD} region are attributed to hydrogen electro-desorption from different surfaces of the platinum crystal [10]. Single crystal studies performed by Will [11] investigated the hydrogen adsorption on the three main platinum faces (100), (111) and (110). This study found that Pt surfaces interacted with hydrogen atoms at different energies due to the different type and overlap between the electronic local density of a site and the adsorbed hydrogen [9].

The featureless region with low measured current between 0.4 and 0.8 V vs. RHE is attributed to double layer charging [9]. This is caused by the interaction at the interface between the electrode and electrolyte solution. Segregation of positive and negative charges by preferential adsorption of either positive or negative ions at the interface takes place and thus, a charge distribution is formed [12]. Double layer charging occurs across the whole potential range, however, there are no electrochemical reactions in this potential range, leaving the residual current from the double layer. Finally, the oxidation of the Pt surface takes place at potentials above 0.8 V vs. RHE on the forward scan of the cyclic voltammogram, followed by oxygen reduction on the reverse scan [13].

The cyclic voltammogram is used to determine the Electrochemically Active Surface Area (ECSA) by integration of H_{UPD} or hydrogen desorption regions and using the double layer as a baseline (Q_{HUPD}). The integrated area is used to determine the total adsorbed (or desorbed) hydrogen charge on the platinum surface. The theoretical hydrogen adsorption charge associated with different Pt crystal surfaces were statistically combined to form an estimated hydrogen adsorption charge for a smooth polycrystalline platinum surface, of 210 $\mu C.cm^2{}_{Pt}$ [14]. Normalising the H_{UPD} charge by the theoretical hydrogen adsorption charge allows for the number of sites which took part in the reaction to be determined. Therefore, the ECSA can be calculated using Equation 2.4:

$$ECSA = \frac{Q_{HUPD}}{L_{Pt}Q_f} \qquad \text{Equation 2.4}$$

Where Q_{HUPD} is the integrated area under the hydrogen adsorption/desorption peak after subtraction of the double layer, L_{Pt} is the platinum loading on the electrode and $Q_f = 210$ $\mu C.cm^2{}_{Pt}$.

CO stripping voltammetry is similar to that of cyclic voltammetry in that it is a potentiodynamic electrochemical measurement. However, during CO stripping a monolayer of CO is adsorbed on the platinum surface, this monolayer is then oxidised and desorbed. CO stripping voltammetry is another technique used to determine the ECSA of a catalyst surface by measuring the peak area of the CO oxidation peak [10]. The adsorption charge for CO stripping voltammetry is $Q_f = 420$ $\mu C.cm^2{}_{Pt}$ since this is a two electron reaction. The ECSA determined by CO stripping voltammetry is typically 1.4 times that of the ECSA calculated from the H_{UPD} method using a standard baseline. This is due to the non-linear contribution of the capacitance of the support material for high surface area catalysts [15].

In addition to the determination of ECSA, CO stripping can also be used to determine the morphology of particles as shown by Fabbri *et al.* [16], based on work by Maillard [17]. It was shown that a morphology fingerprint of the surface can be produced to distinguish between isolated nanoparticles and extended surfaces, as demonstrated in Figure 2.4.

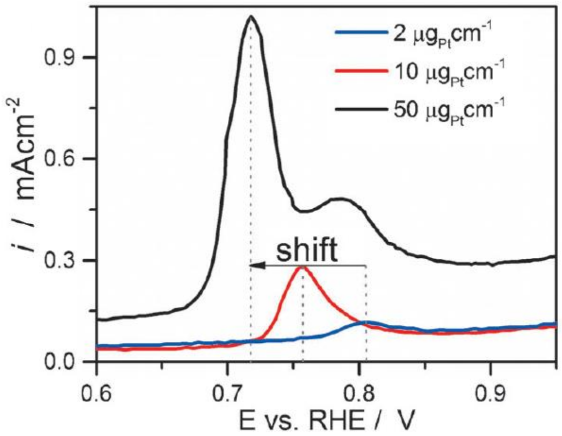

Figure 2.4: CO-stripping voltammograms for different Pt loadings at a scan rate 20 mV.s^{-1}, Ar-saturated 0.1 M $HClO_4$ after CO adsorption at 0.1 V vs. RHE for 15 min in CO-saturated 0.1 M $HClO_4$ [reproduced from 16].

2.2.2 Rotating Disc Electrode (RDE)

Oxygen reduction reaction (ORR) activity measurements were conducted on rotating disc electrodes (RDEs) in an oxygen saturated 0.1 M $HClO_4$ electrolyte, with rotations speeds of 400, 900, 1600 and 2500 rpm. Linear sweep voltammetry is employed with a sweep from high to low potentials, known as the cathodic sweep (1.2 V – 0.05 V), and then potential is swept from low to high potentials, known as the anodic sweep (0.05 V – 1.2 V). The anodic sweep was used to determine the mass and surface area specific ORR activities, corrected for capacitive current and internal resistance (iR). The capacitive current was determined by linear sweep voltammograms in an argon saturated electrolyte. ORR curves consist of a flattened, negligible current at high potentials (1 – 1.2 V vs. RHE), followed by a sharp drop to larger currents (0.4 – 1.0 V vs. RHE) and then the current is stabilised at low potentials of approximately 0.4 V vs. RHE which is referred to as diffusion limiting current (i_d). The diffusion limiting current is dependent on the rotation rate and electrode diameter and the theoretical limiting current value is calculated using the Levich equation (Equation 2.5).

$$i_d = 0.620 \times n \times F \times A \times D^{2/3} \times \omega^{1/2} \times \nu^{-1/6} \times C \qquad \text{Equation 2.5}$$

Where *n* is the number of electrons, *F* is the faraday constant, *A* is the electrode area, *D* is the diffusion coefficient, ω is the angular rotation speed, *v* is the kinematic viscosity of the solution, and *C* is the reactant concentration specific for oxygen in perchloric acid.

The ORR activities of the catalysts were reported at 0.9 V vs. RHE at a rotation rate of 1600 rpm and scan rate of 20 mV.s^{-1} using the anodic sweep. The current reported is kinetically controlled as well as mass transport controlled, therefore the Koutecky-Levich equation was used to correct the current for mass transport limitations in order to determine the kinetic activity (i_k) of the catalyst (Equation 2.6).

$$\frac{1}{i} = \frac{1}{i_k} + \frac{1}{i_d} \qquad \text{Equation 2.6}$$

As studied by Shinozaki *et al.*, numerous factors affect the ORR activity of a catalyst, namely the scan rate, electrolyte purity, temperature, glassware cleanliness and platinum loading on the glassy carbon electrode, thus these parameters were kept constant for each experiment. Moreover, the ink compositions and drying methods were optimised for the catalyst film quality [18].

2.3 Physical Characterisation

2.3.1 Transmission Electron Microscopy (TEM)

Transmission Electron Microscopy (TEM) was used to determine the particle size and particle size distribution of the Pt nanoparticles and the support materials. TEM imaging is a microscopy technique which involves an electron beam transmitted through a sample and an image is formed through the interaction between the electrons and the sample. This 2-dimensional image is subsequently magnified and focused onto a fluorescent screen. The particle sizes were measured in ImageJ 1.51j8 software using 100 particles.

2.3.2 X-Ray Diffraction (XRD)

X-ray Diffraction (XRD) is a technique which focuses X-rays onto a solid surface, this is used to characterise the crystal structure of materials. The incident X-rays diffract in different directions from the surface of a crystal which allows for the analysis of crystallographic structure and size to be determined, since diffraction patterns at incident angles (ϴ) are unique to crystalline structures. Sir W.H. Bragg and Sir W.L. Bragg developed Bragg's Law which describes the relationship between the diffraction patterns of crystals and the incident angle, shown in Equation 2.7.

$$n\lambda = 2d_{hkl}sin\theta \; (n = 1,2,3, \dots) \qquad \text{Equation 2.7}$$

Where: λ is the wavelength of the X-ray source, *d* is the lattice spacing, Θ is the half-value of the diffraction angle, *n* is the order of the reflection.

2.3.3 Energy-Dispersive X-ray Spectroscopy (EDX)

Energy-Dispersive X-ray Spectroscopy (EDX) was used as an elemental analysis tool, this spectroscopy technique involves excitation of the elements by charge particles such as electrons, protons or an X-ray source. The incident beam excites and ejects an electron from an inner shell and creating a hole, an electron from an outer shell, higher energy shell, fills the hole releasing the energy in the form of an X-ray. The subsequent electromagnetic emission spectrum is element specific due to each unique atomic structure. The limits of detection of EDX include 1 wt% [19] and low performance for light elements (Z < 11) [20].

2.3.4 Inductively Coupled Plasma Optical Emission Spectrometry (ICP-OES)

Inductively Coupled Plasma Optical Emission Spectrometry (ICP-OES) was used as an elemental analysis technique to determine the Pt loading on the samples. This emission spectroscopy utilises an inductively coupled plasma to produce electromagnetic radiation by excited atoms and ions in a metal, the wavelength of the electromagnetic radiation is unique to the metal. The measured intensity of the spectrum is compared to known concentrations of the element to quantify the concentration of the sample.

2.3.5 Physisorption

Physisorption is the physical adsorption of a substance with little change to the structure of the atom or molecule. Brunauer-Emmett-Teller (BET) theory is used to describe physisorption of a gas, typically nitrogen, onto the surface of a solid material and describes an analysis technique for determination of the surface area of a solid material. BET theory is an extension of Langmuir theory, a theory describing the adsorption of a molecule from a monolayer, to a multilayer adsorption. BET theory assumes the Langmuir theory is valid for each layer of the adsorbent, the BET equation is described in Equation 2.8.

$$\frac{1}{v[\left(\frac{p_o}{p}\right)-1]} = \frac{c-1}{v_m c}\left(\frac{p}{p_0}\right) + \frac{1}{v_m c} \qquad \text{Equation 2.8}$$

$$c = \exp(\frac{E_1 - E_L}{RT}) \qquad \text{Equation 2.9}$$

$$v_m = \frac{1}{gradient + y - intercept} \qquad \text{Equation 2.10}$$

$$S_{BET} = \frac{v_m \times N \times s}{V \times a} \qquad \text{Equation 2.11}$$

Where v is the quantity of adsorbed gas, v_m is the quantity in a monolayer of gas, c is the BET constant described in Equation 2.9, p is the equilibrium pressure of adsorbates at the temperature of adsorption, p_0 is the saturation pressure of adsorbates at the temperature of adsorption, R is the gas constant, E_1 is the heat of adsorption for the first layer and E_L is the heat of adsorption for the second and higher layers.

The BET equation can be used to plot the adsorption isotherm as a straight line with the y-axis as $\frac{1}{v[(\frac{p_o}{p})-1]}$ and the x-axis as $\frac{p}{p_0}$. This relationship only holds as a linear plot in the range of 0.05 < $\frac{p}{p_0}$< 0.35. Therefore, v_m is calculated using the intercept and gradient of the line per Equation 2.10. Lastly, the BET surface area is determined by Equation 2.11, where N is Avogadro's number, s is the adsorption cross section of adsorbing species, V is the molar volume of the adsorbate gas and a is the mass of the adsorbent.

2.4 Advanced Characterisation

2.4.1 X-ray Photoelectron Spectroscopy (XPS)

X-ray Photoelectron Spectroscopy (XPS) was used to determine the electronic and chemical state of the elements in the catalysts. XPS is a surface sensitive spectroscopy technique, which typically penetrates the sample to a depth of 10 nm, this technique utilises a beam of X-rays to excite electrons in a material while simultaneously measuring the kinetic energy and number of electrons which escape. Analysis of the spectrum first requires calibration for the binding energy of a known bond, typically the binding energy of the C-C sp^2 bond in the C 1s spectrum, which is known to be 284.0 eV [21]. The spectrum is calibrated due to charge induced shifting effects. Charge induced shifting is due to an excess of low voltage (-1 to -20 eV) electrons attached to the surface, or a shortage of electrons (+1 to +15 eV) within the top 1-12 nm of the sample caused by the loss of photo-emitted electrons. This phenomenon is known to occur on insulating or semi-conductive materials.

2.4.2 X-ray Absorption Spectroscopy (XAS)

2.4.2.1 X-ray Absorption Spectroscopy Theory

X-ray Absorption Spectroscopy (XAS) was used to determine the Pt interatomic distances, Pt nanoparticle shapes and Pt d-band vacancies of the catalysts. An XAS experiment consists of a sample being exposed to an incident X-ray beam of a definite energy, some of the X-rays are absorbed by the atoms in the sample and the rest are transmitted through the sample. As shown in Equation 2.12, the intensity of the X-rays transmitted (I_t) through the sample decreases exponentially by the absorption coefficient (μ) and the thickness (x) of the sample. Where I_0 is the intensity of the incident X-ray beam [22].

$$I_t = I_0 e^{-\mu x} \qquad \text{Equation 2.12}$$

The absorbed X-rays cause excitation or ejection of a core electron. Excited electrons are known as photoelectrons and an empty electron orbital due to ejection of a core electron is known as a core hole. Additionally, fluorescence is given off by the excited atoms as an electron fills the core hole. The X-ray absorption by the sample is quantified by comparing the intensity of the incident beam to that of the transmitted beam, or by measuring the fluorescence intensity or the intensity of the Auger electrons from the ejected core electrons, as a function of the incident energy [22].

As the incident beam energy is increased, the absorption decreases until the binding energy of a core electron is reached. The excitation of a core electron results in a sharp increase in absorption, known as an absorption ‘edge’. The energy of the excited core electron (E_k) is calculated using Equation 2.13, where hv is the incident X-ray energy and $E_{binding}$ is the binding energy of the electron.

$$E_k = hv - E_{binding} \qquad \text{Equation 2.13}$$

The labelling of the absorption edge is based on the principle quantum number from which the electron was ejected. Excitation from the 1s orbital corresponds to the K shell (n=1), and the 2s, $2p_{1/2}$ and $2p_{3/2}$ correspond to the L shell (n=2) of L_1, L_2 and L_3 edges, respectively. The features on and close to the edge are known as X-ray Absorption Near-Edge Structure (XANES), while the gradual oscillations above the edge are known as Extended X-ray Absorption Fine Structure (EXAFS).

In the EXAFS region, absorption decreases as energy is increased until the next binding energy is reached. The intensity of the absorption is determined by the absorption coefficient (μ), and according to Fermi's Golden Rule, the probability of the X-ray being absorbed, transmitted or scattered depends on the similarity of the final state to the indeterminate state prior to the XAS measurement.

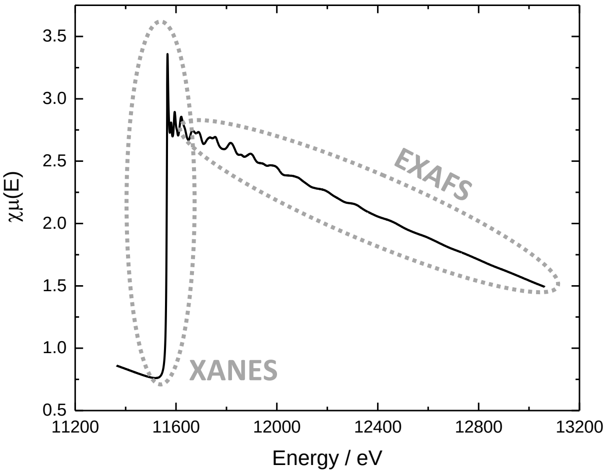

Figure 2.5: X-ray absorption spectrum of a Pt reference foil, with marked XANES and EXAFS regions.

2.4.2.2 Data Pre-Processing

XAS spectra were collected at the B18 Core EXAFS beamline at Diamond Light Source, these spectra were processed using Demeter 0.9.25 using Ifeffit 1.2.12 [23] software package.

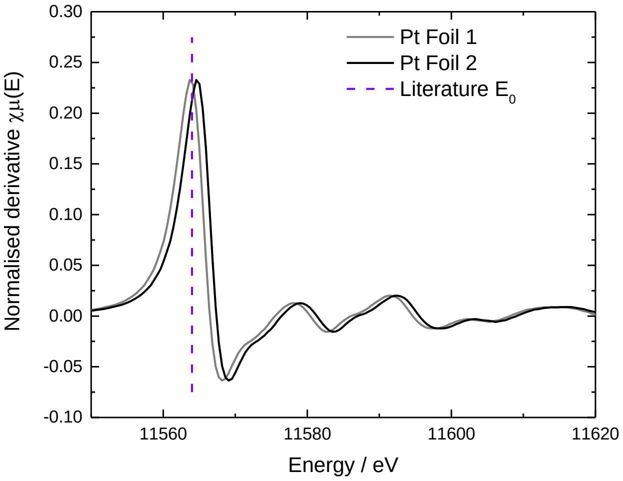

Figure 2.6: Uncorrected normalised XAS spectra of Pt reference foils with a dashed line indicating the literature value for the edge step (E_0).

Pre-processing of the data was completed using the Athena program in the Demeter software package, this processing consisted of energy calibration of the spectrum, merging of multiple scans of the same spectrum and background subtraction. Three spectra were collected for each sample and/or potential controlled experiment in order to increase the quality of data and to reduce noise in the spectrum. Additionally, a Pt reference foil was measured for comparison and modelling purposes discussed below.

The monochromator, responsible for providing a specific energy X-ray, is susceptible to slight variations in energy. This variation in energy is corrected in each spectrum by calibrating the edge step value (E_0) to the literature value, e.g. the Pt L_3 edge energy is 11564 eV. The identification of the edge step value in a spectrum is often chosen from the energy of the 1st peak in the 1st derivative of the spectrum. An example of this spectrum correction is shown in Figure 2.6, the first peak energy is shifted to the literature value, E_0 is then used as a reference point for the fitting of the background, pre- and post – edges.

Once all the spectra are corrected for the literature value of E_0, the multiple spectra collected for a single sample and/or potential controlled experiment are merged to form a single spectrum for further processing. The background of the spectrum is due to the interaction between photons and matter, as energy is increased the probability of absorption of photons decreased. This background is corrected by extrapolating a line in the pre-edge region and the post-edge region as shown in Figure 2.7a, the normalised spectrum is shown in Figure 2.7b. The pre-edge fitting is linear and modelled to the data between 200 eV and 80 eV before E_0 and the post-edge is a quadratic function fitted to pass through the middle of the EXAFS oscillations using data from 150 eV after E_0 to 10 eV from the end of the spectrum. The background is generated using a combination of the pre-edge, the post-edge and a polynomial spline function.

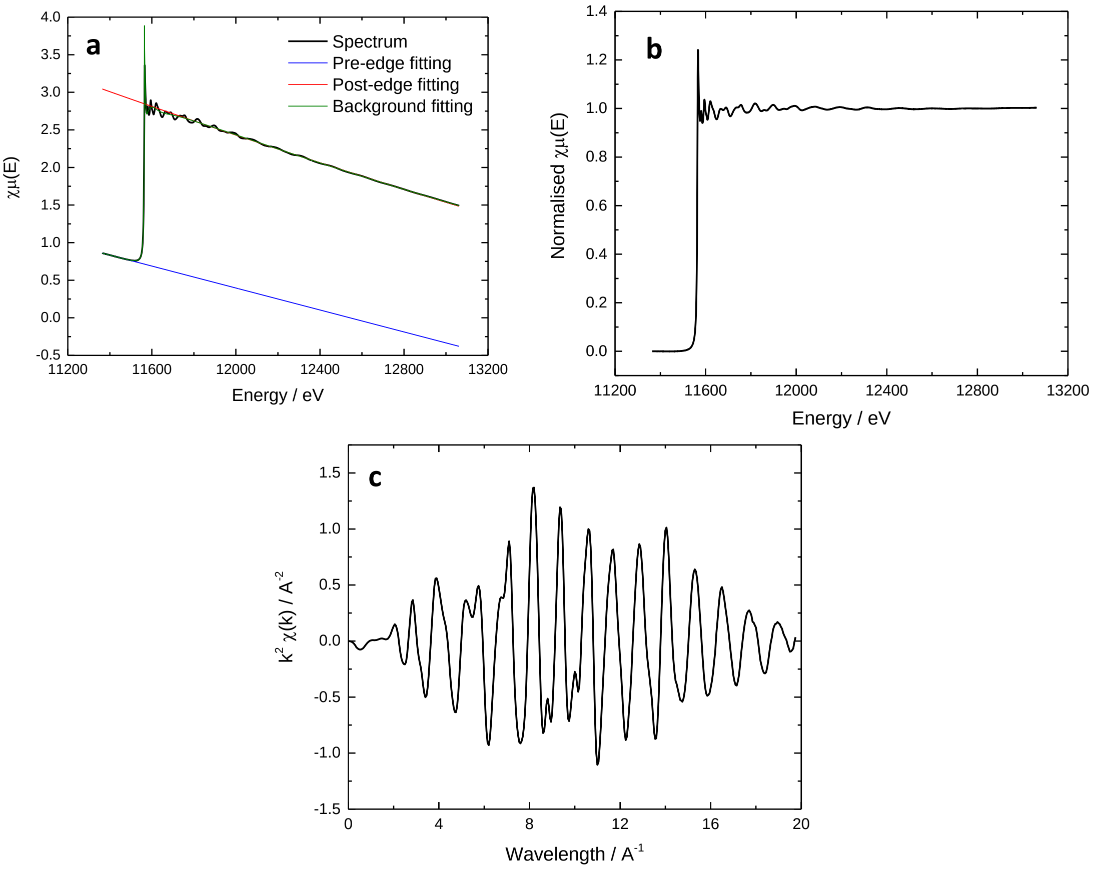

Figure 2.7: XAS spectrum (a) demonstrating the pre-edge, post-edge and background fittings; (b) normalised for the pre- and post-edges; (c) in 'k-space' with a weighting of 2.

EXAFS data are represented in 'k space', referring to the conversion of energy scale to wavelength (A^{-1}) by Equation 2.14. Depending on the element, χ(k) is plotted as a function of k, k^2 or k^3. Light elements are plotted in lower 'k space' since this is where their impact is appreciated, while heavy elements are more impactful at higher 'k'.

$$k = \sqrt{\frac{2m_e E}{\hbar^2}} \qquad \text{Equation 2.14}$$

Where m_e is the mass of an electron and $\hbar = \frac{h}{2\pi}$, with h as Planck's constant.

2.4.2.3 EXAFS Fitting

The fitting of EXAFS data was performed using the Artemis program in the Demeter software package [23], this fitting is in 'R space' which represents radial distance. A Fourier transform is performed on the EXAFS region to convert 'k space' to 'R space'. This Fourier transform excludes the first and/or second oscillations in the χμ(E), spectrum since the χ(k) spectrum at the Pt L_3 edge is distorted due to white line features, and the χ(k) spectrum commonly contains very noisy data at high values of k, this region is also excluded. The Fourier transform region typically used was ~2.2 – 16 $Å^{-1}$, however, this was altered to ensure a stable and robust fitting for each sample.

The modelled spectrum is based on the EXAFS equation, shown in Equation 2.15, as well as Equations 2.16 and 2.17. The spectrum is fitted to this model to obtain the parameters such as co-ordination number, atomic distances and disorder factors.

$$\chi(k,\Gamma) = \sum_{\Gamma} \frac{(N_{\Gamma} S_0^2) F_{\Gamma}(k)}{2kR_{\Gamma}^2} \sin(2kR_{\Gamma} + \phi_{\Gamma}(k)) e^{-2\sigma_{\Gamma}^2 k^2} e^{-2R_{\Gamma}/\lambda(k)} \qquad \text{Equation 2.15}$$

$$k = \sqrt{\frac{2m_e E - E_0}{\hbar^2}} \qquad \text{Equation 2.16}$$

$$R_{\Gamma} = R_{eff} + \Delta R_{\Gamma} \qquad \text{Equation 2.17}$$

These parameters are the number of photoelectron scattering paths (Γ), the degeneracy of the path (N_Γ), the effective photoelectron half path length (R_Γ), the theoretical value for the effective photoelectron half path (R_{eff}) the mean square disorder of the path (σ_Γ), the amplitude reduction factor (S_0^2) and the energy required to remove the photoelectron from the absorbing atom (E_0). Theoretical functions involve the effective scattering amplitude of the photoelectron ($F_\Gamma(k)$), the phase shift of the photoelectron ($\Phi_\Gamma(k)$) and the mean free path of the photoelectron ($\lambda_\Gamma(k)$). The parameters can be defined as expressions containing multiple variables in the Artemis software, which enables complex models with multiple constraints between the variables to be fitted. The crystal structures, and therefore degeneracy, path length and possible single scattering and multiple scattering paths are generated from the Crystallographic Information File (CIF) of the material. These parameters are used as the initial values in the theoretical functions in the EXAFS modelling. The data was fitted from the first co-ordination shell, atoms at the same distance from the absorbing atoms are considered to be in the same shell, and shells are numbered sequentially from the closest neighbouring shell (N_1) to extended distance shells ($N_{2..n}$).

The parameters N_Γ, S_0^2, σ_Γ, E_0 and R_Γ in Equations 2.15 - 2.17 are defined for each scattering path and constrained in their relationships to other paths. The Nyquist theorem is used to determine the upper limit of the number of independent variables (N_{ind}), this is proportional to the k-space range used in the Fourier transform and the R-space range used in the fit, as per Equation 2.18. However, the number of variables is restricted to 50-60% of the N_{ind} determined since not all the assumptions used in the Nyquist theory hold when considering EXAFS spectra.

$$N_{ind} \approx \frac{2\Delta k \Delta R}{\pi} \qquad \text{Equation 2.18}$$

S_0^2 scales the theoretical spectrum along the amplitude and E_0 scales the theoretical spectrum along the energy axis, these are influenced by the beamline and therefore these parameters are represented by a single variable for all the scattering paths modelled. The remaining variables N_Γ, σ_Γ and R_Γ are defined as independent variables under specific constraints. σ_Γ is constrained by the photoelectron free path with a new variable for each single scattering path and multi-scattering paths are constrained within the single scattering variables, as described in Figure 2.8 and Table 2.1. An assumption is made that the path length between the absorbing atom and its closest neighbour is half that of the path length between the absorbing atom and the second closest neighbour [24]. It is known that the Pt crystal structure is highly symmetrical in the cubic close packed structure (fcc), therefore R_{eff} path length is defined by a single variable containing an isotropic expansion, from the theoretical value, for all paths fitted.

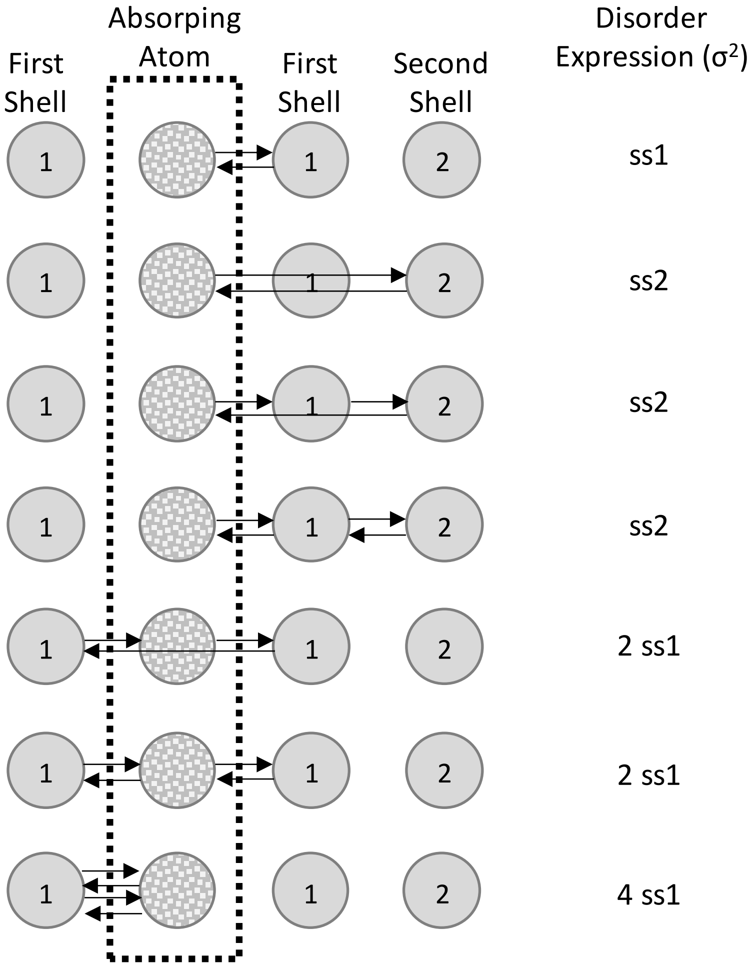

Figure 2.8: Illustration of the constraints and definitions used in the σ^2 parameter fitting, where the first shell consists of the closest neighbouring atoms and consecutive shells are named accordingly.

The theoretical value for the degeneracy (*N*) of the path was assumed for the Pt reference foil, in order to determine the amplitude reduction factor (S_0^2) for the catalyst samples measured, the parameters are described in Table 2.1. Once the amplitude reduction factor is determined, the degeneracy path (N_r) is fitted with a fixed value for S_0^2 in the catalyst samples as degeneracy deviated from theoretical values due to shape and termination effects present in the particle. The surface area of a Pt nanoparticle contributes significantly to the bulk material, therefore the assumption that degeneracy is the same as the bulk theoretical value is not valid and these parameters need to be included as independent variables. The variables for N_r are constrained with a new variable for each single scattering path and multi-scattering paths are constrained within the single scattering variable, with the exception of obtuse triangle paths [25,26]. The σ_r, E_0 and R_r variables are described identically to the Pt reference foil described above.

Table 2.1: Parameters and scattering paths included in the EXAFS fitting model for a Pt reference foil.

Scattering Path	Path Type	N	σ^2 / Å^2	R_{eff} / Å
Pt – Pt$_1$	Single	12	ss1	2.775
Pt – Pt$_2$	Single	6	ss2	3.924
Pt – Pt$_{1a}$ – Pt$_{1b}$	Acute Triangle	48	1.5 ss1	4.162
Pt – Pt$_1$ – Pt$_2$ – Pt$_1$	Double	24	ss1 + ss2/2	4.737
Pt – Pt$_3$	Single	24	ss3	4.806
Pt – Pt$_1$ – Pt$_3$ – Pt$_1$	Obtuse Triangle	48	ss1 + ss3/2	5.178
Pt – Pt$_{1a}$ – Pt$_{1b}$ – Pt$_3$	Obtuse Triangle	96	ss1 + ss3/2	5.178
Pt – Pt$_4$	Single	12	ss4	5.550
Pt – Pt$_{1a}$ – Pt$_{1b}$	Non-forward Linear	12	ss1 + ss4/2	5.550
Pt – Pt$_{1a}$ – Pt$_4$	Forward	24	ss1 + ss4/2	5.550
Pt – Pt$_{1a}$ – **Pt** – Pt$_{1b}$	Forward Through Absorber	12	2ss1	5.550
Pt – Pt$_{1a}$ – Pt$_4$ – Pt$_{1a}$	Double Forward	12	2ss1	5.550
Pt – Pt$_{1a}$ – Pt$_{1b}$ – Pt$_{1a}$	Dog-Leg	48	2ss1	5.550
Pt – Pt$_{1a}$ – Pt$_{1b}$ – Pt$_{1a}$	Triple	48	2ss1	5.550
Pt – Pt$_1$ – Pt$_3$	Obtuse Triangle	48	2ss1	5.550
Pt – Pt$_{1a}$ – Pt$_4$ – Pt$_{1a}$	Dog-Leg	48	4ss1	5.550

The error of the fit in Artemis is calculated using a non-linear least-squares method (Leven-Marquardt) which determines the chi-squared error criterion (χ^2) and Equation 2.19 is used to determine the 'r-factor' [27].

$$\mathrm{r} = \frac{\sum_{i=min}^{max}[Re(\chi_d(r_i) - \chi_t(r_i))^2 + Im(\chi_d(r_i) - \chi_t(r_i))^2]}{\sum_{i=min}^{max}[(Re(\chi_d(r_i))^2 + Im(\chi_d(r_i))^2]} \qquad \text{Equation 2.19}$$

The values calculated for χ^2 and the r-factor are not meaningful due to the measurement of uncertainty calculation in Artemis, approximations in the theory, sample inhomogeneity and non-linearity of detectors. Therefore, these values are used as an estimation of the quality of the fit between two fits, a lower χ^2 determines a better fit while a r-factor of less than 0.05 is a good fit. The error bars reported on parameter fittings are obtained using the diagonal of covariance matrix, scaled by $\sqrt{\chi_v^2}$ in order to ensure error bars are of the correct magnitude. It should be kept in mind that good fits need also make physical and chemical sense.

2.4.2.4 d-Band Vacancy Calculation

The XANES at the $L_{2,3}$ edges originate from exciting 2p core states. The L_2 edge arises from the 2p J=1/2 core states, and the L_3 X-ray absorption edge arises from the 2p J=3/2 core states, excited to vacant d-states. The L_2 and L_3 edges of the samples and Pt reference foil are calibrated for the inflection point in the edge step, using the first crossing of the x-axis in the second derivative of the χμ(E) spectrum and setting this value to 0 eV.

An arctan curve is then fitted to the Pt reference foil to pass through the local minima after the second peak in the L_3 spectrum and the local minima after the edge in the L_2 spectrum, as shown in Figure 2.9. The difference in area between the Pt reference foil and the arctan for both the L_3 and L_2 edges were determined ($\Delta A_{Ref\text{-}Arctan,L3}$ *and* $\Delta A_{Ref\text{-}Arctan,L2}$), as shown in the shaded area in Figure 2.9, for the energy range 0 - 12 eV and 0 - 8 eV. The difference in area between the Pt reference foil and the arctan for both the L_3 and L_2 edges were also determined for the energy range of -10 – 40 eV (ΔA_{L3R} *and* ΔA_{L2R}). The assumption that the bulk Pt d-band vacancy is 0.3 ($h_{R,Pt\ Bulk}$) and the contribution to d-band vacancy is a ratio of 14:1 for the $h_{5/2}$: $h_{3/2}$ d-band holes, was made as described by Mansour *et al.* [28] and Brown *et al.* [29]. The difference in area between the samples and the arctan for both the L_3 and L_2 edges were then determined ($\Delta A_{Sample\text{-}Arctan,L3}$ *and* $\Delta A_{Sample\text{-}Arctan,L2}$) for the energy range 0 - 12 eV and 0 - 8 eV, respectively and Equations 2.20 and 2.21 were used to calculate ΔA_{L3} and ΔA_{L2}.

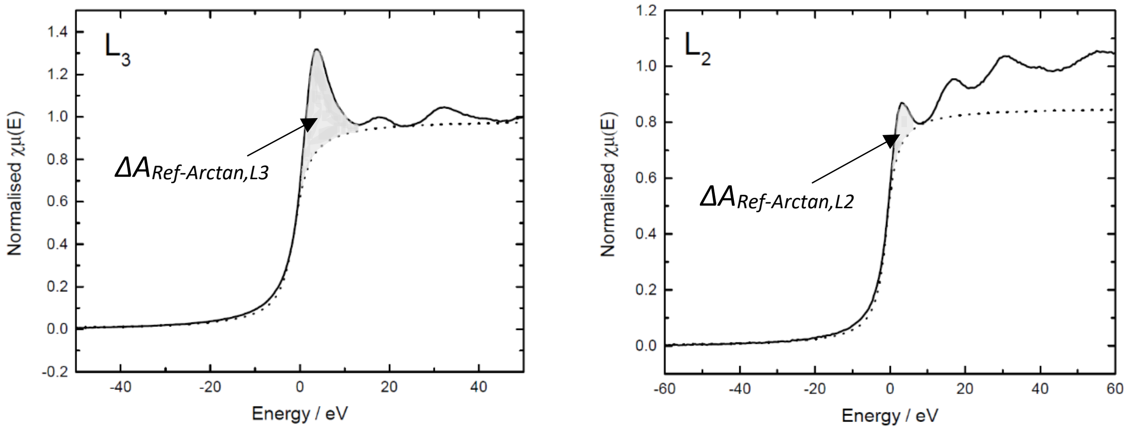

Figure 2.9: A demonstration of the arctan fittings on the normalised L_3 and L_2 XAS spectra, the area between the spectra and arctan fittings ($\Delta A_{Ref\text{-}Arctan,L3}$ *and* $\Delta A_{Ref\text{-}Arctan,L2}$) are shown in the shaded area.

$$\Delta A_{L3} = (\Delta A_{Sample-Arctan,L3} - \Delta A_{Ref-Arctan,L3})\times c\times \rho \qquad \text{Equation 2.20}$$

$$\Delta A_{L2} = (\Delta A_{Sample-Arctan,L2} - \Delta A_{Ref-Arctan,L2})\times c\times \rho \qquad \text{Equation 2.21}$$

$$f_d = \frac{(\Delta A_{L3}+1.11\Delta A_{L2})}{(\Delta A_{L3R}+1.11\Delta A_{L2R})} \qquad \text{Equation 2.22}$$

$$h_T = (1 + f_d)h_R \qquad \text{Equation 2.23}$$

Where ΔA_{L3} and ΔA_{L2} are the normalised values by the X-ray absorption cross section at the edge jump (c) and ρ is the density of platinum [29]. The value of c was previously reported as 117.1 and 54.2 $cm^2.g^{-1}$ at the L_3 and L_2 edge, respectively [30]. ΔA_{L3R} *and* ΔA_{L2R} were also normalised for $c\times\rho$ so all measured areas are in the same units. The calculated fractional change in the number of holes (f_d) (from Equation 2.22) is subsequently used to calculate the total density of the unoccupied d-state (h_T) as shown in Equation 2.23.

2.5 References

1. Malandrino, G. 2009. Chemical Vapour Deposition. Precursors, Processes and Applications. Edited by Anthony, C. Jones and Michael, L. Hitchman. *Angewandte Chemie International Edition.* 48(41):7478-7479.
2. Battiston, G.A., Gerbasi, R. & Rodriguez, A. 2005. *Chemical Vapor Deposition*. 11(3):130-135.

3. Thurier, C. & Doppelt, P. 2008. *Coordination Chemistry Reviews*. 252(1–2):155-169.
4. Morozova, N.B., Zharkova, G.I., Semyannikov, P.P., Sysoev, S.V., Igumenov, I.K., Fedotova, N.E. & Gelfond, N.V. 2001. *Journal de Physique IV France.* 11(PR3):Pr3-609-Pr3-616.
5. Yoda, S., Hasegawa, A., Suda, H., Uchimaru, Y., Haraya, K., Tsuji, T. & Otake, K. 2004. *Chemistry of Materials.* 16(12):2363-2368.
6. Jackson, C., Conrad, O. & Levecque, P. 2017. *Electrocatalysis.* 8(3):224-234.
7. Kumsa, D.W., Bhadra, N., Hudak, E.M., Kelley, S.C., Untereker, D.F. & Mortimer, J.T. 2016. *Journal of Neural Engineering.* 13(5):052001.
8. Angerstein-Kozlowska H, Conway B. E, and Sharp W. B. A. 1973. *Journal of Electroanalytical Chemistry and Interfacial Electrochemistry*. 4:9–36.
9. Climent, V. & Feliu, J. 2011. *Journal of Solid State Electrochemistry.* 15(7-8):1297-1315.
10. Zhang, H., Wang, X., Zhang, J.L. & Zhang, J.W. 2008. *Electrocatalysts and Catalyst Layers Fundamentals and Applications.* London: Springer.
11. Will, F.G. 1965. *Journal of the Electrochemical Society.* 112(4):451-455.
12. Pletcher, D., Greff, R., Peat, R., Peter, L.M. & Robinson, J. 2001. *Instrumental Methods in Electrochemistry.* First ed. Cambridge: Woodhead Publishing Limited.
13. Xing, L., Hossain, M.A., Tian, M., Beauchemin, D., Adjemian, K. & Jerkiewicz, G. 2014. *Electrocatalysis.* 5(1):96-112.
14. Trasatti, S. & Petrii, O.A. 1991. Pure and Applied Chemistry. 63(5):711-734.
15. Mayrhofer, K.J.J., Strmcnik, D., Blizanac, B.B., Stamenkovic, V., Arenz, M. & Markovic, N.M. 2008. *Electrochimica Acta.* 53(7):3181-3188.
16. Fabbri, E., Taylor, S., Rabis, A., Levecque, P., Conrad, O., Kötz, R. & Schmidt, T.J. 2014. *ChemCatChem.* 6(5): 1410–1418.
17. Maillard, F., Schreier, S., Hanzlik, M., Savinova, E.R., Weinkauf, S. & Stimming, U. 2005. *Physical Chemistry Chemical Physics*. 7(2):385-393.
18. Shinozaki, K., Zack, J.W., Richards, R.M., Pivovar, B.S. & Kocha, S.S. 2015. *Journal of the Electrochemical Society*. 162(10):F1144-F1158.
19. Hafner, B. 2013. *Energy Dispersive Spectroscopy on the SEM: A Primer.* Available: http://www.charfac.umn.edu/instruments/eds_on_sem_primer.pdf [10/07/2017].

20. Australian Microscopy & Microanalysis Research Facility 2014. *Quantitative EDS X-ray microanalysis using SEM.* Available: http://www.ammrf.org.au/myscope/analysis/eds/quantitative/ [10/07/2017].
21. Thermo Fischer Scientific Inc. 2016. *Carbon*. Available: http://xpssimplified.com/elements/carbon.php [26/07/2017].
22. Calvin, S. 2013. *XAFS for Everyone.* Taylor & Francis.
23. Ravel, B. & Newville, M. 2005. *Journal of Synchrotron Radiation*. 12:537–541
24. Hudson, E.A., Allen, P.G., Terminello, L.J., Denecke, M.A. & Reich, T. 1996. *Physical Review B.* 54(1):156-165.
25. Frenkel, A., 1999. *Journal of Synchrotron Radiation.* 6(3):293-295.
26. Frenkel, A.I., Hills, C.W. & Nuzzo, R.G. 2001. *The Journal of Physical Chemistry B.* 105(51):12689-12703.
27. Ravel, B. 2017. *Advanced Topics in EXAFS Analysis*. Available: http://xafs.org/Community/NSLSXasTraining?action=AttachFile&do=get&target=stats_in_exfas.pdf [03/08/2017].
28. Mansour, A.N., Cook, J.W. & Sayers, D.E. 1984. *The Journal of Physical Chemistry.* 88(11):2330-2334.
29. Brown, M., Peierls, R.E. & Stern, E.A. 1977. *Physical Review B.* 15(2):738-744.
30. McMaster, W.H., Kerr Del Grande, N., Hubell, J.H. Compilation of X-ray Cross Sections. National Technical Information Service. Springfield, VA.

Chapter 3

Advanced Surface Characterisation of Pt on Silicon Carbide for the Oxygen Reduction Reaction

---

Abstract

This study presents an investigation into silicon carbide (SiC) as an alternative catalyst support material to high surface area carbons for the oxygen reduction reaction in acidic media. XPS spectra confirmed a shift of the Pt 4f spectrum to higher binding energies on the Pt/SiC catalysts relative to Pt/C, as well as a shift in the Si-C bond in Si 2p and C 1s spectra to lower binding energies relative to bare SiC. This relationship suggests a charge transfer between Pt nanoparticles and the SiC support. Additionally, *in-situ* XANES showed a change in the interaction of Pt/SiC with adsorbates over a range of potentials when compared to Pt/C. Although a strong metal-support interaction is demonstrated between the Pt and SiC for the as prepared catalysts, after sonication during ink preparation, these nanoparticles agglomerated into Pt nanoparticle clusters and the true ORR activity could not be determined. Moreover, SiC was not sufficiently conductive to perform electrochemical characterisations on the Pt/SiC catalysts without the addition of carbon to the catalyst ink. The durability testing on the Pt/SiC+C catalyst revealed oxidation of the SiC and/or carbon layer at high potentials, significantly decreasing the ECSA.

3.1 Introduction

The oxygen reduction reaction (ORR) is a multi-electron reaction with a high overpotential which reduces the efficiency of the PEFC. This is a complex challenge for research into PEFCs [1]. Fundamental research into PEFCs is therefore focused on the kinetic activity, stability and cost of the cathode catalysts [2]. Considerable efforts have been made on improving ORR activity via nanoparticulate Pt and Pt alloys supported on high surface area carbon [3-6]. An emphasis is also placed on preventing the loss of catalyst surface area due to support corrosion, Pt dissolution and agglomeration during fuel cell operating conditions [7,8]. The relationship between the rate of the cathode reaction and the oxygen adsorption energy shows a volcano-shaped trend, as seen in Figure 1.2, with platinum closest to the expected peak. Catalytic improvement can be made by producing platinum alloyed with metals which have smaller oxygen binding energies than pure platinum, such as nickel, cobalt, iron and chromium [9]. An attractive method of improving platinum activity and stability for the ORR is by exploiting of strong metal-support interactions (SMSIs) [10-15].

The strong metal-support interaction of Pt on oxide supports, particularly titanium dioxide, is widely studied [16-18]. Additionally, the role of the metal-support interaction on Pt/TiO_2 [10-13] and highly conductive SnO_2-based supports [14,15] on the increased activities for ORR in relation to Pt/C was investigated. Thin film studies on SnO_2-based supports unveiled an interesting dependence of ORR activity on support orientation and/or termination sites of the support [19]. However, comparison between Pt nanoparticles deposited on carbon and oxide supports is potentially difficult due to changes in particle morphology.

Silicon carbide (SiC) is considered a refractory compound which exhibits high chemical inertness [20]. SiC correspondingly displays high stability when exposed to acids [21,22]. Honji *et al.* [23] first proposed SiC as a catalyst support for phosphoric acid fuel cells and similar results were recorded to Pt/C catalysts. Recently, Lv *et al.* [24] investigated the electrochemical activity and stability of SiC at 1.2 V vs RHE for 48 hours and found the electrochemical stability to be remarkably high as minimal change was seen over this period. Lv *et al.* [24] deposited Pt/SiC on carbon to improve ORR activity, the Pt/SiC/C catalyst intrinsic activity was identical to that of Pt/C. SiC nanowires have also been investigated and showed promising results for ORR activity with a current density of 290 $\mu A.cm^{-2}$ at 0.57 V vs. RHE from a cyclic voltammogram on an rotating disc electrode and high stability, however, no comparison was made to Pt/C [25].

In this work, Pt/SiC was investigated as an alternative catalyst support material for the Oxygen Reduction Reaction in acidic media. Electrochemical as well as advanced characterisation techniques were used to clarify the structure-property relationships between catalyst morphology, metal-support interaction, and ORR activity. Extended X-ray absorption fine structure (EXAFS) analysis gave insights into the shape of the clustered nanoparticles while X-ray photoelectron spectroscopy (XPS) and *in-situ* X-ray absorption near-edge spectroscopy

(XANES) analysis provided information into electronic effects and how these relate to metal-support interactions.

3.2 Experimental

Physical Characterisations: The prepared support material was characterised via physisorption using Brunauer, Emmett and Teller (BET) theory (Micromeritics Instrument Corporation TriStar II) to determine the support surface area. X-ray diffraction (XRD) measurements were carried out on a Bruker D8 Advance diffractometer with a Cu Kα radiation source operating at 40 kV to determine the crystalline phases present in the catalyst. Rietveld Refinement on the XRD patterns was completed using Bruker AXS TOPAS software, Version 4.1. Transmission electron microscopy (TEM) was performed on a Tecnai G2 electron microscope operating at 200 kV to determine particle sizes. X-ray photoelectron spectroscopy (XPS) was carried out by Nexus XPS service using a Thermo Scientific K-Alpha instrument with an Al Kα X-ray source. The supported catalyst was characterised using TEM for Pt particle size using an average of at least 100 particle diameters, XRD to verify the Pt crystallite size, XPS to investigate the binding energy and quantify Pt and its oxides, ICP-OES (Varian 730-ES) to confirm the Pt loading on the support.

X-ray Absorption Spectroscopy: Ex-situ and *in-situ* characterisations were completed using X-ray adsorption spectroscopy on the B18 line at the Diamond Light Source. The Pt L_3 edge (11 564 eV) and Pt L_2 edge (13 273 eV) was measured with a ring energy 3 GeV and at a current of 300 mA. A Si(111) monochromator was used and spectra were collected in Quick EXAFS (QEXAFS) mode. A total of three spectra was averaged for each sample. The measurements were collected using the ionisation chambers in transmission mode at 298 K. Calibration of the monochromator was carried out at both edges using Pt foils. The stability of the beam ensured the energy scale did not drift during data collection. XAS was collected for the 20 wt% Pt/C and 20 eq wt% Pt/SiC catalysts only. For *ex-situ* measurements, these catalysts were prepared using boron nitride to bind pellets of the catalysts, the pellets were then placed under a H_2 atmosphere to reduce surface oxides. The absorption spectra were modelled with Demeter© by Bruce Ravel using Ifeffit© by Matt Newville [26] to solve the EXAFS equation.

The *in-situ* measurements were carried out in an *in-situ* electrochemical cell [27], electrodes were prepared by a catalyst ink coated onto teflon coated carbon base layer (Alfa Aesar). The ink formulation for the 20 eq wt% Pt/SiC+C catalyst consisted of 174 mg 40 eq wt% Pt/SiC catalyst, 178 mg carbon (Cabot Corporation), 4.5 ml 5 wt% Nafion solution, 7.5 ml ethanol (Sigma Aldrich), this ink mixture was sonicated and a catalyst layer with a loading of 0.5 $mg_{Pt}.cm^{-2}{}_{Pt}$ was painted onto the carbon base layer. The catalyst coated carbon layer is then hot pressed at 170 °C and 7.8 kPa. All electrodes were flooded prior to use by vacuum filling in ultrapure water. A platinum wire was used as a counter electrode, and $Hg/HgSO_4$ was used as a reference electrode. Potentials are adjusted to vs. RHE using a correction factor of 0.654 V.

Electrochemical characterisation: A catalyst ink was prepared for the electrochemical characterisation techniques. The Pt/SiC catalyst ink consisted of 2.5 mg of the catalyst, 2.5 mg carbon (Cabot Corporation), 1 ml of ethanol (Sigma Aldrich) and 25 µL of 5 wt% Nafion solution. Carbon was added to the ink due to the low conductivity of SiC to show electrochemical reactions. These catalyst inks are referred to as Pt/SiC+C. The mixture was sonicated for 30 minutes and 5 µL was placed on a glassy carbon electrode. The Pt/C catalyst ink consisted of 5 mg of the catalyst, 5 ml of water (Milli-Q 18.2 MΩ.cm), 1.5 ml isopropanol (Kimix) and 25 µL of 5 wt% Nafion solution. The mixture was sonicated for 30 minutes and 10 µL was placed on a glassy carbon electrode. This resulted in a Pt loading of 4.2×10^{-7}, 1.2×10^{-6} and 2.2×10^{-6} g on the glassy carbon electrode for the 10, 20 and 40 eq wt% Pt/SiC+C catalysts, respectively, and 7.7×10^{-7}, 1.6×10^{-6} and 3.1×10^{-6} g for the 10, 20 and 40 wt% Pt/C catalysts, respectively. Prior to this the glassy carbon electrode was polished to a mirror finish using 0.1 and 0.05 µm Al_2O_3 polish on microcloth (Buehler). Cyclic voltammetry was conducted by cycling the potential between 0.05 – 1.2 V vs. RHE with a scan rate of 100 $mV.s^{-1}$ for 50 cycles at room temperature in an oxygen-free 0.1 M $HClO_4$ electrolyte solution to electrochemically clean the catalyst surface. The reference electrode used was $Hg/HgSO_4$ with a platinum counter electrode. The scan rate was then changed to 20 $mV.s^{-1}$ for 5 cycles and the potential cycled between 0.05 – 1.2 V vs RHE at room temperature in an oxygen-free 0.1 M $HClO_4$ electrolyte solution. CO stripping was conducted by purging the electrolyte solution with CO for 20 minutes while holding the potential at 0.1 V vs. RHE, argon was then bubbled for 20 minutes to rid the solution of CO, after which the potential was cycled between 0.05 – 1.2 V vs RHE. The ORR activity was measured by rotating disc electrode experiments in an O_2 saturated 0.1 M $HClO_4$ electrolyte (70% Suprapur - Merck) using the anodic scan between 0.05 and 1.2 V vs. RHE, with a scan rate of 20 $mV.s^{-1}$ and rotation rate of 1600 rpm at room temperature, all reported ORR activities are iR corrected. All scans were normalised for electrochemically active surface area, ohmic drop measured by impedance spectroscopy, and capacitive current in an oxygen free electrolyte. Error margins were obtained from 2 to 4 repeats for each data point. The first durability sequence on the catalysts were completed by cycling between 0.6 – 1.0 V vs. RHE and the second and third degradation studies were completed by cycling between 1.0 – 1.5 V vs. RHE. All degradation studies were completed with a scan rate of 50 mV.s^{-1} in 0.1 M $HClO_4$ electrolyte solution for 6000 cycles at room temperature, and periodically reverted to a cyclic voltammogram between 0.05 – 1.2 V vs. RHE with a scan rate of 20 mV.s^{-1} to investigate the changes to the H_{UPD} region. The reference electrode used was Hg/$HgSO_4$ with a gold counter electrode. The H_{UPD} region was used for changes in ECSA in this instance.

3.3 Results

3.3.1 BET-BJH Analysis

The support surface area, average pore size and pore volume of the supports were evaluated using physisorption with Brunauer, Emmett and Teller (BET) theory and Barrett-Joyner-Halenda (BJH) Analysis respectively, and these are reported in Table 3.1.

Table 3.1: BET surface areas, average pore sizes and pore volumes for the Vulcan and SiC.

Support	Surface Area / m^2.g^{-1}	Average Pore Size / nm	Pore volume / cm^3.g^{-1}
Vulcan	230	8.7	0.499
SiC	35.5	12.0	0.107

Vulcan has a large support surface area of 230 m^2.g^{-1} and large pore volume while the surface area of the SiC is lower at 35.5 m^2.g^{-1} with a smaller pore volume. However, the SiC pore sizes are slightly larger with a pore diameter of 12 nm, compared to Vulcan pore sizes of 8.7 nm.

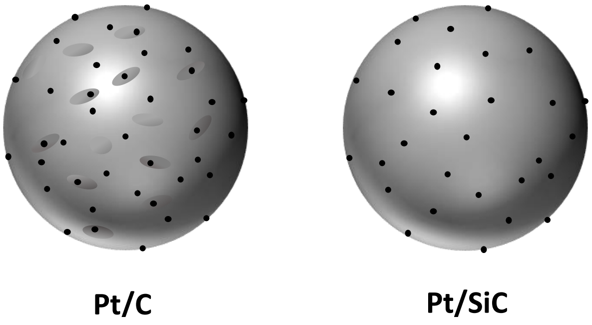

Figure 3.1: Schematic of equivalent Pt loadings on different support surfaces, the grey sphere represents the support material, the small oblong shapes represent the pores of the support and the small black spheres represent the Pt nanoparticles.

The BET surface area was used to normalise the loading of Pt on the surface of the support, therefore Pt/C catalysts can be compared to Pt/SiC catalysts in order to make fundamental observations on catalyst performance. This normalisation technique is needed to maintain a constant Pt coverage per surface area of support which maintains a consistent inter-particle distance and particle size, so that any changes seen in activity can be attributed to a support effect. An illustration of this Pt coverage on the different supports is shown in Figure 3.1. It is imperative to keep particle size and inter-particle distances constant across support surfaces since these, in their own right, can affect ORR activities significantly [28,29].

Table 3.2: Nominal, target and actual catalyst loadings on C and SiC supports.

Nominal wt% Pt/C	Actual wt% Pt/C	Target wt% Pt/SiC	Actual wt% Pt/SiC
10	9.19	1.69	1.67
20	17.5	3.71	4.91
40	37.85	9.33	8.65

Table 3.2 reports the nominal, target and actual catalyst loadings on the Pt/SiC and Pt/C. Therefore, the Pt loading on the carbide supports will be referred to the equivalent weight percent, while Pt loading on carbon will refer to the true weight percent and these catalysts can be directly compared in terms of electrochemical activity.

3.3.2 Transmission Electron Microscopy (TEM)

The particle sizes of the bare supports were measured using TEM imaging, these were measured to be 47.1 ± 12 and 57.0 ± 36 for Vulcan and SiC, respectively. The TEM images for the commercial Pt/C benchmark catalysts and the carbide supported catalysts' TEM images with varied loadings are shown in Figure 3.2. The Pt particle sizes and interparticle distances measured from the TEM images, for all the supported catalysts are reported in Table 3.3. The Pt nanoparticle sizes and particle size distributions slightly larger on the Pt/SiC catalysts when compared to Pt/C. The Pt interparticle distances on the 20 and 40 eq wt% Pt/SiC and the 20 and 40 wt% Pt/C catalysts are similar, however, a large deviation is noted between the interparticle distances on the 10 eq wt% Pt/SiC and 10 wt% Pt/C catalysts.

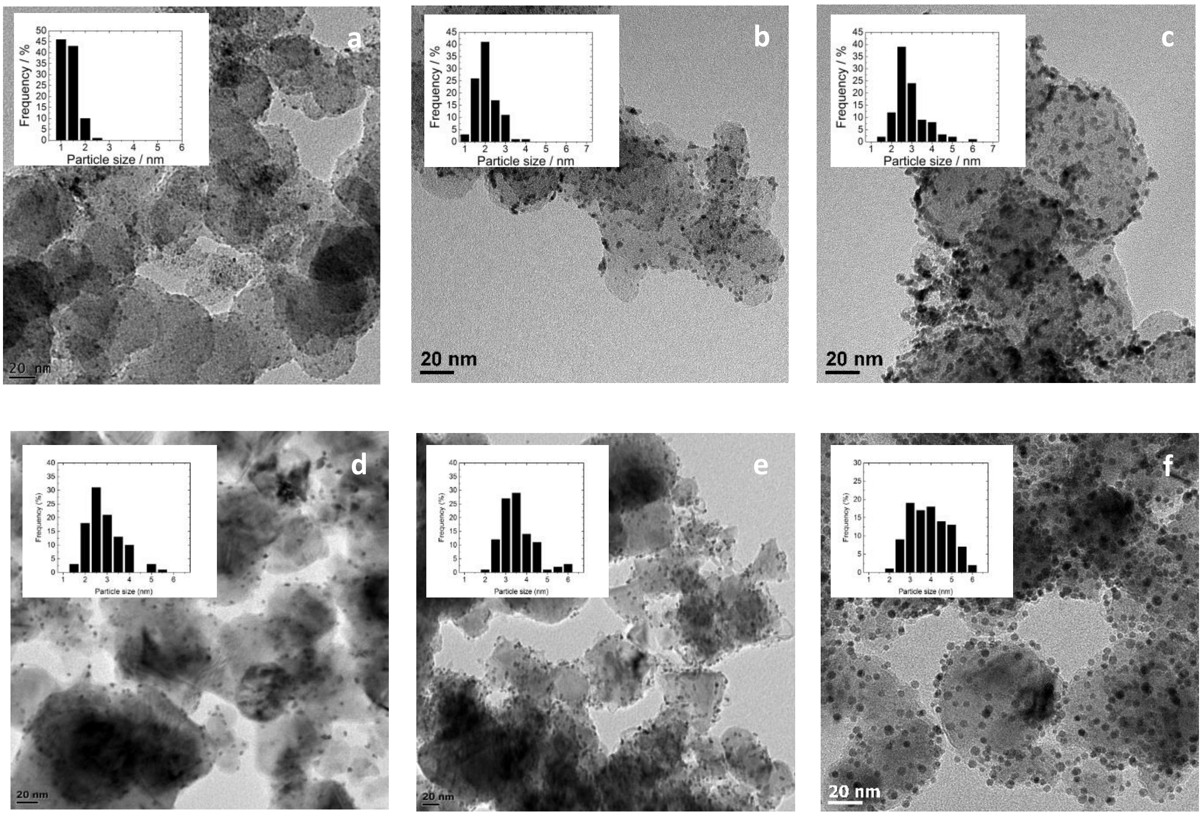

Figure 3.2: TEM images and particle size distribution graphs of (a) 10 wt% Pt/C, (b) 20 wt% Pt/C, (c) 40 wt% Pt/C, (d) 10 eq wt% Pt/SiC, (e) 20 eq wt% Pt/SiC and (f) 40 eq wt% Pt/SiC.

Table 3.3: Pt particle sizes and inter-particle distances measured using TEM images of the different supported catalysts.

Catalyst	Pt particle size / nm	Pt inter-particle distances / nm
10 wt% Pt/C	1.1 ± 0.3	6.6 ± 3
20 wt% Pt/C	2.1 ± 0.5	7.1 ± 2
40 wt% Pt/C	2.7 ± 0.7	5.1 ± 1
10 eq wt% Pt/SiC	2.6 ± 0.8	13.1 ± 6
20 eq wt% Pt/SiC	3.3 ± 0.8	8.3 ± 3
40 eq wt% Pt/SiC	3.6 ± 0.9	5.9 ± 2

3.3.3 X-Ray Diffraction (XRD)

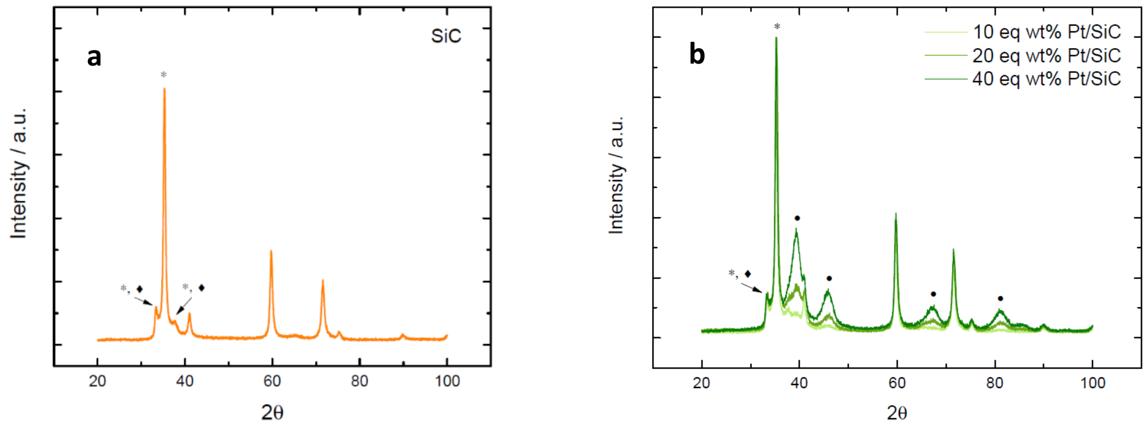

Figure 3.3: XRD pattern of (a) commercial SiC and (b) different loadings of Pt/SiC where (*) denotes the 3C-SiC peaks, (◆) denotes the 189R-SiC peaks and (•) denotes Pt peaks.

Silicon carbide exists in approximately 250 different crystal structures [30], the most common being 3C-SiC and 6H-SiC. Figure 3.3a displays the XRD pattern of the commercial SiC, there are few defining peaks between 3C SiC and 189R SiC, however, the peak height ratios are specific to the crystal structures. Rietveld refinement presented the SiC to comprise of 67% 3C-SiC and 33% 189R-SiC. These peaks are confirmed by literature for 3C-SiC [31] and 189R SiC [32].

Figure 3.3b displays the XRD patterns of the carbide supported catalysts with various Pt loadings. As expected, the Pt peak heights increase (2ϴ ≈ 38°, 46°, 67° and 81°) as the Pt loading increases. Furthermore, the Pt deposition method does not alter the crystallinity of the support material. Rietveld refinement confirmed the average Pt crystallite size to be between 3 - 4.2 nm for the various loadings of Pt/SiC. As expected, the crystallite size determined from the XRD is slightly larger than the size measured by TEM in Table 3.3, since the lower detection limit of XRD is 2 - 2.5 nm, so particle sizes smaller than 2 nm are not identified [33], while these contribute to the TEM particle size measurements. Additionally, the average particle sizes determined from XRD are volume-weighted, therefore larger Pt particles have a larger contribution to the average particle size due to their larger volume.

3.3.4 X-Ray Photoelectron Spectroscopy

XPS was primarily used to investigate the binding energies on the various carbide supports. When analysing XPS data, the results first need to be adjusted for the sample charging effects. The correction to the SiC catalysts was done by identifying the C-C sp^3 bond in the C 1s spectrum, from adventitious carbon, and adjusting this to its true value of 284.8 eV [34], while the correction to the commercial catalysts were adjusted for C-C sp^2 bond's true value of 284 eV [34].

The Pt 4f and Si 2p spectra of the Pt/C and Pt/SiC catalysts are represented in Figure 3.4 and the peak positions from deconvolution of the C 1s and Si 2p spectra are reported in Table 3.4. The Pt 4f spectra clearly shows a shift to higher binding energies of 0.4-0.6 eV from Pt/C, while the Si-C spectra demonstrates a shift to lower binding energies of 0.1 eV and 0.3 eV in the Si 2p and C 1s spectra, respectively. The modelling of the XPS Si 2p and C 1s spectra are shown in Figure S3.1 and S3.2 (See Chapter 3.7), respectively.

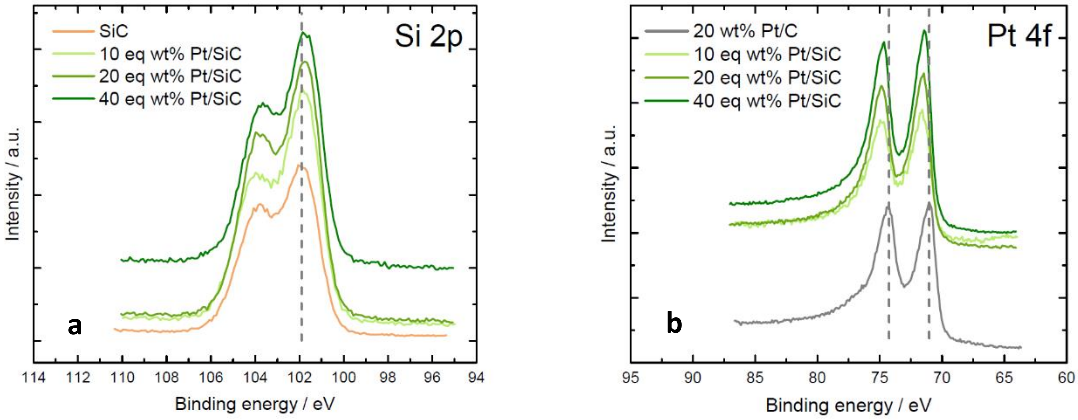

Figure 3.4: XPS spectra of the (a) the Si 2p region of SiC and Pt/SiC catalysts with different loadings and (b) Pt 4f region of the Pt/C and Pt/SiC catalysts.

Table 3.4: Pt 4f, Si-C 2p and Si-C C1s peak positions for the SiC support material and Pt/SiC and Pt/C catalysts.

Catalyst	Pt 4f Peak Positions		Si-C Si 2p bond peak position	Si-C C1s bond peak position
20 wt% Pt/C	71.0	74.2	-	-
SiC	-	-	101.8	284.0
10 eq wt% Pt/SiC	71.6	75.0	101.7	283.7
20 eq wt% Pt/SiC	71.5	74.9	101.7	283.7
40 eq wt% Pt/SiC	71.4	74.6	101.7	283.7

3.3.5 *Ex-situ* EXAFS

Ex-situ X-ray adsorption spectroscopy, namely the Extended X-ray Absorption Fine Structure (EXAFS) region, was used to investigate the Pt L_3 – edge to give insight into the supported Pt morphology. The absorption spectra were modelled with Demeter© using Ifeffit© [26] to solve the EXAFS equation for the first three Pt shell coordination numbers as described by Frenkel *et al.* [35]. The first shell coordination number is strongly related to the particle size and the particle size distribution [36] while the ratio of the third to first coordination number is an indication of particle morphology.

The modelled EXAFS spectra are shown for the 20 wt% Pt/C and 20 eq wt% Pt/SiC catalysts in Figure 3.5. Figures 3.5a and 3.5b are the actual and modelled data of the 20 wt% Pt/C, shown in R space and k space respectively. Figures 3.5c and 3.5d are the actual and modelled data of the 20 eq wt% Pt/SiC in R space and k space, respectively. The fitted model, considering up to the fourth neighbour shells, describes the EXAFS data well for both samples. The coordination numbers (N), distances of neighbouring atoms (R) and the disorder factors (σ^2) of the catalyst supported on carbon and silicon carbide are listed in Table 3.5.

Table 3.5: Coordination numbers and distances of neighbouring atoms and their disorder factors.

Catalyst	Neighbouring atom	N	Distance to neighbour / Å	σ^2	N_3/N_1
20 wt% Pt/C	Pt - Pt_1	10.07 ± 0.32	2.749	0.0059	1.11
	Pt - Pt_2	5.13 ± 1.38	3.888	0.0100	
	Pt - Pt_3	11.15 ± 3.33	4.762	0.0081	
	Pt - Pt_4	8.33 ± 1.29	5.498	0.0105	
20 eq wt% Pt/SiC	Pt - Pt_1	10.86 ± 0.38	2.751	0.0059	1.48
	Pt - Pt_2	4.95 ± 1.43	3.890	0.0087	
	Pt - Pt_3	16.10 ± 4.30	4.764	0.0086	
	Pt - Pt_4	7.92 ± 1.30	5.501	0.0096	

The first and third coordination numbers on 20 eq wt% Pt/SiC are larger than those on 20 wt% Pt/C. The ratio of the third coordination number to the first coordination number for the 20 eq wt% Pt/SiC is larger than that of the 20 wt% Pt/C. The distance to neighbouring atoms, otherwise known as lattice spacing, indicates that the lattice spacings of the 20 eq wt% Pt/SiC catalysts are longer than the lattice spacing seen for the 20 wt% Pt/C catalyst. Lastly, the Debye-Waller disorder factor, σ^2, indicates static disorder in the bond lengths, indicating deviation of the Pt/SiC and Pt/C catalysts from the standard fcc structure.

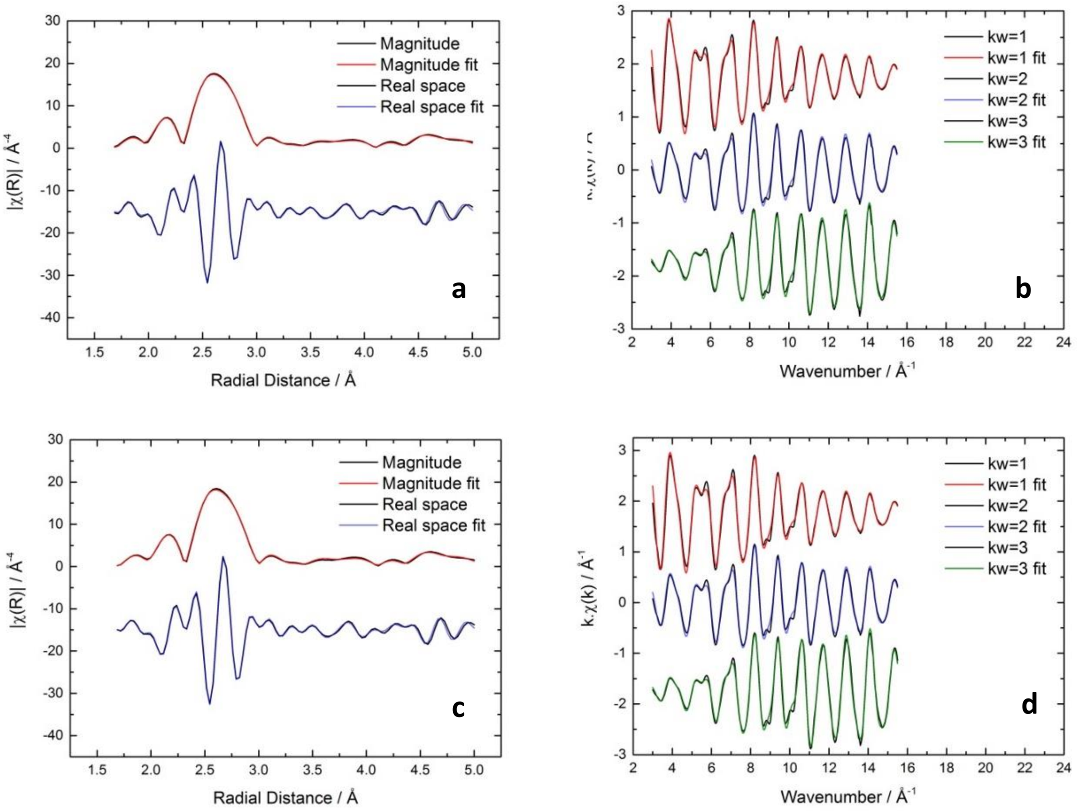

Figure 3.5: Actual and modelled EXAFS data for the 20 wt% Pt/C catalyst is represented in (a) R space with R real space as lχ(R)l – 15 and (b) k space, kw=1 is scaled by 8.2, kw=2 is unscaled and kw=3 is scaled by 0.115. The 20 eq wt% Pt/SiC catalyst is shown in (c) R space and (d) k space, kw=1 is scaled by 8.2, kw=2 is unscaled and kw=3 is scaled by 0.12.

Figure 3.6 is a compilation of the modelled coordination numbers from this study, superimposed onto the modelled coordination numbers for ideally shaped icosahedron, cubocahedron and hcp particles, described by Glasner & Frenkel [37]. The calculated coordination numbers for the Pt/SiC and Pt/C catalysts were superimposed onto the plot, with the error margin in the x-axis defined by theoretical number of atoms calculated from TEM particle sizes and the error in the y-axis is defined by the modelled data in Demeter©.

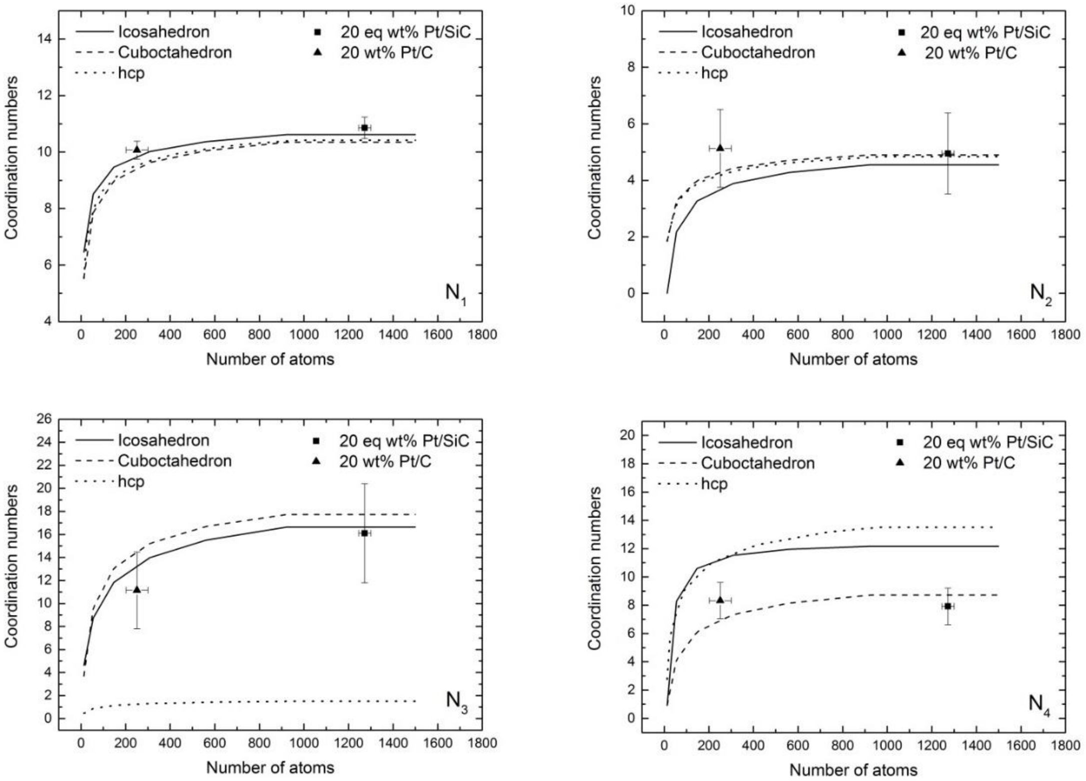

Figure 3.6: Coordination numbers N_1 through N_4 for icosahedron, cuboctahedron and hcp clusters with superimposed calculated coordination numbers from the EXAFS for the 20 eq wt% Pt/SiC and 20 wt% Pt/C. Redrawn from Glasner and Frenkel [37].

3.3.6 Electrochemical Characterisation

The calculated ECSA from CO stripping Voltammetry and ORR activities are shown in Table 3.6. CO stripping voltammetry was used to determine the ECSA via Equation 3.1 and assuming a 420 $\mu C.cm^{-2}_{Pt}$ per CO monolayer adsorbed on the platinum surface, these measurements were taken at room temperature in 0.1 M $HClO_4$ electrolyte solution. The kinetic activities, forming the Tafel plots, were calculated using Equation 3.2 of the cathodic sweep reported at 0.9 V vs RHE with a rotation speed of 1600 rpm. These measurements were completed at 20 $mV.s^{-1}$ at room temperature in an oxygen saturated 0.1 M $HClO_4$ electrolyte solution. It was necessary to add carbon to all the Pt/SiC catalyst inks for electrochemical testing since this material showed little to no electrochemical responses due to the low conductivity of the support material. A 1:1 mass ratio of Pt/SiC and carbon are added to the inks for electrochemical testing. The CO stripping voltammograms and RDE curves are shown in Figure S3.2. Figures 3.7a and 3.8b demonstrates the cyclic voltammograms and Tafel plots of the

Pt/SiC+C catalysts with various loadings, respectively. Figures 3.7c and 3.7d shows the cyclic voltammograms and Tafel plots of the 40 eq wt% Pt/SiC and 40 wt% Pt/C catalysts. A large hydrogen evolution peak, or sharp H_{UPD} peak, is seen at low potentials on the Pt/SiC catalysts.

$$ECSA\ (\frac{cm^2_{Pt}}{g_{Pt}}) = \frac{charge\ (\mu C)}{420\left(\frac{\mu C}{cm^2_{Pt}}\right) \times catalyst\ loading\ (g_{Pt})} \qquad \text{Equation 3.1}$$

$$I_k\ = \frac{I \times I_L}{I_L - I} \qquad \text{Equation 3.2}$$

Table 3.6: Calculated ECSA from CO stripping and ORR activity for the catalysts supported on carbon and SiC at 0.9 V vs. RHE in a 0.1 M $HClO_4$ electrolyte solution at room temperature.

Catalyst	ECSA / $m^2.g^{-1}{}_{Pt}$	$I_{mass\ (0.9V)}$ / $A.g^{-1}{}_{Pt}$	$I_{spec\ (0.9V)}$ / $A.m^{-2}{}_{Pt}$	$I_{k\ (0.9V)}$ / $\mu A.cm^{-2}{}_{Pt}$
10 wt% Pt/C	115 ± 15	146 ± 66	1.2 ± 0.5	150 ± 70
20 wt% Pt/C	82.8 ± 2.5	156 ± 4.5	1.9 ± 0.1	240 ± 10
40 wt% Pt/C	56.0 ± 3.6	120 ± 3.5	2.2 ± 0.1	330 ± 20
10 eq wt% Pt/SiC + C	41.2 ± 1.0	70.5 ± 4.6	1.7 ± 0.1	180 ± 10
20 eq wt% Pt/SiC + C	20.0 ± 0.2	83.2 ± 3.1	4.2 ± 0.2	460 ± 20
40 eq wt% Pt/SiC + C	20.6 ± 0.6	79.4 ± 8.4	3.9 ± 0.3	460 ± 40

The ECSAs of the commercial Pt/C catalysts reported in Table 3.6 are in line with those estimated by the supplier, however, the Pt/SiC+C ECSAs are much lower than expected for the Pt particle size measured using TEM images. The trend in mass specific ORR activity on Pt/C decreased as loading increased while surface area specific ORR activity and kinetic activity increased as loading increased. No trend was seen in the mass specific and surface area specific ORR activities on the Pt/SiC+C catalysts as loading increased, however, an increase in kinetic activity as loading increased is noted. The mass specific ORR activities are significantly lower on the Pt/SiC+C catalysts when compared to Pt/C, however, this trend is reversed for the surface area specific activity and kinetic ORR activities, as seen in Figure 3.7d.

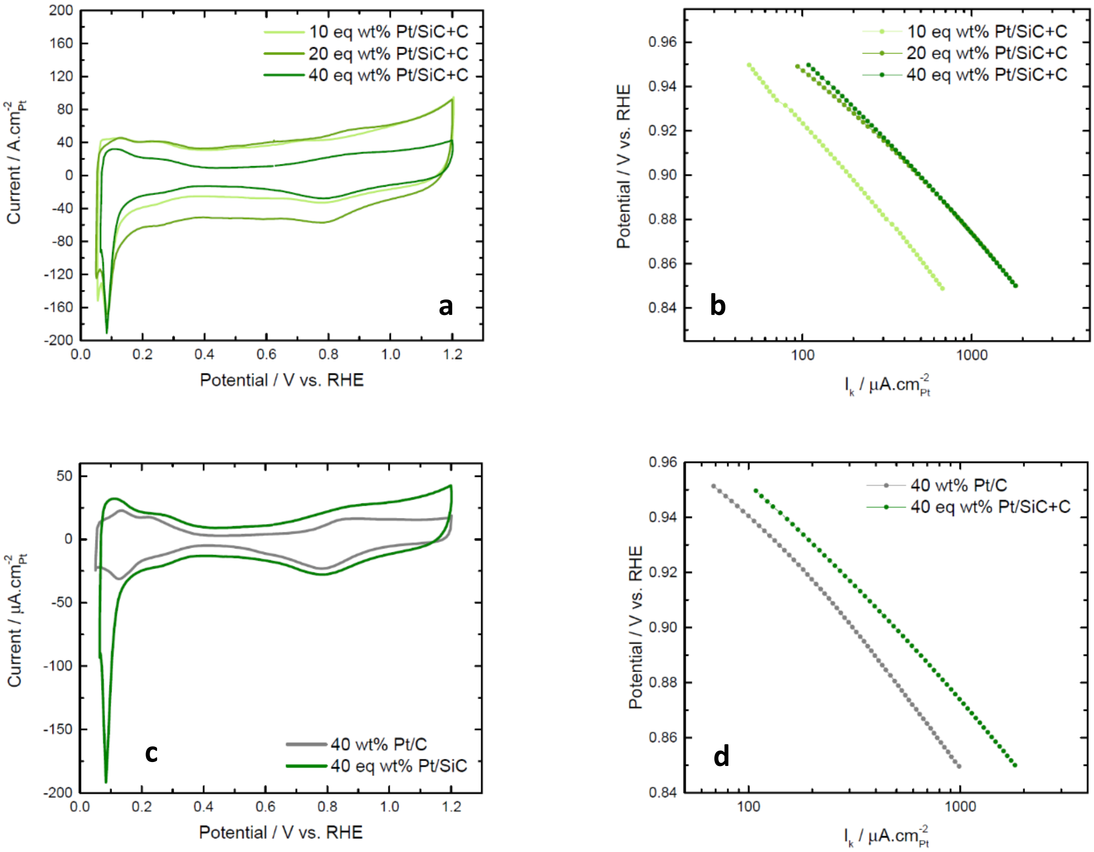

Figure 3.7: Electrochemical characterisation: all experiments performed in 0.1 M $HClO_4$ at room temperature. Cyclic voltammetry (CV) recorded at 20 mV.s^{-1} between 0.05 V and 1.2 V vs RHE. For ORR activity, the cathodic scan was recorded at 1600 rpm between 0.05 V and 1.2 V vs RHE. (a) Cyclic voltammograms for 10, 20 and 40 eq wt% Pt/SiC; (b) Tafel plots for ORR activity for 10,20 and 40 eq wt% Pt/SiC; (c) comparison of cyclic voltammograms of 40 eq wt% Pt/SiC+C and 40 wt% Pt/C and (d) comparison of Tafel plot for ORR activity for 40 eq wt% Pt/SiC+C and 40 wt% Pt/C.

Figure 3.8 reports TEM images of the Pt/SiC+C ink used in the electrochemical characterisations. Figure 3.8a shows significant agglomeration of the Pt/SiC+C ink and Figure 3.8b shows migration of a small number of Pt nanoparticles to the bare carbon surface.

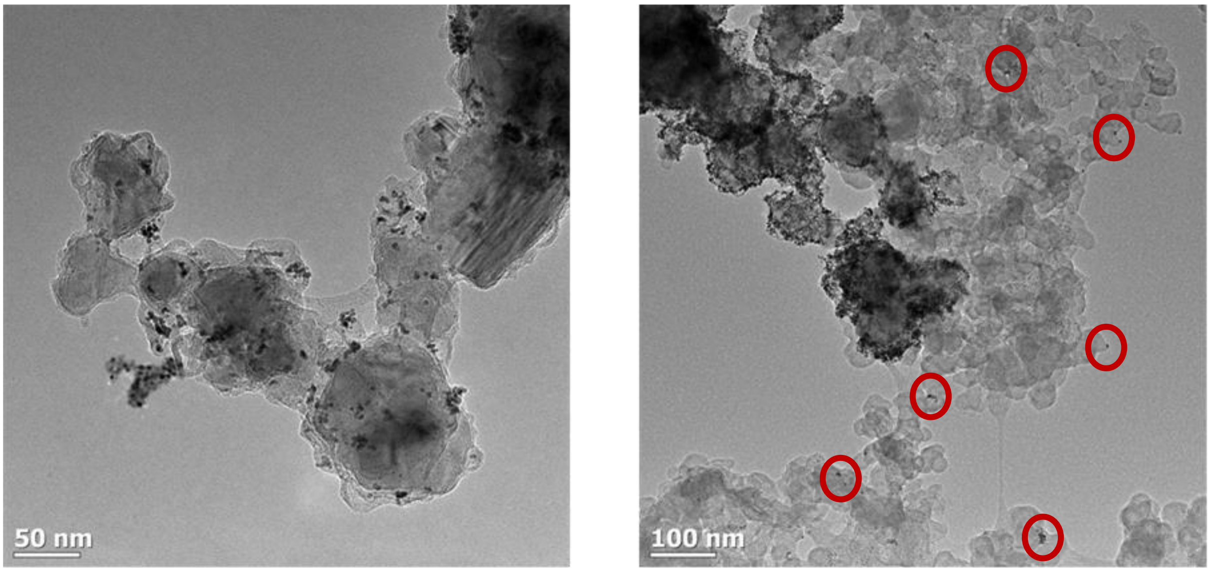

Figure 3.8: TEM images of the 40 eq wt% Pt/SiC+C catalyst ink after sonication, platinum migration to the carbon surface is marked by the red circles.

3.3.7 Electrochemical Durability

The Pt catalyst degradation studies were completed by cycling between 0.6 – 1.0 V vs. RHE in order to determine the Pt stability towards agglomeration and dissolution on the support surface. The durability testing consisted of cycling the potential between 0.6 and 1.0 V vs. RHE for 6000 cycles and returning to the full voltammogram scan limits of 0.05 – 1.2 V vs. RHE to compare changes in the H_{UPD} region and oxygen adsorption and desorption region. The cyclic voltammograms before and after Pt degradation on Pt/C, shown in Figure 3.9a, demonstrates a decrease in H_{UPD} region and the oxygen adsorption and desorption regions. Figure 3.9b shows the cyclic voltammograms of Pt/SiC+C before and after degradation which demonstrates a slight support surface oxidation at these low potentials which results in a less well refined H_{UPD} region and subsequent decrease in ECSA.

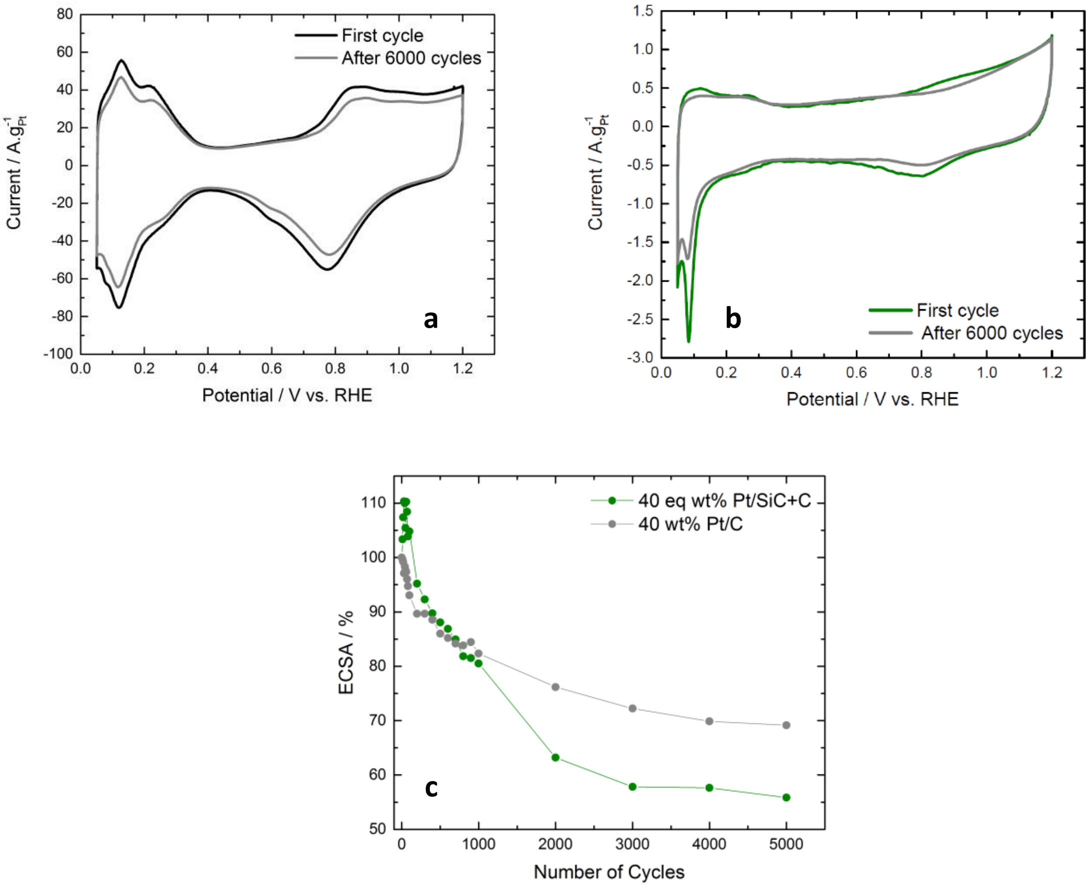

Figure 3.9: Catalyst durability study showing the first and 6000th cycle after degradation cycling between 0.6 – 1.0 V vs. RHE on (a) 40 wt% Pt/C, (b) 40 eq wt% Pt/SiC + C and (c) the change of ECSA over cycling in 0.1 M $HClO_4$ in room temperature at 20 mV.s^{-1}.

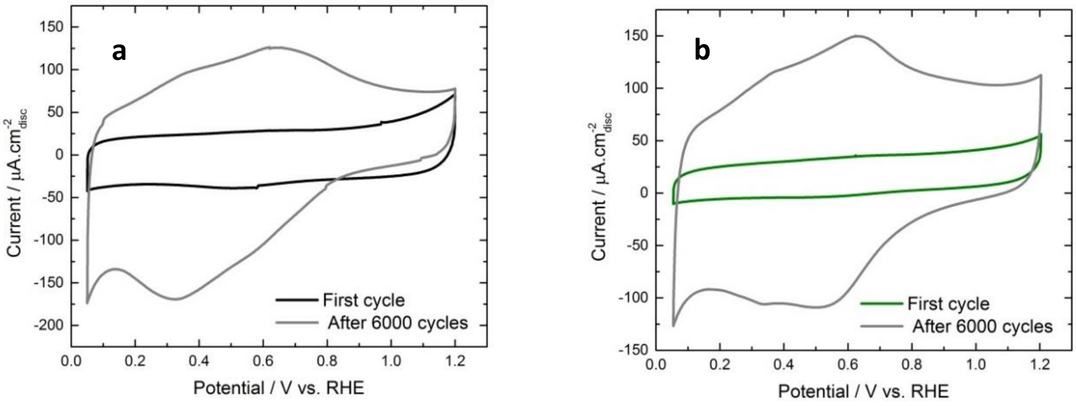

Figure 3.10: Support durability study showing the first and 6000th cycle after degradation cycling between 1.0 – 1.5 V vs. RHE on (a) Vulcan XC-72R and (b) SiC+C in 0.1 M $HClO_4$ in room temperature at 20 mV.s^{-1}.

The second and third durability sequences studied were used to investigate the stability of the support material at high potentials, without the presence of Pt and with the presence of Pt, respectively.

The first and 6000th cyclic voltammograms after durability for the bare supports are displayed in Figure 3.10, and for the catalysed supports, Figure 3.11. Figures 3.10 and 3.11 show a significant increase in capacitance on both the carbon and SiC support materials. Figure 3.11a demonstrates a marked decrease of the H_{UPD} region on the Pt/C catalyst, while the Pt/SiC+C shows little resemblance to the first cyclic voltammogram.

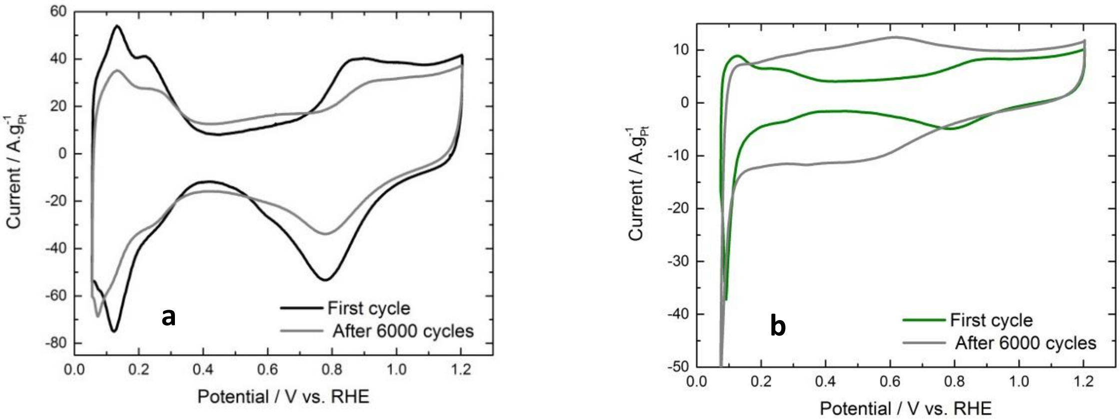

Figure 3.11: Catalyst durability study showing the first and 6000th cycle after degradation cycling between 1.0 – 1.5 V vs. RHE on (a) 40 wt% Pt/C and (b) 40 eq wt% Pt/SiC+C in 0.1 M $HClO_4$ in room temperature at 20 mV.s^{-1}.

3.3.8 *In-Situ* XAS

In-situ X-ray Absorption Near Edge Structure (XANES) was used to investigate the Pt L_3 and L_2 – edge giving insight into the co-ordination numbers, Pt d-band electron vacancies and Pt oxide formation are a function of the potential. The L_3 and L_2 spectra at each potential are shown in Figure S3.3 and the corresponding modelling fits for the L3 edge of Pt/C and Pt/SiC+C are shown in Figures S3.4 and S3.5. The first to fourth coordination numbers for the 20 wt% Pt/C and 20 eq wt% Pt/SiC at different potentials are reported in Table 3.7.

Table 3.7: First to fourth coordination numbers of the 20 wt% Pt/C and 20 eq wt% Pt/SiC catalysts at different potentials.

Catalyst	Potential / V vs. RHE	N (Pt - Pt_1)	N (Pt – Pt_2)	N (Pt – Pt_3)	N (Pt – Pt_4)
20 wt% Pt/C	0.268	11.20 ± 0.6	7.16 ± 2.3	13.81 ± 5.1	8.28 ± 1.7
	0.408	10.95 ± 0.6	6.42 ± 2.2	14.64 ± 5.2	9.00 ± 1.8
	0.778	11.17 ± 0.6	6.55 ± 2.6	15.19 ± 5.7	9.16 ± 1.9
	0.948	10.88 ± 0.6	6.00 ± 2.1	14.83 ± 5.1	8.89 ± 1.8
	1.038	10.34 ± 0.6	5.22 ± 2.1	15.19 ± 5.9	9.38 ± 2.0
20 eq wt% Pt/SiC + C	0.298	10.52 ± 0.48	5.40 ± 1.71	13.62 ± 4.93	9.00 ± 1.73
	0.448	10.67 ± 0.51	5.30 ± 1.75	13.35 ± 4.95	8.43 ± 1.70
	0.728	10.47 ± 0.55	4.83 ± 1.83	13.22 ± 5.46	8.46 ± 1.93
	0.958	10.63 ± 0.50	4.71 ± 1.66	13.89 ± 5.07	8.69 ± 1.75
	1.038	10.09 ± 0.48	4.32 ± 1.53	12.63 ± 4.58	8.75 ± 1.76

The first four coordination numbers from 0.268 – 1.038 V vs. RHE on the Pt/C catalyst and are statistically similar. However, the ratio of N_3/N_1 increases from 1.35 in the double layer region at 0.408 V vs. RHE to 1.49 at 1.038 V vs. RHE, implying a slight change in particle shape at these high potentials. The 20 eq wt% Pt/SiC behaves similarly to the 20 wt% Pt/C catalyst, as the first to fourth coordination numbers for the varying potentials are identical, within the error of modelling. However, the ratio of N_3/N_1 remains at 1.25 in the double layer region at 0.448 V vs. RHE and 1.038 V vs. RHE, confirming a consistent Pt particle shape in this potential range.

Subtle changes to the XANES region due to adsorbate formation and place exchange on the platinum surface are more closely studied by the 'Δμ technique', this method involves subtracting two XANES spectra from each other to investigate changes to the catalyst surface [38]. The subtraction of the two spectra removes the bulk metal-metal interactions and therefore isolates the surface changes due to adsorbates [39]. It is assumed that there are no adsorbates on the Pt surface at potentials in the double layer region, therefore $\mu(0.408)$ and $\mu(0.448)$ were chosen as the reference spectra for the Pt/C and Pt/SiC catalysts, respectively. Figure 3.12a details the $\Delta\mu(0.778)$, $\Delta\mu(0.948)$ and $\Delta\mu(1.038)$ of the Pt/C XANES spectra. The $\Delta\mu$ curves display a peak below the edge energy (E_0) at 11565 eV followed by a positive peak above E_0 at 11570 eV, while the positive peak high increased as potential increased. The $\Delta\mu(0.728)$, $\Delta\mu(0.958)$ and $\Delta\mu(1.038)$ of the Pt/SiC XANES spectra are depicted in Figure 3.12b, similarly to the Pt/C curves in Figure 3.12a, the positive peak is observed with increasing intensity as potential is increased.

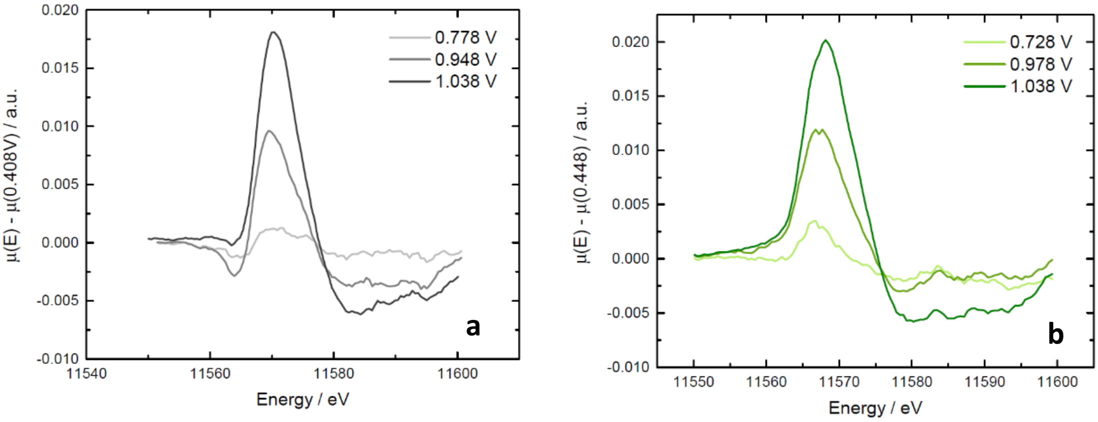

Figure 3.12: the $\Delta\mu$ curves of (a) Pt/C catalyst at different potentials and (b) Pt/SiC+C catalyst at different potentials.

The Pt d-band vacancy was calculated using a method described by Mansour *et al.* [40], and assuming a bulk Pt d-band vacancy of 0.3, as theoretically calculated by Brown *et al.* [41]. The d-band vacancy is measured by using the Pt L_3 and L_2 edges and subtracts the contribution from the *s* states by an arc tangent function which removes the spectral area from the inflection point to the second local minimum [40]. Using this method, the adsorption spectra can be used to calculate the d-band vacancies in the catalysts [40]. The d-band vacancies for the Pt/C and Pt/SiC catalysts at different potentials are reported in Figure 3.13. The d-band vacancies of Pt/C increase considerably after 0.8 V vs. RHE. While the d-band vacancies calculated on Pt/SiC+C catalysts are larger than those of the Pt/C catalyst, they unchanging over those potential range.

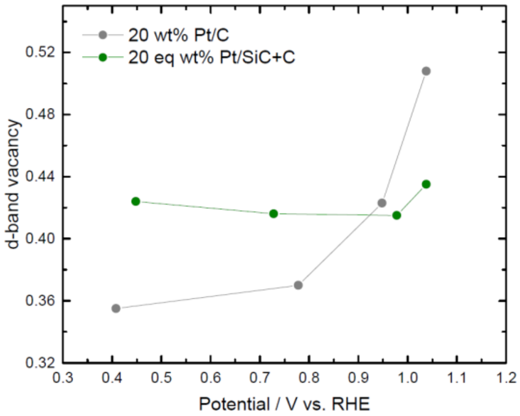

Figure 3.13: d-band vacancies at different potentials on the Pt/C and Pt/SiC+C catalysts.

3.4 Discussion

3.4.1 Pt Nanoparticle and Support Particle Sizes and Shapes

The physisorption results in Table 3.1 report a high specific surface area for the Vulcan support material. Vulcan is well-known to be highly porous which results in the large support surface area. The large surface area, pore sizes and pore volume are essential properties for Pt nanoparticle dispersion and oxygen diffusion to the catalytic surface. The surface area of the SiC is low for numerous reasons, the first being the high density of 3.3 g.cm^{-3}, the slightly larger particle size measured from TEM and the small pore volume. The larger pore sizes seen in the carbide material are, however, an advantage during electrochemical testing, as the oxygen diffusion to the Pt surface is quicker and thus not a limiting factor.

The benchmark 10, 20 and 40 wt% Pt/C catalysts in Figures 3.2a, 3.2b and 3.2c respectively, demonstrate the target Pt nanoparticle dispersion, particle size and particle size range in order for the carbide supported catalysts to be considered competitive alternative support materials to carbon. The Pt particle dispersion (seen in Figure 3.2), is relatively uniform on the Pt/C catalysts. The catalysts show similar Pt inter-particle distances, reported in Table 3.3, throughout the support surface and decreasing inter-particle distances as loading is increased, while maintaining a constant Pt particle size and narrow particle size distribution. The platinum particle sizes of the commercial Pt/C catalysts range from 1.1 – 2.7 nm and the Pt nanoparticles deposited on SiC were well dispersed with average particle sizes ranging from 2.6 – 3.6 nm. Therefore, it can be concluded that platinum was successfully deposited onto a silicon carbide support with particle sizes similar to those on carbon supports. However, the particle size distributions of the Pt/SiC catalysts, seen in Figure 3.2, are wider than those of the commercial Pt/C catalysts. Further evidence of the similarity between the different carbide supported catalysts is that the Pt inter-particle distance, shown in Table 3.3, remains akin to the commercial Pt/C catalysts with the exception of 10 wt% Pt/C and 10 eq wt% Pt/SiC. The 10 wt% Pt/C Pt particle sizes were considerably smaller than the Pt particle sizes on the 10 eq wt% Pt/SiC. However, normalising of the loadings by surface area of the support maintained similar particle sizes and inter-particle distances on the 20 and 40 wt% and eq wt% catalysts. Therefore, observations associated to the support effects on particle size distributions, electrochemical activities for the ORR can be asserted.

Table 3.5 stated the ratio of the third coordination number to the first coordination number for the 20 eq wt% Pt/SiC, which is larger than that of the 20 wt% Pt/C. This ratio is an indication of Pt nanoparticle particle shape [42]. However, the standard deviation of N_3 is large. The first coordination numbers obtained for the supported nanoparticles in this work are simply a representation of particle size. Since the Pt/C catalyst particles are slightly smaller, smaller coordination numbers are expected when compared to Pt/SiC [43]. Additionally, using the method described by Jentys [44], the shape of the platinum nanoparticles deposited on SiC and carbon demonstrated 'distorted cubic' structures. The distribution of bond lengths, shown in Table 3.5 reports similar values for both catalysts for the first to fourth coordination numbers. The combination of coordination numbers and Pt neighbour atomic packing is closely related to the particle shape. It is seen from the superposition of coordination numbers in Figure 3.6 onto ideal particle shapes, that the slight changes to coordination numbers between the Pt/SiC and Pt/C are statistcally similar, since these slight changes are within the error of the calculations. Additionally, the coordination numbers do not represent an ideal geometry. It can be determined that no statistically significant differences in particle shape can be seen between these two supported catalysts. Therefore, similar Pt morphologies/shapes are seen on the different supported catalysts, with larger particle sizes on the SiC supported catalysts.

3.4.2 Charge Transfer Effects

It has been reported in literature that the XPS binding energy of the Pt oxidation states is influenced by a metal-support interaction [45]. Lewera *et al.* [46] demonstrated a shift to lower binding energies in the Pt 4f spectra. In the case of Pt/SiC, significant shifts in Pt 4f peak positions from Pt/C to higher binding energies are seen in Figure 3.4 and Table 3.4. This is accredited to the lower work function of SiC (4.1-4.5 eV) [47] when compared to carbon (4.5 – 4.7 eV [48]), causing a Fermi level equilibration between the support and Pt which results in a charge transfer from the SiC support to the Pt, which is represented by a shift to higher binding energies [49]. Correspondingly, a shift in the Si-C bond in both the Si 2p and C 1s spectra to lower binding energies is observed in Table 3.4, this too suggests a charge transfer from the support material into the Pt nanoparticles.

3.4.3 Electrochemical Characteristics

The Pt/C ECSAs cited in Table 3.6 demonstrate a decrease in ECSA as loading is increased, which is attributed to the increase in particle size and corresponding decrease in the surface area to volume ratio. The Pt/SiC catalysts however, do not have high ECSAs despite the particle size being similar to that of Pt/C. In this case, the TEM images of the 40 eq wt% Pt/SiC+C ink gives insight into the morphology of the Pt nanoparticles in this ink. Figure 3.7 shows agglomerated Pt particles in the ink after sonication and that some Pt nanoparticles have migrated to the carbon added to the catalyst ink. These images demonstrate the instability of Pt on this support and results in the low ECSA measured from CO stripping as the Pt nanoparticles have agglomerated and have therefore lost considerable surface area.

The oxygen reduction activities are also shown in Table 3.5. The Pt/C catalyst activities fall in line with numerous reported values and compilations of values for kinetic ORR activity on these catalysts [50,51]. An exception is seen on the 10 wt% Pt/C catalyst, as the average particle size is 1.1 nm, these have particularly decreased activity for ORR [52], as expected. The mass activities for ORR on the Pt/SiC+C catalysts were lower than that of Pt/C for all loadings, due to the low ECSA. However, the intrinsic activities and kinetic activities were higher across loadings for the Pt/SiC+C catalysts when compared to Pt/C. The results are reiterated in the Tafel plots shown in Figure 3.8d with the 40 eq wt% Pt/SiC+C exhibiting a higher intrinsic activity for ORR at a potential range of 0.85 – 1 V vs. RHE than the 40 wt% Pt/C catalyst. Additionally, Figure 3.8b demonstrates the kinetic activities of the various loadings of platinum on the SiC support. This trend is explained by a particle size effect and agglomeration, as discussed above. The particle size effect on ORR is due to the presence of Pt(100), which is most active surface for ORR. The surface ratio of the crystallographic surfaces of platinum varies in accordance to particle size, as the fraction of the Pt(100) surface decreases rapidly from ~15% surface coverage at 6 nm to 0% surface coverage present below 1.8 nm [53]. Additionally, previously reported surface area specific activities for ORR on different Pt particle sizes [54] show that the surface area specific activities for the 20 eq wt% and 40 eq wt% Pt/SiC+C catalysts are in accordance with the those expected for agglomerates. Therefore, the ORR activity due to an electronic metal-support interaction between the Pt nanoparticles and the SiC support material cannot be measured by RDE techniques.

3.4.4 Accelerated Degradation Studies

The Pt catalyst degradation on Pt/C in Figure 3.9a displays a significant decrease in ECSA after 6000 cycles between 0.6 – 1.0 V vs. RHE. Pt/SiC+C shown in Figure 3.9b, demonstrates slight support surface oxidation at these low potentials which results in a less well refined H_{UPD} region and subsequent decrease in ECSA. The cyclic voltammograms shown before and after 6000 cycles demonstrate less change to the H_{UPD} region when compared to Pt/C but due to the low initial ECSA, small changes to this region result in a larger percentage ECSA lost during cycling. The catalyst support degradation study without Pt described in Figure 3.10, presented significant oxidation seen by an increased capacitance on both the Vulcan and SiC+C support materials. The degradation of carbon at high potentials is described as an increase in interfacial double layer capacitance due to a more hydrophilic surface or an increase in the roughness of the carbon surface [55]. The degradation of SiC was investigated by Lv *et al.* [24] which reported no support degradation when cycled from 0.6 – 1.2 V vs. RHE for 6000 cycles, thus it is likely the degradation seen here is from an increase in the carbon hydrophilicity and/or roughness on the carbon surface.

Insights from the degradation study on the bare supports are important in explaining the trends seen in Figure 3.11, the support degradation study on catalysed supports. Figure 3.11a shows the double layer charging increased after the durability study and the Pt ECSA decreases significantly after 6000 cycles. This phenomenon is explained by the attachment of platinum on the carbon surface being weakened by the oxidation and corrosion of carbon, leading to platinum detachment from the surface. This process will lead to platinum agglomeration as well as platinum dissolution, both resulting in a loss of active surface area and therefore reaction activity. In addition, the process of corrosion is accelerated by the presence of platinum [56]. Finally, Figure 3.11b represents the cyclic voltammograms before and after degradation of the Pt/SiC+C catalyst and little from the H_{UPD} region is visible in the cyclic voltammogram after 6000 cycles. It was asserted above that degradation is attributed to an increase in the carbon hydrophilicity and/or roughness on the carbon surface. Additionally, it appears that degradation of the Pt/SiC+C catalyst mimics that of the Pt/C degradation, and therefore this degradation may be due to the additional carbon in the catalyst ink.

3.4.5 *In-Situ* X-ray Absorption Spectroscopy

Figure 3.8 shows that the ink preparation procedure for the Pt/SiC+C catalyst results in agglomeration of the Pt nanoparticles. This did not seem to affect the *in-situ* XAS analysis since the first co-ordination numbers of the Pt/SiC catalyst in Table 3.7 are similar to the Pt/C. This result is expected since the Pt agglomeration seen in Figure 3.8 does not demonstrate an increase the Pt particle size, but rather clusters of the Pt nanoparticles. The Pt/C Δμ curves in Figure 3.12 demonstrate an initial negative response followed by a positive response. The initial negative response seen on these curves is theoretically ascribed to sub-surface oxygen due to platinum place-exchange [39,57]. Sasaki *et al.* [38] confirmed this relationship between the negative peak in XAS and sub-surface oxygen by X-ray Diffraction (XRD) analysis by oxidising Pt nanoparticle surfaces from metallic Pt to α-PtO_2-type oxide during a potential sweep to 1.5 V. The subsequent positive peak in the Δμ graphs is interpreted as the adsorption of O or OH on surface sites of Pt, this adsorbate coverage increases as the potential increases [38]. The Pt/SiC+C Δμ in Figure 3.12b displays the positive peak attributed to O or OH adsorbate on the Pt surface, with increased coverage as potential increases. Contrarily to Pt/C, Pt/SiC+C does not show signs of subsurface oxygen but a shift of the adsorbate peak to higher energies is evident, this is attributed to n-fold bonded configuration at higher potentials [38].

The d-band vacancies for the Pt/C catalyst over a potential range (Figure 3.13), follows that reported by Mukerjee and co-workers [58, 59]. Additionally, the d-band vacancy of the Pt/C catalyst increased significantly after 0.8 V vs. RHE which is attributed to the -OH bond on the surface of the Pt during ORR [58,59]. The calculated d-band vacancy in the double layer of the Pt/SiC+C catalyst is significantly larger than that of the Pt/C catalyst, this is attributed to larger electron transfer from the SiC support to the Pt nanoparticles. An electron transfer from the support material to Pt results in a more negatively charged particle under UHV conditions, as demonstrated in the XPS spectra in Figure 3.4. This electron transfer is correlated to a shift of potential of zero charge (pzc) to lower potentials resulting in a more positively charged Pt particle in electrochemical environment for the Pt/SiC+C catalyst when compared to Pt/C at the same potentials in the double layer. Additionally, the Pt/SiC+C catalyst demonstrated a higher resilience to adsorption of O or OH on surface sites of Pt as the onset of oxide formation is observed to occur around 1.0 V vs. RHE, 0.2 V after oxide formation is observed to begin on Pt/C.

3.5 Conclusion

Platinum was deposited on a silicon carbide support material, resulting in well dispersed Pt nanoparticles with an average particle size range of 2.6 – 3.6 nm. These loadings were normalised for BET surface area, in order to investigate the fundamental contribution of the support to oxygen reduction reaction activity. The gathered information from XPS shows a shift of the Pt 4f spectra to higher binding energies, while the Si-C bond in both the Si 2p and C 1s spectra shifted to lower binding energies. This correlation suggests an electron transfer from the silicon carbide to Pt metal, under UHV conditions and overall neutrality.

Supporting the XPS interpretations of electron transfer from the SiC support to the Pt nanoparticles, the d-band vacancies calculated from *in-situ* XANES spectra on the Pt $L_{2,3}$ edges report larger electron vacancies in the Pt/SiC catalyst when compared to Pt/C, due to a shift in the pzc of the Pt/SiC catalyst to lower potentials. This strong metal-support interaction also distinctly effects the adsorption of O or OH species on the Pt surface, as this is delayed by 0.2 V on the Pt/SiC catalyst. Correspondingly, the $\Delta\mu$ technique demonstrates a more stable Pt surface during the oxygen reduction reaction since no place-exchange of Pt with oxygen is distinguished, while this phenomenon is detected clearly on the Pt/C catalyst.

The SiC support did not show sufficient conductivity for electrochemical testing, therefore carbon was added to the catalyst ink to improve conductivity of the catalyst. Despite the electronic metal-support interaction, the Pt nanoparticles were unstable on the SiC support material, and Pt agglomerated and some Pt nanoparticles migrated to the carbon surface during sonication in the catalyst ink. Therefore, the low ECSA and mass specific activities were approximately a quarter that of the commercial Pt/C. Consistently, the surface area specific activities and kinetic activities for ORR were considerably higher than the Pt/C counterpart due to this Pt agglomeration.

The catalyst durability on SiC, as well as SiC durability at high potentials was investigated. The low potential durability cycling of Pt/SiC+C catalyst revealed a 15% decrease in durability when compared to Pt/C. This degradation at low potentials was attributed to surface oxidation of the SiC, since oxidation of carbon is not known to occur at these potentials. Moreover, the surface oxidation of carbon was seen in the high potential durability testing which resulted in a featureless H_{UPD} region in the cyclic voltammogram after 6000 cycles.

The strong metal-support interaction was clearly demonstrated on Pt/SiC catalysts in XPS and XAS, however, the ORR activity could not be determined accurately due to agglomeration of the Pt nanoparticles. Furthermore, the Pt/SiC+C catalyst was considerably less durable than Pt/C, rendering the SiC support an unsuitable alternative support material to carbon.

3.6 References

1. Whitesides, G.M. & Crabtree, G.W. 2007. *Science.* 315(5813):796-798.
2. Schmidt, T.J. 2012. *ECS Transactions.* 45(2):3-14.
3. Markovic, N.M., Schmidt, T.J., Stamenkovic, V. & Ross, P.N. 2001. *Fuel Cells.* 1(2):105-116.
4. Rabis, A., Rodriguez, P. & Schmidt, T.J. 2012. *ACS Catalysis.* 2(5):864-890.
5. Wang, C., Markovic, N.M. & Stamenkovic, V.R. 2012. *ACS Catalysis.* 2(5):891-898.
6. Stamenkovic, V., Mun, B.S., Mayrhofer, K.J., Ross, P.N., Markovic, N.M., Rossmeisl, J., Greeley, J. & Nørskov, J.K. 2006. *Angewandte Chemie.* 118(18):2963-2967.
7. Reiser, C.A., Bregoli, L., Patterson, T.W., Yi, J.S., Yang, J.D., Perry, M.L. & Jarvi, T.D. 2005. *Electrochemical and Solid-State Letters.* 8(6):A273-A276.
8. Huang, S., Ganesan, P. & Popov, B.N. 2011. *Applied Catalysis B: Environmental.* 102(1–2):71-77.
9. Nørskov, J.K., Rossmeisl, J., Logadottir, A., Lindqvist, L., Kitchin, J.R., Bligaard, T. & Jónsson, H. 2004. *The Journal of Physical Chemistry B*. 108(46): 17886-17892.
10. Shim, J., Lee, C., Lee, H., Lee, J. & Cairns, E.J. 2001. *Journal of Power Sources.* 102(1–2):172-177.

11. Timperman, L., Lewera, A., Vogel, W. & Alonso-Vante, N. 2010. *Electrochemistry Communications.* 12(12):1772-1775.
12. Vogel, W., Timperman, L. & Alonso-Vante, N. 2010. *Applied Catalysis A: General.* 377(1–2):167-173.
13. Xiong, L. & Manthiram, A. 2004. *Electrochimica Acta.* 49(24):4163-4170.
14. Kakinuma, K., Uchida, M., Kamino, T., Uchida, H. & Watanabe, M. 2011. *Electrochimica Acta.* 56(7):2881-2887.
15. Takasaki, F., Matsuie, S., Takabatake, Y., Noda, Z., Hayashi, A., Shiratori, Y., Ito, K. & Sasaki, K. 2011. *Journal of the Electrochemical Society.* 158(10):B1270-B1275.
16. Tauster, S.J. 1987. *Accounts of Chemical Research.* 20(11):389-394.
17. Dulub, O., Hebenstreit, W. & Diebold, U. 2000. *Physical Review Letters.* 84(16):3646-3649.
18. Horsley, J.A. 1979. *Journal of the American Chemical Society.* 101(11):2870-2874.
19. Rabis, A., Kramer, D., Fabbri, E., Worsdale, M., Kötz , R. & Schmidt, T.J. 2014. *The Journal of Physical Chemistry C.* 118(21):11292-11302.
20. Antolini, E. & Gonzalez, E.R. 2009. *Solid State Ionics.* 180(9–10):746-763.
21. Krasotkina, N.I., Yakovleva, V.S., Voronin, N.I. & Shmitt-Fogelevich, S. 1968. *Refractories.* 9(11-12):723-726.
22. Samsonov, G.V. 1962. *Boron, its compounds and alloys.* US Atomic Energy Commission, Division of Technical Information.
23. Honji, A., Mori, T., Hishinuma, Y. & Kurita, K. 1988. 135(4):917-918.
24. Lv, H., Mu, S., Cheng, N. & Pan, M. 2010. *Applied Catalysis B: Environmental.* 100(1–2):190-196.
25. Niu, J.J. & Wang, J.N. 2009. *Acta Materialia.* 57(10):3084-3090.
26. Ravel, B. & Newville, M. 2005. *Journal of Synchrotron Radiation*. 12:537–541
27. Wise, A.M. 2012. Characterisation of bimetallic alloy and core-shell electrocatalysts. Ph.D. Thesis. University of Southampton.
28. Mayrhofer, K.J.J., Blizanac, B.B., Arenz, M., Stamenkovic, V.R., Ross, P.N. & Markovic, N.M. 2005. *The Journal of Physical Chemistry B.* 109(30):14433-14440.
29. Nesselberger, M., Roefzaad, M., Fayçal Hamou, R., Ulrich Biedermann, P., Schweinberger, F.F., Kunz, S., Schloegl, K., Wiberg, G.K.H., Ashton, S., Heiz, U. Mayrhofer, K.J.J. & Arenz, M. 2013. *Nature Materials.* 12(10):919-924.

30. Cheung, R. 2006. *Silicon Carbide Microelectromechanical Systems for Harsh Environments.*
31. Lomello, F., Bonnefont, G., Leconte, Y., Herlin-Boime, N. & Fantozzi, G. 2012. *Journal of the European Ceramic Society*. 32(3):633-641.
32. Dubey, M., Ram, U.S. & Singh, G. 1973. *Acta Crystallographica Section B.* 29(7):1548-1550.
33. O'Connell, K. & Regalbuto, J.R. 2015. *Catalysis Letters*. 145(3): 777-783
34. Thermo Fischer Scientific Inc. 2016. *Carbon*. Available: http://xpssimplified.com/elements/carbon.php [26/07/2017].
35. Frenkel, A.I., Hills, C.W. & Nuzzo, R.G. 2001. *The Journal of Physical Chemistry B*. 105(51):12689-12703.
36. Russell, A.E. & Rose, A. 2004. *Chemical Reviews.*104(10):4613-4636
37. Glasner, D. & Frenkel, A.I.2006. *AIP Conference Proceedings.* 9-14 July. B. Hedman & P. Pianetta, Eds. 746.
38. Sasaki, K., Marinkovic, N., Isaacs, H.S. & Adzic, R.R. 2016. *ACS Catalysis.* 6(1):69-76.
39. Teliska, M., O'Grady, W.E. & Ramaker, D.E. 2005. *The Journal of Physical Chemistry B.* 109(16):8076-8084.
40. Mansour, A.N., Cook, J.W. & Sayers, D.E. 1984. *The Journal of Physical Chemistry.* 88(11):2330-2334.
41. Brown, M., Peierls, R.E. & Stern, E.A. 1977. *Physical Review B.* 15(2):738-744.
42. Newville, M. 2004. Fundamentals of XAFS: Consortium for Advanced Radiation Sources. University of Chicago.
43. Frenkel, A., 1999. *Journal of Synchrotron Radiation*. 6(3):293-295.
44. Jentys, A. 1999. *Physical Chemistry Chemical Physics.* 1(17):4059-4063.
45. Hall, S.C., Subramanian, V., Teeter, G. & Rambabu, B. 2004. *Solid State Ionics.* 175(1–4):809-813.
46. Lewera, A., Timperman, L., Roguska, A. & Alonso-Vante, N. 2011. *The Journal of Physical Chemistry C.* 115(41):20153-20159.
47. Harris, G.L. & INSPEC 1995. *Properties of Silicon Carbide.* INSPEC, Institution of Electrical Engineers.
48. Liu, P., Wei, Y., Jiang, K., Sun, Q., Zhang, X., Fan, S., Zhang, S., Ning, C. & Deng, J. 2006. *Physical Review B.* 73(23):235412.

49. Watanabe, M., Tryk, D.A., Wakisaka, M., Yano, H. & Uchida, H. 2012. *Electrochimica Acta*. 84:187-201.
50. Garsany, Y., Singer, I.L. & Swider-Lyons, K.E. 2011. *Journal of Electroanalytical Chemistry*. 662(2): 396-406
51. Garsany, Y., Baturina, O.A., Swider-Lyons, K. & Kocha, S.S. 2010. *Analytical Chemistry*. 82(15):6321-6328.
52. Kinoshita, K. 1990. *Journal of the Electrochemical Society*. 137(3):845-848.
53. Fabbri, E., Taylor, S., Rabis, A., Levecque, P., Conrad, O., Kötz, R. & Schmidt, T.J. 2014. *ChemCatChem*. 6(5): 1410–1418.
54. Nesselberger, M., Ashton, S., Meier, J.C., Katsounaros, I., Mayrhofer, K.J.J. & Arenz, M. 2011. *Journal of the American Chemical Society.* 133(43):17428-17433.
55. Speder, J., Zana, A., Spanos, I., Kirkensgaard, J.J.K., Mortensen, K. & Arenz, M. 2013. *Electrochemistry Communications*. 34:153-156.
56. Zhang, H., Wang, X., Zhang, J.L. & Zhang, J.W. 2008. *Electrocatalysts and Catalyst Layers Fundamentals and Applications*. London: Springer.
57. Arruda, T.M., Shyam, B., Ziegelbauer, J.M., Mukerjee, S. & Ramaker, D.E. 2008. *The Journal of Physical Chemistry C.* 112(46):18087-18097.
58. Mukerjee, S., Srinivasan, S., Soriaga, M.P. & McBreen, J. 1995. *Journal of the Electrochemical Society.* 142(5):1409-1422.
59. Mukerjee, S., Srinivasan, S., Soriaga, M.P. & McBreen, J. 1995. *The Journal of Physical Chemistry.* 99(13):4577-4589.

3.7 Supplementary

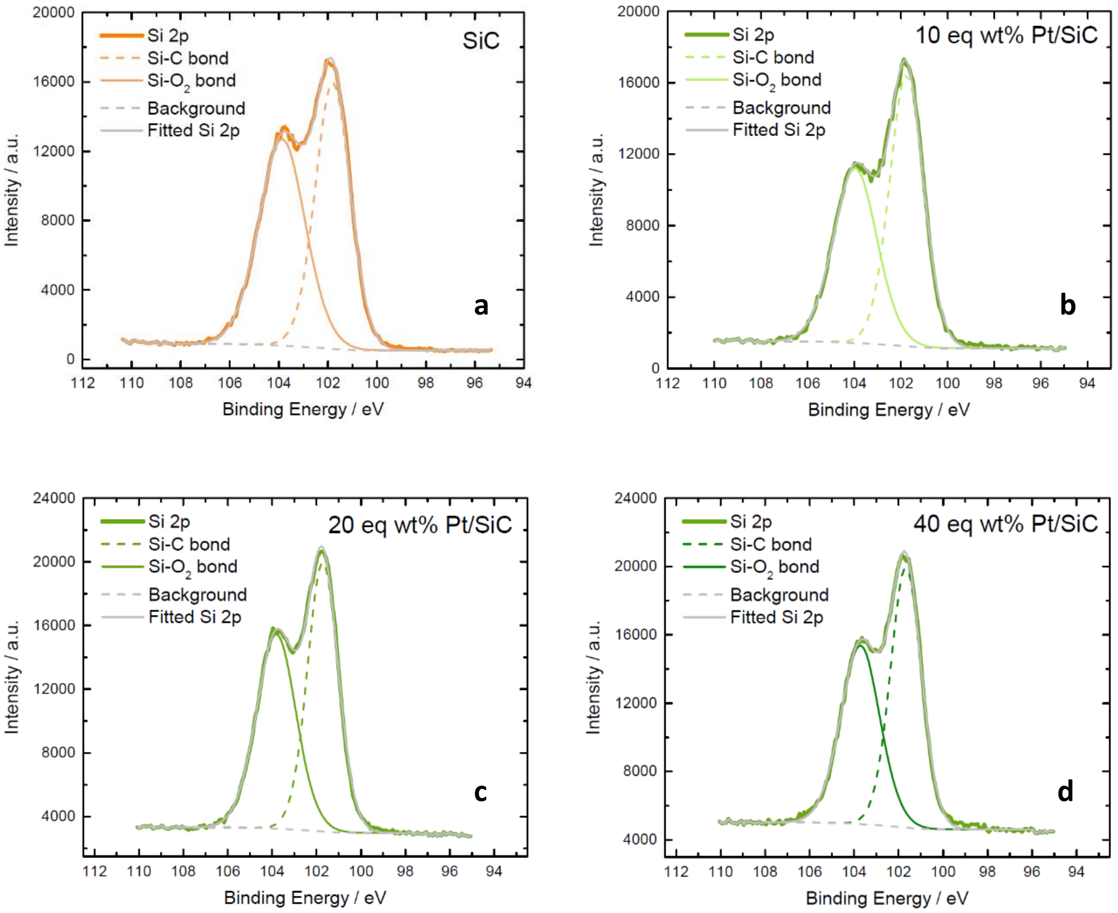

Figure S3.1: XPS Si 2p spectra and modelled (a) SiC, (b) 10 eq wt% Pt/SiC, (c) 20 eq wt% Pt/SiC and (d) 40 eq wt% Pt/SiC.

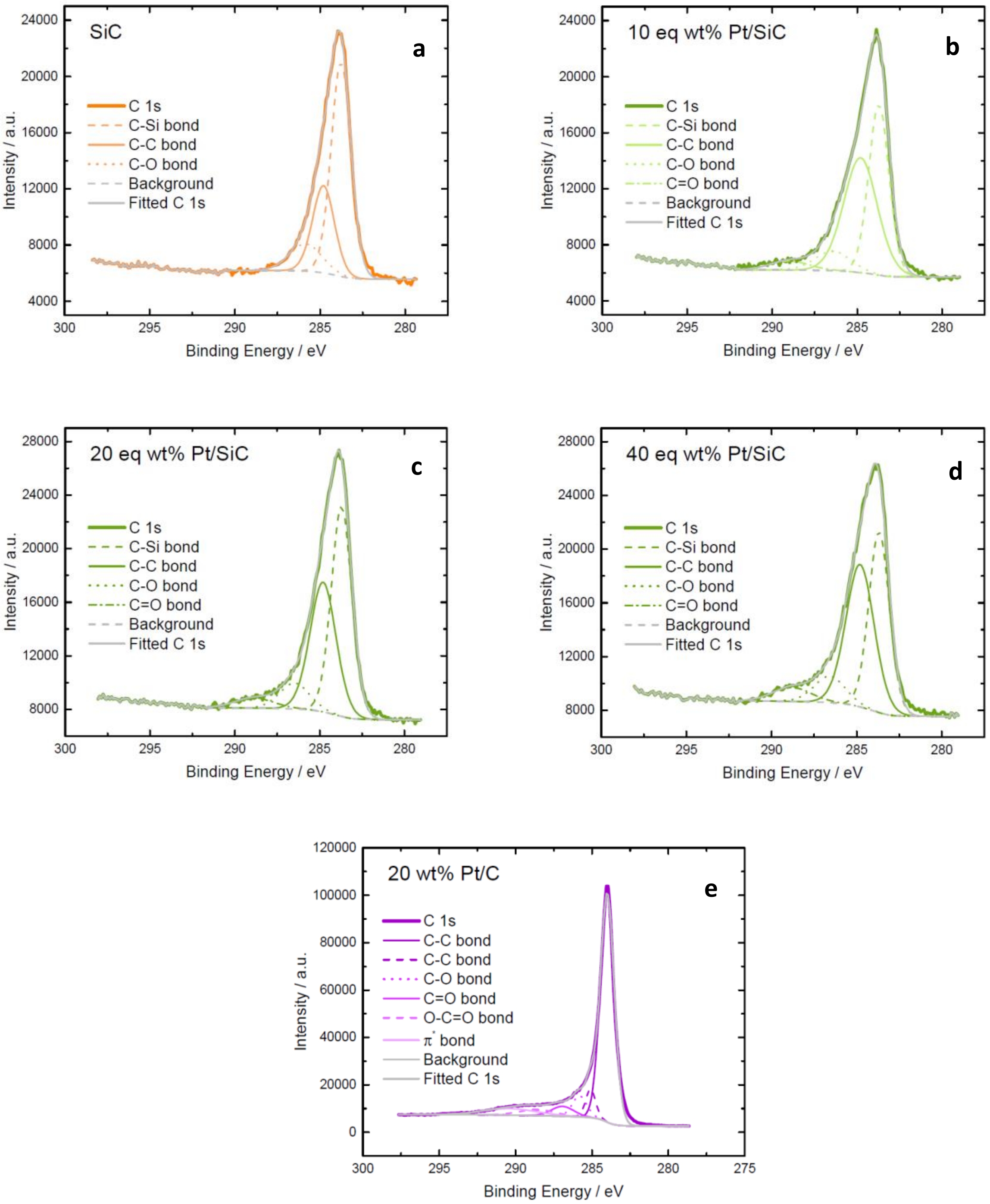

Figure S3.2: XPS C 1s spectra and modelled (a) SiC, (b) 10 eq wt% Pt/SiC, (c) 20 eq wt% Pt/SiC, (d) 40 eq wt% Pt/SiC and (e) Pt/C.

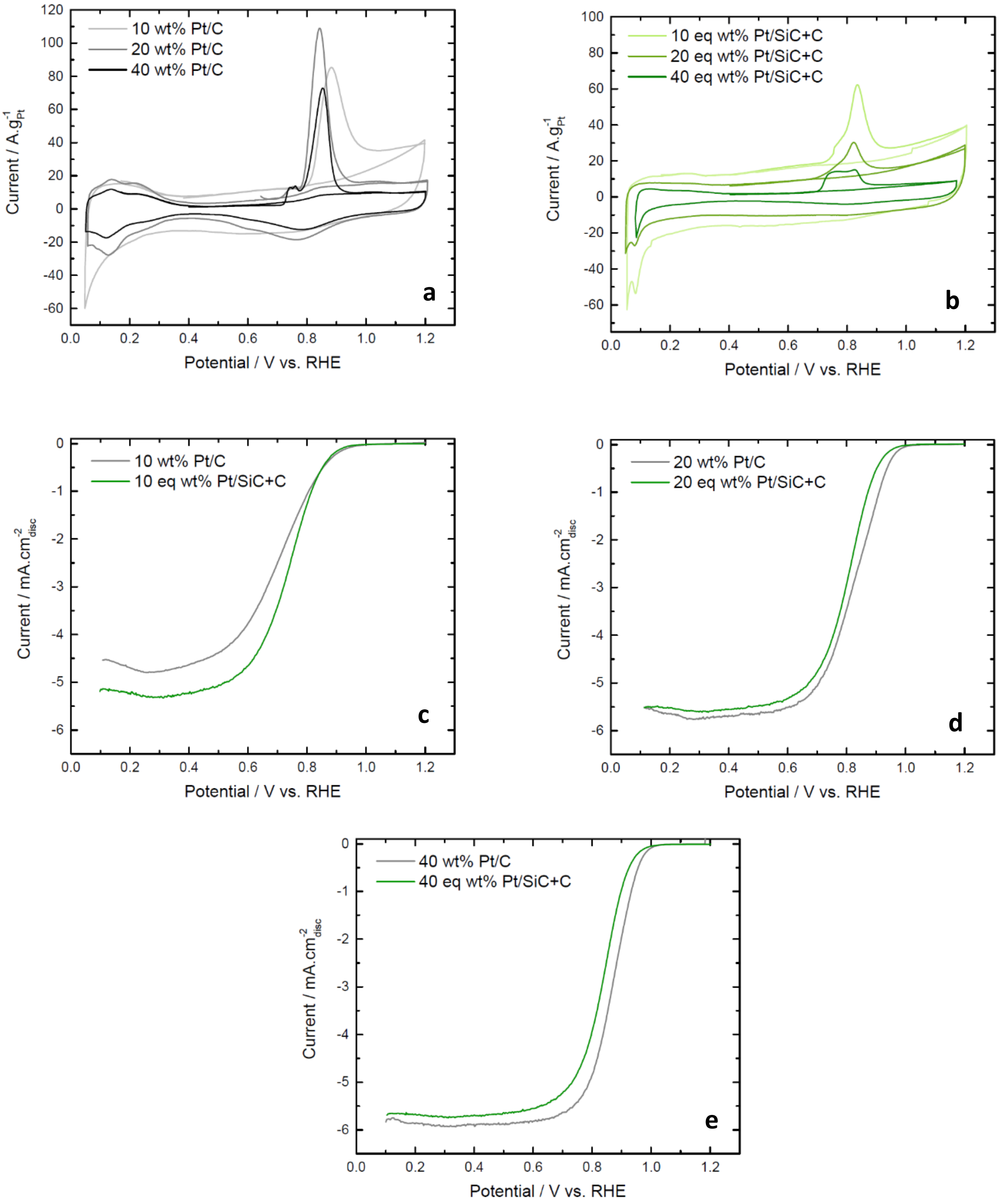

Figure S3.3: The CO stripping voltammograms of (a) Pt/C catalysts and (b) Pt/SiC+C catalysts at room temperature in 0.1 M $HClO_4$ electrolyte solution and a scan rate of 20 mV.s^{-1}. The RDE curves for the ORR of (c) 10 wt% Pt/C and 10 eq wt% Pt/SiC+C, (d) 20 wt% Pt/C and 20 eq wt% Pt/SiC+C and (e) 40 wt% Pt/C and 40 eq wt% Pt/SiC+C.

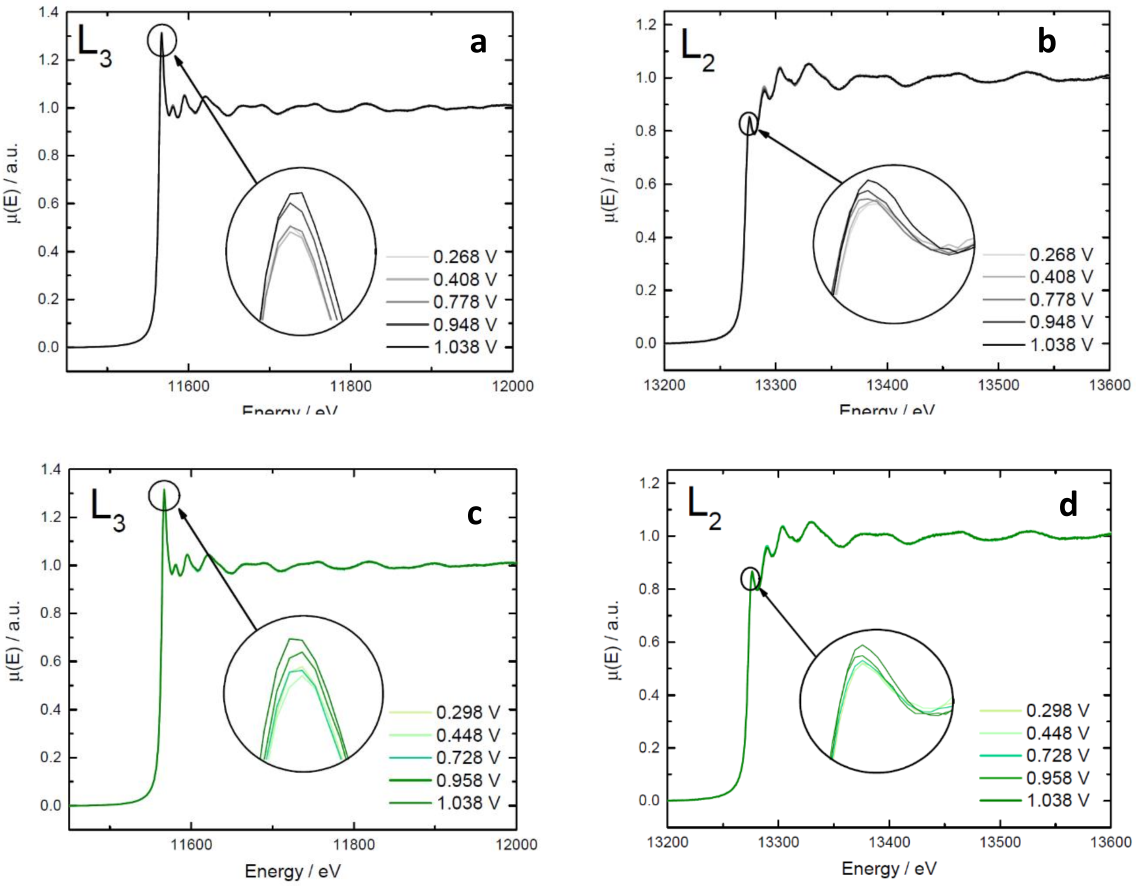

Figure S3.4: The X-ray adsorption spectra for the (a) Pt L_3 edge and (b) Pt L_2 edge of the 20 wt% Pt/C catalyst and (c) Pt L_3 edge and (d) Pt L_2 edge of the 20 eq wt% Pt/SiC+C catalyst with insets of the white line.

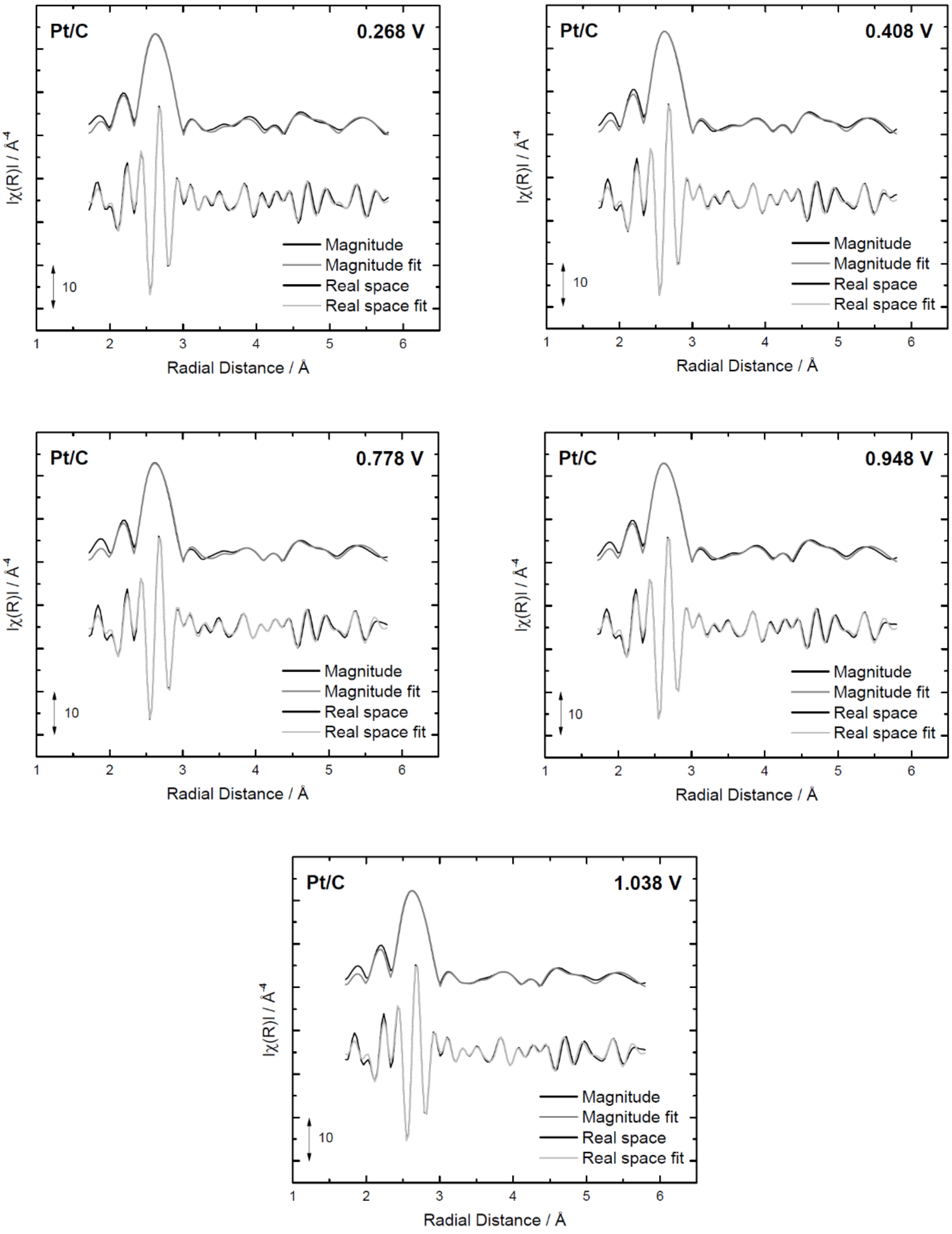

Figure S3.5: EXAFS R space magnitude and real space plots and k space plots of the Pt/C catalyst at different potentials in a 0.1 M $HClO_4$ electrolyte at room temperature.

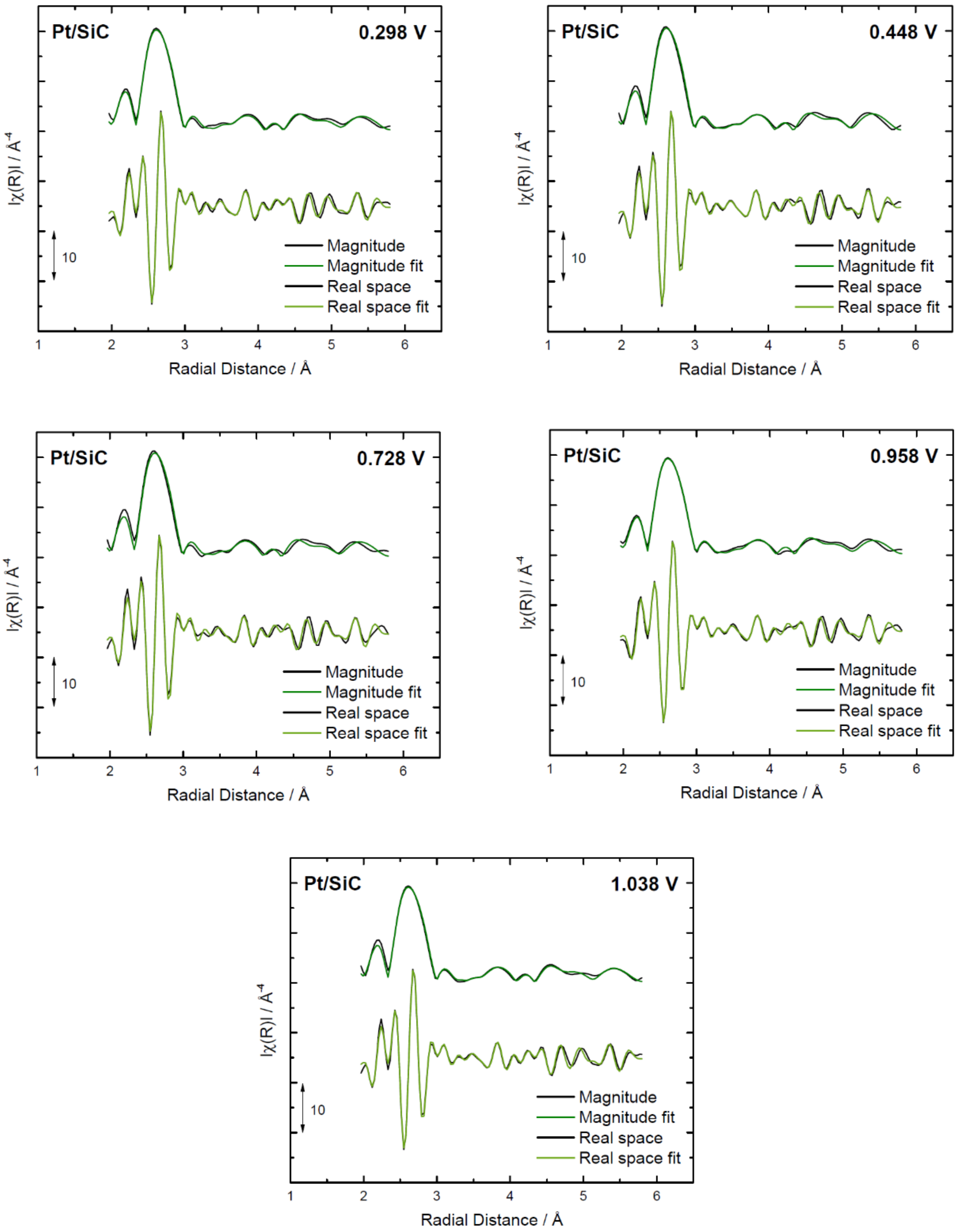

Figure S3.6: EXAFS R space magnitude and real space plots and k space plots of the Pt/SiC catalyst at different potentials in a 0.1 M $HClO_4$ electrolyte at room temperature.

Chapter 4

4.1 Physical Characterisation and Electrochemical Stability of Boron Carbide as an Alternative Platinum Catalyst Support Material for the Oxygen Reduction Reaction

---

Abstract

In this preliminary study, boron carbide was investigated as an alternative support material to carbon for the oxygen reduction reaction, with a focus on physical characterisation and electrochemical stability of both the Pt nanoparticles and the boron carbide support. Physical characterisation was carried out on the support materials using TEM, XRD, BET and resistivity measurements. The boron carbide material investigated was a boron carbide and graphite composite (BC), wherein the graphite component of the support assisted in the electrochemical conductivity of the material. This material was surface treated to improve the Pt nanoparticle dispersion on the surface. The platinum loading was normalised using the BET surface areas of the treated boron carbide composite material (80 $m^2.g^{-1}$) and Vulcan (230 $m^2.g^{-1}$) to develop equivalent Pt loadings of 10, 20 and 40 eq wt% Pt/BC-HNO_3. The platinum deposited on the treated boron carbide composite support exhibited considerable stability with regards to Pt agglomeration during durability testing at high potentials, when compared to carbon. However, an insulating surface layer resulted in a non-conductive surface, and therefore deactivated catalyst, when cycled between 1.0 - 1.5 V vs. RHE.

4.1.1 Introduction

Platinum group metals and platinum based alloys deposited on high surface area carbon remain the standard ORR catalysts due to their high activity [1]. However, the loss of active surface area due to carbon corrosion and subsequent platinum agglomeration at high cathodic potentials is an important research topic [2]. A straightforward approach to this concern is to investigate alternative catalyst support materials which provide a high stability and stronger metal-support interactions to stabilise the Pt nanoparticles in acidic environments and at cathodic potentials.

Boron carbide (B_4C) is a refractory compound which exhibits high chemical inertness and metallic properties [3]. Additionally, B_4C is shown to be electrochemically inert when exposed to potentials of up to 2 V in acid [4]. Moreover, B_4C has previously been synthesized with volumetric surface areas of 194 $m^2.m^{-3}$ [5], higher than carbon with a volumetric surface area of 6.60 $m^2.m^{-3}$. Nanostructured B_4C have too shown promising electrochemical performance similar to that of Pt/C [6].

In this chapter, boron carbide was purchased from a commercial supplier (NaBond Technologies Co., Ltd.) and platinum was deposited using an in-house organo-metallic chemical deposition method. These catalysts were physically and electrochemically characterised via Brunauer, Emmett and Teller (BET) theory, Barrett-Joyner-Halenda (BJH) Analysis, Transmission Electron Microscopy (TEM), Energy-dispersive X-ray spectroscopy (EDX) coupled to a Scanning Electron Microscope (SEM), X-ray photoelectron spectroscopy (XPS), X-ray diffraction (XRD), resistivity measurements, inductively coupled plasma optical emission spectrometry (ICP-OES), cyclic voltammetry (CV), CO stripping voltammetry and rotating disc experiments (RDE).

4.1.2 Experimental

Support Treatments: The as-received boron carbide (NaBond Technologies Co., Ltd.) was treated using two methods. The B_4C was stirred in conc. nitric acid (Kimix Chemicals and Lab Supplies cc.) at room temperature for 8 hrs to produce the BC-HNO_3 support. The BC-H_2 was prepared by treatment of the B_4C at 500 °C for 1 hour in a 5% H_2/Ar gas mixture.

Physical Characterisations: The prepared support material was characterised via physisorption using Brunauer, Emmett and Teller (BET) theory (Micromeritics Instrument Corporation TriStar II) to determine the support surface area. X-ray diffraction (XRD) measurements were carried out on a Bruker D8 Advance diffractometer with a Cu Kα radiation source operating at 40 kV to determine the crystalline phases present in the catalyst and Rietveld Refinement on the XRD patterns was completed using Bruker AXS TOPAS software, Version 4.1. Transmission electron microscopy (TEM) was performed on a Tecnai G2 electron microscope operating at 200 kV to determine particle sizes, the supported catalyst was characterised using TEM for Pt particle size using an average of at least 100 particle diameters. X-ray photoelectron spectroscopy (XPS) was carried out by Nexus XPS service using a Thermo Scientific K-Alpha instrument with an Al Kα X-ray source. XPS to investigate the binding energy and quantify Pt and its oxides, ICP-OES (Varian 730-ES) to confirm the Pt loading on the support.

Electrochemical characterisation: A catalyst ink was prepared for the electrochemical characterisation techniques, The Pt/BC catalyst ink consisted of 2.5 mg of the catalyst, 0.5 ml of ethanol (Sigma Aldrich) and 25 µL of 5 wt% Nafion solution. The mixture was sonicated for 30 minutes and 5 µL was placed on a glassy carbon electrode. The Pt/C catalyst ink consisted of 5 mg of the catalyst, 5 ml of water (Milli-Q 18.2 MΩ.cm), 1.5 ml isopropanol (Kimix) and 25 µL of 5 wt% Nafion solution. The mixture was sonicated for 30 minutes and 10 µL was placed on a glassy carbon electrode. Prior to this the glassy carbon electrode was polished to a mirror finish using 0.1 and 0.05 µm Al_2O_3 polish (Buehler). Cyclic voltammetry was conducted by cycling the potential between 0.05 – 1.2 V vs. RHE with a scan rate of 100 $mV.s^{-1}$ for 50 cycles at room temperature in an oxygen-free 0.1 M $HClO_4$ electrolyte solution to electrochemically clean the catalyst surface. The reference electrode used was $Hg/HgSO_4$ with a platinum counter electrode. The scan rate was then changed to 20 $mV.s^{-1}$ for 2 cycles and the potential cycled between 0.05 – 1.2 V vs RHE at room temperature in an oxygen-free 0.1 M $HClO_4$ electrolyte solution. The ORR activity was measured by rotating disc electrode experiments in an O_2 saturated 0.1 M $HClO_4$ electrolyte (70% Suprapur - Merck) using the anodic scan between 0.05 and 1.2 V vs. RHE, with a scan rate of 20 $mV.s^{-1}$ and rotation rate of 1600 rpm at room temperature. All scans were normalised for electrochemically active surface area, ohmic drop measured by impedance spectroscopy, and capacitive current in an oxygen free electrolyte. The Pt catalyst degradation studies were completed by cycling between 0.6 – 1.0 V vs. RHE and the catalyst support degradation studies were completed by cycling between 1.0 – 1.5 V vs. RHE. Both degradation studies were performed with a scan rate of 50 $mV.s^{-1}$ in 0.1 M $HClO_4$ electrolyte solution for 6000 cycles at room temperature, and periodically reverted back to a cyclic voltammogram between 0.05 – 1.2 V vs. RHE with a scan rate of 20 $mV.s^{-1}$ to investigate the changes to the H_{UPD} region. The reference electrode used was $Hg/HgSO_4$ with a gold counter electrode. The H_{UPD} region was used for changes in ECSA in this instance.

4.1.3 Results

4.1.3.1 BET-BJH Analysis

The support surface area, average pore size and pore volume were evaluated using Brunauer, Emmett and Teller (BET) theory and Barrett-Joyner-Halenda (BJH) Analysis, respectively, and these are reported in Table 4.1.1. The surface area of Vulcan is approximately 4 times larger than that of untreated BC. The largest BC surface area, pore size and pore volume was recorded on the nitric acid treated support material.

Table 4.1.1: BET surface areas, average pore sizes and pore volumes for the Vulcan, treated and untreated BC.

Support	Surface Area / $m^2.g^{-1}$	Average Pore Size / nm	Pore volume / $cm^3.g^{-1}$
Vulcan	230	8.7	0.499
BC	56.7	15.2	0.216
BC - HNO_3	80.5	17.8	0.359
BC - H_2	57.5	13.5	0.194

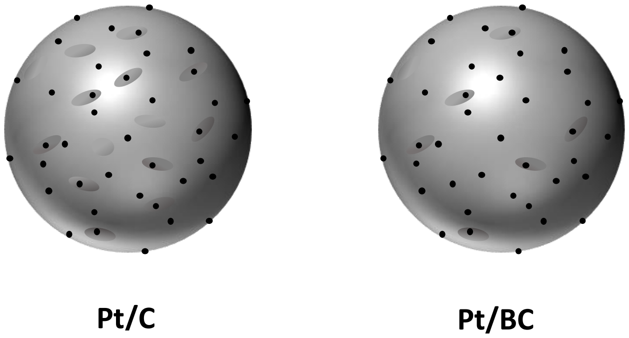

Figure 4.1.1: Schematic of equivalent Pt loadings on different support surfaces, the grey sphere represents the support material, the small oblong shapes represent the pores of the support and the small black spheres represent the Pt nanoparticles.

The BET surface area was used to normalise the loading of Pt on the surface of the support and therefore Pt/C catalysts can be compared to Pt/BC catalysts in order to make fundamental observations of catalyst performance. This normalisation technique was needed to maintain a constant Pt coverage per surface area of support, inter-particle distances and particle size so that any changes seen in activity can be attributed to a support affect, as shown in Figure 4.1.1. It is imperative to keep particle size and inter-particle distances constant across support surfaces since these, in their own right, affect ORR activities significantly [7,8]. Therefore, the Pt loading on the carbide supports will be referred to the equivalent weight percent (eq wt%), while Pt loading on carbon will refer to the true weight percent (wt%) and these catalysts can be directly compared in terms of electrochemical activity.

4.1.3.2 Transmission Electron Microscopy (TEM)

The particle sizes of the stand-alone Vulcan and BC supports were measured using TEM imaging, these are reported in Table 4.1.2. The TEM images of the commercial untreated and treated BC are shown in Figures 4.1.2a – 4.1.2c, these images display spherical, high surface area particles, with little crystallinity visually present, which is similar to what is commonly seen for carbon supports. The particle sizes of the carbides, reported in Table 4.1.2, are in the range acceptable for catalyst support materials. The small particle sizes of the nitric acid treated BC, in conjunction with the large pore volume, benefitted the BET surface area available for Pt deposition.

The TEM images for the commercial Pt/C benchmark catalysts with varied loadings are shown in Figure 4.1.3. The benchmark 10, 20 and 40 wt% Pt/C catalysts in Figures 4.1.3a, 4.1.3b and 4.1.3c, respectively, demonstrate the target Pt nanoparticle dispersion, particle size and particle size range in order for the carbide supported catalysts to be considered a competitive alternative support material to carbon. The Pt particle dispersion is relatively uniform with similar Pt inter-particle distances throughout the support surface, with decreasing inter-particle distances as loading is increased, while maintaining a narrow particle size distribution.

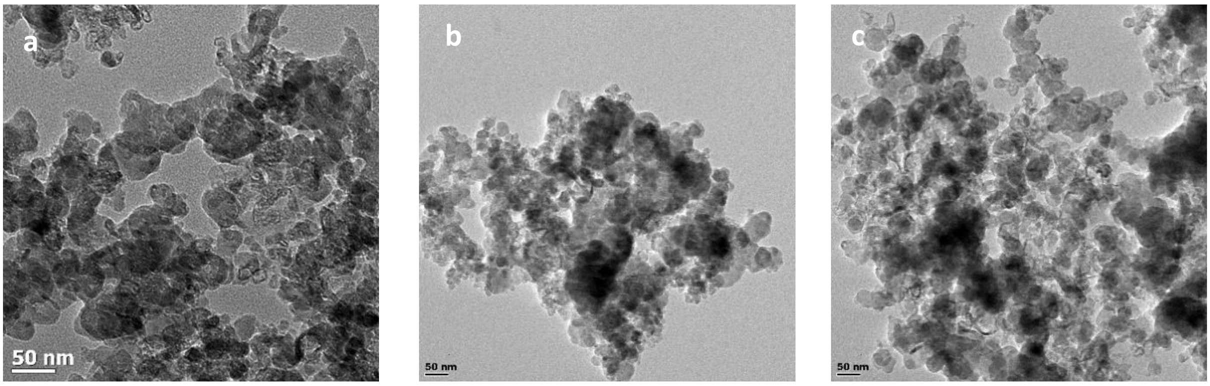

Figure 4.1.2: TEM images of (a) untreated commercial BC, (b) nitric acid treated BC and (c) hydrogen treated BC.

Table 4.1.2: Average particle sizes of Vulcan and carbides measured from TEM images.

Support	Average particle size / nm
Vulcan	47.1 ± 12
BC	33.0 ± 14
BC – HNO_3	34.0 ± 17
BC – H_2	38.1 ± 15

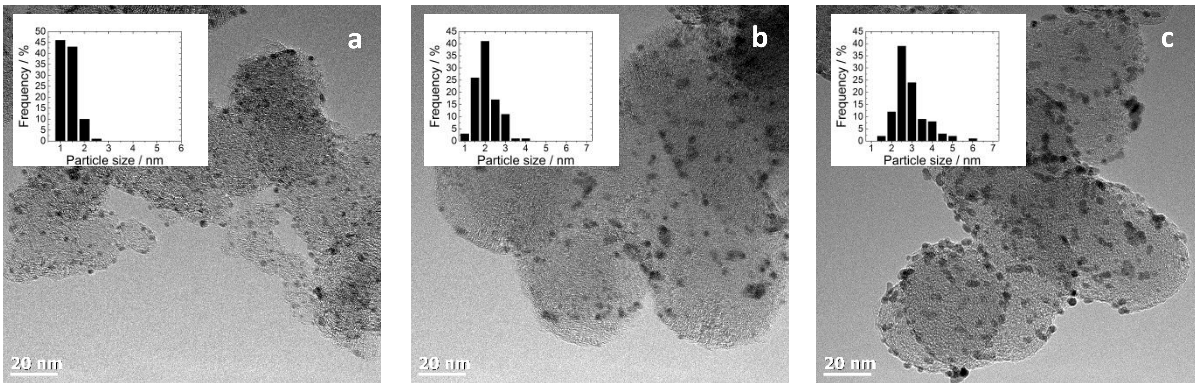

Figure 4.1.3: TEM images and particle size distribution graphs of (a) 10 wt% Pt/C, (b) 20 wt% Pt/C and (c) 40 wt% Pt/C.

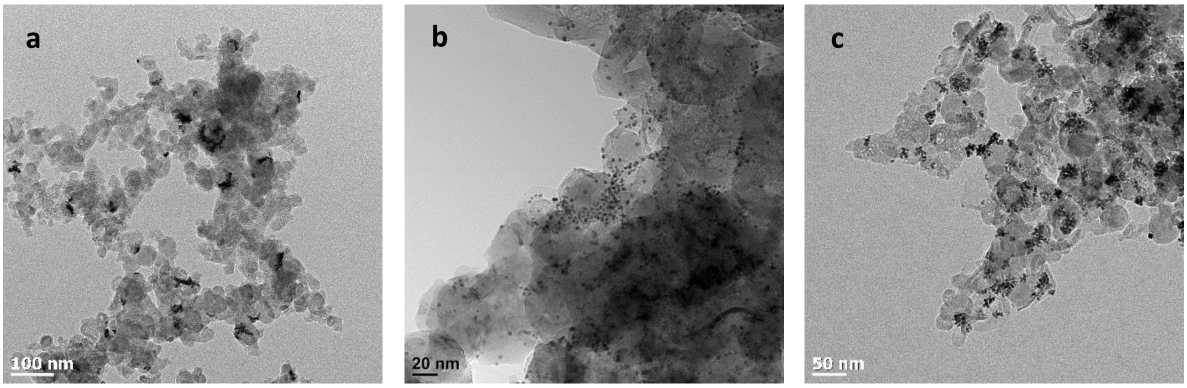

Figure 4.1.4: TEM images of (a) Pt on untreated commercial BC, (b) Pt on nitric acid treated BC and (c) Pt on hydrogen treated BC.

The 20 eq wt% Pt on treated and untreated boron carbide catalysts' TEM images are shown in Figure 4.1.4. Figure 4.1.4 shows Pt agglomeration on the untreated BC and hydrogen treated BC supports, however, the nitric acid treated BC support shows well dispersed, small Pt nanoparticles. TEM images of the prepared Pt/BC-HNO_3 catalysts with varying platinum loadings are shown in Figure 4.1.5. The images in Figures 4.1.5a, 4.1.5b and 4.1.5c show platinum nanoparticles on the nitric acid treated BC supports, with varying equivalent loadings of platinum, these carbide supports are compared to the benchmark Pt/C catalysts shown in Figure 4.1.3. Table 4.1.3 outlines the average platinum particle sizes and inter-particle distances for each nitric acid treated BC catalyst and benchmark catalyst. The platinum particle sizes of the commercial Pt/C catalysts range from 1.1 – 2.7 nm and the platinum nanoparticles are well dispersed on the treated BC support with average particle sizes ranging from 2.3 – 2.9 nm.

Table 4.1.3: Pt particle sizes and inter-particle distances measured using TEM images of the different supported catalysts.

Catalyst	Pt particle size / nm	Pt inter-particle distances / nm
10 wt% Pt/C	1.1 ± 0.3	6.6 ± 2.8
20 wt% Pt/C	2.1 ± 0.5	7.1 ± 2
40 wt% Pt/C	2.7 ± 0.7	5.1 ± 1
10 eq wt% Pt/BC-HNO_3	2.9 ± 0.9	18.6 ± 11

20 eq wt% Pt/BC-HNO_3	2.3 ± 0.7	7.9 ± 3
40 eq wt% Pt/BC-HNO_3	2.6 ± 0.6	5.4 ± 2

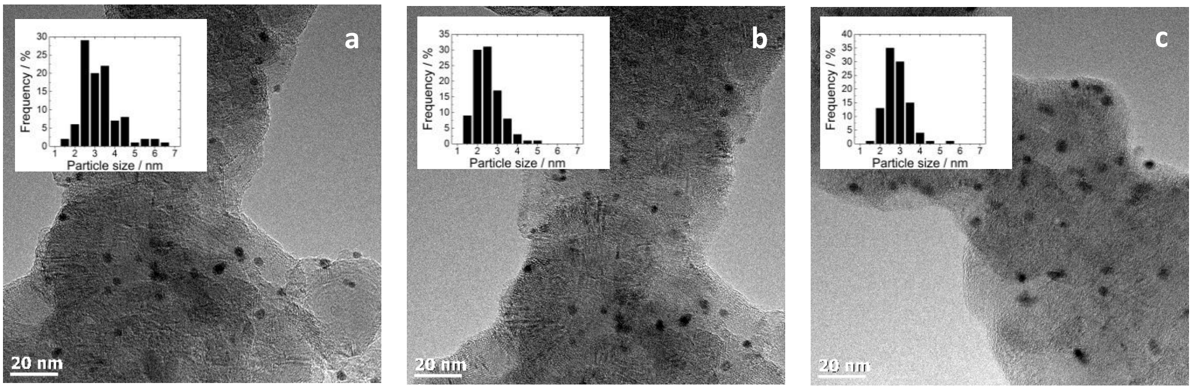

Figure 4.1.5: TEM images of (a) 10 eq wt% Pt/BC-HNO_3, (b) 20 eq wt% Pt/ BC-HNO_3 and (c) 40 eq wt% Pt/ BC-HNO_3.

4.1.3.3 X-Ray Diffraction (XRD)

The XRD pattern of the untreated commercial BC, seen in Figure 4.1.6a, shows amorphous and crystalline features. Figure 4.1.6b represents the XRD pattern for the nitric acid treated BC material, this diffraction pattern clearly shows crystalline peaks, with no amorphous material, indicative of rhombohedral graphite (3R) and hexagonal graphite (2H). Thus, the boron carbide is not pure trigonal rhombohedral B_4C (R3m). Rietveld refinement was used to quantify the pattern and indicated 58.0% graphite, 38.7% B_4C and 3.0% B_2O in the sample.

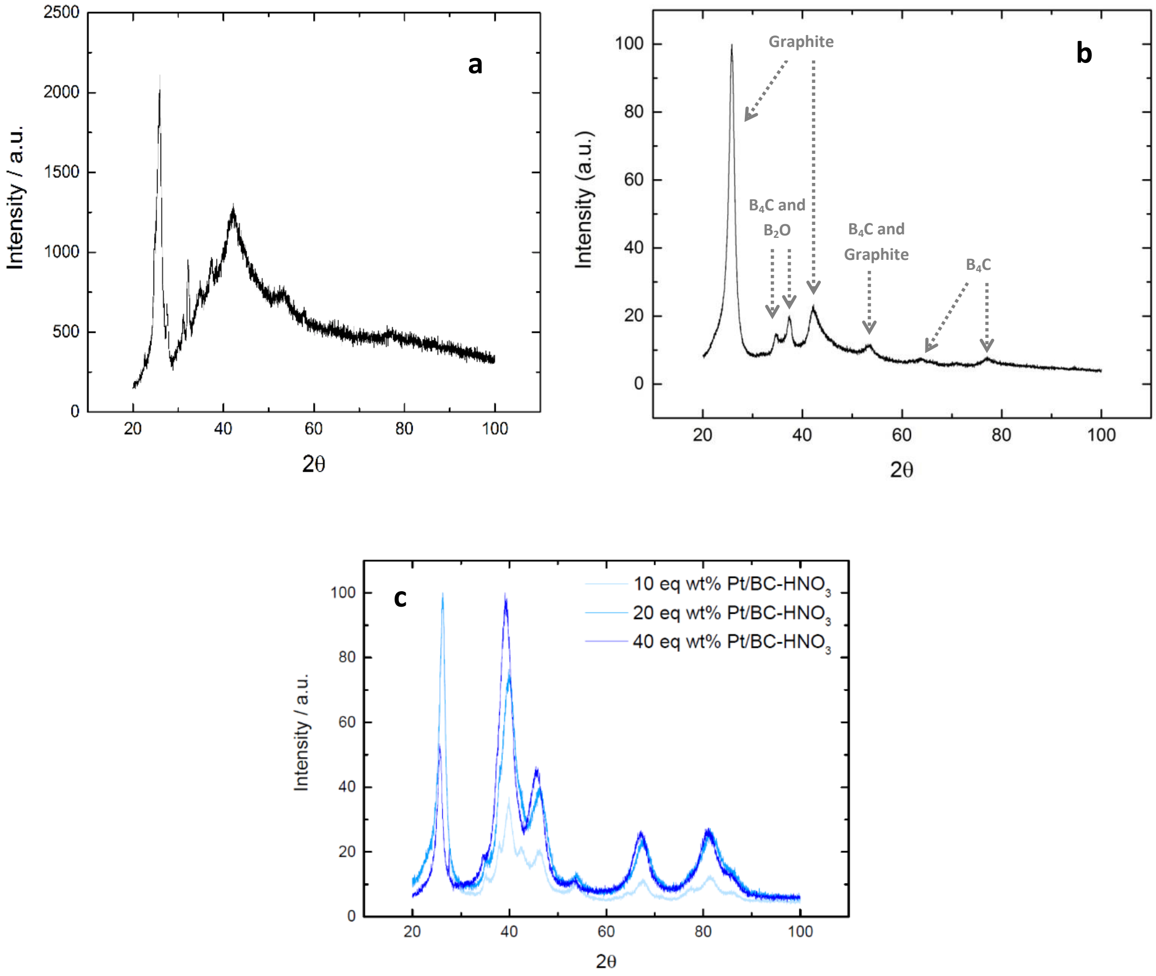

Figure 4.1.6: XRD patterns of (a) untreated commercial BC, (b) nitric acid treated BC and (c) different loadings of Pt on treated BC.

Figure 4.1.6c displays the XRD patterns of the carbide supported catalysts with various Pt loadings. It can be seen in Figure 4.1.6c that the Pt peak height increases as the Pt loading increases. Furthermore, the Pt deposition method does not alter the crystallinity of the support material. The Scherrer equation was used to calculate the average Pt crystallite size to be around 3.9 nm for the various loadings of Pt/BC-HNO_3. It is expected that the crystallite size be slightly larger than the size measured by TEM in Table 4.1.3 since the lower detection limit of XRD is 2 - 2.5 nm, so particle sizes smaller than 2 nm are not identified [9].

4.1.3.4 Conductivity

A conductivity device, pictured in Figure 4.1.7, was designed and manufactured in order to measure the resistivity of the carbide powders. The powder was placed into the center tube, which was manufactured using an insulating material, and a torque wrench was used to place an applied force on the powder. The resistivity measurement was reported as 0.27 Ohm.cm for the nitric acid treated BC support. The resistivity of Vulcan was measured to be around 0.26 Ohm.cm, which is similar to the treated BC measurement.

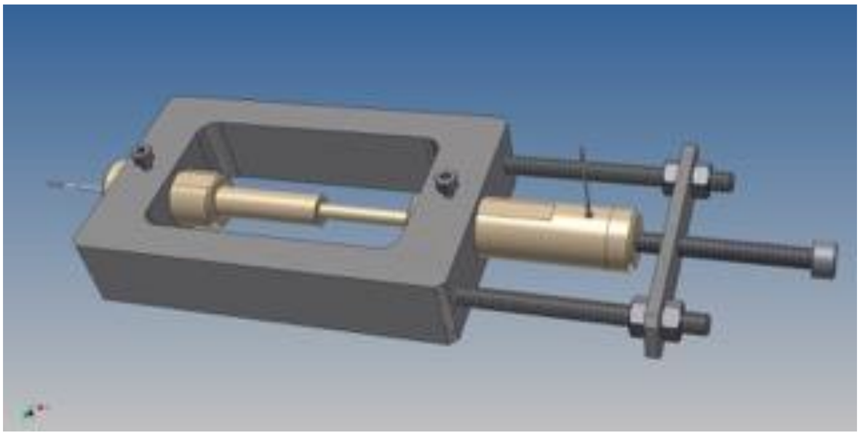

Figure 4.1.7: Schematic of the designed conductivity device.

4.1.3.5 Impurities and Loading Verification

Inductively coupled plasma optical emission spectrometry (ICP-OES) was used to confirm the Pt loadings on the support, the results are tabulated in Table 4.1.4. Determination the Pt loadings on carbides is not trivial, since carbon and boron are often not distinguishable or detected during ICP-OES measurements. Therefore, BC supported catalysts were weighed before ICP analysis, the Pt is dissolved into aqua regia and the concentration is determined in a known volume of solution and related back to the initial weight of the sample. This method contains many sources of error but is the best-known method to determine Pt loading on BC. The Pt loadings measured were in good agreement with the intended loadings calculated using the equivalent loadings correction.

Table 4.1.4: Pt loadings measured on the carbide supported catalysts using ICP-OES.

Catalyst	Pt loading measured using ICP-OES / wt%	Intended Pt loading / wt%
10 eq wt% Pt/BC-HNO_3	2.76	3.05
20 eq wt% Pt/BC-HNO_3	6.86	6.19
40 eq wt% Pt/BC-HNO_3	12.7	15.93

During the SEM-EDX analysis, silicon impurities in the BC-HNO$_3$ composite material samples were detected to be approx. 0.4 wt% in concentration and X-ray photoelectron spectroscopy (XPS) also detected small impurities of Si (0.4 wt%), fluorine (0.6 wt%), and sodium (0.2 wt%).

4.1.3.6 Electrochemical Characterisation

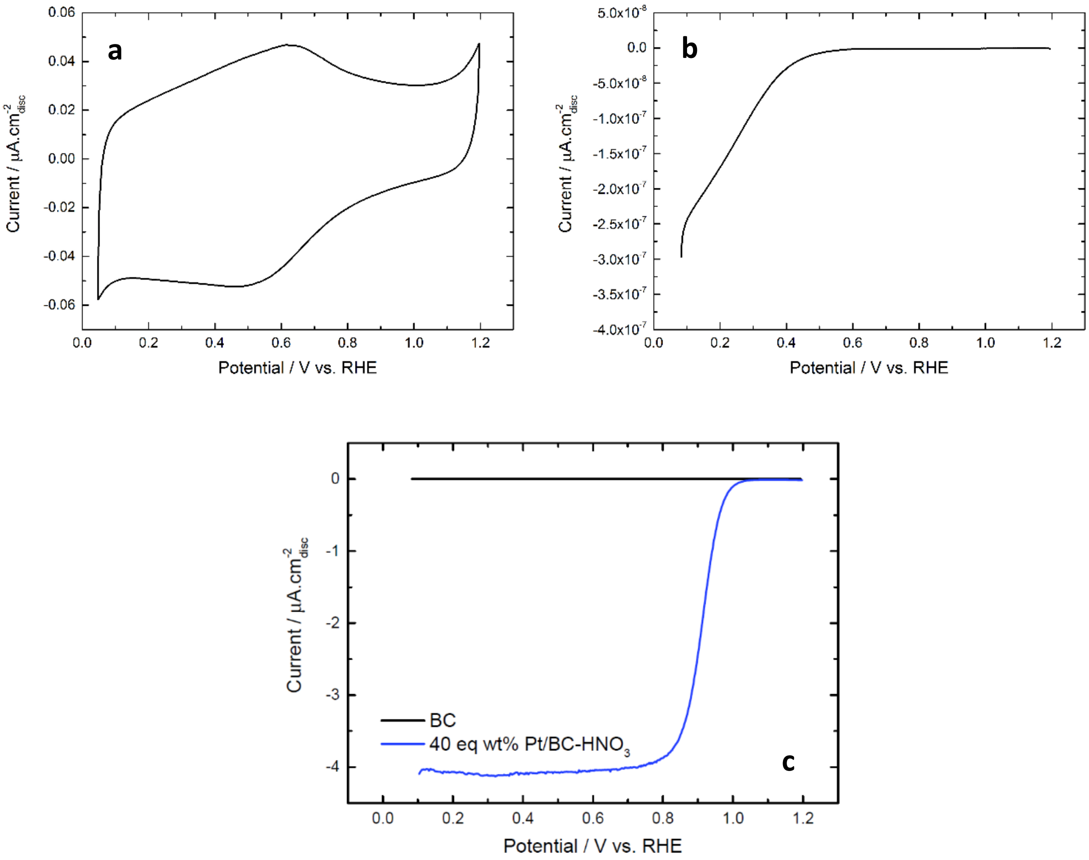

Figure 4.1.8: (a) The cyclic voltammograms of the boron carbide composite support in an argon saturated 0.1 M HClO$_4$ electrolyte solution at room temperature with a scan rate of 20 mV.s^{-1} ; (b) RDE measurements of the BC-HNO$_3$ support in an oxygen saturated 0.1 M HClO$_4$ electrolyte solution at room temperature with a scan rate of 20 mV.s^{-1} at 1600 rpm rotation rate; (c) the RDE measurements of the BC-HNO$_3$ support and 40 eq wt% Pt/BC-HNO$_3$ in an oxygen saturated 0.1 M HClO$_4$ electrolyte solution at room temperature with a scan rate of 20 mV.s^{-1} at 1600 rpm rotation rate.

The cyclic voltammogram (CV) of the bare BC-HNO$_3$ support is shown in Figure 4.1.8a, the RDE measurements during ORR at 1600 rpm for this support is shown in Figure 4.1.8b and the ORR measurements during ORR at 1600 rpm for the support and 40 eq wt% Pt/BC is shown in Figure 4.1.8c.

The CV of the BC-HNO_3 support is similar to that of Vulcan, with redox peaks around 0.6 V vs. RHE. Figure 4.1.8b demonstrates a reductive current at low potentials on the BC-HNO_3 support. However, this does not contribute to the ORR activity at 0.9 V vs. RHE as low currents are detected at these potentials, as seen in Figure 4.1.8c.

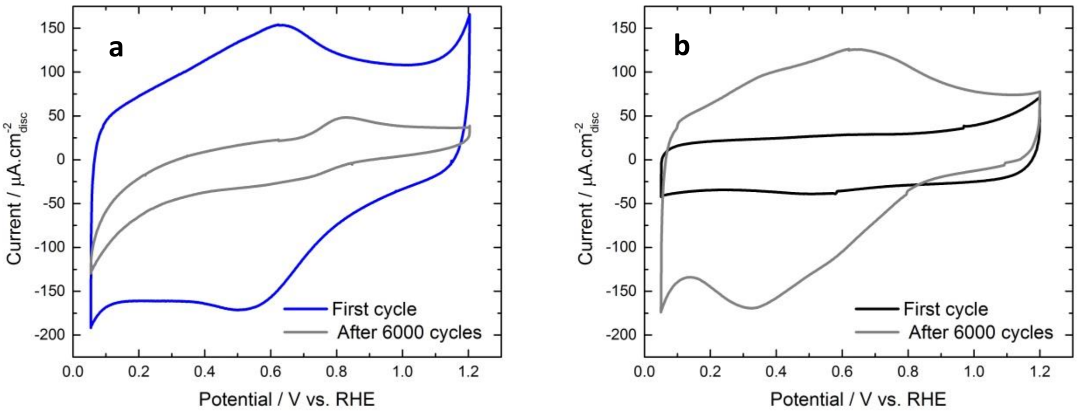

Figure 4.1.9: Support durability study showing the first and 6000th cycle after degradation cycling between 1.0 – 1.5 V vs. RHE on (a) BC-HNO_3 and (b) Vulcan XC-72R in 0.1 M $HClO_4$ in room temperature at 20 mV.s^{-1}.

The first durability sequence studied was used to investigate the stability of the support material at high potentials, without the presence of Pt. The durability testing consisted of cycling the potential between 1.0 and 1.5 V vs. RHE for 6000 cycles and returning to the full voltammogram scan limits of 0.05 – 1.2 V vs. RHE to compare current changes and capacitance changes to the voltammograms. The first and 6000th voltammograms for BC-HNO_3 and Vulcan XC-72R are displayed in Figures 4.1.9a and 4.1.9b, respectively. An increased capacitance in Figure 4.1.9b is observed on the Vulcan support material, while Figure 4.1.9a shows the reverse trend with a significantly decreased capacitance after 6000 cycles for BC-HNO_3.

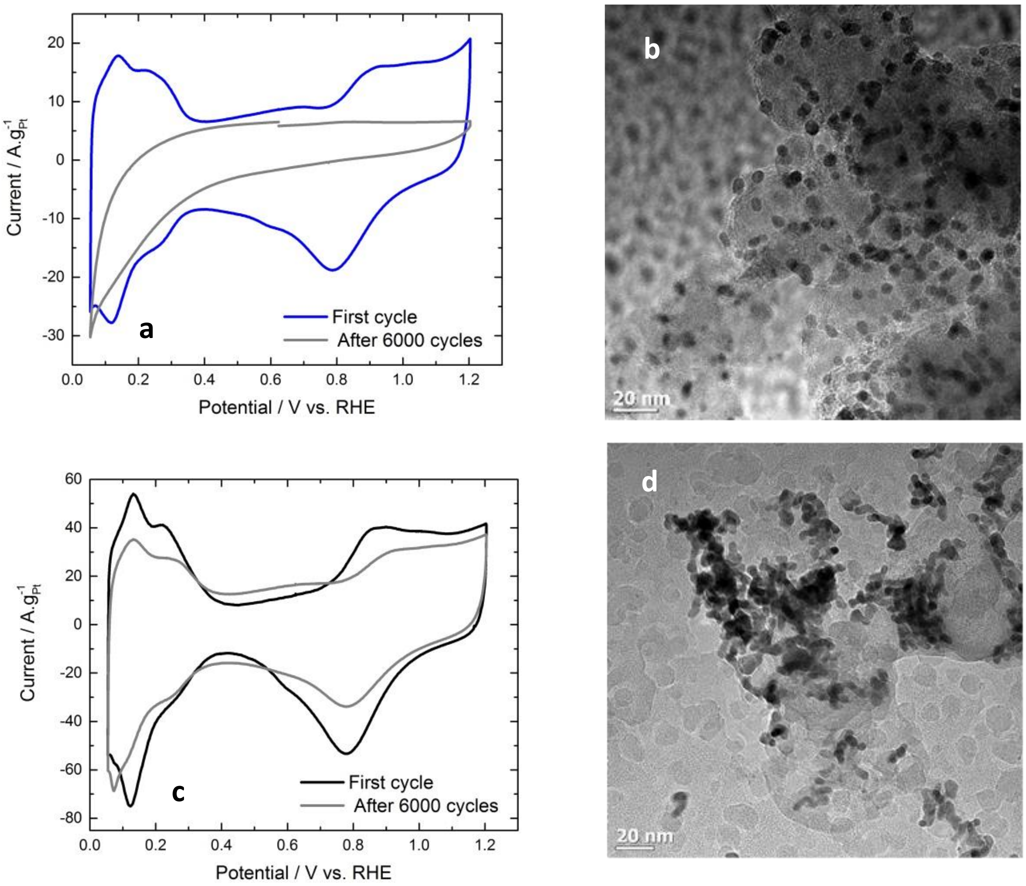

Figure 4.1.10: Catalyst durability study showing the first and 6000th cycle after degradation cycling between 1.0 – 1.5 V vs. RHE on (a) cyclic voltammograms of the 40 eq wt% Pt/BC-HNO_3 catalyst, (b) TEM images after this durability testing; (c) cyclic voltammograms of the 40 wt% Pt/C catalyst and (d) TEM images after this durability testing in 0.1 M $HClO_4$ in room temperature at 20 mV.s^{-1}.

The second durability sequence studied was used to investigate the stability of the support material at high potentials, with the presence of Pt. The durability testing consisted of cycling the potential between 1.0 and 1.5 V vs. RHE for 6000 cycles and returning to the full voltammogram scan limits of 0.05 – 1.2 V vs. RHE to compare current changes, capacitance changes to the voltammograms and Pt active surface area over cycling. The first and 6000th voltammograms for Pt/BC-HNO_3 and Pt/C are displayed in Figures 4.1.10a and 4.1.10c, with TEM images of the Pt/BC-HNO_3 and Pt/C catalysts after 6000 cycles shown in Figures 4.1.10b and 4.1.10d, respectively. Figure 4.1.10c shows the double layer charging on the Pt/C catalyst increased and the Pt ECSA decreases after 6000 cycles. Additionally, Figure 4.1.10d displays significant Pt agglomeration.

The 6000th cycle after degradation on the 40 eq wt% Pt/BC-HNO_3 catalyst, reported in Figure 4.1.10a, shows no peaks relating to oxidation or reduction on platinum. Contrarily, Figure 4.1.10b demonstrates well-dispersed Pt nanoparticles which have not undergone agglomeration, as the Pt nanoparticles on carbon displayed.

4.1.4 Discussion

4.1.4.1 Support Treatments and Physical Characterisation

The untreated BC was not able to produce well dispersed Pt nanoparticles on the surface, as shown in Figure 4.1.4a. The Pt nanoparticles on the untreated BC agglomerated in small sections of the support surface. This phenomenon is due to two possible reasons. Firstly, low density of nucleation sites on the support surface, due to surface functional groups which could prohibit Pt deposition on these sites [10]. Secondly, a smooth support surface may also prohibit Pt deposition, as surface defects increase the number of nucleation sites possible for deposition [11]. In order to increase the number of nucleation sites on the BC support, removal of the current functional groups and roughening of the surface was necessary. Thus, the BC support was treated before platinum deposition using two methods, oxidation treatment with concentrated nitric acid for 8 hours and reduction treatment with hydrogen at 500 °C.

As seen in Figure 4.1.4c, the hydrogen treatment did not increase the number of nucleation sites as there was little change in the Pt deposition on the surface of the support. The removal of the functional groups by reduction is likely to have occurred, however, the reduction treatment did not seem to roughen the surface of the support, since no change is seen on the TEM images before and after treatment (Figures 4.1.4a and 4.1.4c), and therefore the smoothness of the surface continued to prohibit good Pt dispersion. The boron carbide oxidation treatment with nitric acid, seen in Figure 4.1.4b was successful in increasing the number of nucleation sites by exchanging functional groups on the support surface for oxide termination groups and roughening the surface. After nitric acid treatment of the BC, small Pt nanoparticles deposited evenly on the support surface, therefore, this treatment was standardised for all BC supported catalysts.

The physisorption results obtain a surface area of 230 $m^2.g^{-1}$ for Vulcan, this material is well-known to be highly porous which contributes to a large surface area. The surface area of the untreated BC material was measured to be 56.7 $m^2.g^{-1}$, this surface area is lower than Vulcan due to the slightly higher density of boron carbide and the smaller pore volume, as reported in Table 4.1.1. Hydrogen treatment of the BC did not significantly affect the surface area or pore volume, however, after treatment with nitric acid the surface area increased by 40%. The XRD pattern, in Figure 4.1.6a, of the untreated commercial BC shows both an amorphous material and crystalline material. Figure 4.1.6b of the nitric acid treated BC material shows crystalline material only with a composition of 58.0% graphite, 38.7% B_4C and 3.0% B_2O. The amorphous features in the untreated BC are attributed to excess amorphous carbon or boron oxides, which were removed during the treatment process. The increase in BET surface area after nitric acid treatment was attributed to the oxidation of excess amorphous carbon and/or the dissolution of boron oxides in the as received material. This cleaning/removing of amorphous material creates more pore volume, leading to a higher accessible surface area.

The nitric acid treated BC support was the most promising material since well dispersed Pt nanoparticles were supported on the surface and BC-HNO_3 had a large BET surface area (80 $m^2.g^{-1}$), average pore size and pore volume. These are essential properties for Pt dispersion and oxygen diffusion to the catalytic surface. Platinum was successfully deposited onto BC-HNO_3 surface with particle sizes similar to the platinum deposited on carbon supports, however, noting that the average particle size on 10 wt% Pt/C catalyst of 1.1 nm was considerably smaller than that of the 10 eq wt% Pt/BC catalyst (2.9 nm). Further evidence of the similarity between the carbide supported catalysts, confirming the equivalent weight correction factor, is the Pt inter-particle distance which remains similar to the commercial Pt/C catalysts, with the exception of the 10 wt% Pt/C. By normalising the loadings by surface area of the support, the particle size and inter-particle distances remain constant and therefore observations associated with the support effects on particle size distributions, electrochemical activities for the ORR and electrochemical durability could be made.

4.1.4.2 Electrochemical Characterisation and Stability

The cyclic voltammogram of the BC composite support is similar to that of Vulcan, which was expected due to the carbon content of the support, reported above ~58%. The similarities in the cyclic voltammograms lie in the quinone-hydroquinone character of activated carbon and carbon black, resulting in redox coupled peaks [12] around 0.6 V vs. RHE. Figure 4.1.8b demonstrates some peroxide formation at low potentials on the support materials but this current is negligible in comparison to the ORR currents measured on the Pt/BC-HNO_3 catalyst. Since boron carbide is not known to be conductive [13], it is assumed that the graphite content in the BC material assists in the electrochemical conductivity.

The stability of the bare Vulcan support at high potentials, in Figure 4.1.9b, showed an increased capacitance on the Vulcan support, which is attributed to significant oxidation. The degradation of carbon at high potentials is described as an increase in interfacial double layer capacitance, due to a more hydrophilic surface or an increase in the roughness of the carbon surface [13]. Cyclic voltammograms of degradation studies on boron carbide are yet to be reported, however, the Pourbaix diagram for boron indicates the most stable state in low pH at high potentials is H_3BO_3 [14]. Therefore, the reduction in current, in Figure 4.1.9a, could be explained by the oxidation of boron carbide to aqueous H_3BO_3 and thus the support surface is dissolved into the electrolyte, or an insulating oxidative layer on the surface of the support material is formed.

Insights from the degradation study of the bare supports are important in explaining the trends in the degradation of the catalysed supports (seen in Figure 4.1.10). Figure 4.1.10c shows the double layer charging increased and the Pt ECSA decreased after 6000 cycles. This phenomenon is explained by the attachment of platinum on the carbon surface being weakened by the oxidation, corrosion and roughening of carbon, leading to platinum detachment from the surface. This process lead to platinum agglomeration, as well as platinum dissolution, both resulting in a loss of active surface area and therefore loss of activity. In addition, the process of corrosion is accelerated by the presence of platinum [15]. This assertion is confirmed by the TEM images after degradation, shown in Figure 4.1.10d, that display significant agglomeration formation. The deactivation of the Pt/BC-HNO_3 catalyst is explained by an insulating boron oxide layer which reduces the electroactivity of the material. The insulating boron oxide layer produced at high potentials results in a more resistive surface and no Pt is detected on the cyclic voltammogram. However, unlike the Pt/C catalyst at high potentials, TEM images after degradation of the Pt/BC-HNO_3 catalyst did not show Pt agglomeration.

4.1.5 Conclusion

In order for platinum nanoparticles to be successfully deposited onto the BC support, the surface of the boron carbide-graphite composite required treatment with nitric acid to roughen the surface of the support and therefore increase the number of nucleation sites for platinum deposition. The treatment with nitric acid removed amorphous material from the support, leaving behind a boron carbide and graphite composite. The nitric acid treated BC obtained a surface area of 80 $m^2.g^{-1}$, this surface area was used to normalize the Pt loading on the surface to the surface area of Vulcan (230 $m^2.g^{-1}$). After normalisation, platinum nanoparticles were successfully deposited on the BC material with average particle sizes ranging from 2.3 – 2.9 nm for the 10, 20 and 40 eq wt% Pt/BC-HNO_3 catalysts. As a benchmark, the 10, 20 and 40 wt% Pt/C consisted of 1.1 – 2.7 nm Pt particle sizes.

The electrochemical durability testing on the Vulcan support and 40 wt% Pt/C catalyst indicated an increase in interfacial double layer capacitance due to a more hydrophilic surface or an increase in the roughness of the surface. Moreover, the instability of the carbon surface resulted in agglomeration of the Pt nanoparticles during degradation testing. Conversely, the platinum nanoparticles on the BC-HNO_3 support were stable and showed no signs of agglomeration during degradation testing. This lack of Pt agglomeration suggests that the graphite in the support material underwent minimal degradation, however, an insulating boron oxide layer was formed at high potentials which caused rapid deactivation of the Pt catalyst.

4.1.6 References

1. Song, C., Tang, Y., Zhang, J.L., Zhang, J., Wang, H., Shen, J., McDermid, S., Li, J. and Kozak, P. 2007. *Electrochimica Acta*. 52(7): 2552-2561.
2. Huang, S., Ganesan, P. & Popov, B.N. 2011. *Applied Catalysis B: Environmental*. 102(1–2): 71-77.
3. Antolini, E. & Gonzalez, E.R. 2009. *Solid State Ionics*. 180(9–10): 746-763.
4. Ding, H. & Hihara, L. 2006. *ECS Transactions*. 1(4): 103-114.
5. Borchardt, L., Kockrick, E., Wollmann, P., Kaskel, S., Guron, M.M., Sneddon, L.G. & Geiger, D. 2010. *Chemistry of Materials*. 22(16): 4660-4668.

6. Lv, H., Peng, T., Wu, P., Pan, M. & Mu, S. 2012. *Journal of Materials Chemistry*. 22(18): 9155-9160.
7. Mayrhofer, K.J.J., Blizanac, B.B., Arenz, M., Stamenkovic, V.R., Ross, P.N. & Markovic, N.M. 2005. *The Journal of Physical Chemistry B.* 109(30):14433-14440.
8. Nesselberger, M., Roefzaad, M., Fayçal Hamou, R., Ulrich Biedermann, P., Schweinberger, F.F., Kunz, S., Schloegl, K., Wiberg, G.K.H., Ashton, S., Heiz, U., Mayrhofer, K.J.J. & Arenz, M. 2013. *Nature Materials.* 12(10):919-924.
9. Bittencourt, C., Hecq, M., Felten, A., Pireaux, J.J., Ghijsen, J., Felicissimo, M.P., Rudolf, P., Drube, W., Ke, X. & Van Tendeloo, G. 2008. *Chemical Physics Letters.* 462(4–6):260-264.
10. O’Connell, K. & Regalbuto, J.R. 2015. *Catalysis Letters*. 145(3): 777-783
11. Yu, R., Chen, L., Liu, Q., Lin, J., Tan, K., Ng, S.C., Chan, H.S.O., Xu, G. & Hor, T.S.A. 1998. *Chemistry of Materials.* 10(3):718-722.
12. Kinoshita, K. & Bett, J.A.S. 1973. *Carbon.* 11(4):403-411.
13. Wood, C. & Emin, D. 1984. *Physical Review B*. 29(8):4582-4587.
14. Speder, J., Zana, A., Spanos, I., Kirkensgaard, J.J.K., Mortensen, K. & Arenz, M. 2013. *Electrochemistry Communications*. 34:153-156.
15. Brookins, D.G. 2012. *Eh-pH Diagrams for Geochemistry*. Springer Berlin Heidelberg.

4.2 Electronic Metal-Support Interaction Enhanced Oxygen Reduction Activity and Stability of Boron Carbide Supported Platinum

---

Abstract

Catalysing the reduction of oxygen in acidic media is a standing challenge. Although activity of platinum, the most active metal, can be substantially improved by alloying, alloy stability remains a concern. Here we report that platinum nanoparticles supported on graphite-rich boron carbide show a 50–100% increase in activity in acidic media and improved cycle stability compared to commercial carbon supported platinum nanoparticles. Transmission electron microscopy and X-ray absorption fine structure analysis confirm similar platinum nanoparticle shapes, sizes, lattice parameters, and cluster packing on both supports, while x-ray photoelectron and absorption spectroscopy demonstrate a change in electronic structure. This shows that purely electronic metal-support interactions can significantly improve oxygen reduction activity without inducing shape, alloying or strain effects and without compromising stability. Optimising the electronic interaction between the catalyst and support is, therefore, a promising approach for advanced electrocatalysts where optimising the catalytic nanoparticles themselves is constrained by other concerns.

4.2.1 Introduction

The oxygen reduction reaction (ORR) is a standing grand challenge in fundamental research in energy, exemplifying a broader class of multi-electron reactions [1]. Oxygen reduction efficiency and long-term catalyst stability are standing fundamental problems that have to be overcome for polymer electrolyte fuel cells [2] to be used in demanding applications such as automobiles and grid-scale energy storage. The relatively large overpotential of the ORR at technically feasible electrodes under practical operating conditions limits conversion efficiency to typically <50% relative to the thermodynamic limit of more than 80% [3]. Challenging cost targets, especially in the automotive industry, provide further motivation to reduce Pt loadings [4]. Finally, the dissolution and/or loss of Pt surface area in the cathode must be greatly reduced to meet automotive and grid-scale storage stability targets.

The work pioneered by Nørskov [5] has provided a rational design approach to improve ORR activity by tailoring the position of the Pt d-band centre, because it determines the stability of reaction intermediates, especial O_{ads}. Significant efforts have successfully focused on improving ORR activity by d-band centre engineering via nanoparticulate Pt alloys supported on high-surface area carbon [2,6-8]. However, the most active alloys [3,9] are unlikely to show long-term stability under cathodic polymer electrolyte fuel cells conditions [10,11] for thermodynamic reasons. At best, one can hope that dealloying is restricted to the surface, leading to Pt skin structures that are, fortuitously, highly active [3,12,13].

Whether dealloying can be restricted to the surface of the typically 2 nm alloy electrocatalysts over technically relevant lifetimes is an open question. Regardless, stability concerns motivate other design approaches to engineer the Pt d-band characteristics without potentially compromising stability. Recently, research emphasis has shifted to alternative support materials to prevent the loss of catalyst surface area due to support corrosion and dissolution/agglomeration of nanoparticulate Pt [14,15]. Alternative supports also provide an opportunity to indirectly improve ORR activity as well, because a change in support electronic structure can influence the catalyst's d-band manifold via electronic equilibration [16], one aspect of strong metal-support interactions (SMSI).

Utilisation of SMSIs is a promising approach to improve both activity and stability of supported Pt catalysts. The SMSI of Pt on oxide supports, particularly titanium dioxide, is well known [17,18]. These Pt/TiO_2 catalysts have previously exhibited higher activities for ORR in relation to Pt/C [19]. The low conductivity of these materials, however, is a challenge [20]. Highly conductive SnO_2-based supports have, therefore, attracted attention recently [21], and thin film studies unveiled an intriguing dependence of ORR activity on support orientation and/or termination [22].

Changing the physical nature of the support from carbons to oxides is a radical step. It potentially impacts catalyst stoichiometry and particle morphology, which in their own right change electrocatalytic properties via size [4], strain [23] and proximity [24] effects. It is, therefore, nontrivial to experimentally isolate these effects to develop the fundamental understanding needed to rationally exploit SMSIs.

Transition metal carbides have also been widely investigated as promising support materials due to high electrical conductivity, thermal stability and similarities in electronic structure to Pt [25]. However, the low surface area of carbides and liability to oxidation are challenging [26]. Carbides are, nonetheless, attractive to investigate electronic metal-support interactions in isolation, because they are physically closer to carbon than oxides. The material of choice, however, should also show a markedly different electronic structure and resilience against oxidation. Boron carbide (B_4C) is such a material. It is a refractory compound [26] exhibiting high chemical inertness [27], semi-conducing band structure and electrochemical stability [28]. The first study of B_4C as an electrocatalyst support for hydrogen fuel cells was by Grubb & McKee [29] wherein a high resistance to sintering and higher current densities when compared to platinum on carbon black were already observed. More recent work by Lv *et al*. [30] has also shown promising ORR activity.

Pt nanoparticle supported on graphite-rich B_4C composites (BC)* are compared here with Pt supported on Vulcan XC 72R high-surface area carbon (C) to isolate electronic metal-support interactions. Electrochemical as well as advanced *ex-situ* characterisation techniques are used to elucidate the structure-property relationships between catalyst morphology, electronic structure and ORR activity. Transmission electron microscopy (TEM) and extended X-ray absorption fine structure (EXAFS) analysis confirm similar particle size, shape and packing of the clustered nanoparticles on both supports, while X-ray photoelectron spectroscopy (XPS) and X-ray adsorption near edge structure (XANES) analysis show differences in electronic properties due to metal-support interactions. These differences in electronic properties are correlated with enhanced ORR activity: the surface and mass specific oxygen reduction activity of Pt nanoparticles supported on BC under rotating disc electrode (RDE) conditions increases by roughly 40% relative to commercial Pt/C, while the kinetic current at 0.9 V shows a 50–100% improvement. The increased cycle stability of the BC supported catalysts after degradation cycling further promotes the interpretation in terms of increased electronic metal-support interactions on these catalysts. Purely electronic metal-support interactions are, therefore, experimentally

---

*Previously referred to as BC-HNO_3 in Chapter 4.1, is from now on referred to as BC isolated demonstrating that optimising the electronic interaction between the catalyst and support, in conjunction with d-band theory, is a promising approach to designing advanced electrocatalysts without compromising stability under harsh conditions.

4.2.2 Results

4.2.2.1 Naming Scheme

Graphite-rich boron carbide composites (BC) were catalysed with varying amounts of Pt nanoparticles following standard procedures. These Pt/BC catalysts are compared with commercial Pt/C catalysts. It is imperative to keep particle size and dispersion constant between the Pt/BC and benchmark Pt/C catalysts to isolate electronic effects, because these affect ORR activities significantly [4,23,24]. We use a naming convention for all catalysts that follows the nominal platinum loading (that is, wt%) of the commercial benchmark catalysts. The equivalent platinum loading on BC (that is, eq wt%) designates a catalyst that has the same mass platinum per support surface area (Note S4.2.1).

4.2.2.2. Support Surface Area

The BC support Brunauer, Emmett and Teller (BET) surface area was measured to be 80 m^2g^{-1}, in agreement with manufacturer specifications (Figure S4.2.1). This is considerably lower than seen for high-surface area carbons such as Vulcan XC 72R, which has a surface area of 250–260 m^2g^{-1}. To keep the mass platinum per surface area constant, the actual target platinum loading per mass BC support was, therefore, reduced accordingly (Table S4.2.1) to maintain a similar Pt coverage per surface area of support and particle size as seen on the commercial Pt/C benchmark catalysts to isolate support-related activity changes.

4.2.2.3. X-ray Diffraction

The X-ray diffraction pattern of BC (Figure S4.2.2) clearly shows peaks indicative of rhombohedral graphite (3R) and hexagonal graphite (2H) in addition to rhombohedral B_4C (*R3m*), showing the material to be a composite of graphite and rhombohedral B_4C. Using Rietveld refinement, the spectrum indicates 58.0 ± 7.7 wt% graphite, 38.7 ± 7.2 wt% B_4C and 3.0 ± 1.7 wt% B_2O in the sample. This is in reasonable agreement with the average B:C ratio of 39:61 as obtained from EELS. The high graphite content ensures comparative conductivities between BC and C (Note S4.2.2). The graphite consists of approximately 32.0 wt% rhombohedral graphite (3R) and 26.0 wt% hexagonal graphite (2H).

The average Pt crystallite size was confirmed by a fit of the Scherrer equation to the Pt(200), Pt(220) and Pt(311) peaks at 46°, 67° and 81° in the X-ray diffraction (XRD) spectra, respectively (Figure S4.2.3). This analysis yielded a volume-weighted average particle size of ∼3.9 nm for the various loadings, in good agreement with the size measured via TEM (Table 4.2.1). XRD routinely overestimates particle size compared to TEM at the relevant length scale, because particle sizes smaller than 2 nm are not identified due to the lower detection limit of XRD [31].

4.2.2.4. Transmission Electron Microscopy

TEM images of the prepared Pt/BC catalysts as well as the as-received commercial Pt/C benchmark catalysts, taken at 270 k times magnification to illustrate particle dispersion and support morphology, are shown in Figure 4.2.1. The Pt loadings on BC were confirmed via ICP-OES analysis to be 10, 20 and 40 eq wt%, respectively (see Table S4.2.1 for actual loadings). Pt particle size distribution and dispersion for each catalyst are quantified and contrasted in Table 4.2.1, which shows average particle size with s.d. as well as average interparticle distances with s.d. The BC support particles are homogenous with an average particle size of ∼40 nm, and Pt nanoparticles are well dispersed on the BC support with average particle sizes ranging from 2.3 to 2.9 nm. Particle size and interparticle distances are very similar for equivalent loadings on both supports at 20 wt% and 40 wt% with little s.d. Non-conformity is seen between the 10 wt% Pt/C and 10 eq wt% Pt/BC catalysts due to the unusually small Pt size on Pt/C.

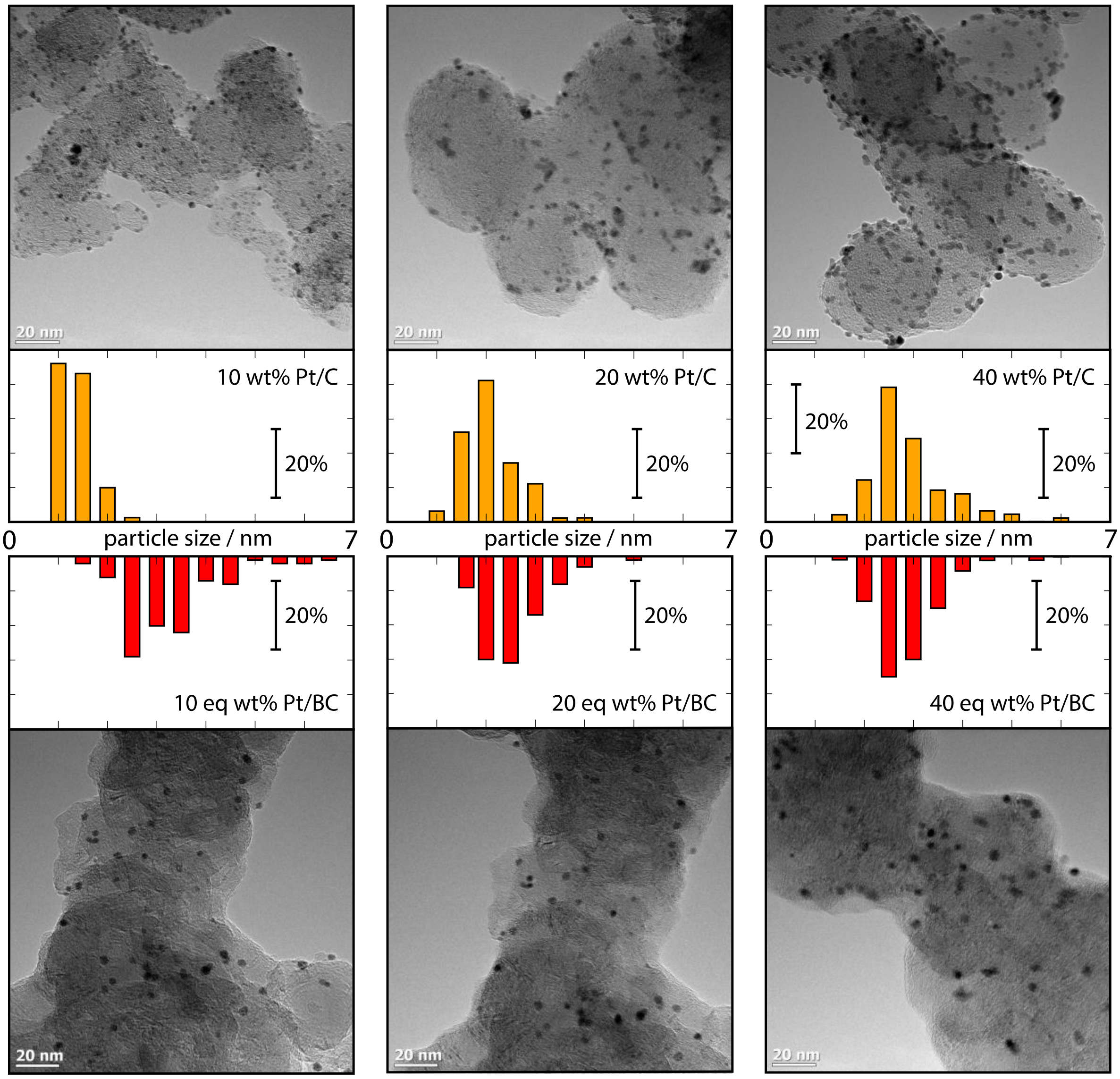

Figure 4.2.1: Catalyst particle size and dispersion. TEM images taken at 270 k magnification showing Pt particle size and dispersion on the C and BC supports, TEM scale bars represent 20 nm; histogram scale bars represent 20%; histograms show Pt size distribution obtained from 100 particles across three images each.

Table 4.2.1: TEM average particle size and proximity. Particle size and interparticle distance distribution mean and s.d. calculated from TEM images.

Catalyst	TEM average particle size / nm	Average inter-particle distances / nm
10 wt% Pt/C	1.1 ± 0.3	6.55 ± 2.8

20 wt% Pt/C	2.1 ± 0.5	7.09 ± 2.1
40 wt% Pt/C	2.7 ± 0.7	5.09 ± 1.3
10 eq wt% Pt/BC	2.9 ± 0.9	18.6 ± 11
20 eq wt% Pt/BC	2.3 ± 0.7	7.94 ± 3.6
40 eq wt% Pt/BC	2.6 ± 0.6	5.35 ± 1.6

4.2.2.5 X-ray Absorption Spectroscopy

The EXAFS was collected for the 20 eq wt% Pt/BC and 20 wt% Pt/C catalysts. The EXAFS at the Pt L_3 edge gives insights to the supported Pt morphology: the first shell co-ordination number is strongly related to average particle size [32] while the fourth co-ordination number is an indication of particle shape.

The measured and modelled EXAFS spectra are shown in Figure S4.2.4. The fitted model, considering up to the fourth neighbour shells, describes the EXAFS data well. The resulting co-ordination numbers (*N*), distances of neighbouring atoms (*R*) and the disorder factors (σ^2) of the catalysts supported on BC and C are listed in Table 4.2.2.

Table 4.2.2: Co-ordination numbers and distances of neighbouring atoms.

Catalyst	Neighbouring atom	N	R / Å *	σ^2 / 10^3
20 wt% Pt/C	Pt - Pt$_1$	10.1 ± 0.3	2.749	5.9 ± 0.17
	Pt - Pt$_2$	5.1 ± 1.4	3.888	10 ± 2.1
	Pt - Pt$_3$	11.2 ± 3.3	4.762	8.1 ± 1.4
	Pt - Pt$_4$	8.3 ± 1.3	5.498	10.5 ± 0.95
20 eq wt% Pt/BC	Pt - Pt$_1$	9.9 ± 0.3	2.751	5.8 ± 0.15
	Pt - Pt$_2$	4.2 ± 1.1	3.891	8.4 ± 1.7
	Pt - Pt$_3$	12.8 ± 3.3	4.766	8.2 ± 1.2
	Pt - Pt$_4$	8.0 ± 1.2	5.502	9.8 ± 0.78

*The error associated with distance to neighbouring atoms for the 20 eq wt% Pt/BC and 20 wt% Pt/C is ±0.00048 Å and ±0.00056 Å, respectively. Values and confidence intervals obtained from EXAFS fits shown in Figure S4.2.4, disorder factors σ^2 are given in the fifth column.

The first, second and fourth Pt co-ordination numbers are slightly smaller for Pt supported on BC, while the third is found to be slightly larger. Differences, however, are within experimental error indicating very similar Pt morphologies as further discussed later. Near-neighbour distances also agree very well between the Pt/BC and Pt/C catalysts.

4.2.2.6 X-ray Photoelectron Spectroscopy

Figure 4.2.2a shows the C 1s and Pt 4f regions of XPS spectra for the Pt/BC and Pt/C catalysts. The XPS spectra are calibrated via alignment of the C(sp2) peak position in the C 1s spectrum to its reference value of 284 eV.

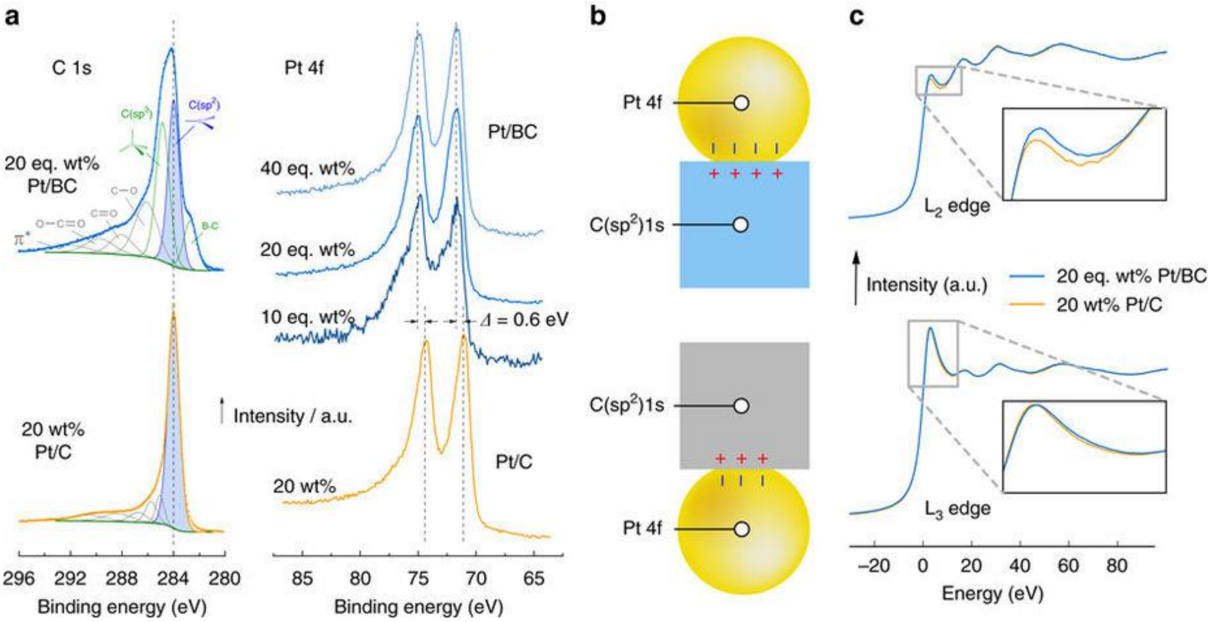

Figure 4.2.2: Electronic equilibration across the catalyst support interface. (a) XPS spectra of the C 1s and Pt 4f region of the Pt/C and Pt/BC catalysts, spectra are aligned to the graphitic C (sp2) peak at 284 eV; (b) Schematic of charge transfer across the support-catalyst interface due to Fermi level equilibration rationalising relative shifts in the XPS Pt 4f and C 1s core levels; (c) *In-situ* XANES L2 and L3 edge measured at 744 mV versus NHE probing d-band occupancy in electrochemical environment.

The C 1s region of the Pt/C catalyst is dominated by the C(sp^2) peak with a small, broad feature at higher binding energies that has been assigned to C–O bonding structures of carboxyl groups [33]. The C 1s spectrum of the Pt/BC catalysts is a convolution of contributions from the B_4C and graphitic carbon within the composite. The C(sp^2) peak is assigned to the graphitic carbon, and the peaks at 282.7 and 284.8 eV are attributed to B_4C. The low energy polymorphs of B_4C [34] provide three C environments at the ends and centre of tri-atomic chains and in the polar position within $B_{11}C$ icosahedra. The low binding energy peak at 282.7 eV was previously attributed to B_4C [35] and is likely due to carbon in low co-ordination (chain centre and/or $B_{11}C$). The C(sp^3) peak at 284.8 eV, which is reminiscent of diamond [36], is also predominantly assigned to B_4C due to the strong similarity of site environment of tetrahedral carbon at the chain ends in B_4C and diamond and the lack of evidence for sp^3 hybridised carbon from XRD.

This assignment is supported by density functional theory calculations (Note S4.2.3) that predict a chemical shift of ∼2.3 eV between the C 1s core electrons in $B_{11}C$ and CBC units (Table S4.2.2), in good agreement with the experimental shift of 2.1 eV. Hence, the relative strength of the C(sp^2) and C(sp^3) peaks corroborates the phase fractions of B_4C and graphitic carbon within the composite derived from XRD.

The Pt 4f spectra of the Pt/C catalyst features the usual spin–orbit splitting into a $4f^{7/2}$ peak at 71.0 eV and a $4f^{5/2}$ peak at 74.3 eV. The same splitting is seen for all Pt/BC catalysts. There is, however, a clear shift of both peaks by ∼0.6 eV to higher binding energies for all Pt loadings on BC to 71.6 and 74.9 eV.

4.2.2.7 *In-situ* X-ray Absorption Near Edge Structure

Figure 4.2.2c shows the XANES Pt L_2 and L_3 edges for the 20 wt% Pt/C and 20 eq wt% Pt/BC catalysts measured under potentiostatic control in electrochemical environment. The increase in the L_2 white line observed for the Pt/BC catalyst indicates an increase in unoccupied d-states above the Fermi level for Pt/BC [37] in electrochemical environments. Using standard post-processing [38], d-band occupancy can be estimated to be 63% for Pt/C and 58% for Pt/BC at 0.744 V versus NHE.

4.2.2.8 Electrochemical Characteristics and Activity

The calculated electrochemically active surface area (ECSA) and ORR activities are summarised in Table 4.2.3. CO stripping voltammetry (Figure S4.2.5) was used to determine the ECSAs assuming a specific charge of 420 $\mu C.cm^{-2}{}_{Pt}$ per CO monolayer adsorbed on the platinum surface. Measurements were taken at room temperature in 0.1 M $HClO_4$ electrolyte solution. No CO stripping peak was seen on the uncatalysed BC support. ECSAs were confirmed using Cu-UPD [39].

Table 4.2.3: Calculated ECSA and ORR activity. ECSA determined by CO stripping and ORR activity measured at 0.9 V versus RHE in a 0.1 M $HClO_4$ electrolyte solution at room temperature. Error margins (s.d.) were obtained from 2 to 4 repeats for each data point.

Catalyst	ECSA / $m^2.g^{-1}_{Pt}$	$I_{mass\ (0.9V)}$ / $A.g^{-1}_{Pt}$	$I_{spec\ (0.9V)}$ / $A.m^{-2}_{Pt}$	$I_{k\ (0.9V)}$ / $\mu A.cm^{-2}_{Pt}$
10 wt% Pt/C	115 ± 15	146 ± 66	1.2 ± 0.5	150 ± 70
20 wt% Pt/C	82.8 ± 2.5	156 ± 4.5	1.9 ± 0.1	240 ± 10
40 wt% Pt/C	56.0 ± 3.6	120 ± 3.5	2.2 ± 0.1	330 ± 20
10 eq wt% Pt/BC	81.1 ± 3.9	224 ± 21	2.8 ± 0.1	320 ± 30
20 eq wt% Pt/BC	67.7 ± 1.9	172 ± 7.0	2.6 ± 0.2	370 ± 30
40 eq wt% Pt/BC	69.5 ± 0.4	209 ± 4.0	3.0 ± 0.1	710 ± 30

The specific and kinetic currents reported in Table 4.2.3 were obtained from RDE measurements at a rotation speed of 1600 rpm. (Figure S4.2.6) during the anodic sweep at 0.9 V versus RHE. Measurements were completed at 20 $mV.s^{-1}$ to minimize double layer charging artefacts at room temperature in an oxygen saturated 0.1 M $HClO_4$ electrolyte [4,40]. The ECSA obtained from CO stripping voltammetry was used to calculate surface area specific currents, and the kinetic current was isolated from mass transport limitations using standard post-processing [41].

The Pt/C catalyst activities fall in line with numerous reported values and compilations of values for ORR activity on these catalysts [4,42-45]. An exception is seen for the 10 wt% Pt/C catalyst, which exhibited large experimental scatter and anomalously small limiting currents during RDE measurements (Figure S4.2.6a) indicative of various detrimental effects [43]. The 10% Pt/C catalyst is, therefore, not considered a suitable benchmark for our purposes.

The ORR activities for the BC supported catalysts consistently show a more active catalyst with higher mass specific (I_{mass}), surface area specific (I_{spec}) and kinetic activities (I_{k}) for the ORR. Additionally, kinetic activity increases as Pt loading increases on both the Pt/C and Pt/BC catalysts, with the least active ORR catalyst being 10 wt% Pt/C and the most active being 40 eq wt% Pt/BC. These trends are further discussed below.

Further electrochemical characteristics are summarised in Figure 4.2.3. Cyclic voltammograms of the BC supported catalysts are shown in the left diagram of Figure 4.2.3a. In addition to the typical characteristics of supported Pt, a slight coupled reversible reaction at ~0.6 V versus RHE is seen for the Pt/BC materials. The large double layer of the Pt/BC catalysts results in a less well defined H_{UPD} region than seen on the Pt/C catalysts. Therefore, no attempt was made to compare the ECSA as obtainable from the H_{UPD} region with the values given in Table 4.2.3. Careful observation of the cyclic votammograms in Figure 4.2.3b, which compares the electrochemical response of Pt/BC with the Pt/C benchmark at 40 wt%, shows slight peak shifts towards higher potentials in the oxide reduction region for Pt/BC.

The kinetic ORR results are reiterated in the Tafel plots shown to the right in Figure 4.2.3 for completeness. Figure 4.2.3a compares kinetic currents of Pt/BC at various loadings. Again, kinetic activity generally increases with Pt loading over the full potential range although the two lower loadings show comparable kinetic currents at lower voltages. Finally, the Tafel plot of Figure 4.2.3b shows that the 40 eq wt% Pt/BC catalyst exhibits higher kinetic activity for ORR over the measured potential range of 0.85–0.95 V versus RHE than the 40 wt% Pt/C benchmark. In fact, relative activity of Pt/BC versus Pt/C seems to increase further with decreasing potential.

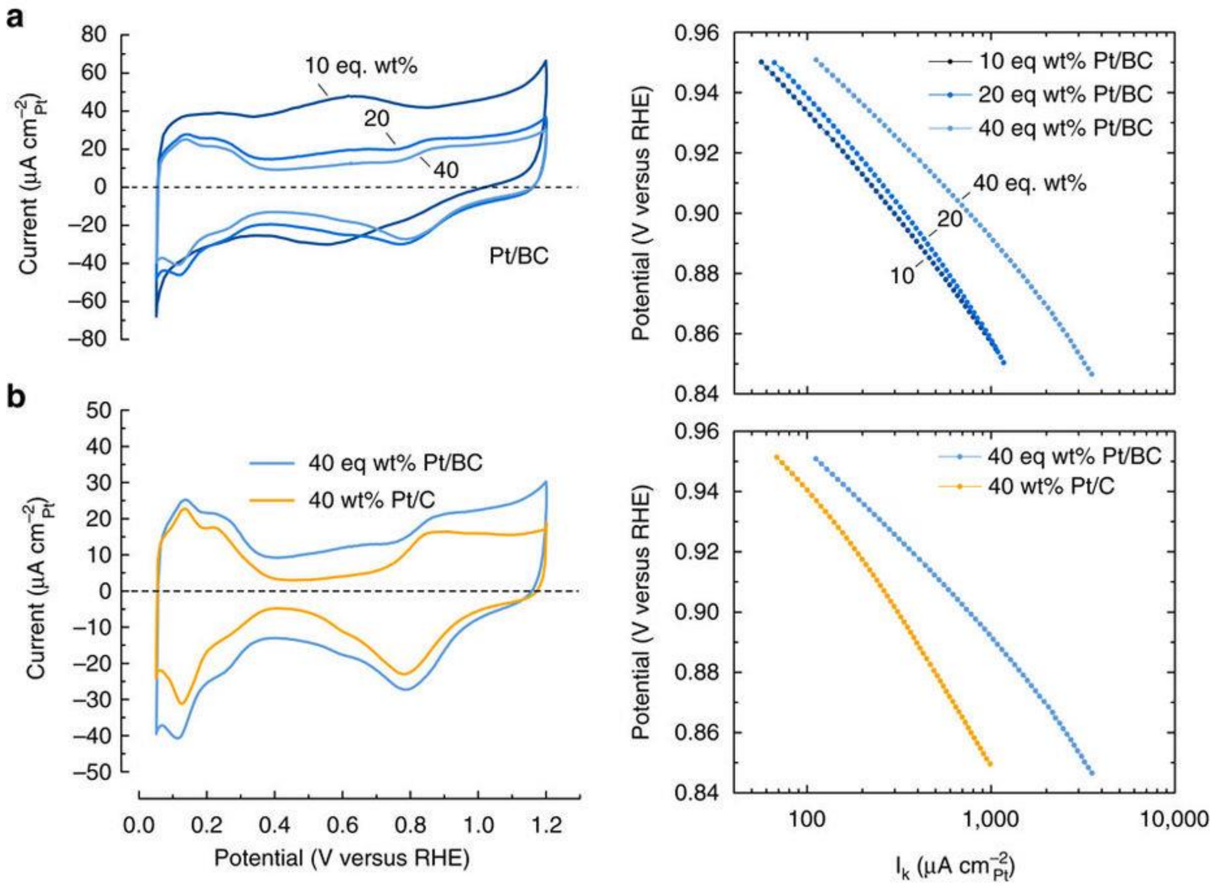

Figure 4.2.3: Electrochemical characterisation. (a) Shows cyclic voltammograms and Tafel plots for 10, 20 and 40 eq wt% Pt/BC, and (b) compares 40 eq wt% Pt/BC with 40 wt% Pt; CVs recorded at 20 mV.s^{-1} between 0.05 and 1.2 V versus RHE and normalised for surface area specific current, Tafel plots obtained from anodic scan recorded at 1600 rpm. between 0.05 and 1.2 V versus RHE and normalised for surface area specific current; all experiments performed in 0.1 M $HClO_4$ at room temperature.

4.2.2.9 Cycle Stability

Catalyst durability was studied for the most active Pt/BC and Pt/C catalysts to investigate the platinum dissolution and platinum agglomeration rate on the different supports. Durability testing consisted of cycling the potential between 0.6 and 1.0 V versus RHE for 6000 cycles at a scan rate of 50 mV.s^{-1} and periodically returning to the full voltammogram scan (0.05–1.2 V versus RHE at 20 mV.s^{-1}) to compare changes in the H_{UPD} region and oxygen adsorption and desorption region.

The voltammograms of the Pt/BC catalyst show significantly less change after 6000 cycles compared to Pt/C (Figure 4.2.4a). Changes in the 1.0–1.2 V range for Pt/BC appear to be not purely related to ECSA loss, because less variation is seen in the H_{UPD} region after cycling. Instead, the reduced current response in the oxidative region is in parts attributed to secondary conditioning effects, which could either be the removal of organic impurities from Pt or oxidative decomposition of other trace impurities in solution amongst other things.

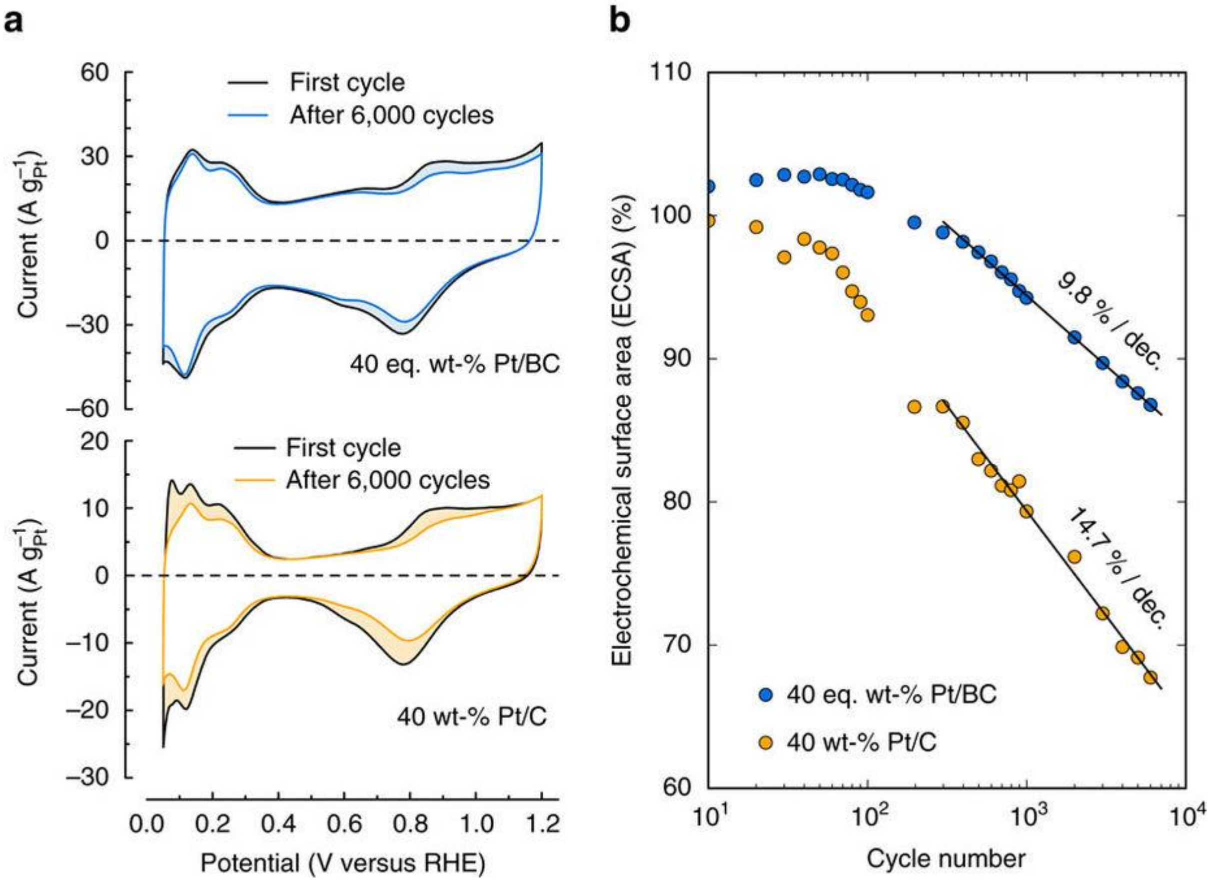

Figure 4.2.4: Catalyst cycle stability. (a) Compares CVs between the first and 6000th cycle, and (b) plots the change in ECSA after cycling at 50 mV.s^{-1} between 0.6 and 1.0 V versus RHE in 0.1 M $HClO_4$ at room temperature.

Cyclic voltammograms of Pt/C before and after cycling show a significantly altered current response in the oxide as well as in the H_{UPD} region while the double layer region remains invariant after 6000 cycles, strongly suggesting catalyst degradation and ECSA loss.

The ECSAs shown in Figure 4.2.4b were periodically obtained from the H_{UPD} region. Both catalysts show a relatively stable ECSA for an initial period of ∼50 – 100 cycles, which might be due to cleaning and/or roughening effects offsetting initial degradation. A logarithmic loss of ECSA is seen for both catalysts beyond this initial conditioning phase. Focusing on the data from cycle 300 onwards, the Pt/C catalyst loses 14.7% ECSA per decade, while the Pt/BC catalysts shows only 9.8% ECSA loss per decade, a 1/3 reduction in logarithmic degradation rate.

ORR activity of cycled catalysts as obtained from RDE measurements (Figure S4.2.7) is compared with ORR activity of the pristine catalysts in Table 4.2.4 for one set of catalysts. For consistency, specific and kinetic activities are based on ECSAs measured again after 6000 cycles by CO stripping (Figure S4.2.8). The ECSAs reported in Table 4.2.4 agree well with the cyclic H-UPD measurements (Figure 4.2.4), showing a significantly larger loss in surface area for the Pt/C catalyst (23% loss after 6000 cycles) than for the Pt/BC catalyst (12% loss after 6000 cycles). Accordingly, mass activity of the cycled Pt/BC catalyst remains with 168 A per g_{Pt} ∼30% higher than seen for the cycled Pt/C catalyst. Relative loss of mass, specific and kinetic activity of the Pt/BC catalyst are in reasonable agreement with the loss in ECSA for the Pt/BC catalyst. The Pt/C catalyst, however, shows a markedly different behaviour. While mass activity also degrades, the relative loss in mass activity (9% loss) is smaller than the reduction in ECSA (23% loss). Correspondingly, surface specific and kinetic activities increase for reasons discussed later. Nonetheless, kinetic activity of the cycled Pt/C catalyst remains significantly lower than seen for the Pt/BC catalyst after 6000 cycles.

Table 4.2.4: Catalyst ORR activity loss. ECSA determined by CO stripping and ORR activity measured at 0.9 V versus RHE in a 0.1 M $HClO_4$ electrolyte solution at room temperature before and after 6000 cycles; mass specific values refer to initial Pt loading.

Catalyst		ECSA / $m^2.g^{-1}_{Pt}$	$I_{mass\,(0.9V)}$ / $A.g^{-1}_{Pt}$	$I_{spec\,(0.9V)}$ / $A.m^{-2}_{Pt}$	I_k / $A.m^{-2}_{Pt}$
40 wt% Pt/C	before cycling	54.4	139	2.55	4.24
	after cycling	41.8	126	3.01	4.71
	relative change	-23%	-9%	+18%	+11%

40 eq wt% Pt/BC	before cycling	69.8	199	2.89	6.95
	after cycling	61.3	168	2.74	5.43
	relative change	-12%	-15%	-5%	-22%

4.2.2.10 Platinum Nanoparticle Size and Shape

Platinum was successfully deposited onto BC with the same average particle sizes as on carbon supports (with the exception of 10 wt% Pt/C) and similar particle size distributions (Table 4.2.1 and Figure 4.2.1). There is no significant increase in particle size for the higher loadings, indicating that the surface area for both supports is sufficient to accommodate high loadings of nanoparticles.

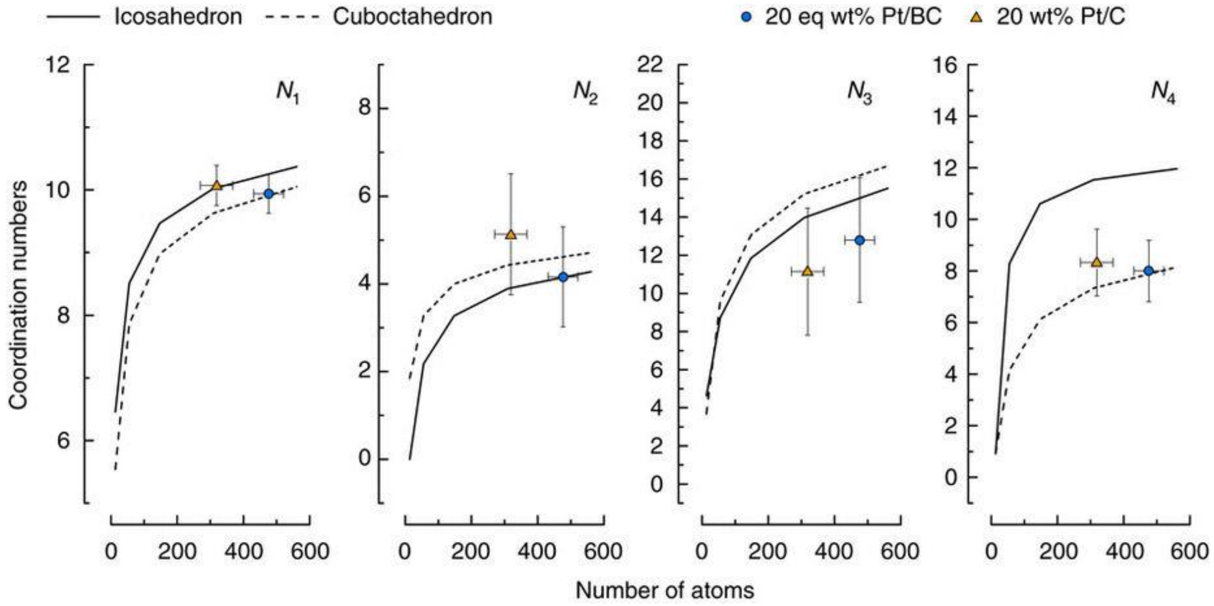

Figure 4.2.5: Catalyst particle shape. Co-ordination numbers N_1 through N_4 for icosahedra and cuboctahedra with superimposed calculated co-ordination numbers from the EXAFS for the 20 eq wt% Pt/BC and 20 wt% Pt/C against average particle size as suggested by TEM. Error bars indicate s.d. of TEM particle size distribution and confidence intervals from EXAFS fit. Shape models adapted from Glasner and Frenkel [48].

Figure 4.2.5 compares the Pt–Pt co-ordination numbers obtained from EXAFS results presented in Table 4.2.2 with co-ordination numbers for ideal icosahedra and cubocahedra [46]. The first four Pt–Pt co-ordination numbers are plotted against average number of atoms per particle as obtained from TEM. The error margins are calculated from the TEM particle size distributions and the confidence interval of the modelled parameters as given by Demeter [47].

The co-ordination numbers $N_{1\ldots4}$ for the two supports are within the error margins of the fits and, therefore, suggest very similar Pt particle sizes and shapes on both supports. N_1 is often used to deduce particle sizes [40]. Comparing N_1 with the expectation values for cuboctahedra and icosahedra shows good agreement with the TEM derived particle sizes for both catalysts.

Particle shape has a stronger influence on more distant platinum shells [32]. N_2 and N_3, however, do not lend themselves to further analysis in our case. The differences between icosahedral and cuboctahedral geometries are too small relative to the precision of our fitted values, which is in part inherently limited by the particle size distribution. For this reason, we have abstained from using the method described by Jentys [48], which relies on the ratio of N_3 to N_1 to deduce particle size and shape. The analysis of N_4, however, is instructive due to the strong shape sensitivity of N_4 for icosahedra and cuboctahedra. The N_4 values of both catalysts agree better with a cuboctahedal shape model, suggesting similar exposure of Pt(001) and Pt(111) facets on both supports. Consequently, EXAFS suggests even stronger than TEM that sample averaged particle sizes and shapes are very similar for the Pt/BC and Pt/C catalysts.

4.2.2.11 Electronic Metal-Support Interaction

As there is no significant change in catalyst size, shape and lattice constant, it is tempting to attribute the significant changes in ORR activity to electronic effects. The Pt 4f spectrum shifts to higher binding energies relative to the C 1 s core levels for Pt/BC (Figure 4.2.2a). Following Lewara *et al.* [17], this might indicate a possible alloy formation with boron or a change in charge transfer between Pt and the support material. There is no evidence of alloy formation in the B 1s XPS (Figure S4.2.9). The B 1s peak does not shift, and a model considering only B–B, B–C and B–O bonds is in perfect agreement with the observed spectra. The very similar Pt lattice constants obtained from EXAFS (Table 4.2.2) provide further evidence for pure Pt particles. The Pt 4f binding energy shift is, therefore, assigned to purely electronic effects.

It is interesting to note that similar electronic effects have been observed for multiwall carbon nanotubes by Ma *et al.* [49] who find a similar but smaller shift of the Pt 4f core levels. These carbons typically show a work function ~0.3–0.5 eV different from graphite [50]. It is, therefore, likely that the measured shift in the Pt 4f core levels are a direct result of changes in the support electronic structure.

Generally, charge is transferred to equilibrate the respective Fermi levels when support and Pt nanoparticle contact. This is qualitatively shown in Figure 4.2.2b. Amongst other factors, the magnitude of the expected charge transfer will depend on the electronic properties of the support material. When changing the support (in this case from C to BC) the extent of this charge transfer changes, resulting in changes in the valence manifolds of the supported catalyst [51] and/or support [52]. This change in electron occupancy can be probed using relative shifts of core levels on either side of the interface [52].

By aligning the C(sp^2) 1s levels for Pt/C and Pt/BC to exclude other effects, a shift in the Pt 4f peak reflects changes in valence state occupancy across the interface as a result of the changing support material, but might also be influenced to some degree by varying final state effects [52]. The reduction of the difference between Pt 4f and C(sp^2) 1 s core levels by ~0.6 eV shown in Figure 4.2.2, therefore, indicates an increase of Pt 4f and/or decrease of C 1 s core level binding energies due to larger electron transfer into Pt under UHV conditions, strongly suggesting that the improved ORR activity and stability originates from electronic metal-support interactions.

4.2.2.12 Charge Transfer and d-Band Occupancy

In principle, one should be able to correlate the sign and magnitude of the relative core level shift with the electronic structure of the respective support materials. There is, however, considerable uncertainty around the electronic properties of the materials reported in the literature. For example, the work function of carbons is usually around 5 eV, but varies as a function of surface termination [53]. Further, the band structure of boron carbides is sensitive to the local stoichiometry of samples, and the Fermi level depends on the type/degree of doping.

The situation is further complicated by the fact that the support material is a composite containing a significant phase fraction of graphitic carbon although we expect the phase fraction on the surface to be significantly smaller than for the bulk support materials due to the aggressive pre-treatment in nitric acid. Regardless, stronger electron transfer should occur from B_4C (typical work function ~4–4.5 eV [54]) to Pt (typical work function ~5.5 eV [55]) than from C (typical work function ~5 eV [53]) to equilibrate the respective Fermi levels as illustrated in Figure 4.2.2b and in agreement with the metal-support interaction suggested by XPS under UHV conditions.

The situation in electrochemical environment, however, is more complex. The *in-situ* XANES spectra shown in Figure 4.2.2c clearly shows an increased hole density in the Pt d-band manifold when particles are supported on BC (that is, more positively charged particles). This apparent contradiction can be resolved by realising that *in-situ* XANES probes a charged interface under potentiostatic control, while *ex-situ* XPS necessarily probes the catalyst under overall neutrality. Because work function and potential of zero charge (pzc) are proportional to each other [56], the smaller support work function of the BC-based catalysts will cause a negative shift of the pzc and, hence, a more positively charged Pt/BC catalyst if held at the same potential as the Pt/C catalyst in the same aqueous electrolyte. Finally, it is noteworthy that the support-induced decrease in d-band filling seen for Pt/BC is reminiscent of electronic effects seen for highly active Pt-alloys [57].

4.2.2.13 Comparison of ORR Activity with Benchmark Data

The trends in ORR kinetic activities (Figure 4.2.3, Table 4.2.3) are not only a function of support material. Particle size effects are likewise relevant. The conventional interpretation [58] in terms of changing surface fractions of Pt(100) and Pt(111), which show different activity for ORR [59], has recently been challenged over the relevant particle size range [40]. However, they are known to significantly impact the results from RDE measurements if the standard protocols and data treatment used here are followed.

Figure 4.2.6, therefore, compares surface area specific activity of the Pt/C and Pt/BC catalysts with benchmark data from Garsany *et al*. [44,45] Note that the data from Garsany *et al*. was corrected for temperature from 30 to 25 °C following a suggestion by Neyerlin *et al*.[60] and to account for the different definition of specific activity used by Garsany *et al*. (Table S4.2.3). Our results for the benchmark Pt/C catalysts are in good agreement with the literature data attesting to the quality of our films and robustness of experimental procedures. As already mentioned, the 10 wt% Pt/C catalyst does not lend itself as a benchmark for our purposes due to the significantly smaller particle size and considerable experimental scatter.

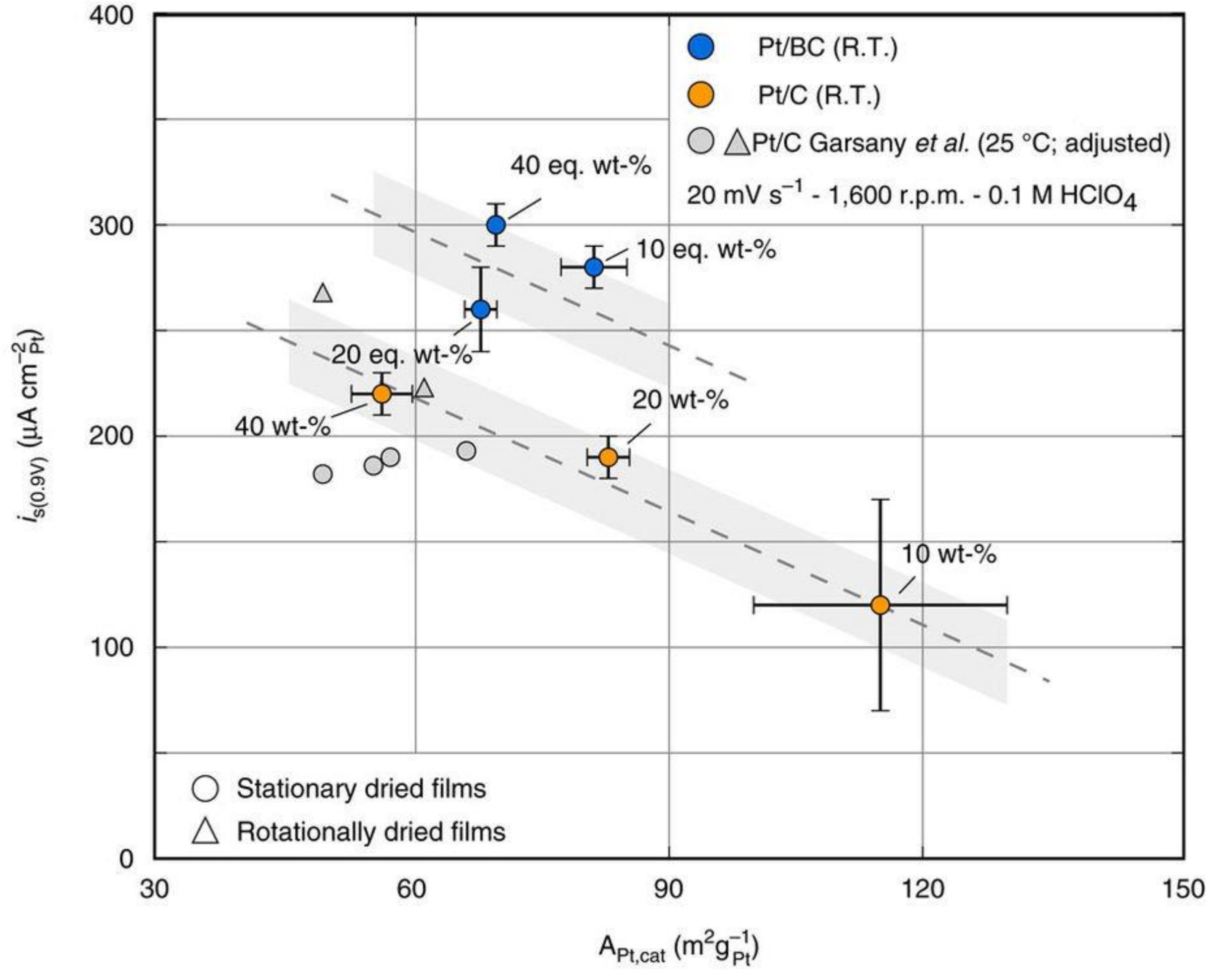

Figure 4.2.6: Comparison of surface area specific ORR activities. Specific current densities at 0.9 V versus RHE for the Pt/BC and Pt/C catalysts are compared with reference data for ORR activity of similar Pt/C catalysts from Garsany *et al.* [44,45] adjusted for temperature [60] and O_2 mass transport correction.

The Pt/BC catalysts broadly follow a similar particle size dependence but with overall ~50% higher surface area specific activity at 0.9 V versus RHE. The increase of surface area specific current density is significantly larger than the expected experimental scatter indicated as grey areas. We, therefore, conclude that purely electronic equilibration between support and catalyst has a bearing on ORR activity of Pt nanoparticles. This is particularly interesting if one considers that the effective charge screening of metals should completely screen the charge redistribution due to Fermi level equilibration between catalyst and support a few atomic distances away from the contact interface [61-63]. Hence, one would not directly expect a pronounced electronic effect on large parts of the more than 20 Å thick Pt particles.

4.2.2.14 Durability

Figure 4.2.4 shows the degradation of ECSA over 6000 cycles for the 40 eq wt% Pt/BC and the 40 wt% Pt/C catalyst. The voltage range was selected to promote platinum dissolution and/or agglomeration over support corrosion [64]. There is a significantly larger rate of ECSA loss for Pt/C after some initial cycles. The consequences of the logarithmic dependence seen in Figure 4.2.4 are worth highlighting. Due to the 1/3 reduction in loss rate per decade, the Pt/BC catalyst retains more than 90% ECSA for about 2000 cycles, while the Pt/C catalyst shows a 10% loss in surface area already after about 200 cycles.

Since particle sizes and shapes of both catalysts are initially similar, this cannot be due to a more stable particle size as starting point. Hence, the results suggest that the stronger electronic metal-support interaction between Pt and the BC support leads to a reduction in platinum dissolution and/or agglomeration. The ORR activities of the cycled catalysts reported in Table 4.2.4 suggest that mostly Pt agglomeration is inhibited for Pt/BC relative to the Pt/C catalyst. While the relative loss of mass specific ORR activity after 6000 cycles is in line with the loss of ECSA for Pt/BC, Pt/C shows an increase in surface specific and kinetic activity after cycling. This increase in surface specific activity and simultaneous loss in mass activity is a clear indication of increasing Pt particle sizes on the Pt/C support. CO stripping voltammetry (Figure S4.2.8) provides further evidence for increased Pt agglomeration on the cycled Pt/C. The pre-peak that is observed for both pristine catalysts has been attributed previously to Pt agglomerates [65]. This pre-peak feature increases for the cycled Pt/C catalyst while it disappears for the cycled Pt/BC catalyst, indicating increased particle agglomeration for cycled Pt/C.

We have argued above that a stronger dipole field is established at the Pt/BC interface relative to Pt/C, which is corroborated by XPS. This stronger dipole interaction likely reduces the mobility of Pt nanoparticles mitigating agglomeration. A similar effect is seen on carbon supports where the rate of platinum nanoparticle agglomeration is seen to reduce when carbon supports are modified with nitrogen and oxygen containing functional groups that strongly interact with nanoparticles [66,67].

Likewise, it suggests that Pt nanoparticles can adopt a lower energy state on BC, which, in principle, should mitigate dissolution. The CVs in Figure 4.2.3b support this interpretation. The oxidation/reduction features of Pt/BC are slightly shifted to more positive potentials relative to Pt/C. Hence, the catalyst might be slightly less prone to surface oxidation/reduction and associated anodic and cathodic Pt dissolution with beneficial implications for cycle stability in this potential range.

4.2.3 Methods

Catalyst preparation: As-received B_4C (NaBond Technologies Co., Ltd.) was stirred in conc. nitric acid (Kimix Chemicals and Lab Supplies cc.) at room temperature for 8 h. Organo-metallic chemical deposition was used to deposit platinum onto the treated B_4C to prepare 10, 20 and 40 eq wt% Pt/BC, where the eq wt% was calculated from surface areas calculated from nitrogen physisorption using a TriStar II 3,020 (Micrometrics) and interpreted using BET theory. The catalyst deposition was carried out using platinum acetoacetate (Sigma Aldrich) at 350 °C under an argon atmosphere [68,69]. As-received Pt/C catalysts from Alfa Aesar (HiSpec 2000, 3000, 4000) were used as a commercial standard for electrochemical activities.

Ex-situ catalyst physical characterisation: The prepared support material was characterised by nitrogen physisorption, analysed using BET theory (Micromeritics Instrument Corporation TriStar II), to determine the support surface area. XRD measurements were carried out on a Bruker D8 Advance diffractometer with a Cu Kα radiation source operating at 40 kV to determine the crystalline phases present in the catalyst. Rietveld refinement on the XRD patterns was completed using Bruker AXS TOPAS software, Version 4.1. TEM was performed on a Tecnai G2 electron microscope operating at 200 kV to determine particle sizes and a Tecnai F20 with a FEG at 200 kV to obtain images shown in Figure 4.2.1. Elemental analyses were carried out by using a Cs probe-corrected JEOL ARM200F (cold-FEG) TEM/STEM operated at 200 kV and equipped with a Gatan GIF spectrometer. EELS data were acquired with an energy dispersion of 0.25 eV per channel. XPS was carried out by Nexus XPS service at Newcastle University using a Thermo Scientific K-Alpha instrument with an Al Kα X-ray source. The supported catalysts were characterised using TEM for Pt particle size using an average of at least 100 particle diameters sampled across three images for each catalyst; particle distances were obtained by measuring the closest neighbouring platinum particle distance for 100 particles across three TEM images for each catalyst. XRD was used to verify the Pt crystallite size, XPS to investigate the binding energies, and ICP-OES (Varian 730-ES) to confirm the Pt loading on the support. *Ex-situ* advanced surface characterisations were completed using X-ray adsorption spectroscopy on the B18 line at the Diamond Light Source to investigate the morphology of Pt on the surface of the support. The Pt L_2 and L_3 edges (13,273 and 11,564 eV) were measured on beamline B18 at Diamond Light Source which operated with a ring energy 3 GeV and at a current of 300 mA. The monochromator used Si(111) crystals operating in Quick EXAFS (QEXAFS) mode. A total of three spectra were averaged for each sample. The measurements were collected using the ionisation chambers in transmission mode at 298 K. Calibration of the monochromator was carried out at both edges using Pt foils. XAS was collected for the 20 wt% Pt/C and 20 eq wt% Pt/BC catalysts only. These catalysts were prepared using boron nitride to bind pellets of the catalysts, the pellets were then placed under a H_2 atmosphere to reduce surface oxides. The absorption spectra were modelled with Demeter by Bruce Ravel using Ifeffit by Matt Newville [17] to solve the EXAFS equation for the first four Pt shell co-ordination numbers as described by Frenkel *et al*. [49] The ink formulation for the 20 eq wt% Pt/BC catalysts used for XANES consisted of 228 mg catalyst, 3.42 ml 5 wt% Nafion solution, 7.6 ml ethanol (Sigma Aldrich); a catalyst layer of 91.46 mg was coated onto a Teflon coated carbon base layer.

Catalyst electrochemical characterisation: Catalyst inks were prepared for the electrochemical characterisation techniques. The Pt/BC catalyst ink consisted of 2.5 mg of the catalyst, 0.5 ml of ethanol (Sigma Aldrich) and 25 µl of 5 wt% Nafion solution. The mixture was sonicated for 30 min and 5 µl was placed on a glassy carbon electrode. The Pt/C catalyst ink consisted of 5 mg of the catalyst, 5 ml of water (Milli-Q 18.2 MΩcm), 1.5 ml isopropanol (Kimix) and 25 µl of 5 wt% Nafion solution. The mixture was sonicated for 30 min and 10 µl was placed on a glassy carbon electrode. Prior to this, the glassy carbon electrode was polished to a mirror finish using 0.1 and 0.05 µm Al_2O_3polish (Buehler). The reference electrode used was $Hg/HgSO_4$ with a platinum counter electrode. Cyclic voltammetry was conducted by cycling the potential between 0.05–1.2 V versus RHE with a scan rate of 50 mV.s^{-1} for 50 cycles at room temperature in an oxygen-free 0.1 M $HClO_4$ electrolyte solution to electrochemically clean the catalyst surface. The scan rate was then changed to 20 mV.s^{-1} for 5 cycles and the potential cycled between 0.05 and 1.2 V versus RHE at room temperature in an oxygen-free 0.1 M $HClO_4$ electrolyte solution. CO stripping was conducted by purging the electrolyte solution with CO for 20 min while holding the potential at 0.1 V versus RHE, argon was then bubbled for 20 min to rid the solution of CO, after which the potential was cycled between 0.05 and 1.2 V versus RHE. The ORR activity was measured by RDE experiments in an O_2 saturated 0.1 M $HClO_4$ electrolyte (70% Suprapur—Merck) using the anodic scan between 0.05 and 1.2 V versus RHE, with a scan rate of 20 mV.s^{-1} and rotation rate of 1600 rpm. at room temperature. All scans were normalised for ECSA and corrected for ohmic drop measured by impedance spectroscopy and capacitive current in an oxygen-free electrolyte. Error margins were obtained from 2 to 4 repeats for each data point. The catalyst degradation studies were completed by cycling between 0.6 and 1.0 V versus RHE with a scan rate of 50 mV.s^{-1} in 0.1 M $HClO_4$ electrolyte solution for 6000 cycles at room temperature, and periodically reverted to a cyclic voltammogram between 0.05 and 1.2 V versus RHE with a scan rate of 20 mV.s^{-1} to investigate the changes to the H_{UPD} region. The reference electrode used was $Hg/HgSO_4$ with a gold counter electrode. The H_{UPD} region was used for changes in ECSA in this instance. ORR activity and ECSA were reassessed after cycling using RDE and CO stripping following the procedures described above.

4.2.4 References

1. Whitesides, G.M. & Crabtree, G.W. 2007. *Science.* 315(5813):796-798.
2. Rabis, A., Rodriguez, P. & Schmidt, T.J. 2012. *ACS Catalysis.* 2(5):864-890.
3. Stamenkovic, V.R., Fowler, B., Mun, B.S., Wang, G., Ross, P.N., Lucas, C.A. & Marković, N.M. 2007. *Science.* 315(5811):493-497.
4. Gasteiger, H.A., Kocha, S.S., Sompalli, B. & Wagner, F.T. 2005. *Applied Catalysis B: Environmental.* 56(1–2):9-35.
5. Nørskov, J.K., Bligaard, T., Rossmeisl, J. & Christensen, C.H. 2009. *Nature Chemistry.* 1(1):37-46.

6. Markovic, N.M., Schmidt, T.J., Stamenkovic, V. & Ross, P.N. 2001. *Fuel Cells.* 1(2):105-116.
7. Wang, C., Markovic, N.M. & Stamenkovic, V.R. 2012. *ACS Catalysis.* 2(5):891-898.
8. Stamenkovic, V., Mun, B.S., Mayrhofer, K.J., Ross, P.N., Markovic, N.M., Rossmeisl, J., Greeley, J. & Nørskov, J.K. 2006. *Angewandte Chemie.* 118(18):2963-2967.
9. Greeley, J., Stephens, I. E. L., Bondarenko, A. S., Johansson, T. P., Hansen, H. A., Jaramillo, T. F., Rossmeisl, J., Chorkendorff, I. Nørskov, J.K. 2009. *Nature Chemistry.* 1(7):552-556.
10. Mayrhofer, K., Hartl, K., Juhart, V. & Arenz, M. 2009. *Journal of the American Chemical Society*. 131: 16348–16349.
11. Chen, S., Gasteiger, H.A., Hayakawa, K., Tada, T. & Shao-Horn, Y. 2010. *Journal of the Electrochemical Society.* 157(1): A82-A97.
12. Strasser, P., Koh, S., Anniyev, T., Greeley, J., More, K., Yu, C., Liu, Z., Kaya, S. Nordlund, D., Ogasawara, H., Toney, M. F. & Nilsson, A. 2010. *Nature Chemistry.* 2(6):454-460.
13. Escudero-Escribano, M., Malacrida, P., Hansen, M.H., Vej-Hansen, U.G., Velázquez-Palenzuela, A., Tripkovic, V., Schiøtz, J., Rossmeisl, J., Stephens, I. E. L., Chorkendorff, I. 2016. *Science.* 352(6281):73-76.
14. Reiser, C.A., Bregoli, L., Patterson, T.W., Yi, J.S., Yang, J.D., Perry, M.L. & Jarvi, T.D. 2005. *Electrochemical and Solid-State Letters.* 8(6): A273-A276.
15. Huang, S., Ganesan, P. & Popov, B.N. 2011. *Applied Catalysis B: Environmental.* 102(1–2):71-77.
16. Cheon, J.Y., Kim, J.H., Kim, J.H., Goddeti, K.C., Park, J.Y. & Joo, S.H. 2014. *Journal of the American Chemical Society.* 136(25):8875-8878.
17. Lewera, A., Timperman, L., Roguska, A. & Alonso-Vante, N. 2011. *The Journal of Physical Chemistry C.* 115(41):20153-20159.
18. Dulub, O., Hebenstreit, W. & Diebold, U. 2000. *Physical Review Letters.* 84(16):3646-3649.
19. Xiong, L. & Manthiram, A. 2004. *Electrochimica Acta.* 49(24): 4163-4170
20. Chen, G., Bare, S.R. & Mallouk, T.E. 2002. *Journal of the Electrochemical Society.* 149(8): A1092-A1099.
21. Takasaki, F., Matsuie, S., Takabatake, Y., Noda, Z., Hayashi, A., Shiratori, Y., Ito, K. & Sasaki, K. 2011. *Journal of the Electrochemical Society.* 158(10): B1270-B1275.

22. Rabis, A., Kramer, D., Fabbri, E., Worsdale, M., Kötz, R. & Schmidt, T.J. 2014. *The Journal of Physical Chemistry C.* 118(21):11292-11302.
23. Du, M., Cui, L., Cao, Y. & Bard, A.J. 2015. *Journal of the American Chemical Society.* 137(23):7397-7403.
24. Nesselberger, M., Roefzaad, M., Fayçal Hamou, R., Ulrich Biedermann, P., Schweinberger, F.F., Kunz, S., Schloegl, K., Wiberg, G.K.H., Ashton, S., Heiz, U., Mayrhofer, K.J.J. & Arenz, M. 2013. *Nature Materials.* 12(10):919-924.
25. Liu, Y., Kelly, T.G., Chen, J.G. & Mustain, W.E. 2013. *ACS Catalysis.* 3(6):1184-1194.
26. Antolini, E. & Gonzalez, E.R. 2009. *Solid State Ionics.* 180(9–10):746-763.
27. Samsonov, G.V. 1962. *Boron, its compounds and alloys.* US Atomic Energy Commission, Division of Technical Information.
28. Ding, H. & Hihara, L. 2006. *ECS Transactions.* 1(4):103-114.
29. Grubb, W.T. & McKee, D.W. 1966. *Nature.* 210(5032):192-194.
30. Lv, H., Peng, T., Wu, P., Pan, M. & Mu, S. 2012. *Journal of Materials Chemistry.* 22(18):9155-9160.
31. O’Connell, K. & Regalbuto, J. 2015. *Catalysis Letters*. 145: 777–783.
32. Frenkel, A.I., Hills, C.W. & Nuzzo, R.G. 2001. *The Journal of Physical Chemistry B.* 105(51):12689-12703.
33. Assumpção, M.H.M.T., Moraes, A., De Souza, R.F.B., Reis, R.M., Rocha, R.S., Gaubeur, I., Calegaro, M.L., Hammer, P. Lanza, M.R.V. & Santos, M.C. 2013. *Applied Catalysis A: General.* 462–463:256-261.
34. Fanchini, G., McCauley, J.W. & Chhowalla, M. 2006. *Phys.Rev.Lett.* 97(3):035502.
35. Vincent, C., Vincent, H., Mourichoux, H. & Bouix, J. 1992. *Journal of Materials Science.* 27(7):1892-1900.
36. Mérel, P., Tabbal, M., Chaker, M., Moisa, S. & Margot, J. 1998. *Applied Surface Science.* 136(1–2):105-110.
37. Yoshitake, H., Mochizuki, T., Yamazaki, O. & Ota, K. 1993. *Journal of Electroanalytical Chemistry.* 361(1-2): 229-237
38. Mansour, A.N., Cook, J.W. & Sayers, D.E. 1984. *The Journal of Physical Chemistry.* 88(11):2330-2334.
39. Green, C.L. & Kucernak, A. 2002.*The Journal of Physical Chemistry B.* 106(5):1036-1047.

40. Nesselberger, M., Ashton, S., Meier, J.C., Katsounaros, I., Mayrhofer, K.J.J. & Arenz, M. 2011. *Journal of the American Chemical Society.* 133(43):17428-17433.
41. Paulus, U.A., Schmidt, T.J., Gasteiger, H.A. & Behm, R.J. 2001. *Journal of Electroanalytical Chemistry.* 495(2):134-145.
42. Fabbri, E., Taylor, S., Rabis, A., Levecque, P., Conrad, O., Kötz, R. & Schmidt, T.J. 2014. *ChemCatChem.* 6: 1410–1418.
43. Mayrhofer, K.J.J., Strmcnik, D., Blizanac, B.B., Stamenkovic, V., Arenz, M. & Markovic, N.M. 2008. *Electrochimica Acta.* 53(7):3181-3188.
44. Garsany, Y., Baturina, O.A., Swider-Lyons, K. & Kocha, S.S. 2010. *Analytical Chemistry.* 82(15):6321-6328.
45. Garsany, Y., Singer, I.L. & Swider-Lyons, K.E. 2011. *Journal of Electroanalytical Chemistry.* 662(2): 396-406
46. Glasner, D. & Frenkel, A.I.2006. *AIP Conference Proceedings.* 9-14 July. B. Hedman & P. Pianetta, Eds. 746.
47. Ravel, B. & Newville, M. 2005. *Journal of Synchrotron Radiation*. 12: 537–541.
48. Jentys, A. 1999. *Physical Chemistry Chemical Physics.* 1(17):4059-4063.
49. Ma, J., Habrioux, A., Morais, C., Lewera, A., Vogel, W., Verde-Gómez, Y., Ramos-Sanchez, G., Balbuena, P.B. Alonso-Vante, N. 2013. *ACS Catalysis.* 3(9):1940-1950.
50. Liu, P., Wei, Y., Jiang, K., Sun, Q., Zhang, X., Fan, S., Zhang, S., Ning, C. Deng, J. 2006. *Physical Review B.* 73(23):235412.
51. Wakisaka, M., Mitsui, S., Hirose, Y., Kawashima, K., Uchida, H. & Watanabe, M. 2006. *The Journal of Physical Chemistry B.* 110(46):23489-23496.
52. Mitsuhara, K., Kitsudo, Y., Matsumoto, H., Visikovskiy, A., Takizawa, M., Nishimura, T., Akita, T. & Kido, Y. 2010. *Surface Science.* 604(5-6): 548-554.
53. Fabish, T.J. & Hair, M.L. 1977. *Journal of Colloid and Interface Science.* 62(1):16-23.
54. Du, J., Li, Q., Xia, Y., Cheng, X., Gan, Y., Huang, H., Zhang, W. & Tao, X. 2013. *Journal of Alloys and Compounds.* 581: 128-132
55. Haynes, W.M. 2012. *CRC Handbook of Chemistry and Physics, 93rd Edition.* Taylor & Francis.
56. Bockris, J. & Argade, S. 1968. *The Journal of Chemical Physics*. 49: 5133–5134
57. Mukerjee, S., Srinivasan, S., Soriaga, M.P. & McBreen, J. 1995. *Journal of the Electrochemical Society.* 142(5):1409-1422.

58. Kinoshita, K. 1990. *Journal of the Electrochemical Society.* 137(3):845-848.
59. Markovic, N.M., Gasteiger, H.A. & Ross, P.N. 1995. *The Journal of Physical Chemistry.* 99(11):3411-3415.
60. Neyerlin, K., Gu, W., Jorne, J. & Gasteiger, H. 2006. *Journal of The Electrochemical Society*. 153(10): A1955- A1963.
61. Joyner, R.W., Pendry, J.B., Saldin, D.K. & Tennison, S.R. 1984. *Surface Science.* 138(1): 84-94
62. Tripković, V., Abild-Pedersen, F., Studt, F., Cerri, I., Nagami, T., Bligaard, T. & Rossmeisl, J. 2012. *ChemCatChem.* 4(2):228-235.
63. Jiang, Z., Zhang, W., Jin, L., Yang, X., Xu, F., Zhu, J. & Huang, W. 2007. *The Journal of Physical Chemistry C.* 111(33):12434-12439.
64. Wu, J., Yuan, X.Z., Martin, J.J., Wang, H., Zhang, J., Shen, J., Wu, S. & Merida, W. 2008. *Journal of Power Sources.* 184(1):104-119.
65. Maillard, F., Schreier, S., Hanzlik, M., Savinova, E.R., Weinkauf, S. & Stimming, U. 2005. *Physical Chemistry Chemical Physics.* 7(2):385-393.
66. Yu, X. & Ye, S. 2007. *Journal of Power Sources.* 172(1):145-154.
67. Zhou, Y., Neyerlin, K., Olson, T.S., Pylypenko, S., Bult, J., Dinh, H.N., Gennett, T., Shao, Z., O'Hayre, R. 2010. *Energy & Environmental Science.* 3(10):1437-1446.
68. Naidoo, Q., Naidoo, S., Petrik, L., Nechaev, A. & Ndungu, P. 2012. *International Journal of Hydrogen Energy.* 37(12):9459-9469.
69. Taylor, S., Fabbri, E., Levecque, P., Schmidt, T.J. & Conrad, O. 2016. *Electrocatalysis.* 7(4):287-296.

4.2.5 Supplementary

Note S4.2.1: Determination of target Pt loadings on BC

We aim to keep the mass Platinum per surface area support constant across supports:

$$\frac{m_{Pt}^{C}}{A_C} = \frac{m_{Pt}^{BC}}{A_{BC}} \qquad \text{Equation 4.2.1}$$

The weight percent Platinum is defined as

$$x_C = \frac{m_{Pt}^{C}}{m_{Pt}^{C} + m_C} \text{ and } x_{BC} = \frac{m_{Pt}^{BC}}{m_{Pt}^{BC} + m_{BC}} \qquad \text{Equation 4.2.2}$$

Combining Equation 4.2.1 and 4.2.2, the target weight percent Platinum on BC that yields the same mass

Platinum per surface area as on C can be calculated from

$$x_{BC} = \frac{\gamma(x_C^{-1}-1)^{-1}}{\gamma(x_C^{-1}-1)^{-1}+1} \qquad \text{Equation 4.2.3}$$

with $\gamma = a_{BC}/a_C$ being the ratio of specific surface areas of both support materials. We used a value of γ = 80.4/259 = 0.31 to calculate the target weight percent on BC from the actual weight percent on C in Table S4.2.1.

Note S4.2.2: Conductivity

The conductivity of the powders was measured using a custom-made conductivity device, the graphite rich boron carbide and Vulcan XC 72R conductivities were measured to be 3.8 ± 0.5 $S.cm^{-1}$ and 3.9 ± 0.5 $S.cm^{-1}$ at room temperature.

Note S4.2.3: C 1s chemical shifts in B4C from Density Functional Theory

Density Functional Theory (DFT) in the Generalised Gradient Approximation (GGA) as parameterised by Perdew, Burke, and Ernzerhof (PBE) was used to quantify the chemical shift of the C 1s core electrons within B_4C. The Partially Augmented Wave (PAW) formalism was used as implemented in Quantum Espresso V5.4.

The $B_{11}C_p$-CBC polymorph with experimental lattice parameters and atomic coordinates obtained from the Inorganic Crystal Structure Database (ICSD) were used (rhombohedral primitive cell with a=4.9424 Å and α=66.07˚).

The C 1s core binding shift was calculated as the change in total energy between placing a C 1s core hole at C in tetrahedral coordination (CBC) and the polar position ($B_{11}C$), respectively:

$$\Delta = E^{1s^*}_{B_{11}C} - E^{1s^*}_{CBC}$$

A supercell approach was used to minimized spurious screened hole interactions between supercell images.

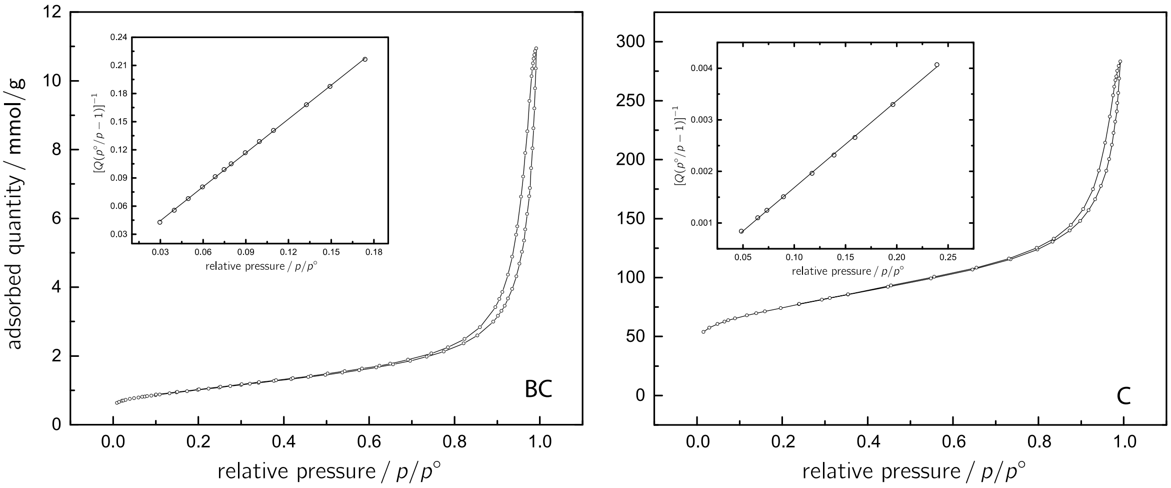

Figure S4.2.1: Nitrogen adsorption isotherms for BC and C supports; insets show linear fit to the BET equation from which BET surface areas are obtained.

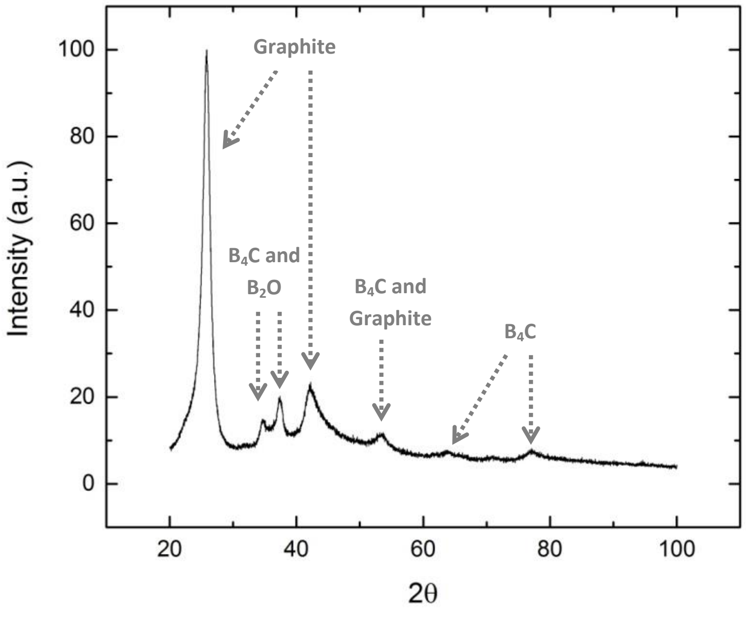

Figure 4.2.2: X-ray diffraction pattern of the graphite rich boron carbide catalyst support.

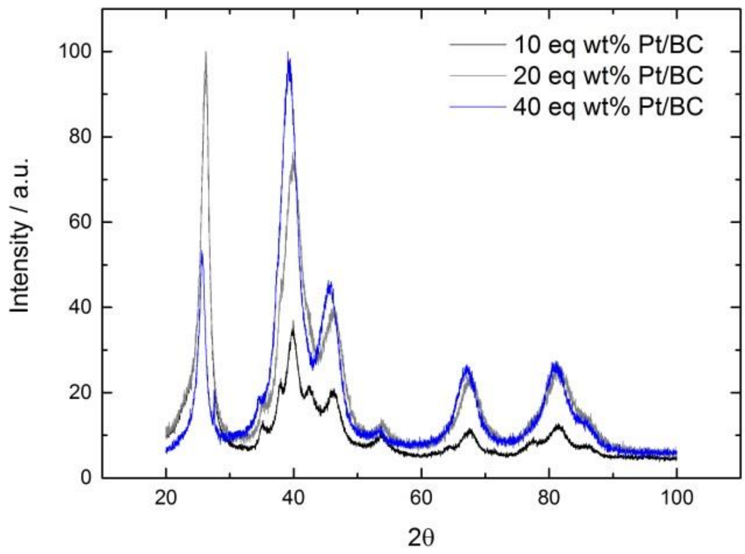

Figure 4.2.3: X-ray diffraction pattern of the 10, 20 and 40 eq wt% Pt/BC catalysts.

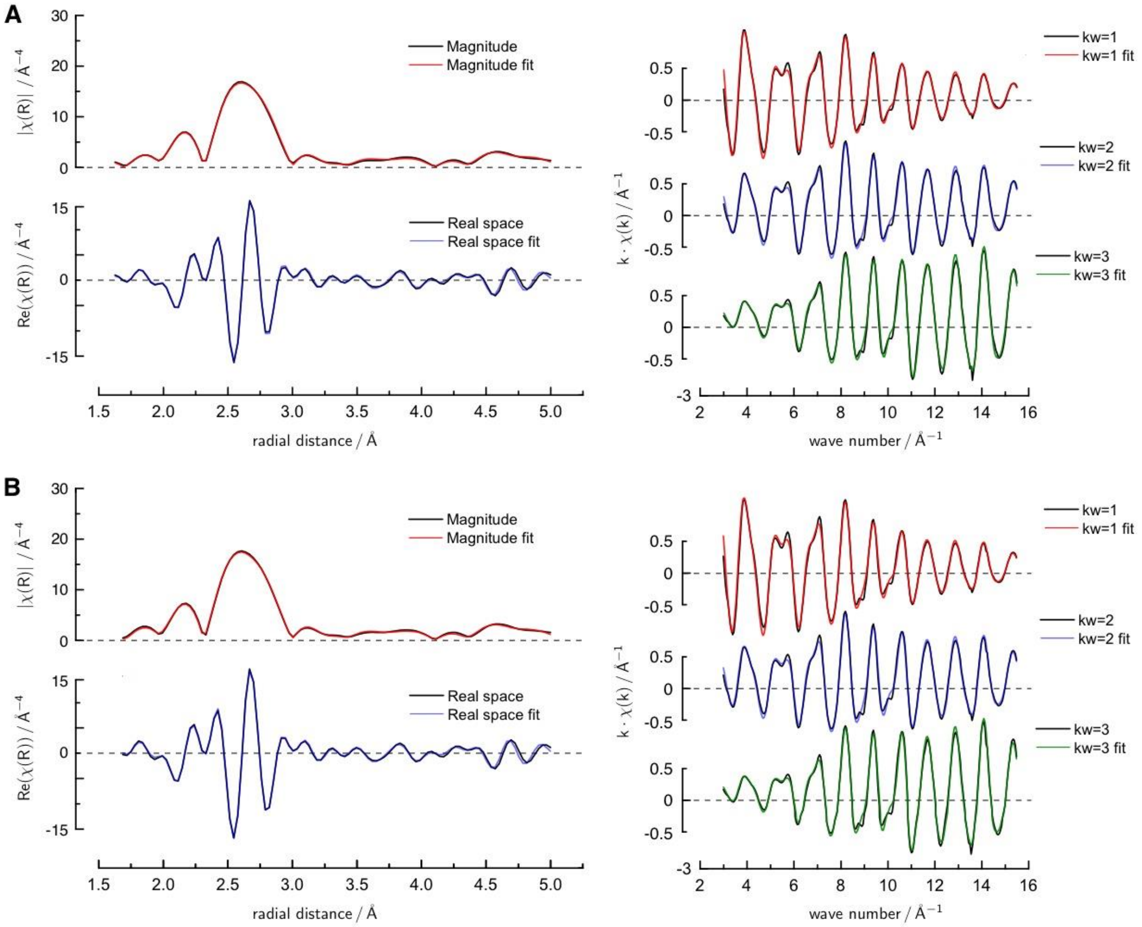

Figure S4.2.4: Actual and modelled EXAFS data. A) R space and k space plots for the 20 eq wt% Pt/BC catalyst, k weighting (kw)=1 is scaled by 7.665, kw=2 is unscaled and kw=3 is scaled by 0.119; B) R space and k space plots for the 20 wt% Pt/C catalyst, kw=1 is scaled by 7.403, kw=2 is unscaled and kw=3 is scaled by 0.106.

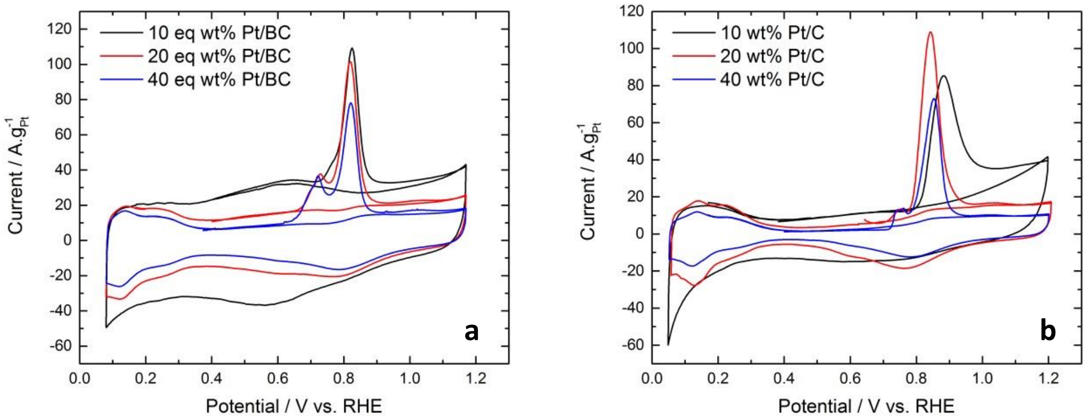

Figure 4.2.5: CO stripping voltammograms for (a) 10 eq wt% Pt/BC, 20 eq wt% Pt/BC and 40 eq wt% Pt/BC catalysts and (b) 10 wt% Pt/C, 20 wt% Pt/C and 40 wt% Pt/C catalysts: all experiments performed in 0.1 M $HClO_4$ at room temperature, recorded at 20 mV.s^{-1} between 0.05 V and 1.2 V vs RHE.

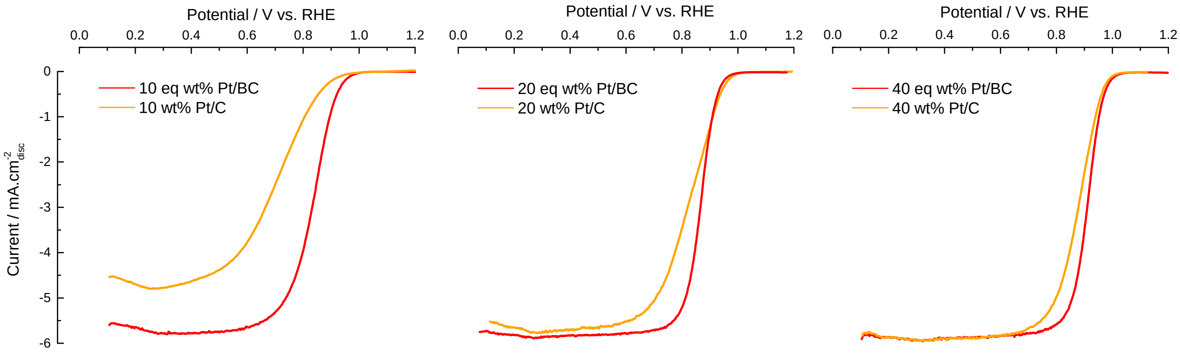

Figure 4.2.6: Current-Voltage curves as obtained by RDE measurements of A) 10 eq wt% Pt/BC and 10 wt% Pt/C, B) 20 eq wt% Pt/BC and 20 wt% Pt/C, C) 40 eq wt% Pt/BC and 40 wt% Pt/C. The anodic scan was recorded at 1600 rpm between 0.05 V and 1.2 V vs RHE, all experiments performed in 0.1 M $HClO_4$ at room temperature recorded at 20 mV.s^{-1} using a 5 mm disc; corrected for iR and capacitive charging.

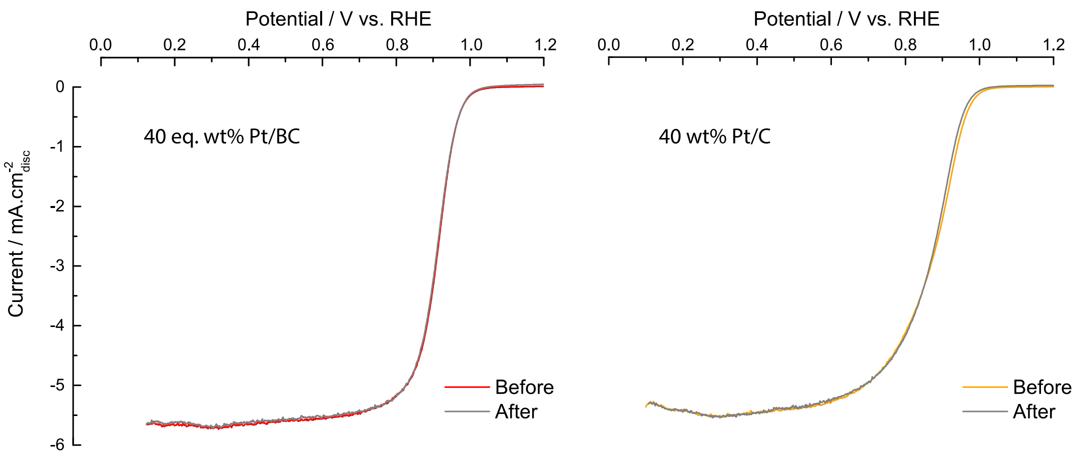

Figure S4.2.7: Current-Voltage curves as obtained by RDE measurements of the 40 eq wt% Pt/BC and 40 wt% Pt/C catalysts before and after cycling; the anodic scan was recorded at 1600 rpm between 0.05 V and 1.2 V vs RHE, all experiments performed in 0.1 M $HClO_4$ at room temperature recorded at 20 mV.s^{-1}; corrected for iR and capacitive charging.

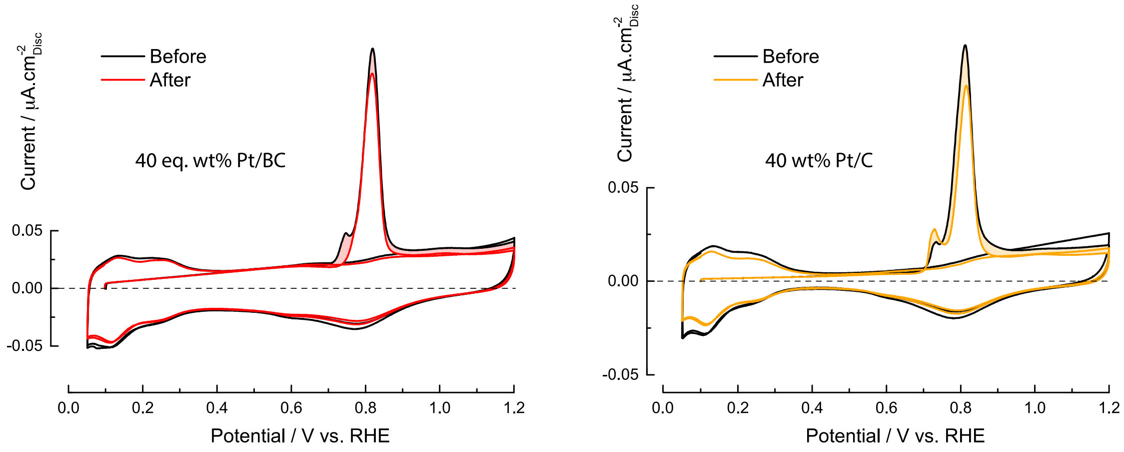

Figure S4.2.8: CO stripping voltammograms for 40 eq wt% Pt/BC and 40 wt% Pt/C catalysts before and after cycling: all experiments performed in 0.1 M $HClO_4$ at room temperature, recorded at 20 mV.s^{-1} between 0.05 V and 1.2 V vs RHE.

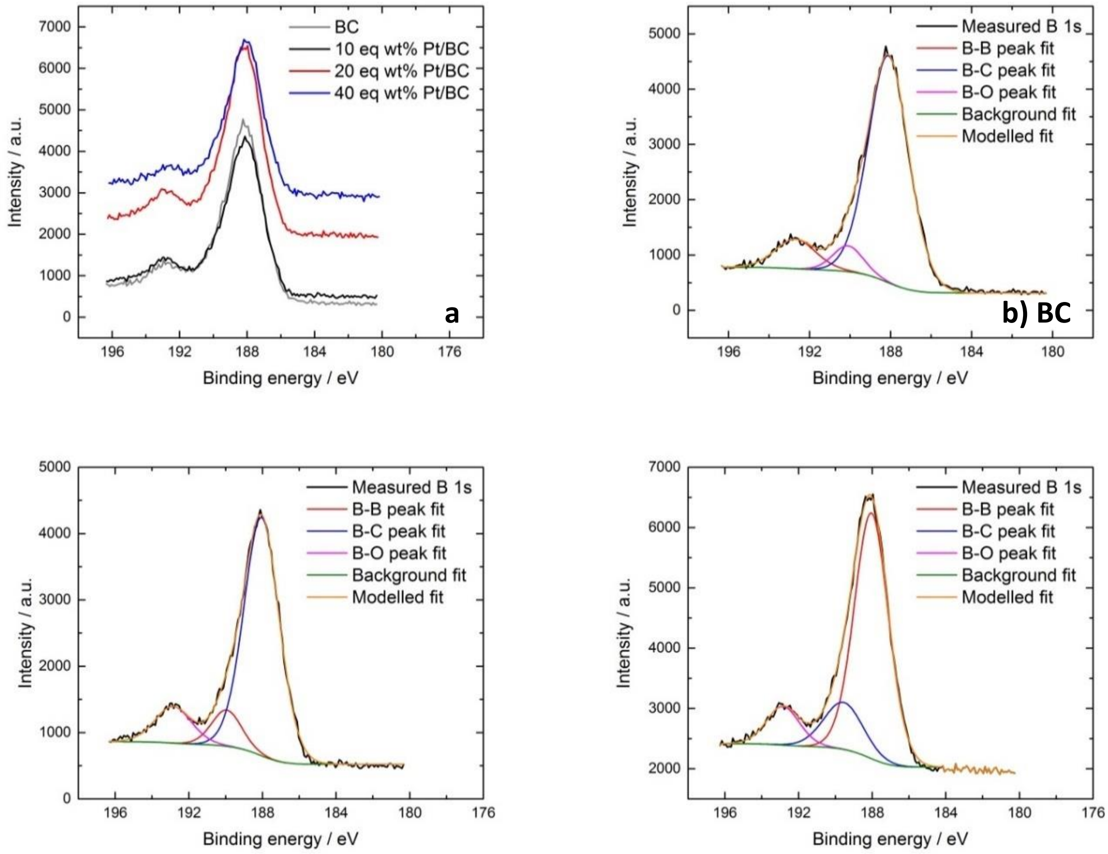

c) 10 eq wt% Pt/BC

d) 20 eq wt% Pt/BC

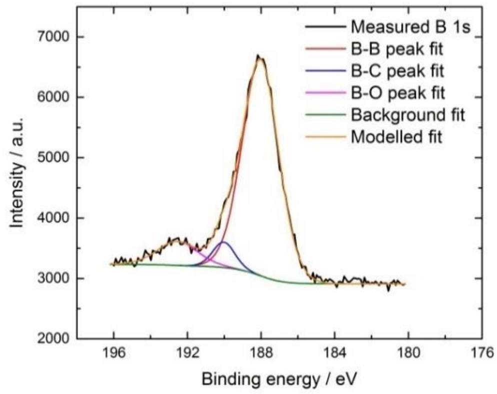

e) 40 eq wt% Pt/BC

Figure S4.2.9: XPS spectra of the (a) B 1s region of BC and Pt/BC catalysts, (b) modelled and actual B1s region of BC support material, (c) modelled and actual B1s region of 10 eq wt% Pt/BC, (d) modelled and actual B1s region of 20 eq wt% Pt/BC, (e) modelled and actual B1s region of 40 eq wt% Pt/BC.

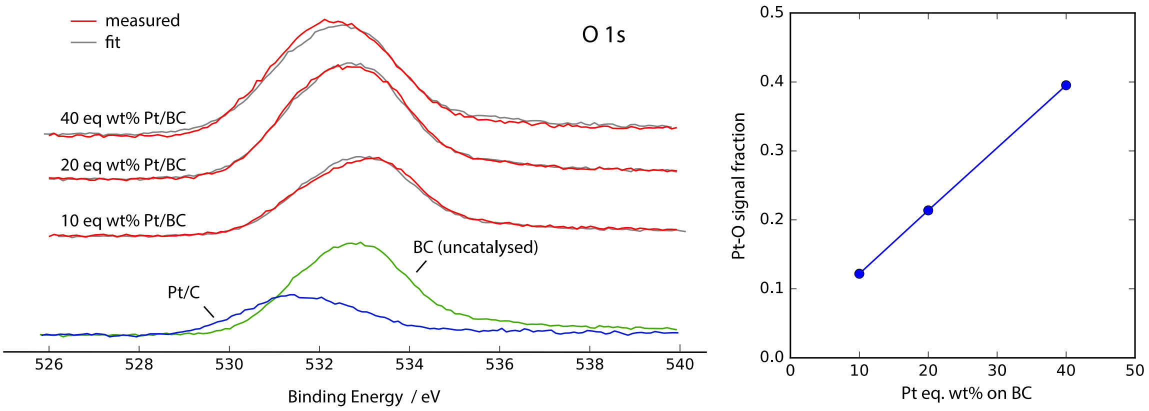

Figure S4.2.10: XPS spectra of the O 1s region of uncatalysed BC (green), 20 wt% Pt/C (blue), and 10 eq wt%, 20 eq wt%, and 40 eq wt% Pt/BC catalysts (red); the O 1s region of the BC supported catalysts can be understood as a linear combination of contributions from impurity phase B_2O and oxygen species on Pt (grey); the relative contribution from Pt-O species increases linearly with loading.

Table S4.2.1: Nominal, actual, and target catalyst loadings on C and BC supports.

Nominal wt% Pt/C	Actual wt% Pt/C	Target wt% Pt/BC	Actual wt% Pt/BC
10	9.19	3.05	2.76
20	17.5	6.19	6.86
40	37.85	15.93	12.74

Table S4.2.2: C 1s chemical shift calculated from DFT.

Supercell	# atoms	k-point mesh	Chemical shift Δ / eV
1x1x1	15	6x6x6	2.18
2x2x2	120	3x3x3	2.28
3x3x3	405	Γ only	2.32

Table S4.2.3: Literature ORR activity of comparable commercial Pt/C catalysts; temperature correction [60] with 10 kJ/mol activation energy; a limiting current j_{lim} of 6 mA.cm$^{-2}_{\text{geo}}$ was used to compensate for O$_2$ mass transport corrections applied in the literature according to $1/j_s = 1/j_k + 1/j_{\text{lim}}$; data used for comparison in Figure 4.2.6 is highlighted; in 0.1 M HClO$_4$ recorded at 20 mV.s^{-1} and 1600 rpm.

Catalyst	L_{Pt} / µg.cm$^{-2}_{\text{geo}}$	ECSA / m^2.g$^{-1}_{\text{Pt}}$	j_k(30 °C) / µA.cm$^{-2}_{\text{Pt}}$	j_k(25 °C) / µA.cm$^{-2}_{\text{Pt}}$	j_s(25 °C) / µA.cm$^{-2}_{\text{Pt}}$	Comment
40% Pt/VC (JM)	**20**	**49**	**538**	**500**	**268**	**Rotational drying; Ref. [45]**
40% Pt/VC (JM)	**20**	**49**	**284**	**264**	**181**	**Stationary drying; Ref. [45]**
19.7% Pt/VC (E-TEK)	**22**	**61**	**511**	**475**	**223**	**Rotational drying; Ref. [45]**
19.7% Pt/VC (E-TEK)	**22**	**55**	**333**	**310**	**186**	**Stationary drying; Ref. [45]**
20% Pt/Vulcan	**20**	**61**	**347**	**323**	**190**	**Good film; Ref. [44]**
20% Pt/Vulcan	**14.3**	**66**	**305**	**284**	**193**	**Good film; Ref. [44]**
20% Pt/Vulcan	20	57	272	253	168	Intermediate film; Ref. [44]
20% Pt/Vulcan	20	42	230	214	163	Bad film; Ref. [44]

Chapter 5

5.1 Investigation into the Influence of Metal-Support Interaction between Pt and a Boron Carbide-Graphite Composite Material on the Ion Adsorption

---

Abstract

This study was an investigation into the influence of strong metal-support interactions on the adsorption properties of a Pt catalyst supported on a boron carbide-graphite composite material. The potential of total zero charge (ptzc) and $ECSA_{HUPD}/ECSA_{CO}$, with a CO bulk oxidation baseline, for the Pt/BC and Pt/C catalysts were similar to one another. The CO displacement charge gradient displayed a clear increase in the charge density of both anions (<ptzc) and cations (>ptzc) on the Pt/BC catalysts when compared to Pt/C, at potentials close to the ptzc. This increase in charge density was Pt loading dependent, with the largest charge displacement gradient reported on the 40 eq wt% Pt/BC catalyst. Although not well understood, these results give an indication of the electronic interaction between platinum and the boron carbide-graphite composite support and the differences in electrosorption on the Pt supported nanoparticles compared to Pt/C.

5.1.1 Introduction

In the 1960s, boron carbide was first investigated as a support for the phosphoric and alkaline fuel cells. Grubb & McKee [1] investigated Pt/B_4C catalysts for the anode of the phosphoric acid fuel cell and recognised that this catalyst showed better stability and mass activity to Pt/C and Pt/graphite catalysts. This was attributed to stability and a support promotional effect [1]. However, this promotional effect was conjecture and not studied in the paper.

More recently, Lv *et al.* [2] studied the catalytic activity of Pt/B_4C for the Oxygen Reduction Reaction (ORR). Platinum was deposited on nano-B_4C catalysts via ethylene glycol reduction method. The reported ECSA was 88 $m^2.g^{-1}$ compared to Pt/C's 62 $m^2.g^{-1}$, this higher ECSA was attributed to fast hydroxyl adsorption and high OH_{ad} coverage occurring during the hydrogen desorption process [2]. The ORR intrinsic activity was similar to that of Pt/C. Moreover, these catalysts were investigated for methanol oxidation activity and CO tolerance in acidic media. The methanol oxidation activity was reported to increase by nearly two-fold on the Pt/B_4C catalysts, due to a marked increase in CO tolerance [2]. This research too, however, did not provide detailed fundamental investigations into metal-support interactions to support their findings.

The research was continued in the same group, by Mu *et al.* [3] which focused on nano-size boron carbide intercalated graphene as high-performance catalyst supports and electrodes for PEM fuel cells. The boron carbide support material was stabilised by modulating 2D graphene sheets. The strong restriction effect of nano-ceramics in graphene interlayers was reported to improve the usage and electrochemical stability of Pt catalysts. The graphene/B_4C supported Pt catalyst (Pt-RGO/B_4C) presented an enhanced electrochemical surface area of 121 $m^2.g^{-1}_{Pt}$, twice that of Pt/C and an ORR mass activity (185 $A.g^{-1}_{Pt}$) which was 2.9 times higher than Pt/C towards ORR. Additionally, after the accelerated durability test for 10000 cycles, the Pt-RGO/B_4C catalyst retained 45.2% initial electrochemical surface area, while the Pt/RGO and Pt/C retained 29.7 and 23.4%, respectively [3].

In our previous works [4] (Chapter 4.2), the strong metal-support interaction of Pt supported on a boron carbide-graphite composite (Pt/BC) was investigated by X-ray photoelectron spectroscopy (XPS), extended X-ray absorption fine structure (EXAFS) and density functional theory (DFT). These Pt/BC catalysts demonstrated a 50% increase in surface area specific ORR activity and a 20% increase in catalyst stability after 6000 cycles, seen through accelerated durability studies, when compared to commercial Pt/C. This enhanced activity and stability was attributed to an electronic interaction, supported by XPS spectra, between platinum and the BC support.

In this chapter, the role of strong metal-support interactions on species adsorption to the platinum surface is investigated in an acidic media. Hydrogen and CO adsorption were investigated using cyclic voltammograms, CO stripping voltammetry and CO displacement techniques.

5.1.2 Experimental

Catalyst Preparation, Physical and Electrochemical Characterisation: Catalysts were prepared and characterised as described in Chapter 4.

Electrochemical Characterisation: A catalyst ink was prepared for the electrochemical characterisation techniques. The Pt/BC and BC catalyst ink consisted of 2.5 mg of the catalyst, 0.5 ml of ethanol (Sigma Aldrich) and 25 µL of 5 wt% Nafion solution. The mixture was sonicated for 30 minutes and 5 µL was placed on a glassy carbon electrode. The Pt/C and Vulcan catalyst ink consisted of 5 mg of the catalyst, 5 ml of water (Milli-Q 18.2 MΩ.cm), 1.5 ml isopropanol (Kimix) and 25 µL of 5 wt% Nafion solution. The mixture was sonicated for 30 minutes and 10 µL was placed on a glassy carbon electrode. This resulted in a Pt loading of 6.9 x10^{-7}, 1.7 x10^{-6} and 3.2 x10^{-6} g on the glassy carbon electrode for the 10, 20 and 40 eq wt% Pt/BC catalysts, respectively, and 7.7 x10^{-7}, 1.6 x10^{-6} and 3.1 x10^{-6} g for the 10, 20 and 40 wt% Pt/C catalysts, respectively. Prior to this the glassy carbon electrode was polished to a mirror finish using 0.1 and 0.05 µm Al_2O_3 polish (Buehler). Cyclic voltammetry was conducted by cycling the potential between 0.05 – 1.2 V vs. RHE with a scan rate of 50 mV.s^{-1} for 50 cycles at room temperature in an oxygen-free 0.1 M $HClO_4$ electrolyte (70% Suprapur - Merck) solution to electrochemically clean the catalyst surface. The reference electrode used was $Hg/HgSO_4$ with a platinum counter electrode. The scan rate was then changed to 20 mV.s^{-1} for 2 cycles and the potential cycled between 0.05 – 1.2 V vs RHE at room temperature in an oxygen-free 0.1 M $HClO_4$ electrolyte solution. These scans were used to determine the H_{UPD} surface area. CO stripping was conducted by purging the electrolyte solution with CO for 20 minutes while holding the potential at 0.1 V vs. RHE, argon was then bubbled for 20 minutes to rid the solution of CO, after which the potential was cycled between 0.05 – 1.2 V vs RHE. These scans were used to determine the ECSA from CO stripping voltammetry. CO displacement was conducted in a 0.1 M $HClO_4$ electrolyte at room temperature in an argon saturated electrolyte. The potential of the working electrode is held for 2 minutes, thereafter CO is introduced into the electrolyte and the transient current response over time is recorded. A baseline is then assumed from the argon saturated solution current before CO displacement, and the areas under the oxidative and reductive peaks are measured.

5.1.3 Results

5.1.3.1 Hydrogen and Carbon Monoxide Absorption

Figure 5.1.1 reports the $ECSA_{HUPD}/ECSA_{CO}$ ratios for each loading on the Pt/C and Pt/BC catalysts. Figure 5.1.1a displays the $ECSA_{HUPD}/ECSA_{CO}$ ratios versus the actual loading on the catalysts, where $ECSA_{HUPD}$ is measured via a straight baseline from the double layer region. This plot shows significant deviation between the Pt/C and Pt/BC catalysts. Figure 5.1.1b displays the $ECSA_{HUPD}/ECSA_{CO}$ ratios versus the equivalent loadings, where $ECSA_{HUPD}$ is measured via a CO poisoned cyclic voltammogram. The $ECSA_{HUPD}/ECSA_{CO}$ ratios in Figure 5.1.1b are similar for the Pt/C and Pt/BC catalysts, with the exception of the 10 eq wt% Pt/BC and 10 wt% Pt/C.

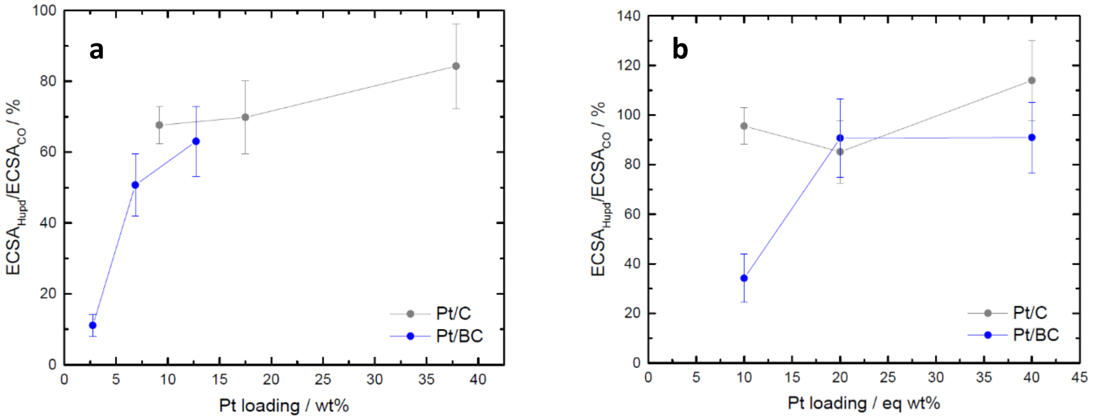

Figure 5.1.1: (a) ratio of ECSA calculation via H_{UPD} to ECSA calculated via CO stripping for 10, 20 and 40 wt% Pt/C and 10, 20, 40 eq wt% Pt/BC and (b) the corrected H_{UPD} for support contribution to double layer.

5.1.3.2 Potential of Total Zero Charge

Table 5.1.1 states the particle sizes, potential of total zero charge (ptzc) measured from CO displacement, and the charge displacement gradients (Figure 5.1.2) for the Pt/C and Pt/BC catalysts. The ptzc's for the Pt/C and Pt/BC catalysts are comparable. The charge displacement gradients on the Pt/C catalysts are similar to one another, while the charge displacement gradients are significantly larger on the Pt/BC catalysts and increase with Pt loading.

Table 5.1.1: Particle size, potential of total zero charge calculated from CO displacement and charge displacement gradient of the Pt disc, Pt/C and Pt/BC catalysts.

Catalyst	Particle Size / nm	Potential of Total Zero Charge / V vs. RHE	Charge Displacement Gradient / mC.m$^{-2}_{Pt}$.V^{-1}
Pt disc electrode	-	0.291	-0.122
10 wt% Pt/C	1.1 ± 0.3	0.235	-4300
20 wt% Pt/C	2.1 ± 0.5	0.259	-4720
40 wt% Pt/C	2.7 ± 0.7	0.263	-4310
10 eq wt% Pt/BC	2.9 ± 0.9	0.241	-3690
20 eq wt% Pt/BC	2.3 ± 0.7	0.250	-7460
40 eq wt% Pt/BC	2.6 ± 0.6	0.266	-19570

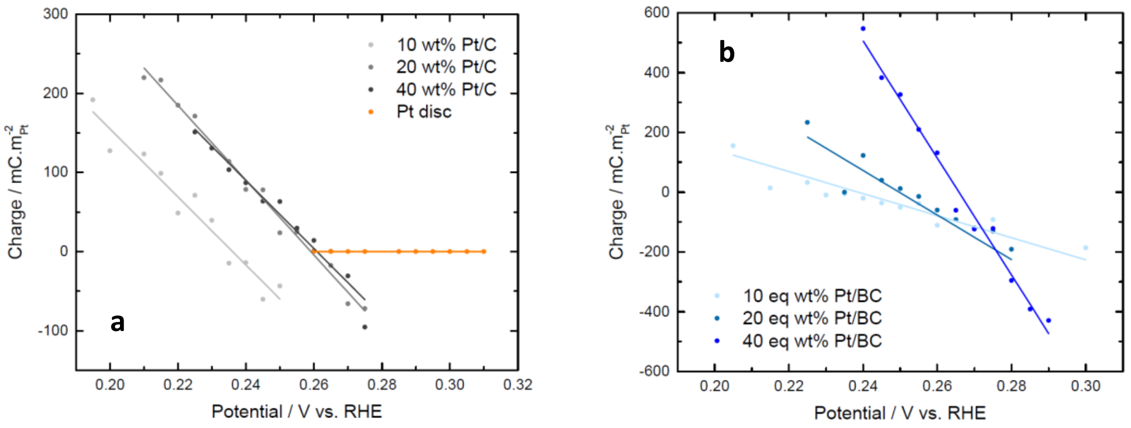

Figure 5.1.2: the CO displacement charge density curves for (a) Pt disc electrode, 10, 20 and 40 wt% Pt/C catalysts and (b) 10, 20, 40 eq wt% Pt/BC catalysts.

5.1.4 Discussion

5.1.4.1 ECSA Ratios

Investigations into the hydrogen adsorption and carbon monoxide adsorption onto the surface of a Pt catalyst gives further insight into charging effects occurring on the surface, and subsequently the effect of the support on the Pt surface charge and interaction with adsorbates. Mayrhofer *et al.* [5] investigated the relationship between ECSA calculated from H_{UPD} region and CO stripping voltammetry for particle sizes of 1, 2 and 5 nm. The $ECSA_{HUPD}/ECSA_{CO}$ for 1, 2 and 5 nm particle sizes were measured to be 0.71, 0.80 and 0.91 respectively. Assuming a logarithmic trend in $ECSA_{HUPD}/ECSA_{CO}$ vs. particle size and the values reported [5], the 10, 20 and 40 wt% Pt/C $ECSA_{HUPD}/ECSA_{CO}$ ratios for these particle sizes (Table 5.1.1) should theoretically show 0.73, 0.80 and 0.83, respectively. This calculation is in reasonable agreement with the measured 10, 20 and 40 wt% Pt/C catalyst $ECSA_{HUPD}/ECSA_{CO}$ ratios of 0.67, 0.70 and 0.84, respectively. The relationship between particle size and $ECSA_{HUPD}/ECSA_{CO}$ was explained by the differences in adsorption sites for hydrogen and CO. Hydrogen adsorbs onto hollow-three-fold sites, where the frequency of sites is particle size dependent and less frequent for smaller particle sizes, while CO adsorbs on a-top sites, were the site frequency is not size dependent [6].

The theoretical $ECSA_{HUPD}/ECSA_{CO}$ ratios based on Pt particle size for the 10, 20 and 40 eq wt% Pt/BC are calculated to be 0.84, 0.81 and 0.82, respectively, these are divergent to the measured values shown in Figure 5.1.1a, of 0.11, 0.51 and 0.63, respectively. As stated by Mayrhofer *et al.* [5], the determination of ECSA via H_{UPD} contains significant systematic errors, since this technique does not take into consideration the significant influence of the support capacitance on the H_{UPD} region. Furthermore, the contribution of the catalyst support is not constant over this potential range, resulting in an underestimation of the catalyst ECSA when measured by the H_{UPD} region. Therefore, Figure 5.1.1b shows the corrected H_{UPD} region after support capacitance is accurately measured by using the CO bulk oxidation cyclic voltammograms as the baseline for the H_{UPD} region.

Figure 5.1.1a was plotted as $ECSA_{HUPD}/ECSA_{CO}$ versus actual Pt loadings for Pt/BC since platinum loading significantly effects the capacitance contribution from the catalyst support material [7,8]. As platinum loading is decreased, the support contribution in the H_{UPD} is increased which leads to an underestimation in $ECSA_{HUPD}$ [7,8]. Once the support contribution to H_{UPD} was accurately determined, the ECSA calculated from H_{UPD} follows that of $ECSA_{CO}$, with the exception of 10 eq wt% Pt/BC. It is assumed the large discrepancy associated with $ECSA_{HUPD}$ on the 10 eq wt% Pt/BC is due to the small H_{UPD} region and the subsequent difficulty in determining this area accurately. After the support capacitance correction, little difference is shown in this $ECSA_{HUPD}/ECSA_{CO}$ ratio, leading to the assertion that this technique is insufficiently sensitive to investigate differences in adsorbates on a platinum surface due to metal-support interactions. Moreover, work by Schmies *et al.* [9] demonstrates that the $ECSA_{HUPD}/ECSA_{CO}$ ratio is more complicated when a strong metal support interaction is present and influences adsorption in an inconsistent manner.

5.1.4.2 CO Displacement

The influence of the adsorption process at the metal-electrolyte interface on the potential of zero charge (pzc) was first presented by Frumkin & Petrii [10]. This study described the total charge at the metal-electrolyte interface as the free charge related to the adsorbed monopoles and the charge associated to the chemical bond formation. Thus, potential of zero charge can be described as the sum of the potential of zero free charge (pzfc) and the potential of total zero charge (ptzc). The potential of zero free charge of an electrode is directly related to its work function [11]. However, the experimentally measurable parameter is the ptzc, the point at which the free electronic excess charge density plus the charge density transferred during adsorption processes equals zero. This technique is not used to gain absolute values for ptzc but rather when conducted under the same conditions, changes and trends in surface properties of various Pt-electrodes can be evaluated [11].

Climent *et al.* [12] described CO displacement as a method for determining the potential of total zero charge (ptzc). Due to the strong adsorption of CO to the platinum surface, this neutral molecule displaces weakly adsorbed anions and cations completely from the surface. Additionally, CO adsorption on the surface results in a zero net charge passing through the interface, therefore the subsequent transient charge is a result of the initially adsorbed species. Thus, the potential at which a charge density curve plotted against displacement potential crosses zero is considered to be ptzc, if it is assumed that no other reactions take place and the remaining charge density on the surface can be neglected. Using the CO displacement method to determine ptzc, Table 5.1.1 reports ptzc determined from the CO displacement curves in Figure 5.1.2. Potential of total zero charge is closely related to the particle size of Pt nanoparticles, as described by Mayrhofer *et al.* [11], the ptzc is proportional to the Pt particle size in the 1 – 30 nm particle size range. The values reported in Table 5.1.1 are in accordance with those reported by Mayrhofer *et al.* [11] for these particle sizes.

There are notable changes to the gradient of charge density curves normalised for platinum surface area versus potential for the different catalysts, displayed in Figure 5.1.2. The gradient shown in Figure 5.1.2a for CO displacement on the Pt disc electrode is gentle, with very little change in charge displacement as a function of potential, compared to the Pt/C catalysts displayed in this figure. The charge displacement gradient is identical on the 10, 20 and 40 wt% Pt/C catalysts, while steeper gradient is appreciated on the Pt/C catalysts when compared to the Pt disc. This trend is an indication of the metal-electrolyte interface on the different platinum surfaces, as less adsorbates are perceived on the Pt disc electrode, whereas more adsorbates are observed on the Pt/C catalysts at lower or higher potentials than ptzc. These results suggest an influence on the Pt nanoparticles or support on the density of adsorbates on the platinum surface, which impacts the various loadings of Pt on carbon identically.

A different observation is made for the Pt/BC catalysts, as the charge displacement gradient is dependent on catalyst loading. The charge displacement gradients reported in Table 5.1.1 and represented in Figure 5.1.2b show a significant change in gradients to steeper slopes as the Pt loading is increased on the BC support. While this phenomenon cannot yet be explained in detail, it is clear that the concentration of adsorbates on the Pt surface at potentials lower and higher than the ptzc is influenced by the metal-support interaction. Trasatti and Parsons [13] reported that the change in work function of a catalyst can be correlated to changes in the potential of total zero charge at the metal-solution interface. The changes to ptzc subsequently affects the electrosorption properties of the metal catalyst, as described by Frumkin *et al.* [14]. Although no noteworthy deviations in the ptzc were appreciated between the Pt/C and Pt/BC catalysts, the electrosorption properties as seen in the charge displacement gradients (Figure 5.1.2), show significant changes to the anion and cation adsorption before and after the ptzc.

5.1.5 Conclusion

The adsorption of species on the surface of platinum nanoparticles and the possible influence of metal-support interactions on this adsorption were investigated on Pt/C and Pt/BC catalysts. The potential of total zero charge was studied by CO displacement measurements, as expected, the ptzc was strongly affected by Pt particle size, however, no deviations were seen due to a possible metal-support interaction. A less studied relationship is the charge displacement gradient over potentials around the potential of total zero charge. These findings display an independence of charge displacement gradient on Pt loading on the Pt/C catalysts, while a large dependency of charge displacement gradient on Pt loading is appreciated on the Pt/BC catalysts. It is hypothesised that changes to the pzc due to metal-support interactions on the Pt/BC was present and these changes affected the electrosorption properties on platinum nanoparticles, particularly at higher loadings.

5.1.6 References

1. Grubb, W.T. & McKee, D.W. 1966. Boron Carbide. *Nature*. 210(5032):192-194.
2. Lv, H., Peng, T., Wu, P., Pan, M. & Mu, S. 2012. *Journal of Materials Chemistry*. 22(18):9155-9160.
3. Mu, S., Chen, X., Sun, R., Liu, X., Wu, H., He, D. & Cheng, K. 2016. *Carbon*. 103:449-456.
4. Jackson, C., Smith, G.T., Inwood, D.W., Leach, A.S., Whalley, P.S., Callisti, M., Polcar, T., Russell, A.E., Levecque, P., Kramer, D. 2017. *Nature Communications*. 8:15802.
5. Mayrhofer, K.J.J., Strmcnik, D., Blizanac, B.B., Stamenkovic, V., Arenz, M. & Markovic, N.M. 2008. *Electrochimica Acta*. 53(7):3181-3188.
6. Maillard, F., Pronkin, S. & Savinova, E.R. 2010. In *Handbook of Fuel Cells.* John Wiley & Sons, Ltd.
7. Schwanitz, B., Rabis, A., Horisberger, M., Scherer, G.G. & Schmidt, T.J. 2012. *CHIMIA International Journal for Chemistry*. 66(3):110-119.
8. Fabbri, E., Taylor, S., Rabis, A., Levecque, P., Conrad, O., Kötz, R. & Schmidt, T.J. 2014. *ChemCatChem*. 6(5):1410-1418.
9. Schmies, H., Bergmann, A., Drnec, J., Wang, G., Teschner, D., Kühl, S., Sandbeck, D.J.S., Cherevko, S. Gocyla, M., Shviro, M., Heggen, M., Ramani, V., Dunin-Borkowski, R.E., Mayrhofer, K.J.J. & Strasser, P. *Advanced Energy Materials:* 701663
10. Frumkin, A.N. & Petrii, O.A. 1975. *Electrochimica Acta.* 20(5): 347-359.
11. Mayrhofer, K.J.J., Blizanac, B.B., Arenz, M., Stamenkovic, V.R., Ross, P.N. & Markovic, N.M. 2005. *The Journal of Physical Chemistry B*. 109(30):14433-14440.
12. Climent, V., Gomez, R., Orts, J. M., Rodes, A., Aldaz, A., Feliu, J. M. 1999. *Interfacial Electrochemistry: Theory: Experiment, and Applications*. New York. Taylor & Francis.
13. Trasatti, S. & Parsons, R. 1986. *Journal of Electroanalytical Chemistry and Interfacial Electrochemistry*. 205(1-2):359-376.

14. Frumkin, A.N., Petrii, O.A. & Damaskin, B.B. 1980. *Potentials of Zero Charge. In Comprehensive Treatise of Electrochemistry: The Double Layer*. J.O. Bockris, B.E. Conway & E. Yeager, Eds. Boston, MA: Springer US. 221-289.

5.2 Support Induced Charge Transfer Effects on Electrochemical Characteristics of Pt Nanoparticle Electrocatalysts

Abstract

The electrokinetic properties of Pt nanoparticles supported on Carbon (Pt/C) and Boron Carbide-Graphite composite (Pt/BC) are compared over a wide potential range. The influence of the support on the electronic state of Pt was investigated via *in-situ* X-ray Absorption Spectroscopy. Pt d-band filling, determined from XANES white line analysis, was lower and nearly constant between 0.4 and 0.95 V vs. RHE for Pt/BC, indicating more positively charged particles in the double layer region and a delay in the onset of oxide formation by about 0.2 V compared to the Pt/C catalyst, which showed a marked increase in d-band vacancies above 0.8 V vs. RHE. Moreover, $\Delta\mu$ analysis of the XANES data indicated a lack of sub-surface oxygen for the Pt/BC catalyst compared to the Pt/C catalyst above 0.9 V vs. RHE. Additional anion adsorption on the Pt/BC in the double layer region, detected by CO displacement, was also confirmed by XANES analysis of the d-band occupancy. The H_2 oxidation activities of electrodes with low catalyst loadings were assessed under high mass transport conditions using the floating electrode methodology. The metal-support interaction between the Pt and BC support improved the maximum hydrogen oxidation current density by 1.4 times when compared to Pt/C.

5.2.1 Introduction

Much current research on polymer electrolyte fuel cells (PEFC) is focused on membrane electrode assembly development since significant challenges remain in increasing kinetic activity, and stability and reducing the cost of catalysts [1]. Typically, Pt nanoparticles supported on carbon are used as catalysts in the hydrogen PEFC anode and cathode, which perform the hydrogen oxidation reaction (HOR) and the oxygen reduction reaction (ORR), respectively. However, the oxidation of the carbon support at high potentials decreases the catalyst lifetime; in addition, Pt dissolution and agglomeration decreases the electrochemically active surface area [2]. Main group carbides have shown promise as alternative support materials with improved Pt catalyst activity and durability reported [3,4].

Recently, some of us have experimentally isolated electronic metal-support interactions for Pt supported on a boron carbide-graphite composites (Pt/BC) compared to commercial Pt/C [4]. This study was carried out using rotating disc electrode (RDE) electrochemical testing, X-ray Photoelectron Spectroscopy (XPS), and X-ray Absorption Spectroscopy (XAS), supported by Density Functional Theory (DFT). The Pt loading on the support surface, particle size, shape and interparticle distances were kept constant in order to investigate electronic metal-support interactions without the effects of other influential factors. The Pt/BC catalysts demonstrated a 50% increase in surface area specific ORR activity at 0.9 V vs. RHE using a standard RDE technique [5] and a ~20% increase in catalyst durability after 6000 cycles in terms of electrochemical surface area (ECSA) retention. The enhanced activity and durability were attributed to changes in electronic metal-support interactions between platinum and the boron carbide-graphite composite support, which were supported by XPS spectra analysis and XANES.

In the study presented herein, we build on this work by further exploring the effects of varying charge transfer between the catalyst and support. The hydrogen oxidation reaction under conditions of high mass transport is used as a surface probe in the oxide region and CO displacement was used to investigate interface changes in the double layer region. The observed electrochemical characteristics are correlated to differences in the electronic state of the Pt particles determined *in-situ* using X-ray absorption spectroscopy.

Analysis of the d-band vacancies of the Pt particles as a function of the applied potential was conducted using white line analysis [6]. Additionally, the presence or absence of sub-surface oxygen was explored using the $\Delta\mu$ analysis of the X-ray absorption near edge spectra (XANES) as previously established by Adzic and co-workers [7].

Fundamental investigations of the electrocatalytic performance of catalysts for HOR and ORR are commonly carried out on RDEs. The RDE technique tends to be favoured over PEFC testing [5] as it is cost effective, uses small amounts of catalyst, and the well-defined hydrodynamic conditions and testing protocols tend to give reproducible results [8]. Whilst it is advantageous and convenient to employ the RDE technique, the extrapolation of RDE data to predict performance in PEFCs often leads to inaccurate conclusions, since factors such as oxide coverage, low reactant concentration and differences in water activity are not considered [9,10].

A ‘floating electrode’ technique recently developed by some of us [11] was tailored to incorporate the advantages of both the RDE method and PEFC measurements to enable studies under high mass transport and low catalyst loading conditions to be performed. Current densities of 600 ± 60 $mA.cm^{-2}_{Pt}$ (~5700 $mA.cm^{2}_{geo}$ at 10.15 $\mu g_{Pt}.cm^{-2}$) at peak potential for HOR at standard temperature and pressure (STP) were obtained for a commercial Pt/C catalyst. In comparison, RDE measurements for the same catalyst reached limiting current at 2.5 $mA.cm^{-2}_{geo}$. The floating electrode results are comparable to kinetic activities for HOR and ORR reported in PEFCs [11,12]. This high mass transport technique allows fundamental studies on HOR and ORR to be carried out in a facile manner, providing data that is comparable to that obtained in more complex PEFC experiments. Additionally, floating electrode studies have established that the HOR is sensitive to surface sites and adlayer morphology and, therefore, can be used as a probe into relative coverages on the platinum surface [13].

5.2.2 Experimental

Catalyst Preparation and Characterisation: The 20 wt% Pt/C catalysts used in this study were HiSPEC® 3000 commercial catalysts. The 20 eq wt% Pt/BC was prepared in house as reported previously [4]. The full physical characterisation of both catalysts were presented in that previous report and are not repeated. In short, the Pt nanoparticle shapes and particle sizes were the same, however, the electronic properties were found to depend on the nature of the support.

In-situ XAS: electrodes were prepared by formation of a catalyst ink which was then coated on to a Teflon coated carbon base layer (Alfa Aesar) and used as the working electrode in an *in-situ* XAS cell [14]. The Pt/C ink formulation consisted of 150 mg of catalyst, 4 ml ultrapure water (Milli-Q 18.2 MΩ.cm), 1 ml isopropanol (Sigma-Aldrich) and 2 ml 5 wt% Nafion. The Pt/BC ink formulation consisted of 150 mg of catalyst, 5 ml ethanol (Sigma-Aldrich) and 2 ml 5 wt% Nafion. Inks were painted on to carbon layer to give a loading of 0.5 $mg_{Pt}.cm^{-2}_{Pt}$. The catalyst coated carbon layer was then hot pressed at 170 °C and 7.8 kPa. All electrodes were flooded prior to use by vacuum filling in ultrapure water. A platinum wire was used as a counter electrode, and Hg/$HgSO_4$ was used as a reference electrode. All potentials have been corrected to RHE using a conversion of 0 V. vs. Hg/$HgSO_4$ = 0.654 V vs. RHE.

The XAS data were collected at the B18 line at the Diamond Light Source, operated with a typical ring energy of 3 GeV with a ring current of 300 mA. Data were collected at the Pt L_3 edge (11 564 eV) and Pt L_2 edge (13 277 eV) in Quick EXAFS (QEXAFS) mode using a Si(111) monochromator and using the ionisation chambers in transmission mode at 298 K. A total of three spectra were averaged for each sample at each potential. Calibration of the monochromator was carried out at both edges using Pt foils. The absorption spectra were modelled out to the fourth Pt shell with Demeter© using Ifeffit© [15] to solve the EXAFS equation.

CO displacement on RDE: CO displacement was conducted in a 0.1 M $HClO_4$ electrolyte at room temperature in an argon saturated electrolyte. The potential of the working electrode is held for 2 minutes, thereafter CO is introduced into the electrolyte and the transient current response over time is recorded. A baseline is then assumed from the argon saturated solution current before CO displacement, and the areas under the oxidative and reductive peaks are measured. A platinum counter electrode was used and the reference electrode used was Hg/$HgSO_4$, with potentials reported vs. RHE as described above. Three of the CO displacement curves are shown in Figure S5.2.3 for both catalysts.

Floating electrode studies: The catalyst layer was prepared as described by Zalitis *et al.* [11]. Porous polycarbonate track etched (PCTE) membranes (Sterlitech, PCTF0447100) with a pore size of 400 nm and a porosity of 0.125 were coated with a 100 nm gold layer by sputter deposition (Emitech K575X). These gold coated PCTE membranes were then rinsed with propan-2-ol (Sigma-Aldrich, ACS reagent) in a Soxhlet extractor for 8 hours, followed by ultra-pure water in the Soxhlet extractor for 8 hours. The commercial Pt/C (Alfa Aesar) catalyst ink consisted of 5 mg catalyst, 5 ml ultra-pure water, 1.5 ml propan-2-ol and 25 µl 5 wt% Nafion, 10 µl of this first Pt/C catalyst ink is diluted in 7.7 ml water and 2.3 ml propan-2-ol. The Pt/BC catalyst ink consisted of 2.5 mg catalyst, 0.5 ml ethanol (Sigma-Aldrich, Absolute for HPLC), and 25 µl 5 wt% Nafion, 10 µl of this first Pt/BC catalyst ink was diluted in 10 ml of ethanol. 250 µl of the diluted inks were vacuum filtrated onto 2 mm diameter spots on separate gold coated PCTEs. After deposition of the catalyst layer, a hydrophobic coating of an amorphous fluoropolymer (AF) (DuPont DeNemours, a copolymer of 2,2-bistrifluoromethyl-4,5,difluoro-

1,3-dioxile and tetrafluoroethylene with the trade name Teflon AF 2400, 2.1 $\mu g.cm^{-2}_{geo}$) dissolved in Fluorinert FC-40 (Sigma, F9755) was applied to the unmodified side of the gold coated PCTE membrane. The electrodes were then dried at 90 °C for 8 hours at 25 mbar before cleaning in ultra-pure water in the Soxhlet extractor for 8 hours. Table 5.2.1 reports the Pt loadings and roughness factors of the electrodes, where roughness factor was calculated by dividing the Pt active area, determined via CO stripping, by the area of the geometric electrode surface area, using one repeat for each catalyst.

Table 5.2.1: Roughness factor and Pt loading on the 20 eq wt% Pt/BC and 20 wt% Pt/C electrodes.

Catalyst	Roughness Factor	Pt loading / $\mu gPt.cm^{-2}_{geo}$
20 wt% Pt/C	1.2 ± 0.1	1.5 ± 0.1
20 eq wt% Pt/BC	0.75 ± 0.1	1.1 ± 0.1

Glassware for the floating electrode measurements was soaked for 8 hours in a NoChromix® solution and then boiled in water (Milli-Q, 18.2 MΩ.cm) five times before use. This cleaning procedure was repeated before each electrochemical test. The electrolytes were prepared from Suprapur® grade $HClO_4$ (Merck) and Millipore water (Milli-Q, 18.2 MΩ.cm), while the gases used were ≥ 5.8N (Air Products, BIP PLUS) utilising all stainless high purity regulators (Druva Ultra high purity).

A three electrode setup was employed with a platinum counter electrode and hydrogen reference electrode, using an AutoLab potentiostat. 1 M $HClO_4$ was used as the electrolyte to decrease the iR drop. The electrolyte was thoroughly purged with N_2 before electrochemical testing was performed and during electrochemical measurements the cell's headspace was continuously purged as diffusion through the electrolyte was considered negligible. Cyclic voltammograms were obtained from 0.05 – 1.2 V vs. RHE at 100 $mV.s^{-1}$ for 50 cycles at room temperature to electrochemically clean the catalyst surface. The scan rate was then changed to 10 $mV.s^{-1}$ for two cycles and the potential cycled between 0.05 – 1.1 V vs RHE at room temperature. The cyclic voltammograms are reported in Figure S5.2.4a.

The electrochemical surface area was measured by stripping of an adsorbed CO monolayer. CO was flowed into the cell's headspace for 5 minutes while holding the potential at 0.1 V vs. RHE, N_2 was then flowed in the headspace for 5 minutes to rid the solution of CO, after which the potential was cycled between 0.05 – 1.2 V vs RHE. The CO stripping voltammograms are reported in Figure S5.2.4b. Due to the 400 nm pore size of the gold coated PCTE, some smaller catalyst particles are lost through the membrane during vacuum filtration. As reported by Zalitis *et al.* [11], the amount of catalyst which is washed through the membrane is related to catalyst loading on the electrode. Although the amount of catalyst deposited can be determined from H_{UPD} measurements, it was found that measurements became difficult at loadings less than 5 $\mu g_{Pt}.cm^{-2}$ for commercial HiSPEC 9100 60 wt% Pt/C (Johnson Matthey Fuel Cells) catalyst due to the difficulty of establishing a reliable background. In order to estimate the loading of the platinum, they utilised a quadratic fit calibrated using the H_{UPD} on higher loading electrodes. Rather than using H_{UPD} as a measure of surface area, we have used CO-adsorption and stripping, which allows better separation from the background. In the study reported herein, we have assumed a stripping charge of 420 $mC.cm^{-2}{}_{Pt}$ for both types of catalysts.

The HOR activity was measured at a scan rate of 10 $mV.s^{-1}$ between 0.05 – 1.1 V vs RHE at room temperature and with flowing H_2 into the cell's headspace. All HOR scans were normalised for electrochemically active surface area and Ohmic drop measured by impedance spectroscopy. Impedance was completed with H_2 in the cell's headspace, at the open circuit potential (OCP) and a frequency of 10 kHz. Error margins on HOR activities were obtained from one repeat for each catalyst. A previously published kinetic model by one of us [16] was used to interpret the HOR data close to equilibrium (0 - 0.2 V vs. RHE). The fitting of the HOR curves was done for both electrodes simultaneously for each catalyst in Excel using the GDG non-linear solver with Multistart and a population of 100, using the method described by Kucernak & Zalitis [16]. The fitted and measured HOR curves are compared in Figures S5.2.5.

5.2.3 Results

5.2.3.1 *In-Situ* XAS

In-situ XANES at the Pt L_3 and L_2 – edges for the 20 eq wt% Pt/BC and 20 wt% Pt/C catalysts at each potential are shown in Figure 5.2.1, which have been presented to highlight the potential dependence of the white line at the Pt L_3 edge and variations in the post-edge features at the Pt L_2 edge. An increase in the L_3 and L_2 white line intensity as potential increased is seen for both the Pt/BC and Pt/C catalysts.

The XANES at the $L_{2,3}$ edges originate from exciting 2p core states. The L_2 edge arises from the 2p J=1/2 core states, and the L_3 X-ray absorption edge arises from the 2p J=3/2 core states, excited to vacant d-states. Comparison of the spectra for the two edges enables assessment of the d-band vacancy per Pt atom using a method described by Mansour *et al.* [6]. The d-band vacancies calculated using this method, assuming a bulk Pt d-band vacancy of 0.3 as theoretically calculated by Brown *et al.* [17], are reported in Figure 5.2.2. The d-band vacancies of the 20 wt% Pt/C catalyst increased significantly as potential increased from approximately 0.8 V vs. RHE. The d-band of the 20 eq wt% Pt/BC was less occupied at lower potentials than found for the Pt/C catalyst. However, the Pt/BC d-band occupancy is significantly less sensitive to potential than seen for Pt/C and remained unchanged until approximately 1.0 V vs. RHE.

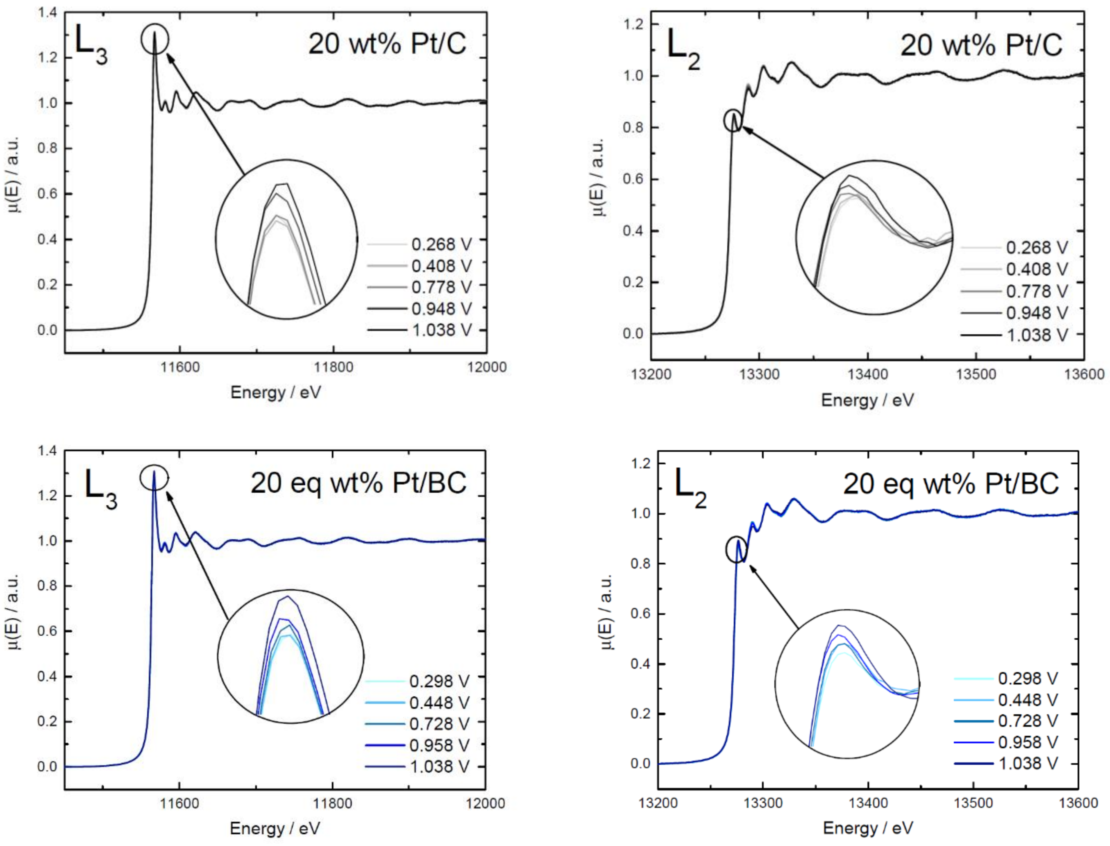

Figure 5.2.1: The X-ray adsorption spectra for the (a) Pt L_3 edge and (b) Pt L_2 edge of the 20 wt% Pt/C catalyst and (c) Pt L_3 edge and (d) Pt L_2 edge of the 20 eq wt% Pt/BC catalyst. Circles

showing the expansion of the leading peak are all performed at the same magnification. The intensity of the post edge feature (white line) increases with potential for both catalysts.

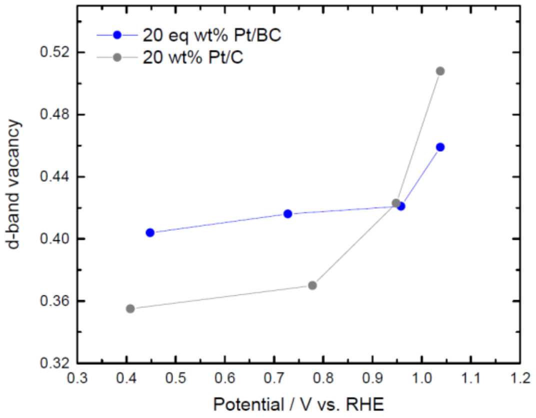

Figure 5.2.2: d-band vacancy at different potentials on the Pt/C and Pt/BC catalysts.

Subtle changes to the XANES L_3 region due to adsorbate formation and place exchange on the platinum surface can be more closely studied by the Δμ technique, which involves subtracting two XANES spectra of the same sample at different potentials from each other [7]. The subtraction of the two spectra removes the bulk metal-metal interactions if the metal-metal coordination of the particles is unchanged (implying no significant particle shape change or extensive oxide formation) over the potential range explored, and, therefore, isolates the surface changes due to adsorbates [18]. These assumptions were verified by analysis of the EXAFS data (presented in the Supplementary Information Figures S5.2.1 – 5.2.2, and Tables S5.2.1 – 5.2.2). No changes in Pt-Pt coordination numbers or Pt-Pt distances within the error in the fits were observed for the first four coordination shells over the explored potential range.

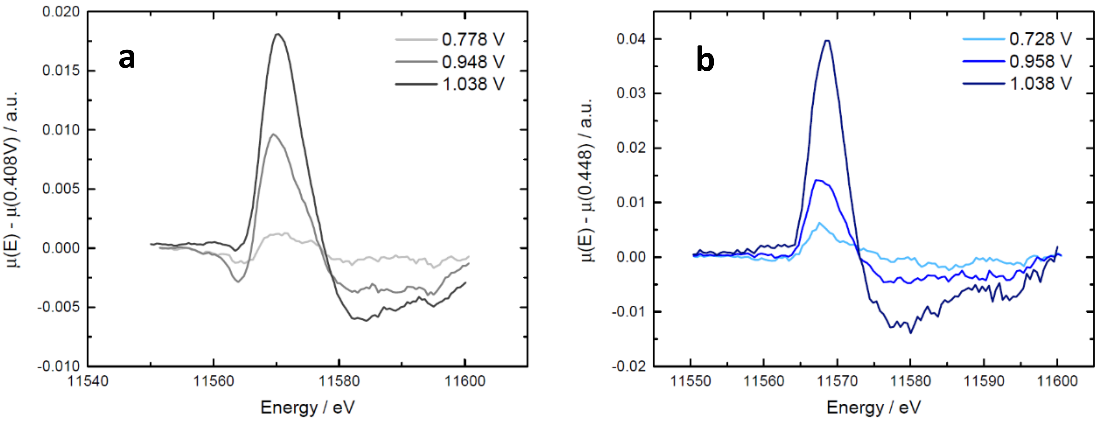

Figure 5.2.3: the calculated Δμ curves at different potentials on the (a) Pt/C and (b) Pt/BC catalysts. The reference spectrum was obtained at 0.408 V vs RHE for the Pt/C and 0.448 V vs RHE for the Pt/BC catalysts. The peak at 11570 eV in the difference spectra increases with sample potential for both catalysts.

The Δμ spectra were calculated using the spectra obtained in the double layer region as the reference, where it is assumed that the Pt surface is free of oxides, at 0.408 V and 0.448 V for the Pt/C and Pt/BC catalysts, respectively. The potential difference between the Pt/C (0.408V) and Pt/BC (0.448V) is not significant to d-band occupancy, since these are in the double layer region. Figure 5.2.3a details the Δμ(0.778), Δμ(0.948) and Δμ(1.038) curves of the Pt/C XANES spectra. The Δμ curves display a peak below the edge energy (E_0) at 11565 eV followed by a positive peak above E_0 at 11570 eV. The Δμ(0.728), Δμ(0.958) and Δμ(1.038) curves of the Pt/BC XANES spectra are shown in Figure 5.2.3b. Whilst the positive peak at energies above the edge is present in the difference spectra for both catalysts, the initial negative Δμ response, seen for Pt/C (Figure 5.2.3a), is not seen on the Pt/BC Δμ curves (Figure 5.2.3b).

5.2.3.2 CO Displacement versus Potential

CO displacement measurements were conducted over a wide potential range. There are notable changes to the gradient of the charge density curves normalised for platinum surface area versus potential for the different catalysts, displayed in Figure 5.2.4. The curves show a positive displacement charge at low potentials, attributed to the displacement of H species. At higher potentials, a negative displacement charge is observed and is understood as an indication of anion adsorption in the double layer region. The charge displacement gradient observed for Pt/BC is steeper than that for Pt/C, with a larger minimum charge of ~600 mC.m$^2_{Pt}$ compared to Pt/C (~200 mC.m$^2_{Pt}$). At potentials above ~0.5 V vs. RHE, a reduction of displacement charge is seen because of the onset of CO oxidation to CO_2. The values for the potential of total zero charge (ptzc) are 0.25 and 0.26 V vs. RHE on the Pt/BC and Pt/C catalysts, respectively.

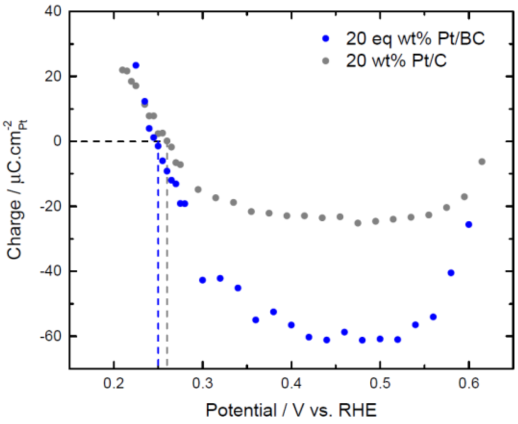

Figure 5.2.4: the CO displacement charge density curves for the 20 wt% Pt/C and 20 eq wt% Pt/BC catalysts. The vertical dashed lines indicated the potential of total zero charge (ptzc).

5.2.3.3 Hydrogen Oxidation Reaction under High Mass Transport Conditions

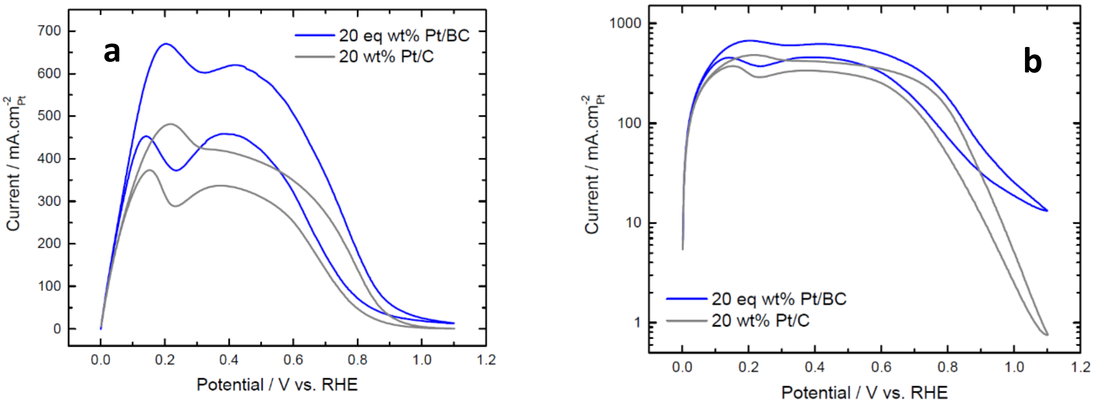

Figure 5.2.5: (a) Plots of H_2 oxidation on 20 eq wt% Pt/BC and 20 wt% Pt/C catalysts in a 1 M $HClO_4$ electrolyte solution at room temperature and a scan rate of 10 mV.s^{-1} and (b) the corresponding logarithmic. Catalyst loadings were 1.5 ± 0.1 µgPt.cm$^{-2}_{geo}$ and 1.1 ± 0.1 µgPt.cm$^{-2}_{geo}$ for Pt/C and Pt/BC, respectively.

Table 5.2.2: Maximum hydrogen oxidation activities for the 20 eq wt% Pt/BC and 20 wt% Pt/C catalysts.

Catalyst	Mass Activity ($A.mg^{-1}_{Pt}$)	Surface Area Specific Activity ($mA.cm^{-2}_{Pt}$)
20 wt% Pt/C	380 ± 18	459 ± 22
20 eq wt% Pt/BC	437 ± 16	646 ± 24

The HOR was studied on the 20 wt% Pt/C and 20 eq wt% Pt/BC catalysts under high mass transport and low catalyst loading conditions. Figure 5.2.5 shows the surface area specific HOR activity, normalised by using the ECSA obtained from the CO stripping measurements. Starting from equilibrium at 0 V vs. RHE, the Faradaic current first increases, then passes through maxima, and finally decreases at high potential. Peaks observed in Figure 5.2.5a between 0.20 – 0.42 V vs. RHE have previously been ascribed to different Pt sites [19], followed by an asymptotic decrease at potential above 0.42 V vs. RHE. Additionally, a hysteresis occurs between the forward and reverse scans. Table 5.2.2 reports the mass specific and surface area specific current densities for these catalysts. A maximum surface area specific current density of 646 ± 24 $mA.cm^{-2}_{Pt}$ is obtained on the Pt/BC catalyst, which is approximately 1.4 times that obtained on the Pt/C catalyst at 459 ± 22 $mA.cm^{-2}_{Pt}$ although somewhat less than that obtained on HiSpec 9100 60 wt% Pt/C catalyst (ca. 650 $mA.cm^{2}$) [11].

5.2.4 Discussion

5.2.4.1 Catalyst State of Charge at Intermediate Potentials

The d-band vacancy over a wide potential range is reported in Figure 5.2.2. Firstly, the d-band vacancy of the commercial Pt/C catalyst follows that reported by Mukerjee and co-workers [20,21] for similar catalysts. The d-band vacancy of the Pt/C catalyst increases slightly between 0.4 and 0.8 V vs RHE. This increase in d-band vacancy is attributed to an increasing amount of OH_{ads} species and anion adsorption on the surface of Pt [20,21]. A significantly more vacant d-band is calculated for the Pt/BC catalyst in the double layer region compared to Pt/C. This indicates more positively charged Pt particles at a given potential in the potential range between about 0.4 to 0.8 V vs RHE for Pt/BC. We have argued previously [4] that a lower work function of the boron carbide support should result in a decrease in the potential of zero charge (pzc) of the Pt/BC catalyst when compared to Pt/C [4]. This is tentatively understood to imply additional anion adsorption as well. CO displacement, as described by Climent *et al.* [22], is a method for determining the potential of total zero charge (ptzc) on a platinum surface. CO displaces weakly adsorbed anions and cations completely from the surface, due to the strong adsorption of CO onto Pt. It is assumed that CO adsorption on the surface results in a zero-net charge passing through the interface. The subsequent transient charge, therefore, is a result of displacement of the initially adsorbed anion and cation species. The displacement charge is zero at the ptzc, assuming that no other reactions take place and the remaining charge on the surface after CO adsorption can be neglected. Therefore, the CO displacement charge on the catalysts at potentials above the ptzc is largely attributed to the displacement of anions. Figure 5.2.4 confirms the assertions from d-band vacancy of a larger coverage of anions on the surface of Pt/BC compared to Pt/C in the double layer potential region (0.4 – 0.5 V vs. RHE). The displacement charge is almost 3x larger on Pt/BC and corresponds to roughly $\frac{1}{3}e^{-}$ per surface Pt. This indicates a very substantial coverage given the size of likely anions (ClO^{-}_4 from the electrolyte and SO_3^- from the ionomer). CO displacement, therefore, confirms the conclusion reached from XANES that Pt/BC is more positively charged at intermediate potentials with stronger anion adsorption approaching full coverage.

5.2.4.2 Surface Oxidation at High Potentials

The Pt d-band vacancy at higher potentials change more strongly as the adsorbed OH_{ads} anions are replaced by more strongly adsorbing oxygen. This strongly adsorbing oxygen leads to a non-linear increase in d-band vacancy at higher potentials as seen in Figure 5.2.2. This is seen for both catalysts. The delay of about 0.2 V seen for Pt/BC, however, indicates a lower tendency of Pt to oxidise if supported on BC relative to being supported on C.

Similarly to the Pt/C curves in Figure 5.2.3a, the Pt/BC Δμ curves shown in Figure 5.2.3b have a positive peak which is attributed to O or OH adsorbates on the Pt surface. The positive peak generally increases with increasing potential and is attributed to an increased coverage with oxygen species at the surface on both catalysts [7]. The Δμ technique also showed an initial negative response on the Pt/C curves. This feature has previously been correlated with sub-surface oxygen due to platinum place-exchange [18,23]. Sasaki *et al.* [7] confirmed this relationship between the negative peak in XAS and sub-surface oxygen by X-ray Diffraction (XRD) analysis. The absence of the negative peak for Pt/BC is noteworthy and ascribed to a smaller tendency to form sub-surface oxygen on the Pt/BC catalyst, broadly in agreement with the lower tendency of Pt to oxidise on BC, which might indicate less strongly bound oxygen on the Pt nanoparticles when supported on the boron carbide-graphite composite.

5.2.4.3 HOR at Low Potentials

The HOR results shown in Figure 5.2.5 are in agreement with previous studies of HOR on a Pt/C catalyst under high mass transport and low catalyst loading conditions [11,12]. Zaliltis *et al.* [24] thoroughly investigated the HOR current density behaviour and underlying causes under different experimental conditions; this was followed up by a study utilising theoretical modelling yielding further insights [16]. Parameters such as electrolyte, electrolyte concentration, roughness factors, gas partial pressures, temperature and scan limits were investigated for the influence on hydrogen oxidation and oxygen reduction reactions, obtaining a maximum surface area specific current density of 600 ± 60 $\text{mA.cm}^{-2}{}_{\text{Pt}}$ for a commercial 60 wt% Pt/C catalyst. In those studies, it was proposed that the two peaks are correlated to reactivity at two different surface sites, edges or Pt atoms with low coordination numbers (low potential peak) and facets (higher potential peak) [24]. The initial current density drop after the higher potential peak was attributed to anion adsorption impeding the HOR. This hindrance of the reaction is expected to be most influential at potentials between the potential of total zero charge (ptzc) and ~0.8 V vs. RHE, where adsorbed anions are displaced by more strongly adsorbed oxides further impeding the HOR [24].

Noteworthy differences in absolute HOR activity are observed across the entire potential range. Figure 5.2.5 and Table 5.2.2 show that the maximum surface area specific current densities are approximately 1.4 times larger on the 20 eq wt% Pt/BC catalyst when compared to the 20 wt% Pt/C catalyst.

$$H_{2,surf} + 2S \leftrightarrows 2S - H_{ad} \qquad (k_{ad}/k_{des}) \quad \text{Tafel} \qquad \text{Equation 5.2.1}$$

$$2S - H_{ad} \leftrightarrows 2S + 2H^{+} + 2e^{-} \qquad (k_{2}^{eq}/k_{-2}^{eq}) \quad \text{Volmer} \qquad \text{Equation 5.2.2}$$

Table 5.2.3: Rate constants of the Tafel and Volmer steps for hydrogen oxidation on 20 wt% Pt/C and 20 eq wt% Pt/BC. The molecular symmetry factor, β, is assumed to be ½.

Catalyst	H adsorption $\boldsymbol{k_{ad}}$ / $\times\mathbf{10^{-6}}$ mol.cm^{-2}.s^{-1}	H desorption $\boldsymbol{k_{des}}$ / $\times\mathbf{10^{-6}}$ mol.cm^{-2}.s^{-1}	H oxidation $\boldsymbol{k_2^{eq}}$ / $\times\mathbf{10^{-6}}$ mol.cm^{-2}.s^{-1}	H reduction $\boldsymbol{k_{-2}^{eq}}$ / $\times\mathbf{10^{-6}}$ mol.cm^{-2}.s^{-1}
20 wt% Pt/C	2.44	4.96	5.45	3.82
20 eq wt% Pt/BC	3.65	9.57	4.71	2.91

The HOR data in the potential range 0 - 0.2 V vs. RHE (i.e. below the ptzc, where anion adsorption is expected to be negligible) was fitted using the theoretical model derived by Kucernak and Zalitis [16] to gain further insights. The Tafel and Volmer steps (described in Equations 5.2.1 and 5.2.2, respectively) were fitted to determine the rate constants of each reaction step. Table 5.2.3 includes the rate constants determined at the equilibrium potential, where k_{ad} and k_{des} are associated with the forward and reverse Tafel steps, respectively, and k_2^{eq} and k_{-2}^{eq} are associated with the forward and reverse Volmer steps, respectively. The fitting of k_{des} contained a high degree of uncertainty since the hydrogen evolution potential region was not measured. However, this parameter was assumed to be less relevant at positive potentials and is, therefore, not included in the analysis of the data, all parameters are included in Table S5.2.3. Table 5.2.3 shows the adsorption of hydrogen to be rate limiting above the ptzc for both the Pt/C and Pt/BC catalysts. However, the hydrogen adsorption rate constant on Pt/BC is determined to be approximately 1.5 times faster than on Pt/C, indicating that the observed higher HOR activity on Pt/BC is due to a more facile Tafel step.

This is broadly in agreement with theoretical work by Nørskov [25]. Modelling by Nørskov [25] found the Pt-H adsorption state to be the highest energy state (ΔG_{H*} = +0.03 eV) at high coverages of Pt(111) fcc sites. Therefore, the adsorption of hydrogen (Tafel step) is expected to be the rate limiting step of the hydrogen oxidation reaction at high H coverages. Changes in the d-band filling (and therefore d-band centre relative to the Fermi level) are suggested to have consequences for covalently stabilised reaction intermediates following Nørskov's d-band theory [26], although electrostatics and other effects should also be considered [27]. In any case, the faster rate of adsorption of H_{ad} at equilibrium suggests a decrease in the Pt-H energy state on the Pt/BC catalysts due to electronic metal-support interactions.

However, the work of Nørskov [25] also indicated that H is more strongly adsorbed at low H coverage, which could indicate a change in the rate limiting step above ptzc. Thus, more work is needed to fully understand the HOR characteristics above the ptzc. Interestingly, the 20 wt% Pt/C and 20 eq wt% Pt/BC catalysts demonstrate qualitatively the same HOR behaviour, with a loss in current density from 0.42 – 0.8 V vs. RHE of approximately 70% on both catalysts. As this has previously been attributed to anion adsorption blocking Pt sites for HOR, it is not immediately clear why the relative loss in HOR activity seems to be largely insensitive to the larger anion coverage on Pt/BC that we inferred from CO displacement. The anion adsorption in this potential range include SO_3^- groups, present due to the Nafion on the electrode, and ClO_4^- in the electrolyte. There is the possibility of specifically adsorbed anions carrying different charge on the surface of Pt/C than on Pt/BC, which introduces some uncertainty for the interpretation of CO displacement charges. At the same time, changes in the catalyst state of charge can be expected to not only influence the binding energy of charged adsorbates due to electrostatics, but will also bear consequences for reaction intermediates as discussed above. It is, therefore, not immediately clear how these competing effects affect overall activity. Further work is, therefore, needed to disentangle contributions from anion adsorption and reaction intermediates to overall HOR activity between the ptzc and the oxide region.

5.2.4.4 HOR at High Potentials

Turning to potentials above 0.8 V vs. RHE, the HOR is adversely impacted by oxide species at both Pt/C and Pt/BC. The Pt/BC catalyst, however, shows a better retention of HOR activity, leading to an order of magnitude higher HOR current at 1.1 V vs RHE compared to Pt/C, as clearly shown in Figure 5.2.5. The HOR improvement at 1.1 V vs. RHE on the 20 eq wt% Pt/BC is reportedly due to less oxide formation at these potentials, and thus more free Pt sites for hydrogen oxidation to occur [16]. This is in agreement with the observed trends in d-band vacancies on the 20 eq wt% Pt/BC shown in Figure 5.2.2, which also suggested less oxide formation or strongly bonded oxygen species at high potentials.

5.2.5 Conclusion

The influence of charge transfer due to electronic metal-support interactions on electrochemical characteristics of supported Pt nanoparticles was investigated over a wide range of potentials. *In-Situ* X-ray Absorption Spectroscopy demonstrated significantly different responses to potential changes and adsorbates on Pt/BC when compared to Pt/C catalysts. The d-band vacancy of the Pt/BC catalyst in the double layer region is larger than that of the Pt/C catalyst; this was correlated with increased anion adsorption at potentials positive of the ptzc. Additionally, a 0.2 V delay in oxide formation on the Pt/BC compared to Pt/C was observed.

The Δμ technique, employed to analyse the XAS spectra, enhanced the sensitivity of the spectra to enable detection of -OH adsorption on the Pt surface, and the subsequent vulnerability of the Pt nanoparticles when supported on carbon to disruption by the presence of sub-surface oxygen. This sub-surface oxygen was not detected on the Pt/BC catalysts, suggesting a platinum surface that is more stable when supported on the boron carbide-graphite composite support material.

The Hydrogen Oxidation Reaction (HOR) studies under high mass transport and low catalyst loading conditions showed enhanced activity on the Pt/BC catalyst, when compared to the Pt/C catalyst. This increase in activity is attributed to changes in the Tafel step. Pt supported on BC led to a faster rate of adsorption of H_{ad} at equilibrium, suggesting an increase in Pt-H adsorption energy on Pt/BC catalysts close to equilibrium and, therefore, enhanced HOR activity on Pt/BC. Additionally, less oxide formation at higher potentials was noticed in HOR activity at 1.1 V vs. RHE on the 20 eq wt% Pt/BC, confirming the resilience of Pt/BC against sub-surface oxidation as asserted from the d-band vacancy at high potentials.

5.2.6 References

1. Schmidt, T.J. 2012. *ECS Transactions*. 45(2): 3-14.
2. Shao, Y., Yin, G. & Gao, Y. 2007. *Journal of Power Sources*. 171(2):558-566.
3. Lv, H., Mu, S., Cheng, N. & Pan, M. 2010. *Applied Catalysis B: Environmental.* 100(1–2):190-196.
4. Jackson, C., Smith, G.T., Inwood, D.W., Leach, A.S., Whalley, P.S., Callisti, M., Polcar, T., Russell, A.E., Levecque, P., Kramer, D. 2017. *Nature Communications*. 8:15802.

5. Mayrhofer, K.J.J., Strmcnik, D., Blizanac, B.B., Stamenkovic, V., Arenz, M. & Markovic, N.M. 2008. *Electrochimica Acta*. 53(7):3181-3188.
6. Mansour, A.N., Cook, J.W. & Sayers, D.E. 1984. *The Journal of Physical Chemistry.* 88(11):2330-2334.
7. Sasaki, K., Marinkovic, N., Isaacs, H.S. & Adzic, R.R. 2016. *ACS Catalysis.* 6(1):69-76.
8. Maillard, F., Pronkin, S. & Savinova, E.R. 2009. *In Fuel Cell Catalysis*. John Wiley & Sons, Inc. 507-566.
9. Owejan, J.P., Owejan, J.E. & Gu, W. 2013. *Journal of the Electrochemical Society*. 160(8):F824-F833.
10. Greszler, T.A., Caulk, D. & Sinha, P. 2012. *Journal of the Electrochemical Society*. 159(12):F831-F840.
11. Zalitis, C.M., Kramer, D. & Kucernak, A.R. 2013. *Physical Chemistry Chemical Physics*. 15(12):4329-4340.
12. Zalitis, C.M., Kramer, D., Sharman, J., Wright, E. & Kucernak, A.R. 2013. *ECS Transactions*. 58(1):39-47.
13. Offer, G. J. 2007. Quantitative measurement of species adsorbed on electrocatalysts during fuel cell relevant reactions. Ph.D. Thesis. Imperial College London.
14. Wise, A.M. 2012. Characterisation of bimetallic alloy and core-shell electrocatalysts. Ph.D. Thesis. University of Southampton.
15. Ravel, B. & Newville, M. 2005. *Journal of Synchrotron Radiation*. 12:537–541.
16. Kucernak, A.R. & Zalitis, C. 2016. *The Journal of Physical Chemistry C.* 120(20):10721-10745.
17. Brown, M., Peierls, R.E. & Stern, E.A. 1977. *Physical Review B.* 15(2):738-744.
18. Teliska, M., O'Grady, W.E. & Ramaker, D.E. 2005. *The Journal of Physical Chemistry B.* 109(16):8076-8084.
19. Zalitis, C. M., Kucernak, A. R., Sharman, J. & Wright, E. Design principles for platinum nanoparticles catalysing the hydrogen reaction: edges are much more active than facets. (unpublished)
20. Mukerjee, S., Srinivasan, S., Soriaga, M.P. & McBreen, J. 1995. *Journal of the Electrochemical Society.* 142(5):1409-1422.
21. Mukerjee, S., Srinivasan, S., Soriaga, M.P. & McBreen, J. 1995. *The Journal of Physical Chemistry.* 99(13):4577-4589.

22. Climent, V., Gomez, R., Orts, J. M., Rodes, A., Aldaz, A., Feliu, J. M. 1999. *Interfacial Electrochemistry: Theory: Experiment, and Applications*. New York. Taylor & Francis.
23. Arruda, T.M., Shyam, B., Ziegelbauer, J.M., Mukerjee, S. & Ramaker, D.E. 2008. *The Journal of Physical Chemistry C.* 112(46):18087-18097.
24. Zalitis, C.M., Sharman, J., Wright, E. & Kucernak, A.R. 2015. *Electrochimica Acta*. 176:763-776.
25. Nørskov, J.K., Bligaard, T., Logadottir, A., Kitchin, J. R., Chen, J.G., Pandelov, S. & Stimming, U. 2005. *Journal of the Electrochemical Society*. 152(3): J23-J26.
26. Nørskov, J.K., Bligaard, T., Rossmeisl, J. & Christensen, C.H. 2009. *Nature Chemistry*. 1(1):37-46.
27. Quaino, P., Juarez, F., Santos, E., Schmickler, W., 2014. *Journal of Nanotechnology*. 5:846-854.

5.2.7 Supplementary

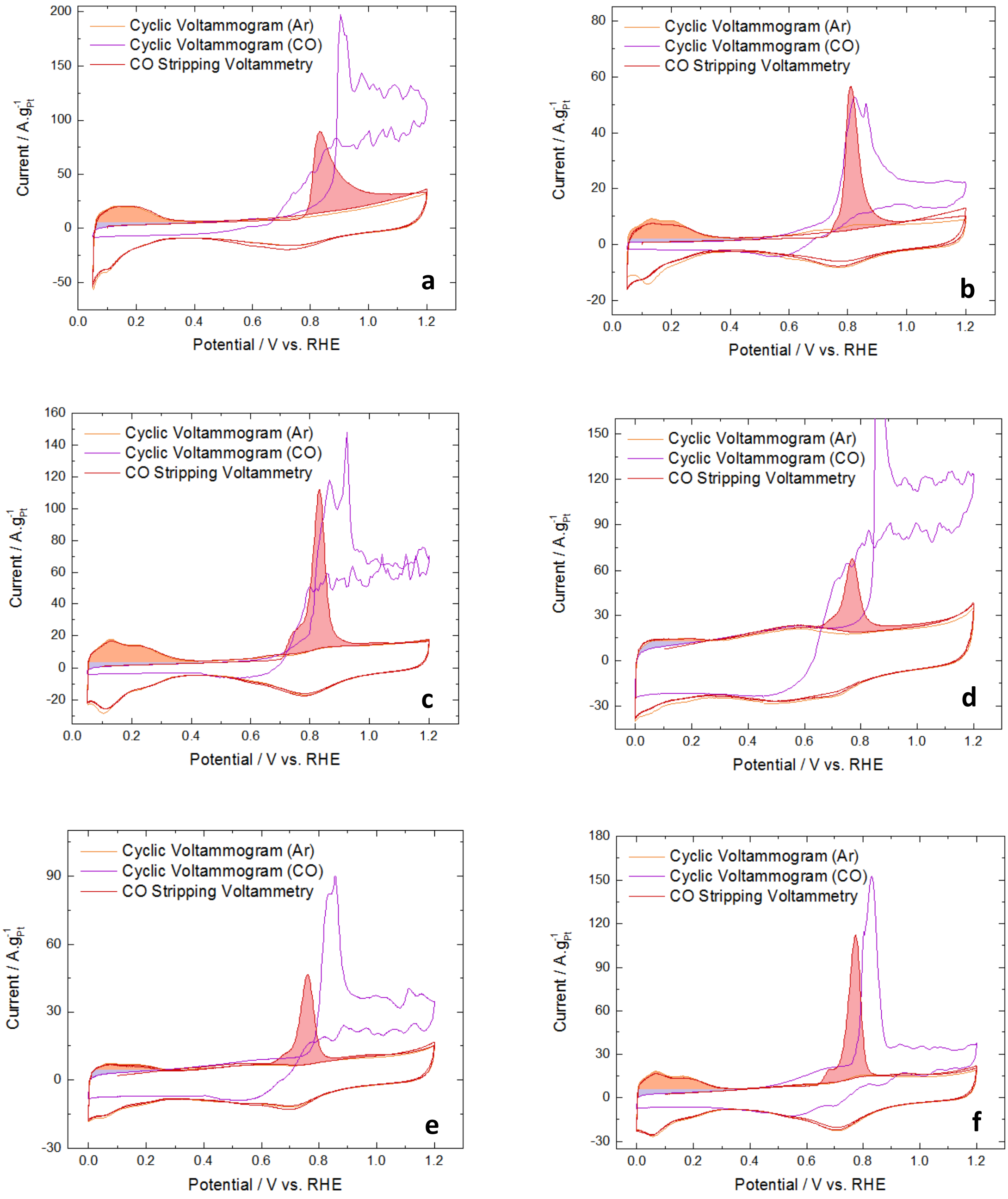

Figure S5.1.1: Cyclic voltammograms in Ar, Cyclic voltammograms in CO and CO stripping voltammograms in 0.1 M $HClO_4$ at room temperature for a) 10 wt% Pt/C, b) 20 wt% Pt/C, c) 40 wt% Pt/C, d) 10 eq wt% Pt/BC, e) 20 eq wt% Pt/BC and f) 40 eq wt% Pt/BC.

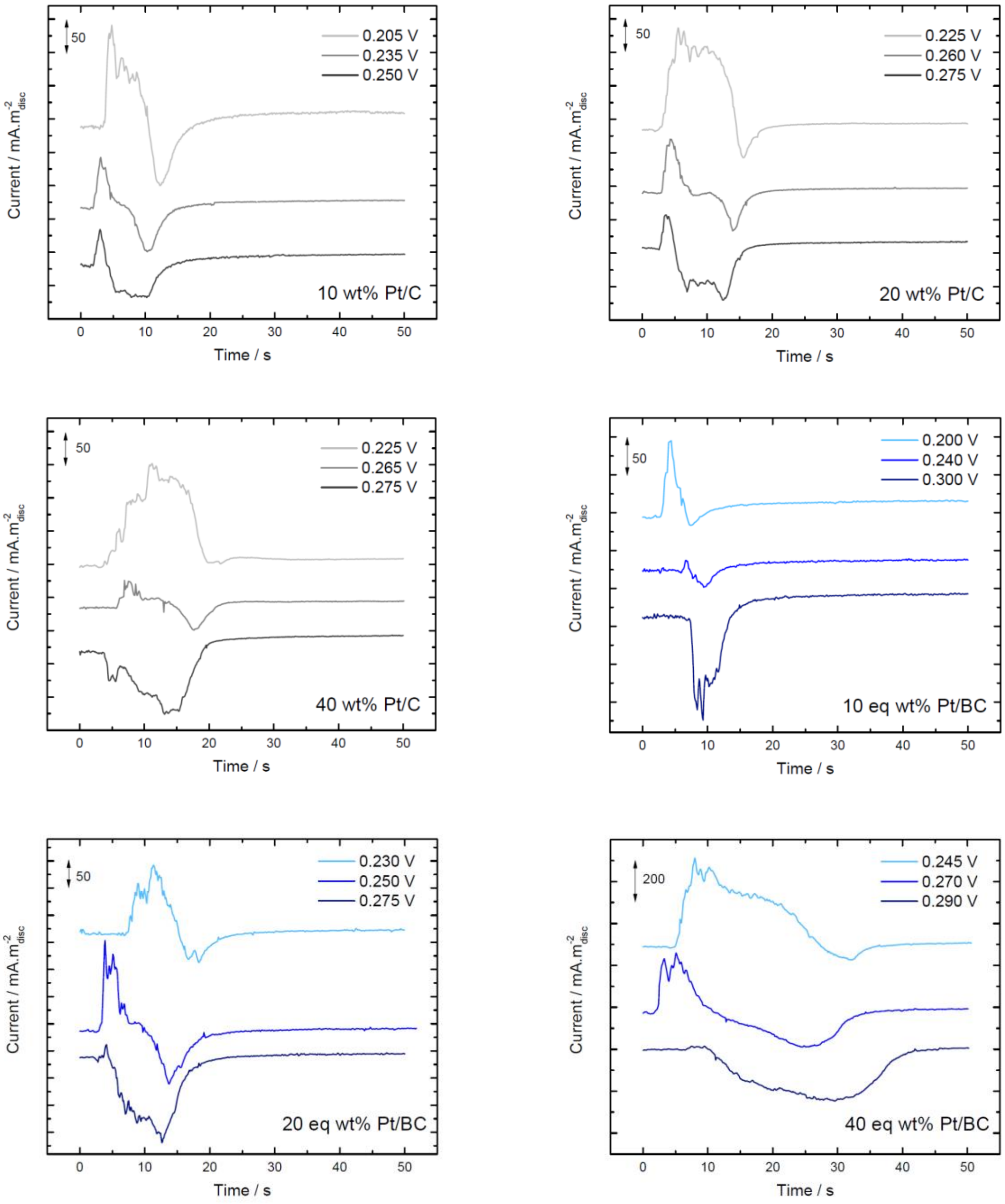

Figure S5.1.2: 3 representative CO displacement curves in 0.1 M $HClO_4$ at room temperature for the 10, 20 and 40 wt% Pt/C and 10, 20, 40 eq wt% Pt/BC catalysts.

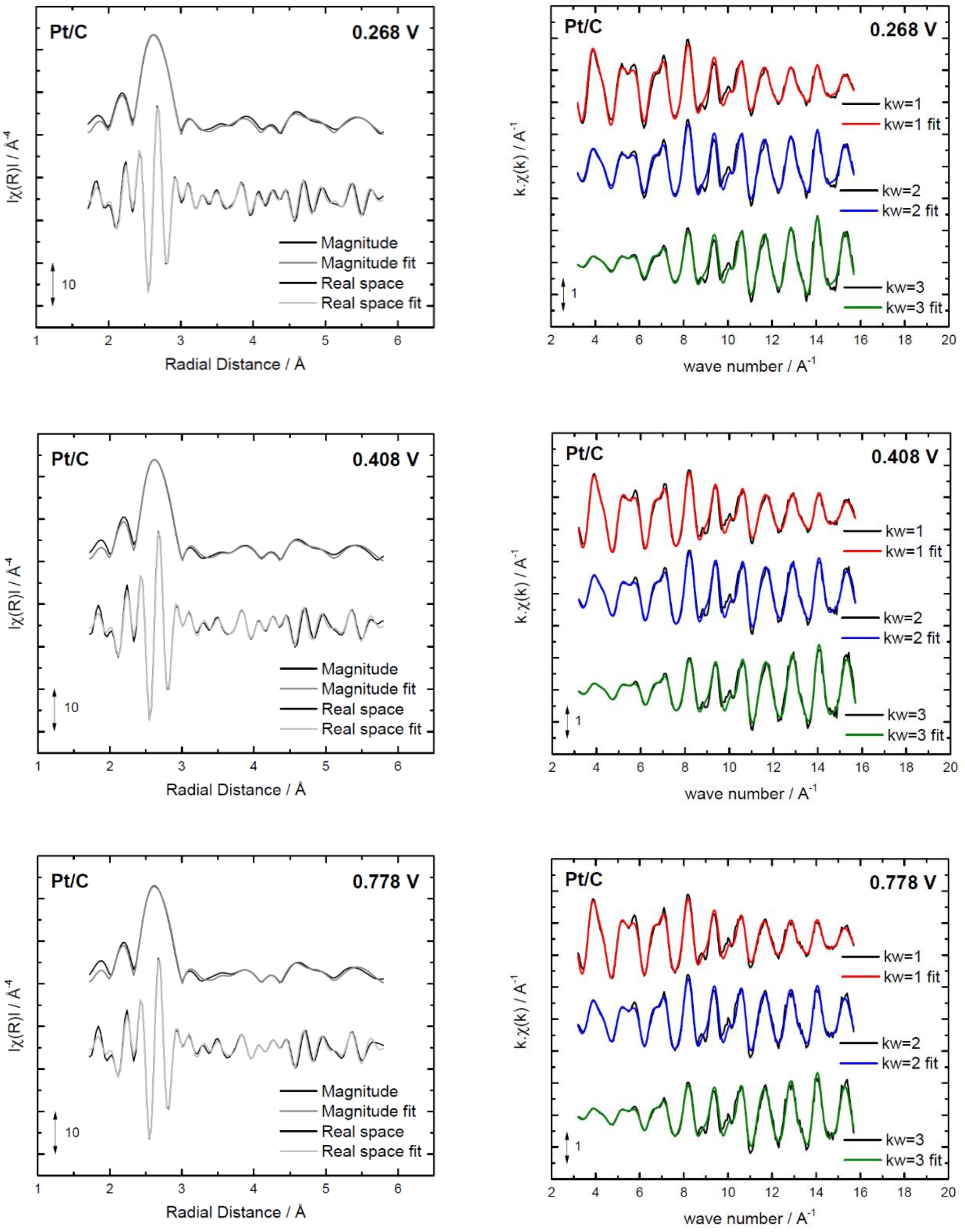

Figure S5.2.1. Figure caption on next page.

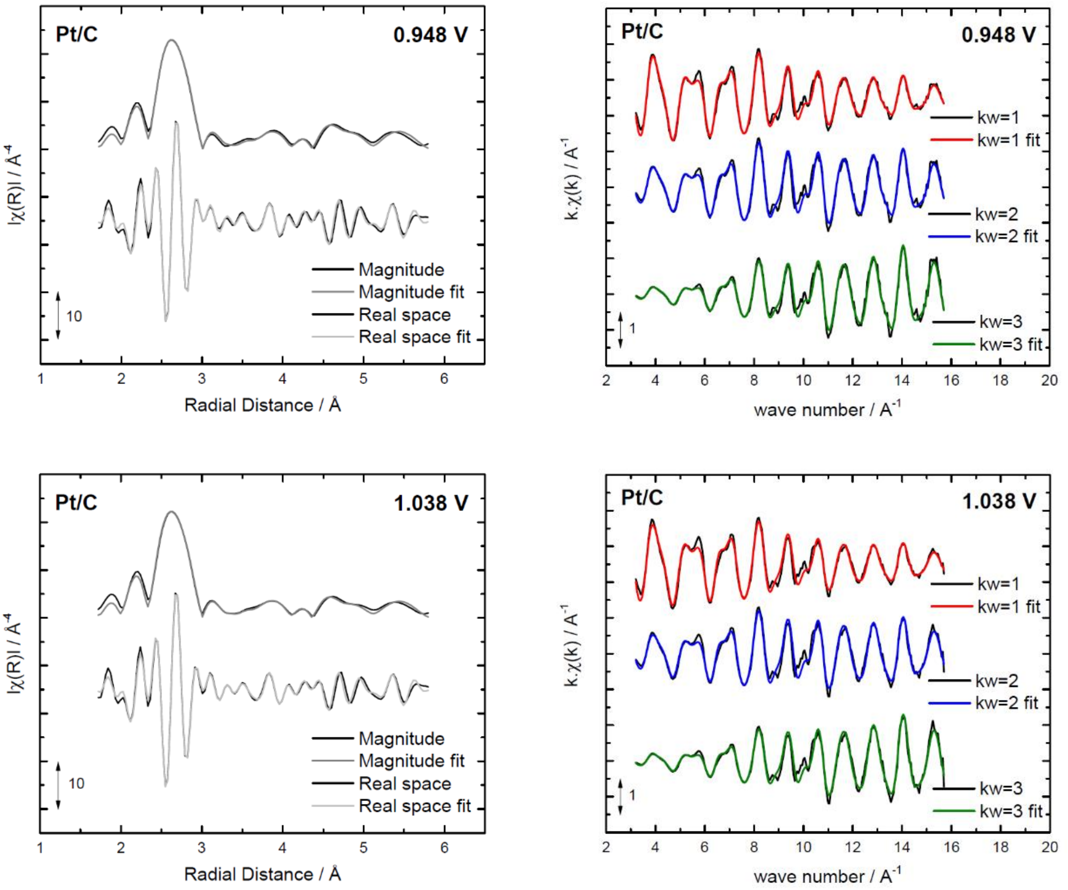

Figure S5.2.1: EXAFS R space magnitude and real space plots and k space plots, k weighting (kw)=1 is scaled by 8.2, kw=2 is unscaled and kw=3 is scaled by 0.09 of the Pt/C catalyst at different potentials in a 0.1 M $HClO_4$ electrolyte at room temperature.

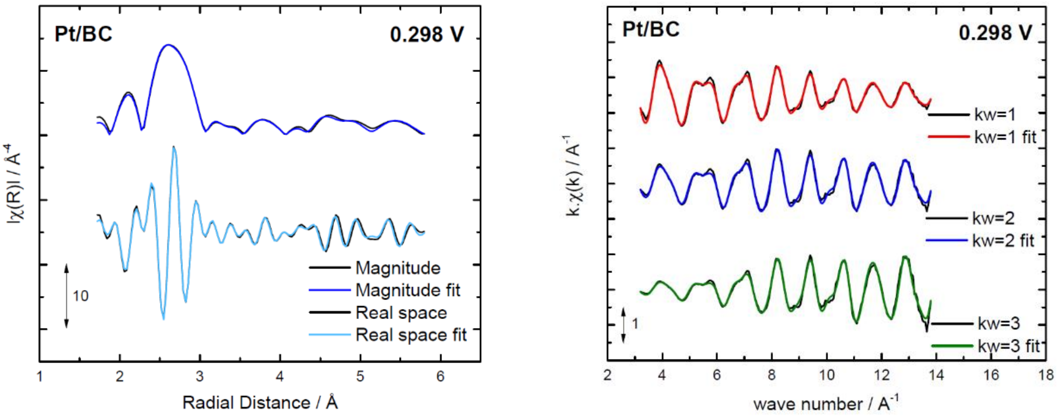

Figure S5.2.2. Figure caption on page 159.

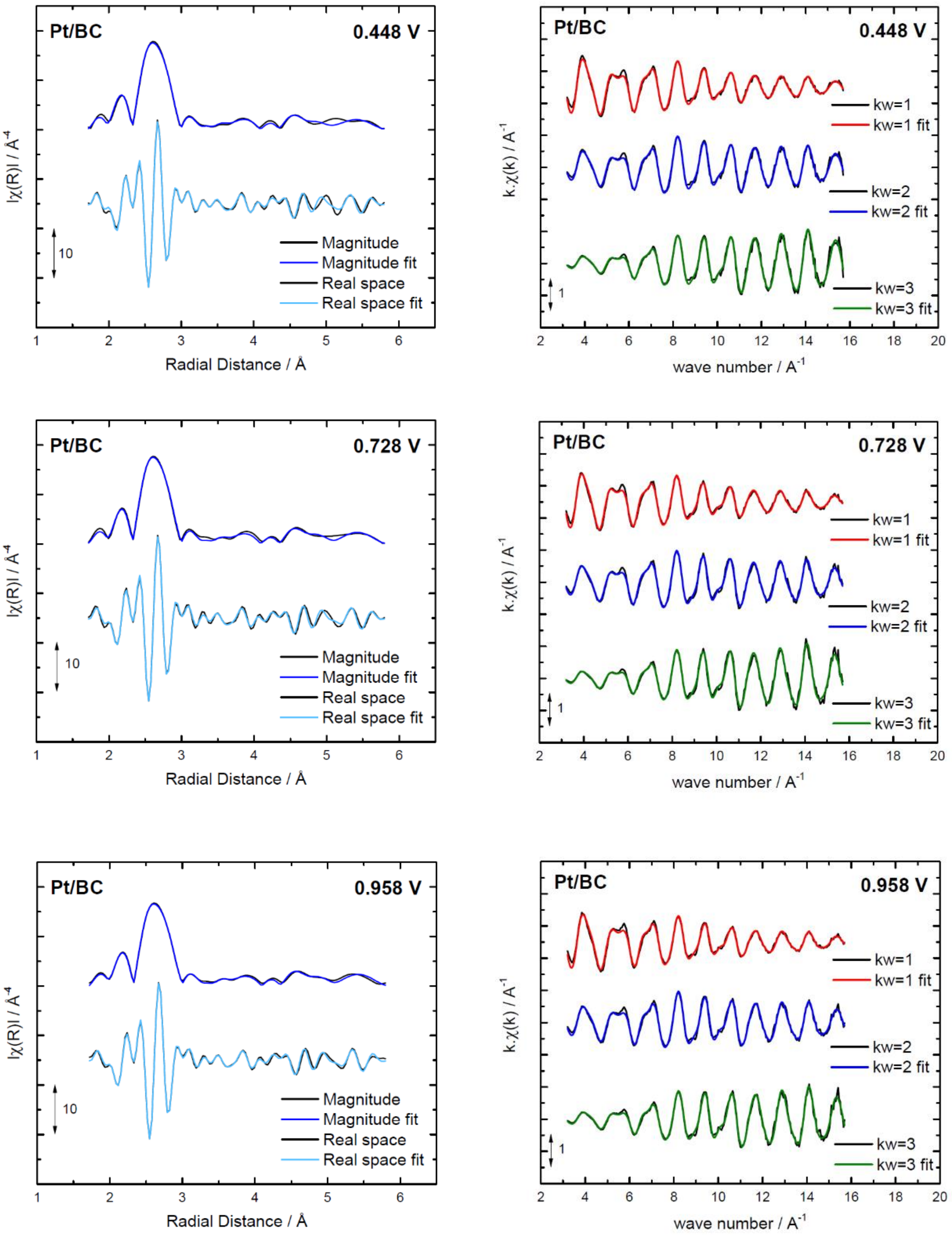

Figure S5.2.2, continued. Figure caption on next page.

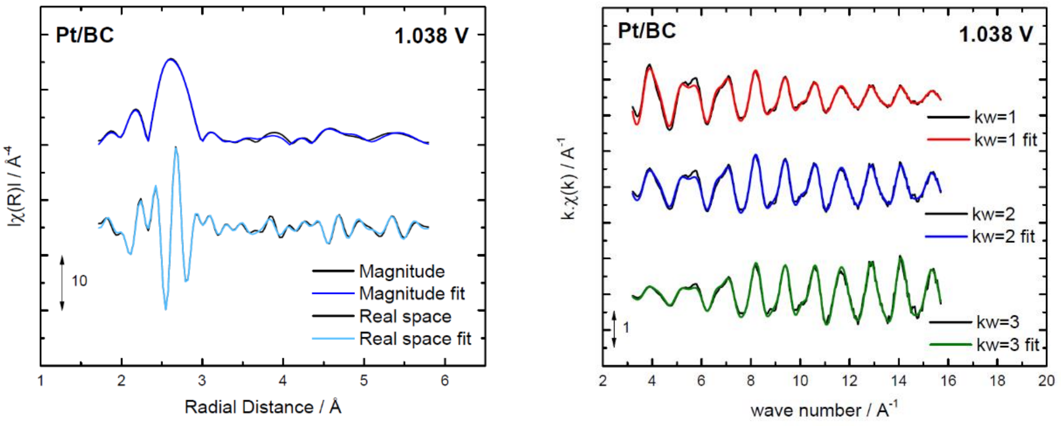

Figure S5.2.2: EXAFS R space magnitude and real space plots and k space plots, k weighting (kw)=1 is scaled by 6.9, kw=2 is unscaled and kw=3 is scaled by 0.11 of the Pt/BC catalyst at different potentials in a 0.1 M $HClO_4$ electrolyte at room temperature.

Table S5.2.1: First to fourth coordination numbers of the 20 wt% Pt/C and 20 eq wt% Pt/BC catalysts at different potentials.

Catalyst	Potential / V vs. RHE	N (Pt - Pt_1)	N (Pt – Pt_2)	N (Pt – Pt_3)	N (Pt – Pt_4)
20 wt% Pt/C	0.268	11.20 ± 0.6	7.16 ± 2.3	13.81 ± 5.1	8.28 ± 1.7
	0.408	10.95 ± 0.6	6.42 ± 2.2	14.64 ± 5.2	9.00 ± 1.8
	0.778	11.17 ± 0.6	6.55 ± 2.6	15.19 ± 5.7	9.16 ± 1.9
	0.948	10.88 ± 0.6	6.00 ± 2.1	14.83 ± 5.1	8.89 ± 1.8
	1.038	10.34 ± 0.6	5.22 ± 2.1	15.19 ± 5.9	9.38 ± 2.0
20 eq wt% Pt/BC	0.298	9.62 ± 0.5	4.33 ± 2.0	10.83 ± 4.3	7.94 ± 1.8
	0.448	9.72 ± 0.4	3.89 ± 1.7	12.52 ± 4.6	8.94 ± 1.7
	0.728	9.77 ± 0.4	4.42 ± 1.7	11.38 ± 3.9	8.19 ± 1.5
	0.958	9.78 ± 0.4	4.91 ± 1.7	11.23 ± 3.8	8.30 ± 1.4
	1.038	9.30 ± 0.4	4.38 ± 1.8	9.89 ± 3.5	8.03 ± 1.6

Table S5.2.2: First to fourth distances of neighbouring atoms of the 20 wt% Pt/C and 20 eq wt% Pt/BC catalysts at different potentials.

Catalyst	Potential / V vs. RHE	R (Pt - Pt_1) / Å	R (Pt – Pt_2) / Å	R (Pt – Pt_3) / Å	R (Pt – Pt_4) / Å	R Error / 10^4 Å
Pt/C	0.268	2.759	3.902	4.779	5.518	7.10
	0.408	2.759	3.902	4.779	5.518	6.69
	0.778	2.760	3.903	4.781	5.520	7.43
	0.948	2.761	3.905	4.782	5.522	7.00
	1.038	2.761	3.905	4.783	5.523	7.55
Pt/BC	0.298	2.751	3.891	4.766	5.503	7.64
	0.448	2.752	3.891	4.767	5.505	6.43
	0.728	2.753	3.893	4.768	5.506	6.36
	0.958	2.753	3.893	4.768	5.506	6.25
	1.038	2.753	3.893	4.768	5.506	6.61

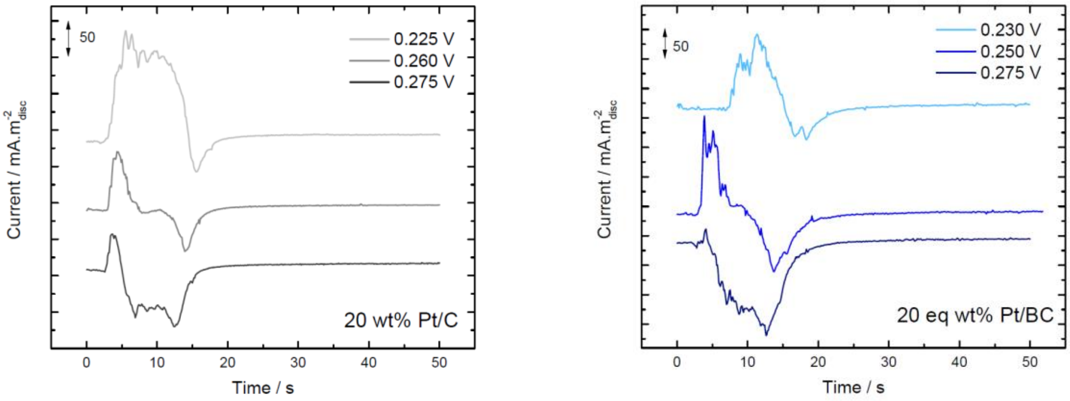

Figure S5.2.3: The CO displacement transient curves for 3 potentials on the 20 wt% Pt/C and 20 eq wt% Pt/BC catalysts in 0.1 M $HClO_4$ at room temperature.

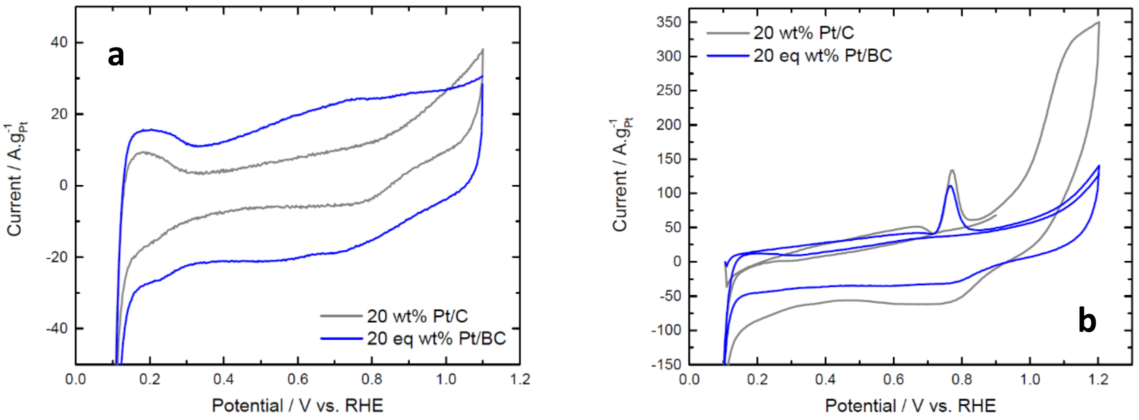

Figure S5.2.4: (a) Cyclic voltammograms and (b) CO stripping voltammetry of Pt/C and Pt/BC in a nitrogen saturated 1 M $HClO_4$ electrolyte solution at room temperature and a scan rate of 10 mV.s^{-1}.

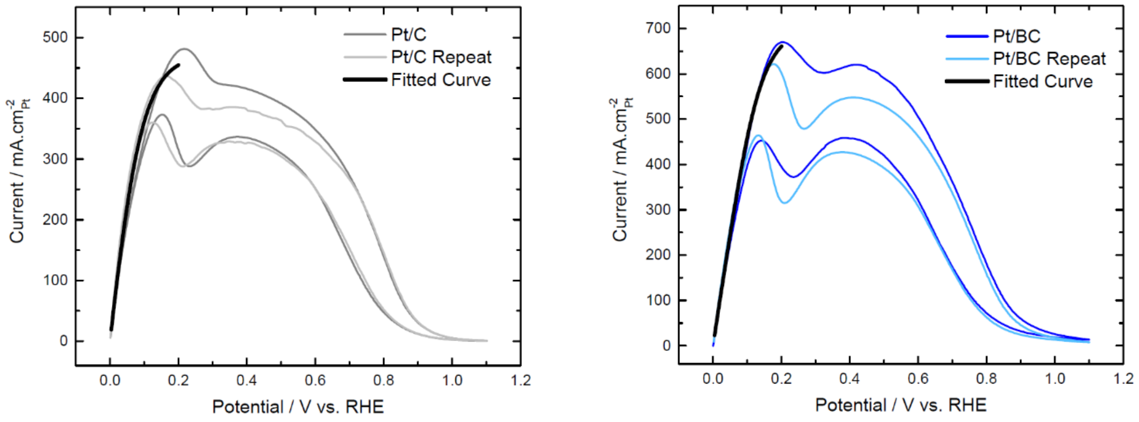

Figure S5.2.5: HOR curves for Pt/C and Pt/BC catalysts with the fitted model in the potential range of 0 – 0.2 V vs. RHE.

Table S5.2.3: Fitted and Derived Parameters used to model HOR data, where β is the molecular symmetry factor, $\theta_{Had}^{TV,eq}$is the coverage of H_{ad} species at equilibrium and $\Delta_{ads}G_{H2}^{\theta}$ is the free energy of adsorption per mole of bimolecular hydrogen [16].

	Type	20 wt% Pt/C	20 eq wt% Pt/BC
B (where $B = \sqrt{\frac{a_{H2}k_{ad}}{k_{des}}}$)	Fit	0.702	0.618
Z (where $Z = \frac{k_2^{eq}}{k_{des}}$)	Fit	1.100	0.492
β	Fixed	0.5	0.5
$\theta_{Had}^{TV,eq}$ (where $\theta_{Had}^{TV,eq} = \frac{1}{1+\frac{1}{B}}$)	Derived	0.412	0.382
$\Delta_{ads}G_{H2}^{\theta}$	Derived	1755 J.mol^{-1}	2390 J.mol^{-1}
k_{des}	Derived	4.96 x10^{-6} mol.cm^{-2}.s^{-1}	9.57 x10^{-6} mol.cm^{-2}.s^{-1}
k_{ad}	Derived	2.44 x10^{-6} mol.cm^{-2}.s^{-1}	3.65 x10^{-6} mol.cm^{-2}.s^{-1}
k_2^{eq}	Derived	5.45 x10^{-6} mol.cm^{-2}.s^{-1}	4.71 x10^{-6} mol.cm^{-2}.s^{-1}
k_{-2}^{eq} (where $k_{-2}^{eq} = \frac{Bk_2^{eq}}{a_{H+}}$)	Derived	3.82 x10^{-6} mol.cm^{-2}.s^{-1}	2.91 x10^{-6} mol.cm^{-2}.s^{-1}
Real change current density (where $\frac{j_0^{TV}}{k_{des}} = F\Theta_{Had}^{TV,eq}Z$	Derived	0.217 A.cm^{-2}	0.173 A.cm^{-2}
Linear extrapolation exchange current	Derived	0.130 A.cm^{-2}	0.131 A.cm^{-2}

(where $\frac{j_0^{TV}}{k_{des}} = F\Theta_{Had}^{TV,eq}(\frac{1}{\left(\frac{1}{Z}+\frac{1}{4}+\frac{1}{4B}\right)})$			
Anodic Limiting Current (where $\frac{j_0^{TV}}{k_{des}} = 2FB^2$)	Derived	0.472 A.cm^{-2}	0.704 A.cm^{-2}
Cathodic Limiting Current (where $\frac{j_0^{TV}}{k_{des}} = 2F$)	Derived	-0.958 A.cm^{-2}	-1.846 A.cm^{-2}

Chapter 6

Conclusion and Future Outlook

Platinum was successfully deposited on silicon carbide and boron carbide-graphite composite support materials. These catalysts were compared to commercial Pt/C catalysts in order to investigate metal-support interactions and this influence thereof on electrocatalytic activity and catalyst durability.

6.1 Metal-Support Interaction and Adsorption

The carbide/carbide-graphite supported Pt catalysts were more positively charged under potentiostatic control in electrochemical environments when compared to Pt/C. The electronic interaction between Pt and the support was first explored using X-ray photoelectron spectroscopy (XPS). Once the spectra were normalised for the same C-C peak in the C 1s spectra, shifts in the binding energy of Pt 4f in relation to this C-C peak were used as an indication of charge transfer differences between supports. The Pt/SiC XPS spectra showed a shift of the Pt 4f spectra to higher binding energies of 0.4 - 0.6 eV from Pt/C, while the Si-C bond in both the Si 2p and C 1s spectra shifted to lower binding energies when compared to bare SiC. A similar trend was observed in the XPS Pt 4f spectra on the Pt/BC catalysts, with a shift of ~ 0.6 eV to higher binding energies from the Pt 4f spectra of Pt/C. These increases in Pt 4f binding energy on the SiC and BC supported catalysts, compared to Pt/C, suggested more electron transfer from the SiC and BC to Pt metal than from C to Pt. This stronger electron transfer can be rationalised by a larger difference in work function (Φ), as illustrated in Figure 6.1. The equilibration of the respective Fermi levels resulted in a more negatively charged Pt particle on the Pt/SiC and Pt/BC catalysts under UHV conditions by a metal-support interaction.

Characterisation of the carbide/carbide-graphite composite supported catalysts in electrochemical environment suggested, however, more positively charged Pt particles on the Pt/SiC and Pt/BC catalysts as *in-situ* X-ray absorption near edge spectra *(*XANES) showed an increase in Pt d-band vacancy, compared to Pt/C. This apparent reverse in charge was explained by noting the difference between UHV and potential controlled environments.

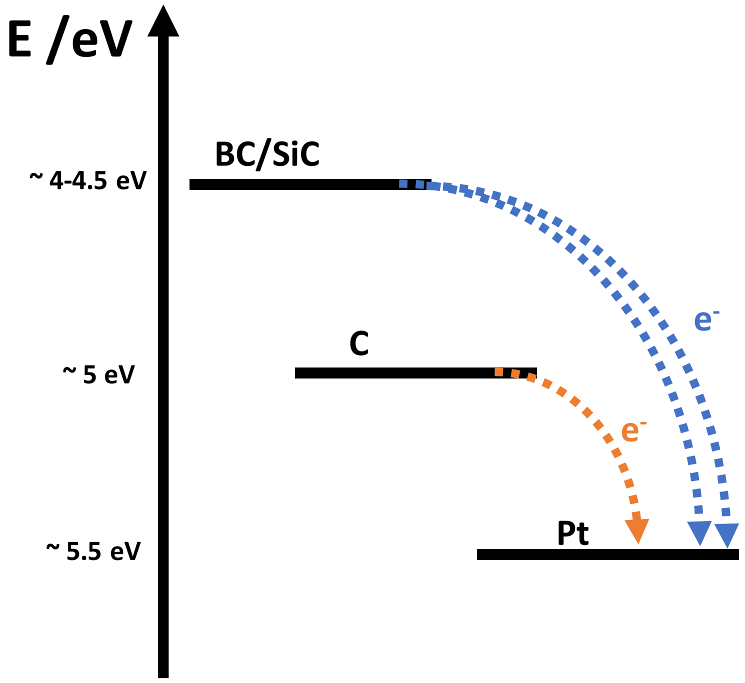

Figure 6.1: Illustration of equilibration of fermi levels on charge transfer from support to Pt

The XPS spectra were collected under UHV and, hence, overall charge neutrality, whereas electrochemical responses were influenced by the potential and adsorbates on the Pt surface. As illustrated in Figure 6.2, the catalyst work function is proportional to the potential of zero charge (pzc), thus the smaller work functions of the Pt/SiC and Pt/BC catalysts compared to Pt/C catalyst should result in a shift to lower pzc's. Under the same potential, the supported catalysts are at varying ΔV from their pzc (Figure 6.2), with Pt/SiC and Pt/BC further from pzc compared to Pt/C. The larger the ΔV, the more positively charged the Pt surface, therefore the Pt/SiC and Pt/BC catalysts demonstrate a more positively charged surface than the Pt/C at the same potential. The d-band vacancies on the catalysts in the double layer potential region, as given by *in-situ* XANES, follow the order Pt/SiC (0.424 holes) < Pt/BC (0.404 holes) < Pt/C (0.355 holes), which is in reasonable agreement with expected support work functions.

This simple understanding, however, should be expected to have limited validity in electrochemical environments as electrosorption phenomena complicate the interaction between charged catalyst particles and the electrolyte/adsorbates/intermediates. The CO displacement charge was investigated on the Pt/BC and Pt/C catalysts to probe electrosorption characteristics. These CO displacement results displayed a clear increase in charge density of both anions (<ptzc) and cations (>ptzc) on the Pt/BC catalysts at potentials around the ptzc. Further, the gradient of the CO displacement charge was Pt loading dependent for Pt/BC (larger gradient for higher loading), whereas such a dependence of the gradient could not be seen for Pt/C. The charge displacement gradient is not well understood. However, these results give an indication of an effect on electrosorption on the Pt supported nanoparticles for cations, as well as anions, due to an electronic metal-support interaction.

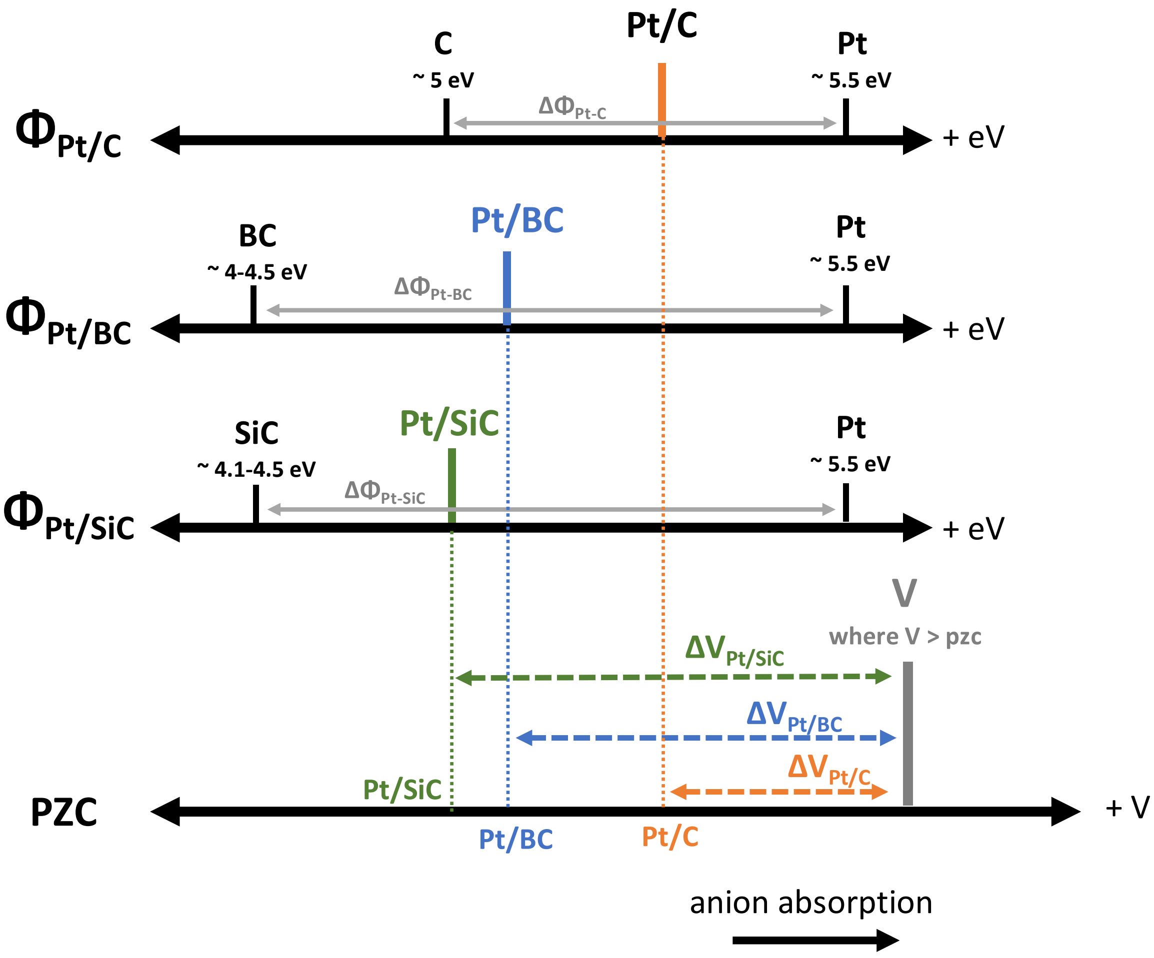

Figure 6.2: Illustration of the proposed relationship between the work functions of Pt and the support materials on the overall catalyst work function, the work function relationship with potential of zero charge (pzc) and potential of zero charge and anion adsorption at a potential (V).

6.2 Oxide Formation on Carbide Supported Catalysts

The Pt/SiC and Pt/BC catalysts were less prone to oxidation. The Pt d-band vacancy at potentials in the oxide adsorption region change more strongly as the adsorbed anions are replaced by more strongly adsorbing OH and oxygen species. The strongly adsorbing oxygen species lead to a non-linear increase in d-band vacancy at higher potentials. This non-linear increase in d-band vacancy was seen on all catalysts, however, a delay of about 0.2 V was seen on the Pt/SiC and Pt/BC catalysts, indicating a lower tendency of Pt to oxidise if supported on the carbides relative to being supported on C.

Correspondingly, the Δμ technique demonstrated a more stable Pt surface during O or OH species adsorption. The Δμ technique showed an initial negative response on the Pt/C curves, attributed to sub-surface oxygen on the Pt surface due to place-exchange. The absence of the negative peak on the Pt/SiC and Pt/BC catalysts is noteworthy and ascribed to a lower tendency to form sub-surface oxygen on the SiC and BC supported catalysts. This was in agreement with the lower tendency of Pt to oxidise on carbide support materials. Additionally, less oxide formation at higher potentials was noticed in HOR activity at 1.1 V vs. RHE on the Pt/BC, confirming the assertions from the d-band vacancy at high potentials.

6.3 Electrochemical Activity

The Pt/BC catalysts showed higher activity for the oxygen reduction reaction (ORR) under rotating disc electrode (RDE) conditions. The Pt/BC catalysts followed a similar particle size dependence as seen for Pt/C, but a ~50 % higher surface area specific activity at 0.9 V vs. RHE. The increase of surface area specific current density was significantly larger than the commercial Pt/C catalyst activities measured in this study, and other published research utilising similar carbons. It was, therefore, concluded that electronic equilibration between the support material and the Pt nanoparticles affected the ORR activity of the catalyst. At high potentials, higher ORR activity was correlated with lower oxophilicity of the Pt surface. The more positively charged Pt surface at intermediate potentials, with anion adsorption approaching full coverage, seems to not be too strongly adsorbed as to hinder oxygen reduction activity, while the delay in the onset of a strongly bonded oxide surface assists in oxygen reduction activity. This phenomenon is not completely understood.

HOR studies under high mass transport and low catalyst loading conditions showed enhanced activity on the Pt/BC catalyst, when compared to the Pt/C catalyst. This increase in activity was attributed to changes in the Tafel step at potentials below the ptzc. Pt/BC was shown to have a faster rate of adsorption of H_{ad} at equilibrium, suggesting an increase in Pt-H adsorption energy on these catalysts close to equilibrium and, therefore, enhanced HOR activity on Pt/BC.

The SiC support was not sufficiently conductive and therefore carbon was added to the catalyst ink to improve conductivity of the Pt/SiC catalysts for electrochemical testing. Although electronic metal support interactions on these catalysts was observed, the Pt nanoparticles were unstable on the SiC support which resulted in Pt agglomerated and some Pt migration into the carbon surface during sonication of the catalyst ink. Consequently, the influence of a metal-support interaction on ORR activity could not be determined accurately on the Pt/SiC catalysts.

6.4 Accelerated Durability Tests

The degradation of ECSA during the catalyst durability study (0.6 – 1 V vs. RHE) was considerably faster on the Pt/C catalyst compared to the Pt/BC catalyst. Since particle sizes and shapes of both catalysts were initially similar, this difference in degradation rate between the catalysts was not attributed to differences in particle size or shape. Therefore, a stronger electronic metal-support interaction between Pt and the BC support is suggested to reduce platinum dissolution and/or agglomeration during potential cycling. The ORR activities of the degraded catalysts suggested that Pt agglomeration was inhibited for Pt/BC relative to the Pt/C catalyst, and degradation on the Pt/BC catalyst was predominantly due to Pt dissolution. It was proposed that a stronger dipole field was formed at the Pt:BC interface relative to Pt:C interface. This stronger dipole interaction was suggested to reduce the mobility of Pt nanoparticles on the surface of the BC support and thus reduced Pt agglomeration during degradation cycling. In principle, the stronger dipole field allows the Pt nanoparticles to adopt a lower energy state on BC, which may mitigate dissolution as well. Additionally, the Pt/BC catalysts have demonstrated a decrease in surface oxidation at potentials below 1 V vs. RHE, associated with Pt dissolution, further assisting with stability during degradation cycling. Catalyst degradation on Pt/SiC+C showed slight support surface oxidation at these potentials which resulted in a less well refined H_{UPD} region and subsequent decrease in ECSA. The cyclic voltammograms shown before and after 6000 cycles demonstrate less change to the H_{UPD} region when compared to Pt/C, however, due to the low initial ECSA and changes to the support capacitance after degradation, small changes to this region result in a larger percentage ECSA loss during cycling. However, the electrochemical characterisations for the Pt/SiC+C catalysts were unreliable due to the Pt agglomeration during sonication of the ink before testing.

Catalysts on all supports showed clear activity loss if cycled at high potentials. However, activity loss on C and SiC+C was attributed to carbon corrosion and Pt detachment/dissolution, while activity loss on BC was suggested to be due to formation of an insulating oxide layer rather than Pt detachment/dissolution. The support durability (1.0 – 1.5 V vs. RHE) was completed on the bare supports, as well as the Pt/BC, Pt/SiC+C and Pt/C catalysts. The cyclic voltammograms after degradation of the bare carbon and SiC+C materials presented significant oxidation, indicated by an increased capacitance. The degradation of carbon at high potentials was described as an increase in interfacial double layer capacitance due to a more hydrophilic surface or an increase in the roughness of the carbon surface. The increase in capacitance in the SiC+C cyclic voltammograms was also attributed to an increase in the carbon hydrophilicity and/or roughness on the carbon surface. The BC degradation showed a reduction in current after cycling, this was attributed to the oxidation of boron carbide, and thus the support surface is dissolved into the electrolyte or, more likely, an insulating oxide layer is formed on the surface of the support material.

The Pt/C cyclic voltammograms after cycling (1.0 – 1.5 V vs. RHE) showed the double layer charging increased after the durability study and the Pt ECSA decreased significantly after 6000 cycles. This was explained by the weakening of the attached platinum on the carbon surface by the oxidation of carbon, leading to platinum detachment from the surface. This process leaded to platinum agglomeration as well as platinum dissolution, both resulting in a loss of active surface area and therefore reaction activity. This assertion was confirmed by TEM images of Pt/C after degradation (1.0 – 1.5 V vs. RHE), which displayed significant Pt agglomeration. Cyclic voltammograms before and after degradation of the Pt/SiC+C catalyst demonstrated a significantly reduced H_{UPD} region after 6000 cycles. It was asserted that degradation was due to an increase in the carbon hydrophilicity and/or roughness on the carbon surface, as it appeared the degradation of Pt/SiC+C mimicked that of Pt/C. However, the Pt/SiC+C catalyst was considerably less durable than Pt/C, rendering the SiC+C support an unattractive alternative support material to carbon. The deactivation of the Pt/BC catalyst was explained by an insulating boron oxide layer, which reduced the electroactivity of the material. The insulating boron oxide layer formed at high potentials caused a more resistive support, which resulted in a cyclic voltammogram without Pt features. However, unlike the Pt/C catalyst at high potentials, TEM images after degradation of the Pt/BC catalyst did not show Pt agglomeration. This continued stability of the Pt nanoparticles when supported on BC, despite the oxidation of the BC surface, re-affirmed the lower mobility of Pt nanoparticles on the surface of the BC support and thus reducing Pt agglomeration during degradation cycling. It also allowed to speculate that degradation might be reversible if the support can be reversibly reduced again after oxide formation.

6.5 Future Outlook

In this thesis, the electronic metal support interactions between platinum and selected carbide based supports were explored, which were shown to influence the electrochemical characteristics of the catalyst. Stronger conclusions on the validity of the theory described above can be only be drawn if further investigations take place on a number of different supports with a range of work functions. In addition, the work functions of carbides vary significantly by changes to the crystal structure and surface features. Therefore, measurements of the work functions of the supports used should be done. Additionally, the correlation between potential of total zero charge, charge displacement gradients and work function requires a deeper understanding in future works.

Further investigations are also needed into the stability of alternative support materials at high potentials (1 – 1.5 V vs. RHE) and the formation of the insulating oxidised layer on the support at these potentials. This investigation should include high temperature (80 °C) degradation studies at high potentials to more accurately mimic degradation in a fuel cell. It would also be interesting to widen the research into other support materials, such as stable oxides. Lastly, it is imperative to test these catalysts in a fuel cell, to investigate if the *ex-situ* characterisations hold true under more relevant conditions.